

UNCLASSIFIED

AD NUMBER

AD905043

LIMITATION CHANGES

TO:

Approved for public release; distribution is unlimited.

FROM:

Distribution authorized to U.S. Gov't. agencies only; Test and Evaluation; SEP 1972. Other requests shall be referred to Army Materials and Mechanics Research Center, ATTN: AMXMR-PL, Watertown, MA 02172.

AUTHORITY

AMMRC per DTIC form 55

THIS PAGE IS UNCLASSIFIED

AD905043



AD

AMMRC CTR 72-19

BRITTLE MATERIALS DESIGN, HIGH TEMPERATURE GAS TURBINE

Technical Report By:

Arthur F. McLean, Ford Motor Company, Dearborn, Michigan 48121

Eugene A. Fisher, Ford Motor Company, Dearborn, Michigan 48121

Raymond J. Bratton, Westinghouse Electric Corporation, Pittsburgh, Pennsylvania 15235

September, 1972

Interim Report, January 1, 1972 to June 30, 1972

Contract Number DAAG 46-71-C-0162

Sponsored by the Advanced Research Projects Agency

ARPA Order Number 1849

Project Code Number 1D10

Agency Accession Number DA OD 4733

Distribution limited to U. S. Government agencies only; Test and Evaluation data; September 1972. Other requests for this document must be referred to the Director, Army Materials and Mechanics Research Center, ATTN: AMXMR-PL, Watertown, Massachusetts 02172

DDC  
R  
NOV 24 1972  
R  
L  
U  
G  
C

Prepared for

ARMY MATERIALS AND MECHANICS RESEARCH CENTER  
Watertown, Massachusetts 02172

THIS REPORT HAS BEEN DELIMITED  
AND CLEARED FOR PUBLIC RELEASE  
UNDER DOD DIRECTIVE 5200.20 AND  
NO RESTRICTIONS ARE IMPOSED UPON  
ITS USE AND DISCLOSURE.

DISTRIBUTION STATEMENT A

APPROVED FOR PUBLIC RELEASE;  
DISTRIBUTION UNLIMITED.

The findings in this report are not to be construed as an official Advanced Research Projects Agency, Department of the Army, or U.S. Government position, either expressed or implied, unless so designated by other authorized documents.

Mention of any trade names or manufacturers in this report shall not be construed as advertising nor as an official indorsement or approval of such products or companies by the United States Government

#### DISPOSITION INSTRUCTIONS

Destroy this report when it is no longer needed. Do not return it to the originator.

AMMRC CTR 72-19

**BRITTLE MATERIALS DESIGN, HIGH TEMPERATURE GAS TURBINE**

Technical Report By:

Arthur F. McLean, Ford Motor Company, Dearborn, Michigan 48121  
Eugene A. Fisher, Ford Motor Company, Dearborn, Michigan 48121  
Raymond J. Bratton, Westinghouse Electric Corporation, Pittsburgh, Pennsylvania 15235

September 1972

Interim Report, January 1, 1972 to June 30, 1972

Contract Number DAAG 46-71-C-0162

Sponsored by the Advanced Research Projects Agency

ARPA Order Number 1849

Project Code Number 1D10

Agency Accession Number DA OD 4733

Distribution limited to U. S. Government agencies only; Test and Evaluation data; September 1972. Other requests for this document must be referred to the Director, Army Materials and Mechanics Research Center, ATTN: AMXMR-PL, Watertown, Massachusetts 02172

Prepared for:

ARMY MATERIALS AND MECHANICS RESEARCH CENTER  
Watertown, Massachusetts 02172

## ABSTRACT

The "Brittle Materials Design, High Temperature Gas Turbine" program is to demonstrate successful use of brittle materials in demanding high temperature structural applications. A small vehicular gas turbine and a large stationary gas turbine, each utilizing uncooled ceramic components, will be used in this iterative design and materials development program. Both the contractor, Ford Motor Company, and the subcontractor, Westinghouse Electric Corporation, have had in-house research programs in this area prior to this contract.

In the vehicular turbine project, the improved second generation (Design B) stationary ceramic components made of reaction bonded silicon nitride have undergone initial engine tests successfully. A computer program has been developed to determine heat transfer in the rotor, attachment, and shaft assembly. A design study was completed for the attachment of the rotor to the shaft. A complete integral rotor has been fabricated by chemical vapor deposition of silicon carbide, although material quality needs improvement. An etching technique has been developed permitting microstructure study of any form of silicon nitride, and significant determinations were made of ceramic material properties.

In the stationary turbine project, a first generation 3-piece vane assembly was designed and analyzed. A complete set of silicon nitride airfoil vanes were fabricated. Engineering properties of silicon nitride and silicon carbide have been characterized. A better understanding of the effects of microstructure on properties of hot pressed silicon nitride was obtained. Data was obtained on static oxidation kinetics and corrosion-erosion behavior.

## FOREWORD

This report is the second semi-annual technical report of the "Brittle Materials Design, High Temperature Gas Turbine" program initiated by the Advanced Research Projects Agency, ARPA Order Number 1849, and monitored by the Army Materials and Mechanics Research Center, under Contract Number DAAG-46-71-C-0162. This is an incrementally-funded five year program.

Since this is an iterative design and materials development program, design concepts and materials selection and/or properties presented in this report will probably not be those finally utilized. Thus all design and property data contained in the semi-annual reports must be considered tentative, and the reports should be considered to be illustrative of the design, materials, processing, and NDT techniques being developed for brittle materials.

The principal investigator of this program is Mr. A. F. McLean, Ford Motor Company, and the technical monitor is Dr. A. E. Gorum, AMMRC. The authors would like to acknowledge the valuable contributions in the performance of this work by the following people:

### Ford Motor Company

D. Alexander, R. R. Baker, P. Beardmore, D. J. Cassidy, J. C. Caverly, D. A. Davis, G. C. DeBell, W. A. Fate, M. U. Goodyear, D. L. Hartsook, P. H. Havstad, E. R. Herrmann, R. A. Jeryan, C. F. Johnson, J. A. Mangels, W. E. Meyer, T. Mohr, P. F. Nicholls, A. Paluszny, J. J. Schuldies, J. M. Seofield, K. H. Styhr, W. Trela, N. F. Waugh, T. J. Whalen.

### Westinghouse Electric Corporation

C. R. Booher, Jr., S. M. DeCorso, J. DeKlerk, E. S. Diaz, D. M. Fantozzi, W. C. Frazier, A. N. Holden, D. D. Lawthers, L. Kish, R. Kossowsky, F. F. Lange, S. Y. Lee, S. D. Leshnoff, D. G. Miller, S. Mumford, T. J. Rahaim, J. D. Roughgarden, R. J. Schaller, S. C. Singhal, S. Twiss, C. Visser, E. H. Wiley, D. D. Wood, W. E. Young.

## TABLE OF CONTENTS

	<u>Page No.</u>
Title Page . . . . .	i
Abstract . . . . .	ii
Forward . . . . .	iii
Table of Contents . . . . .	iv
List of Illustrations . . . . .	v
List of Tables . . . . .	xiii
1. Introduction . . . . .	1
2. Summary of Progress . . . . .	9
2.1 Vehicular Turbine Project . . . . .	9
2.2 Stationary Turbine Project . . . . .	11
2.3 Materials Technology — Vehicular & Stationary Turbine Projects	13
3. Progress on the Vehicular Turbine Project . . . . .	15
3.1 Ceramic Rotor Development . . . . .	15
3.1.1 Design and Analysis . . . . .	17
3.1.2 Materials and Fabrication . . . . .	28
3.2 Metal Rotor Development . . . . .	51
3.3 Ceramic Stators, Shrouds, and Nose Cones . . . . .	55
3.3.1 Materials and Fabrication . . . . .	56
3.3.2 Testing . . . . .	58
4. Progress on the Stationary Turbine Project . . . . .	65
4.1 Stator Vanes . . . . .	65
4.1.1 Design . . . . .	66
4.1.2 Stress Analysis . . . . .	69
4.1.3 Materials Fabrication . . . . .	74
4.1.4 Static Test Rig Modification . . . . .	80
4.2 Rotor Blade Development . . . . .	83
4.2.1 Three-Dimensional Finite Element Stress Analysis . . .	83
5. Progress on Materials Technology — Vehicular and Stationary Turbine Projects . . . . .	87
5.1 Materials Engineering Data . . . . .	89
5.1.1 Spin Testing of Ceramic Materials . . . . .	89
5.1.2 Hot MOR of Reaction Sintered $Si_3N_4$ . . . . .	94
5.1.3 Physical Properties of Hot-Pressed Silicon Nitride . . .	96
5.2 Material Sciences . . . . .	129
5.2.1 Characterization of Reaction Sintered $Si_3N_4$ . . . . .	131
5.2.2 Elastic Properties of Silicon Nitride and Silicon Carbide	141
5.2.3 Microstructure Characteristics of Hot Pressed Silicon Nitride . . . . .	147
5.2.4 Gas-Solid Reactions . . . . .	155
5.3 Non Destructive Evaluation of Materials . . . . .	169
5.3.1 Ultrasonic NDE . . . . .	170
5.3.2 Acoustic Emission . . . . .	189
5.3.3 X-Ray Radiography . . . . .	193
6. References . . . . .	197

## LIST OF ILLUSTRATIONS

	<u>Page No.</u>
Figure 1.1 Flow Path Schematic of Vehicular Gas Turbine . . . . .	2
Figure 1.2 30 Mw Test Turbine Flow Path . . . . .	3
Figure 1.3 Brittle Material Design/High Temperature Gas Turbine — Breakdown of Major Elements Reported . . . . .	4
Figure 1.4 Brittle Material Design/High Temperature Gas Turbine — Block Diagram Flow Chart of Iterative Development . . . . .	6
Figure 3.1 Schematic of the Design Process for Rotors and Attachment. . . . .	19
Figure 3.2 Finite Difference Model of Ceramic Hot Flow Section . .	19
Figure 3.3 Rotors and Attachment Assembly . . . . .	20
Figure 3.4 Finite Element Model of Rotor and Attachment Assembly	22
Figure 3.5 Finite Element Model of First Stage Rotor . . . . .	23
Figure 3.6 Finite Element Model of Second Stage Rotor . . . . .	24
Figure 3.7 Curvic Coupling Master Set . . . . .	26
Figure 3.8 Curvic Coupling Inspection Equipment . . . . .	26
Figure 3.9 Enlargement of Hot Pressed Silicon Nitride Curvic Coupling Tooth. . . . .	27
Figure 3.10 Nitriding Results Under Various Conditions . . . . .	30
Figure 3.11 Nitriding Results Using a Static Nitrogen Atmosphere . .	32
Figure 3.12 % MgO and % Li <sub>2</sub> O Remaining After Nitriding, as a Function of Temperature . . . . .	33
Figure 3.13 Blade Indicating the Portion of the Base Sliced Out . . .	34
Figure 3.14 Hot Pressed Rotor Blank . . . . .	39
Figure 3.15 Hot Pressed Silicon Nitride Turbine Blade . . . . .	40
Figure 3.16 Simulated Blade Welding Assembly Fixture . . . . .	41
Figure 3.17 Cast Blades and Integral Rotor Mandrel . . . . .	42

	<u>Page No.</u>
Figure 3.18 Ceramic Mold with Tungsten Barrier Layer . . . . .	43
Figure 3.19 Silicon Carbide Airfoil Segments in Ceramic Mold . . . . .	43
Figure 3.20 Tungsten Mold After Removing Beryllium Copper Mandrel . . . . .	44
Figure 3.21 Chemically Vapor Deposited Integral Silicon Carbide Rotor . . . . .	44
Figure 3.22 Airfoil Detail in CVD SiC Rotor . . . . .	45
Figure 3.23 Ultrasonic Machining Tool . . . . .	46
Figure 3.24 Airfoil Slots Machined in $\text{Si}_3\text{N}_4$ Disk . . . . .	47
Figure 3.25 Ultrasonically Machined Surface . . . . .	48
Figure 3.26 Diamond Ground Surface . . . . .	48
Figure 3.27 Rotor Failure After 8 Hours, 4 min. of Hot Running. . . . .	52
Figure 3.28 Rotor Showing Rubbed Area of Rim . . . . .	52
Figure 3.29 Failed Rotor with Crack in Hub . . . . .	53
Figure 3.30 Design B Hot Flow Path Configuration . . . . .	59
Figure 3.31 Ceramic Stator Showing Metal Deposits on Vane Tips . . . . .	63
Figure 4.1 Schematic of 20 Mw Test Turbine Flow Path. . . . .	67
Figure 4.2 Schematic of Vanes and End Caps Cut Away to Show Tenon Design . . . . .	68
Figure 4.3 End Cap Recess Showing Cylindrical Approximation for Load Analysis . . . . .	70
Figure 4.4 Elliptical Contact Surface and the Cylindrical Section Analog Used to Calculate Maximum Stresses Under Combined Compressive and Tangential Loads . . . . .	70
Figure 4.5 Dimensions of Blunted Leading and Trailing Edges of Ceramic Vane . . . . .	72
Figure 4.6 Thermal Quench Cylinder Coordinate System . . . . .	72
Figure 4.7 Temperature Decay for a Thermocouple at Position #3 in Thermally Quenched Cylinders of SiC . . . . .	73
Figure 4.8 Temperature Decay and Maximum Transient Tensile Stress in the Axial Direction for Silicon Carbide Cylinders Cooled in Test Passage . . . . .	73

	<u>Page No.</u>
Figure 4.9 Airfoils Machined From HS-130 $\text{Si}_3\text{N}_4$ by the Norton Company . . . . .	76
Figure 4.10 Energy Research CVD Silicon Carbide Hollow Vane . . . . .	79
Figure 4.11 Modified Static Test Rig for 2500°F Test of Ceramic Vanes . . . . .	80
Figure 4.12 Eight Node Isoparametric Element . . . . .	84
Figure 4.13 Twenty Node Isoparametric Element . . . . .	84
Figure 4.14 Thirty-two Node Isoparametric Element . . . . .	85
Figure 4.15 Mixed Isoparametric Element . . . . .	85
Figure 5.1 Schematic of Method For Spin Testing of Ceramic Disks	90
Figure 5.2 Ultrasonic C-Scans of LAS Disks, with Fracture Lines Superimposed . . . . .	92
Figure 5.3 Spin Test of $\text{Si}_3\text{N}_4$ at Point of Fracture . . . . .	93
Figure 5.4 Ultrasonic C-Scan of $\text{Si}_3\text{N}_4$ Disk No. 2 . . . . .	93
Figure 5.5 Strength vs Temperature for Reaction Sintered $\text{Si}_3\text{N}_4$ . .	94
Figure 5.6 Illustrations of Specimen Direction and Strength Values With Respect to Hot Pressing Direction . . . . .	97
Figure 5.7 Effects of Mode of Testing on the Strength of $\text{Si}_3\text{N}_4$ . . .	98
Figure 5.8 Predicted Tensile Strength of Hot Pressed $\text{Si}_3\text{N}_4$ vs Temperature and Strain Rate . . . . .	99
Figure 5.9 Predicted Tensile Strength for Hot Pressed $\text{Si}_3\text{N}_4$ vs Temperature and Strain Rate . . . . .	99
Figure 5.10 Predicted Tensile Strength of Hot Pressed $\text{Si}_3\text{N}_4$ vs Temperature and Strain Rate . . . . .	100
Figure 5.11 Modulus of Elasticity of Hot Pressed Silicon Nitride vs Temperature (Inert Atmosphere) . . . . .	101
Figure 5.12 Creep Specimen . . . . .	102
Figure 5.13 Creep Curve, 10,000 psi, 2300°F . . . . .	103
Figure 5.14 Stress Rupture Properties of $\text{Si}_3\text{N}_4$ . . . . .	103
Figure 5.15 Strain Rate vs Stress, 2300°F in Helium Atmosphere . .	104

	<u>Page No.</u>
Figure 5.16 Strength vs Temperature for Two Forms of $\text{Si}_3\text{N}_4$ (HS-110 and HS-130) Fabricated by Norton Co. . . . .	105
Figure 5.17 Strength vs Temperature for the Weak and Strong Directions of HS-130 $\text{Si}_3\text{N}_4$ . . . . .	106
Figure 5.18 Log Plot of Strength vs Loading Rate at Different Temperatures for HS-130 $\text{Si}_3\text{N}_4$ . . . . .	106
Figure 5.19 Fracture Surface Topography of HS-130 $\text{Si}_3\text{N}_4$ Fractured at $2550^{\circ}\text{F}$ . . . . .	107
Figure 5.20 Flexural Strength vs Temperature for Hot-Pressed SiC Fabricated by Norton Company . . . . .	108
Figure 5.21 Flexural Failure Stress of Energy Research Chemical Vapor Deposition Silicon Carbide as a Function of Temperature . . . . .	109
Figure 5.22 Fatigue Test. . . . .	110
Figure 5.23 Cyclic Fatigue Behavior of Norton HS-130 Hot Pressed $\text{Si}_3\text{N}_4$ at 1800 cpm. . . . .	111
Figure 5.24 Cyclic Fatigue Behavior of Norton HS-110 Hot Pressed $\text{Si}_3\text{N}_4$ at 1800 cpm. . . . .	111
Figure 5.25 Fracture Surfaces, Fatigue Specimen, HS-110 Material a) $472^{\circ}\text{F}$ b) $2200^{\circ}\text{F}$ . . . . .	112
Figure 5.26 Thin Foil Transmission Micrographs of Fatigue Specimens . . . . .	113
Figure 5.27 Thin Foil Transmission Micrographs of Creep Specimen, HS-110 Material . . . . .	114
Figure 5.28 Normalized Stress as a Function of Life Time HS-110 Grade $\text{Si}_3\text{N}_4$ . . . . .	115
Figure 5.29 Non-Dispersive X-Ray Analysis of Corrosion Layer, HS-110 Material, 8 Hours at $2200^{\circ}\text{F}$ in Air . . . . .	116
Figure 5.30 Non-Dispersive X-Ray Analysis of Corrosion Layer, HS-130 Material, 100 Hours at $2200^{\circ}\text{F}$ in Air . . . . .	117
Figure 5.31 High-Temperature Dilatometer as Used for Direct-View Expansion Measurements . . . . .	118
Figure 5.32 Thermal Diffusivity Apparatus . . . . .	119
Figure 5.33 Thermal Conductivity of Hot Pressed $\text{Si}_3\text{N}_4$ as a Function of Direction and Temperature . . . . .	120

	<u>Page No.</u>
Figure 5.34 Thermal Diffusivity of Hot Pressed $\text{Si}_3\text{N}_4$ as a Function of Direction and Temperature. . . . .	120
Figure 5.35 Thermal Expansion of Silicon Nitride as a Function of Temperature and Direction . . . . .	121
Figure 5.36 Silicon Nitride and Alumina Specimens in the Holding Fixture After 250 Hours of Testing in Turbine Test Passage . . . . .	122
Figure 5.37 Scanning Electron Micrograph of the Leading Edge on a $\text{Si}_3\text{N}_4$ Specimen after 250 Hours of Testing in Turbine Test Passage at 2000°F Showing Glass Flow Lines and Erosion on the Surface . . . . .	123
Figure 5.38 Scanning Electron Micrograph and Non-Dispersive X-Ray Analysis of Surface Deposit on $\text{Si}_3\text{N}_4$ Specimen After 250 Hours of Exposure in Turbine Test Passage at 2000°F .	123
Figure 5.39 Weight Change Data for Norton HS-130 $\text{Si}_3\text{N}_4$ in Turbine Test Passage at 2000°F and 3 Atmospheres Pressure . .	125
Figure 5.40 Flexural Failure Stress of $\text{Si}_3\text{N}_4$ vs Exposure Time in the Turbine Test Passage . . . . .	126
Figure 5.41 Breakaway Coefficient of Friction of Silicon Nitride vs Silicon Nitride as a Function of Temperature . . . . .	127
Figure 5.42 Wear and Fret Test Apparatus . . . . .	127
Figure 5.43 % Alpha $\text{Si}_3\text{N}_4$ vs Etch Time . . . . .	136
Figure 5.44 Microstructure of Reaction-Sintered Silicon Nitride . .	137
Figure 5.45 Microstructure of Reaction-Sintered Silicon Nitride . .	138
Figure 5.46 Microstructure of Reaction-Sintered Silicon Nitride . .	139
Figure 5.47 Fracture Surface of Reaction Sintered $\text{Si}_3\text{N}_4$ . . . . .	140
Figure 5.48 Schematic Diagram of Ultrasonic Equipment . . . . .	142
Figure 5.49 Shear Modulus vs Temperature for Hot-Pressed $\text{Si}_3\text{N}_4$ .	142
Figure 5.50 Shear Modulus of $\text{Si}_3\text{N}_4$ vs Density . . . . .	143
Figure 5.51 Young's Modulus vs Temperature for Hot-Pressed SiC .	144
Figure 5.52 Shear Modulus vs Temperature for Hot-Pressed SiC . .	144
Figure 5.53 Poisson's Ratio vs Temperature for Hot-Pressed SiC . .	145
Figure 5.54 Young's Modulus vs Temperature for Hot-Pressed $\text{Si}_3\text{N}_4$ . . . . .	145

Figure 5.55	Shear Modulus vs Temperature for Hot Pressed $\text{Si}_3\text{N}_4$ Calculated from Young's Modulus Curve and Assumed Poisson's Ratio Curve . . . . .	146
Figure 5.56	Poisson's Ratio vs Temperature for Hot Pressed Silicon Nitride Assumed from Low Temperature Data and Shape of SiC Curve . . . . .	146
Figure 5.57	Typical Features of an As-Received $\text{Si}_3\text{N}_4$ Billet . . . . .	148
Figure 5.58	Common Inclusions on Fractured Surfaces Causing Strength Degradation . . . . .	150
Figure 5.59	Large Inclusions That Caused Premature Failures in Fatigue Specimens . . . . .	151
Figure 5.60	Distribution of Impurity Elements . . . . .	152
Figure 5.61	Low Magnification (335X) Microprobe Scanning Micro- graph Showing Fe Distribution in HS-130 Grade Material	153
Figure 5.62	Microscopic Distribution of Impurity Particles . . . . .	153
Figure 5.63	Transmission Electron Micrographs of $\text{Si}_3\text{N}_4$ Hot Pressed with 5% MgO . . . . .	154
Figure 5.64	Pressures of Various Volatile Spies Over $\text{SiO}_2(s)$ at $1600^{\circ}\text{K}$ . . . . .	156
Figure 5.65	Comparison of Oxidation Rates of Different Grades of Norton $\text{Si}_3\text{N}_4$ in Oxygen at 1 Atmosphere Pressure . . . . .	158
Figure 5.66	Effect of Temperature on Oxidation of Norton HS-130 $\text{Si}_3\text{N}_4$ in Oxygen at 1 Atmosphere Pressure . . . . .	159
Figure 5.67	Parabolic Plot of Oxidation of $\text{Si}_3\text{N}_4$ in Oxygen at 1 Atmosphere Pressure . . . . .	160
Figure 5.68	Arrhenius Type Plot Showing Parabolic Rate Constant for Oxidation of $\text{Si}_3\text{N}_4$ in 1 Atmosphere Oxygen as a Function of Temperature . . . . .	161
Figure 5.69	Oxidation Rates for Norton HS-130 $\text{Si}_3\text{N}_4$ in Various Oxygen-Nitrogen Gas Mixtures at $2300^{\circ}\text{F}$ and 1 Atmospheric Total Pressure . . . . .	163
Figure 5.70	Non-Dispersive X-Ray Analysis of Unoxidized Silicon Nitride Specimen Showing Tungsten Carbide Inclusions .	164
Figure 5.71	Scanning Electron Micrographs of Surfaces of Silicon Nitride Specimens Oxidized for 30 Hours in 1 Atmosphere Oxygen at Different Temperatures . . . . .	165
Figure 5.72	Scanning Electron Micrographs of Surfaces of Silicon Nitride Specimens Oxidized for 30 Hours in 1 Atmosphere Oxygen at Different Temperatures . . . . .	165

	<u>Page No.</u>	
Figure 5.73	Scanning Electron Micrograph of a Transverse Section of $\text{Si}_3\text{N}_4$ Specimen Oxidized at 2300°F for 30 Hours in 1 Atmosphere Oxygen . . . . .	166
Figure 5.74	Scanning X-Ray Pictures Showing Concentrations of Mg and Ca in the Surface Oxide on Silicon Nitride . . . . .	167
Figure 5.75	Scanning X-Ray Pictures Showing Concentrations of Al and Fe in the Surface Oxide on Silicon Nitride . . . . .	167
Figure 5.76	X-Ray Radiographic Reversal Print of Hot Pressed Silicon Nitride Disks . . . . .	170
Figure 5.77	C-Scan of Silicon Nitride Disk No. 2 . . . . .	171
Figure 5.78	C-Scan of Silicon Nitride Disk No. 1 . . . . .	172
Figure 5.79	C-Scan of Silicon Nitride Disk No. 3 . . . . .	173
Figure 5.80	Flaw Characterization - Disk No. 1 . . . . .	175
Figure 5.81	Flaw Characterization - Disk No. 2 . . . . .	175
Figure 5.82	Flaw Characterization - Disk No. 3 . . . . .	176
Figure 5.83	X-Ray Radiographic Reversal Print of Reaction-Sintered Silicon Carbide Disks . . . . .	176
Figure 5.84	C-Scans of Silicon Carbide Disks Nos. 1 and 2 . . . . .	177
Figure 5.85	C-Scans of Silicon Carbide Disks Nos. 3 and 4 . . . . .	178
Figure 5.86	C-Scans of Silicon Carbide Disks Nos. 5 and 6 . . . . .	179
Figure 5.87	Ultrasonic Nondestructive Test of Hot Pressed Silicon Nitride . . . . .	181
Figure 5.88	C-Scan of LAS Calibration Block and LAS Spin Test Specimen with the Flaw Analysis View Direction Shown .	182
Figure 5.89	Enlargements of Flaws 1 and 2 in LAS Disk No. 2 . . .	183
Figure 5.90	Flaw Signals from LAS Disk No. 2 . . . . .	184
Figure 5.91	C-Scan of LAS Calibration Block and Segment of LAS Spin Test Specimen 13 with the Flaw Analysis View Direction Shown . . . . .	185
Figure 5.92	Enlargements of Flaw 1 in Segment of LAS Spin Test Specimen No. 13 . . . . .	185

	<u>Page No.</u>
Figure 5.93 Flaw Signals from Segment of LAS Spin Test Specimen No. 13 . . . . .	186
Figure 5.94 C-Scan of LAS Calibration Block and LAS Test Block Specimen with the Flaw Analysis View Direction Shown . . . . .	187
Figure 5.95 Flaw Signals from LAS Test Block Specimen . . . . .	187
Figure 5.96 Enlargement of Flaw 1 in LAS Test Block Specimen . . . . .	188
Figure 5.97 Reproduction of AE vs Relative Load Curve Showing the Magnitude of Events Occurring at Low Loads . . . . .	190
Figure 5.98 Fracture Surface of Test Specimen No. 7-15 Showing the Crack Initiation Site in the Lower Right Hand Corner . . . . .	191
Figure 5.99 Reproduction of AE vs Relative Load Curve Showing the Magnitude of Events Occurring at Low Loads . . . . .	191
Figure 5.100 Fracture Surface of Test Specimen No. 3-4 Showing the Crack Initiation Site in the Middle of the Lower Surface . . . . .	192
Figure 5.101 X-Ray Radiographic Reversal Prints of Ultrasonic Calibration Block No. 2 . . . . .	194
Figure 5.102 Adjusted Positive Print of Radiographed Airfoil . . . . .	195

## LIST OF TABLES

	<u>Page No.</u>
Table 3.1      Nitriding Results for GT-22 and GT-209 Silicon Bars . . . . .	32
Table 3.2      X-Ray Analyses of Silicon Nitride Blades . . . . .	35
Table 3.3      Results of Hot-Pressed AME Silicon Nitride Relating Hot-Pressing Conditions, Density, Grain Size, Chemistry, and Strength . . . . .	38
Table 3.4      Mechanical Properties of Rotor Material . . . . .	52
Table 3.5      Second Stage Turbine Rotor Failures . . . . .	53
Table 3.6      Summary of Testing of Ceramic Nose Cones, Stators and Shrouds . . . . .	61
Table 4.1      Properties of Norton HS-130 Silicon Nitride . . . . .	75
Table 4.2      MOR Test Results of Energy Research CVD SiC . . . . .	77
Table 5.1      Tensile Test Data for Silicon Nitride . . . . .	100
Table 5.2      Creep Results, Helium Atmosphere, Specimens Machined from Norton Billet 011072B1 . . . . .	102
Table 5.3      Emission Spectrographic Analysis of Surface Deposition on $\text{Si}_3\text{N}_4$ and $\text{Al}_2\text{O}_3$ Samples Tested in Turbine Passage in Clean Diesel Fuel at $2000^{\circ}\text{F}$ and 3 Atmospheres Pressure . . . . .	124
Table 5.4 $K_i$ Values for the $\text{Si}_3\text{N}_4$ System . . . . .	132
Table 5.5      X-Ray Diffraction Results from the Brick-Lined Furnace	133
Table 5.6      X-Ray Diffraction Results from the Metal Furnace . . .	134
Table 5.7      Phase Composition, Impurity Concentration, and Etch Times for Various Silicon Nitrides . . . . .	135
Table 5.8      Spectrographic Analysis of $\text{Si}_3\text{N}_4$ . . . . .	147
Table 5.9      Thermochemical Data for the Si-N-O System . . . . .	155

	<u>Page No.</u>
Table 5.10      Theoretical Values of Maximum Oxygen Pressures to Remove all the Oxide on Silicon Nitride Surface . . . . .	157
Table 5.11      Parabolic Rate Constants for Oxidation of $\text{Si}_3\text{N}_4$ in 1 Atmosphere Oxygen . . . . .	161
Table 5.12      Comparison of Activation Energies for Parabolic Oxidation . . . . .	162
Table 5.13      Dynamic Modulus of Elasticity of Silicon Nitride Disks . . . . .	174
Table 5.14      Properties of Silicon Carbide Disks . . . . .	180
Table 5.15      Kilovolt Levels and Exposure Times Used for Low Voltage X-Ray Study . . . . .	194

## 1. INTRODUCTION

As stipulated by the Advanced Research Projects Agency of the Department of Defense, the major purpose of this program is to demonstrate that brittle materials can be successfully utilized in demanding high temperature structural applications. The gas turbine engine, utilizing uncooled ceramic components in the hot flow path, was chosen as the vehicle for this demonstration. Two hundred hours of operation over a representative duty cycle at ceramic temperatures up to 2500°F is required for the demonstration.

It is the further purpose of this program to develop design technology for ceramic materials on a systems basis requiring close integration of design, engineering, materials selection, materials processing and fabrication, testing and evaluation.

The progress of the gas turbine engine has been closely related to the development of materials capable of withstanding the engine's environment at high operating temperature. Since the early days of the jet engine, new metals have been developed which have allowed a gradual increase in operating temperatures. Today's nickel-chrome superalloys are in use without cooling at turbine inlet gas temperatures of 1800° to 1900°F. However, there is considerable incentive to further increase turbine inlet temperature to improve specific air and fuel consumptions. The use of ceramics in the gas turbine engine as a demonstration vehicle for this program promises to make a major step in increasing turbine inlet temperature. Success will offer significant advances in engine efficiency, power per unit weight, cost, pollution abatement, and fuel utilization.

This program will demonstrate the use of ceramics in two demanding gas turbine applications:

- (1) A small-vehicular type of engine (Ford). Such an engine would have a major impact on the technology of mobile field power units, military vehicles and craft. As a consequence of its significantly increased operating temperature it would not only provide more horsepower/unit weight than current engines, but would also provide improved fuel economy. In addition, the benefits of low emissions and multi-fuel capability are attained. A simplified schematic of the flow path of this regenerative type of engine is shown in Figure 1.1. A brief explanation of this flow path will be given to familiarize the reader with the various components considered for ceramics. Air is induced through an intake silencer and filter into a radial compressor, and then is compressed and ducted through one side of each of two rotary regenerators. The hot compressed air is then supplied to a combustion chamber where fuel is added and combustion takes place.

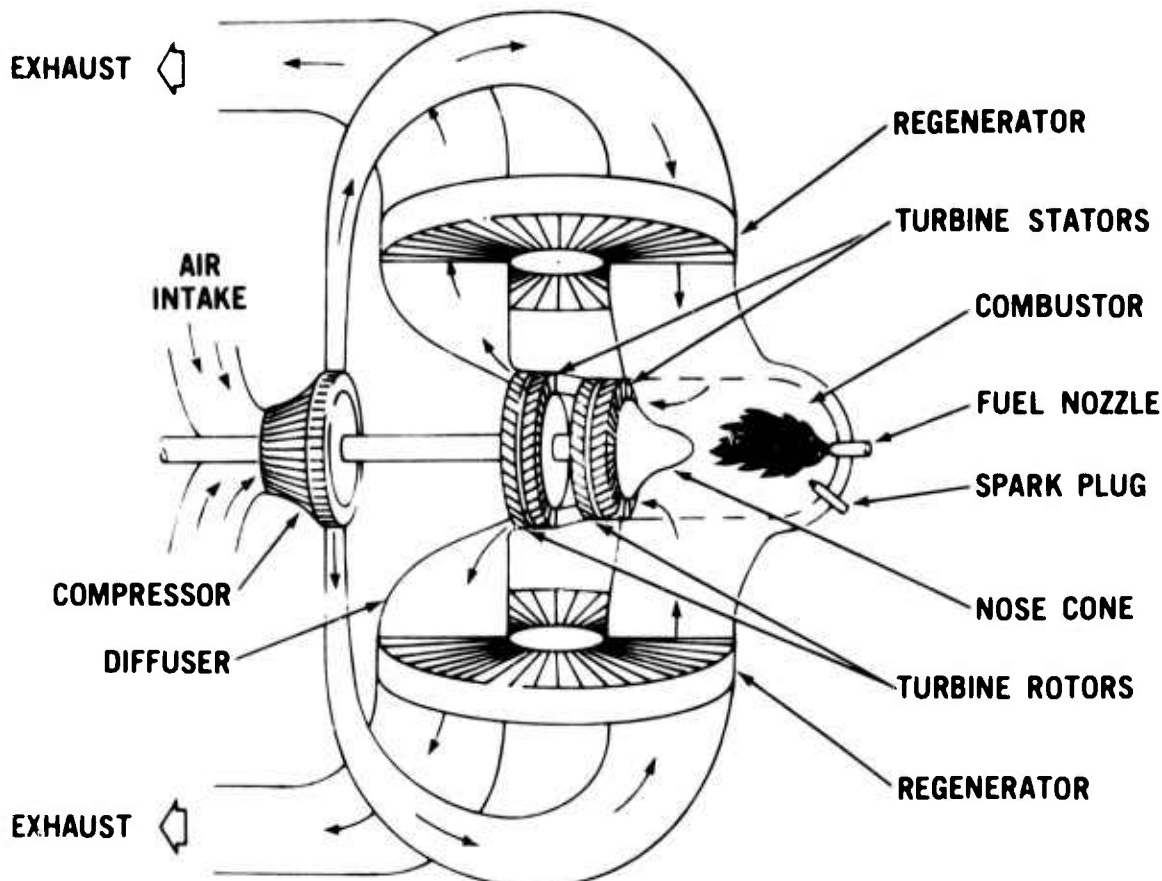


Figure 1.1 — Flow Path Schematic of Vehicular Gas Turbine

The hot gas discharging from the combustor is then directed into the turbine stages by a turbine inlet structure, in this case shown as a nose cone. The gas then passes through the turbine stages which comprise two turbine stators, each having stationary airfoil blades which direct the gas onto each corresponding turbine rotor. In passing through the turbine, the gas expands and generates work to drive the compressor and supply useful power. The expanded turbine exhaust gas is then ducted through the hot side of each of the two regenerators which, to conserve fuel consumption, transfer much of the exhaust heat back into the compressed air.

The parts which are subject to the peak cycle temperature and are made out of superalloys in today's gas turbine are the combustor, the turbine inlet nose cone, the turbine stators and the turbine rotors. These are areas where ceramics could be exploited to the fullest and have been selected for application in the vehicular turbine project.

(2) A large-stationary gas turbine for electric power production (Westinghouse). Such an engine would be most desirable for DOD installations requiring on site power generation. Not only will ceramics facilitate significantly increased operating temperatures with attendant improvement in power and fuel economy, but, because of their improved corrosion-erosion resistance they will also facilitate use of low cost residual fuel. In addition, the environmental benefits of low emissions and lack of cooling water (with its attendant thermal pollution problems) are attained. A simplified sketch of the hot flow path of the engine is shown in Figure 1.2. As with the vehicular turbine project, a brief explanation of the flow path of the stationary turbine will be given to help the reader understand the function of the components to be made from ceramic materials.

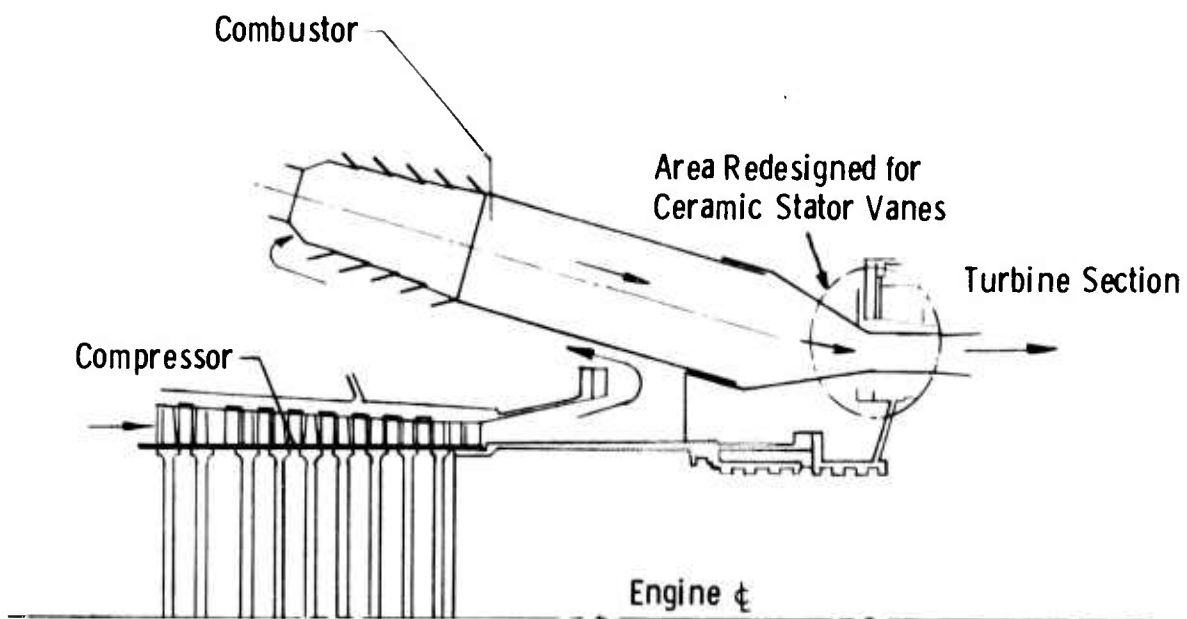
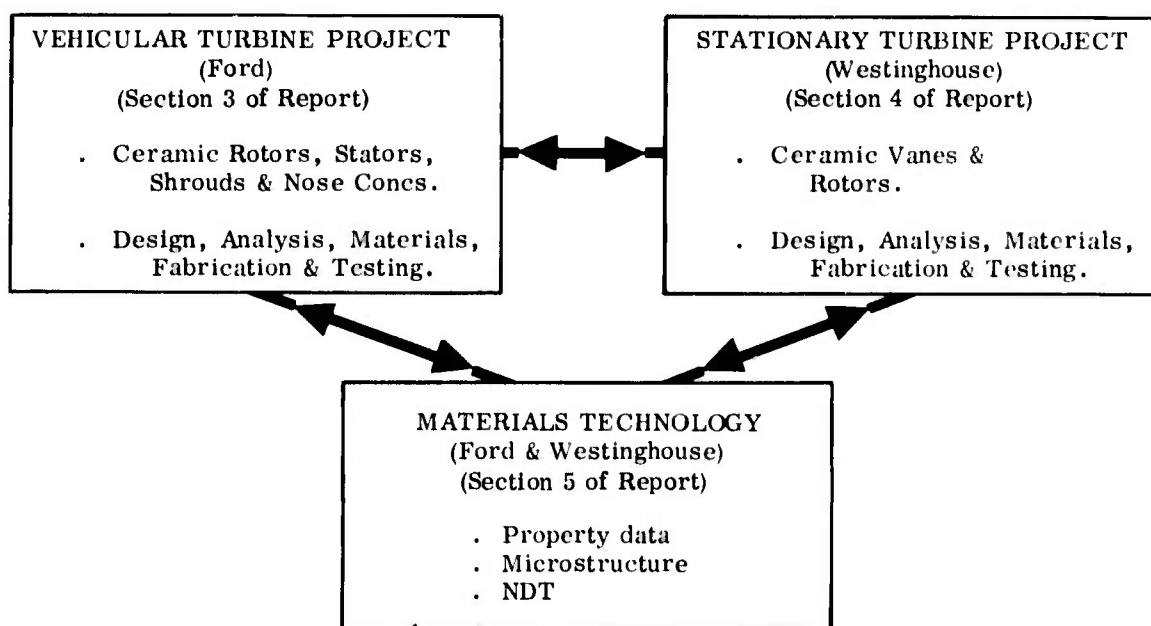


Figure 1.2 — 30 Mw Test Turbine Flow Path

Air is induced through a large intake silencer and filter into an 18 stage axial compressor where it is compressed before entering the combustor housing. The combustor housing supplies air at 650°F to combustion cans assembled in a circumferential array. Air is mixed with distillate fuel or natural gas and ignited in the primary combustion zone. The gas passes downstream through the combustors mixing with secondary air. Flow continues from the combustion section, through the transition zone, and enters the power turbine at a gas temperature of 2500°F. The hot gases expand through the three stage turbine section and are either exhausted through a stack or ducted into a reheat boiler as part of a combined cycle power generating unit.

The parts, where ceramics could be exploited to the fullest, selected for application in the stationary turbine project are the first stage turbine stator vanes and the first stage turbine rotor.

To maintain coherence, progress on the vehicular and stationary turbine projects are reported separately. Also reported separately is the common link between these two programs, materials technology. Information presented under materials technology is general, and does not specifically apply to one or the other of the gas turbine engines. On the other hand, items reported under the vehicular and stationary turbine projects are categorized by components and therefore relate directly to those projects (even these items, however, are indirectly related when it comes to such considerations as design techniques, etc.). Figure 1.3 has been prepared to help the reader understand the interrelationship between the major elements of the report.



**Figure 1.3 — Brittle Material Design/High Temperature Gas Turbine - Breakdown of Major Elements Reported**

Successful demonstration of a high temperature gas turbine engine will involve a complex iterative development. One cannot divorce the development of ceramic materials from processes for making parts; no more so can one isolate the design of those parts from how they are made or from what they are made. Likewise, the design of mountings and attachments between metal and ceramic parts within the engine are equally important. Innovation in the control of the environment of critical engine components is another link in the chain. Each of these factors has a relationship with the others, and to obtain success in any one may involve compromises in the others. Testing plays an important role during the iterative development since it provides a positive, objective way of evaluating the various combinations of factors involved. If successful, the test forms the credibility to move on to the next link in the development chain. If unsuccessful, the test flags a warning and prompts feedback to earlier developments to seek out and solve the problem which has resulted in failure. Finally, all of the links in the chain are evaluated by a complete engine test, by which means the ultimate objective of the program will be demonstrated.

Figure 1.4 shows a block diagram flow chart of the major factors involved including the feedback loops, which serves to illustrate this complex and comprehensive iterative development program. The starting point is the concept of a design to use brittle materials. From this, a design layout is prepared and analyzed leading to the detailed design and analysis of the gas turbine engine components made of or involving ceramics. In parallel with the design phase, ceramic materials are developed and screened for application to the gas turbine engine. Process development of candidate ceramics then takes place and material science and property evaluation are used to improve materials and processes, and to feed information back into the design phase. Next with the first detail designs completed and with the process for the selected ceramics reasonably developed, tooling can be designed and fabrication development started to make actual ceramic turbine engine components. Non-destructive testing of these parts will be developed to form a feedback for improving material and fabrication methods. In conjunction with non-destructive evaluation, techniques will be developed for proof testing ceramic components prior to use in engines. In parallel with ceramic part fabrication, proof testing, and non-destructive evaluation, metal parts for the ceramic turbine engine and test rigs are made per the detail design requirements. The ceramic and metal parts are then dimensionally inspected and instrumented for engine testing. Assembly techniques for brittle materials are developed, and testing and durability developments in both test rigs and engines are performed. Failure analysis from test rig and engine testing forms the feedback loops for corrective action; almost all of the factors involved in the development could be affected by experience learned in the test phase of the program. Finally, when engine durability has reached a given level of development, the 200 hour demonstration test will be conducted to meet the program objective.

It should be noted that both the contractor and subcontractor had in-house research programs in this area prior to the initiation of this program. Many ceramic materials were extensively tested and screened leading to the selection of silicon nitride and silicon carbide. In the stationary turbine program, preliminary design concepts were in existence before the award of the contract. In the vehicular turbine program, development was fairly well along and at least one pass had been completed through all of the factors shown in Figure 1.4 prior to the initiation of this program. This one pass, involving many minor iterations led to a vehicular turbine hot flow path having all ceramic stationary components and designated Design 'A'. Based on further experience gained during engine testing, a modified flow path was generated and designated Design 'B'.

Since initiation of this program with AMMRC, work on both the vehicular and stationary gas turbine projects was accelerated. Work accomplished during the first reporting period included, for the vehicular turbine project, initial fabrication development and successful preliminary testing of Design 'B' turbine stators and nose cones made of reaction sintered silicon nitride. Design studies of ceramic turbine rotors showed that computed operating stresses can be withstood by dense silicon carbide and dense silicon nitride. Development programs were started to explore several approaches to fabricate rotors in these materials.

Accomplishments on the stationary turbine project during the first reporting period included obtaining physical property data of hot pressed silicon nitride ceramic and identifying microstructural details of this material. The initial design of ceramic stator vanes was completed and calculated vane stresses were reduced 40% by decreasing the stator vane chord.

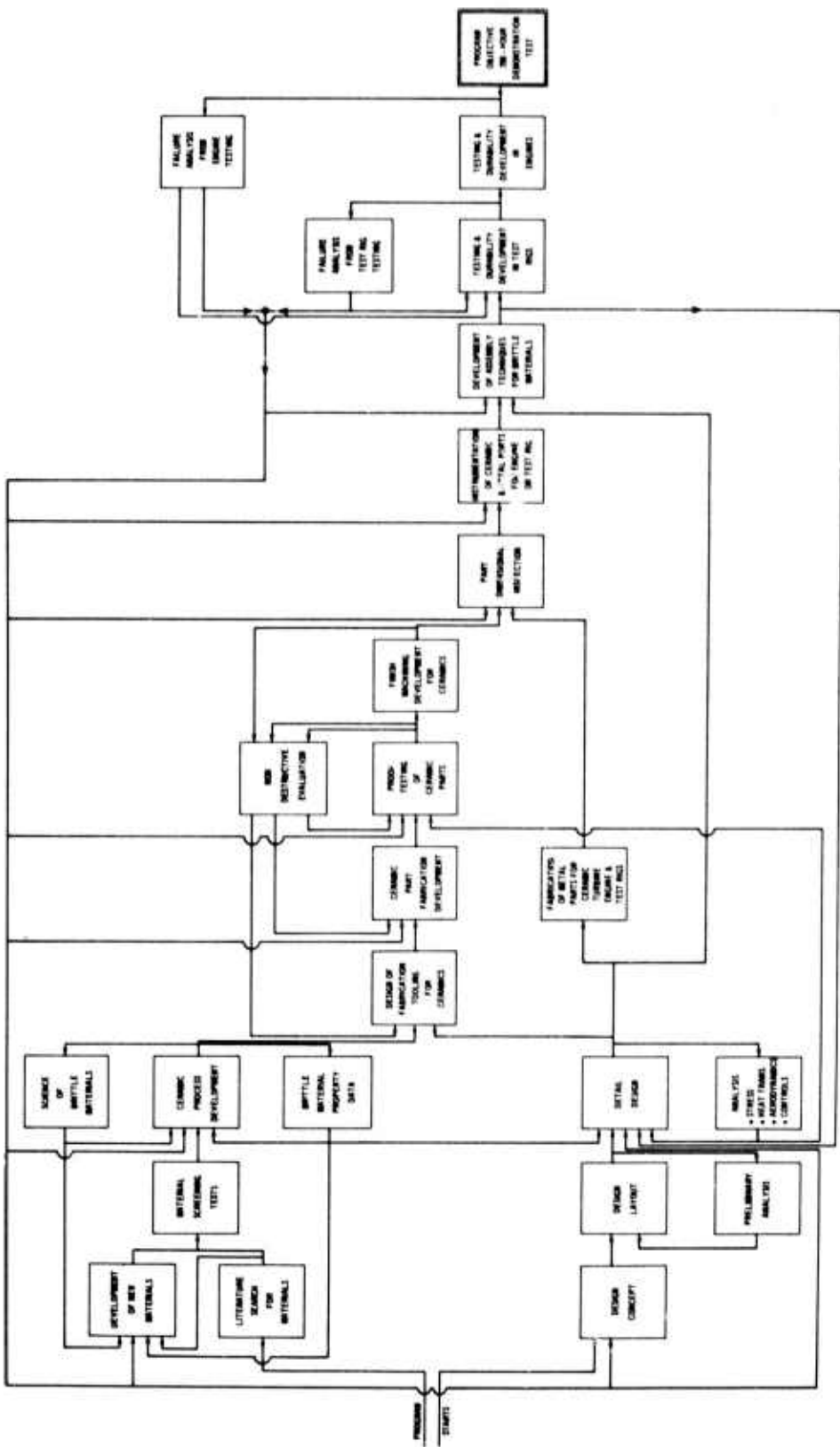


Figure 1.4 – Brittle Material Design/High Temperature Gas Turbine – Block Diagram Flow Chart of Iterative Development

The results of work accomplished during this second reporting period include, for the vehicular turbine project, continued fabrication development as well as rig and engine testing of the second generation design (Design 'B') turbine stators and inlet nose cones. Ceramic turbine rotor design studies were performed on an expanded two-dimentional heat transfer computer program to include rotor attachment designs. Progress is reported on the multi-approaches being explored to fabricate a one-piece, intricately-shaped, turbine rotor from candidate high strength ceramic materials.

The results of work accomplished on the stationary turbine project include the stress analysis and design of first stage vanes as well as a preliminary report on the rig for statically testing the stator vanes. Progress on the development of a new three-dimensional, finite-element, stress analysis computer program for subsequent use in ceramic rotor blade design is also reported.

Development in materials technology for both the vehicular and stationary gas turbines is reported and includes continued compilation of material property data, continued characterization of material structure, and development of non-destructive evaluation techniques such as ultrasonics, radiography and acoustic emission.

This report covers the progress in the period January 1, 1972 to June 30, 1972.

## 2. SUMMARY OF PROGRESS

### 2.1 VEHICULAR TURBINE PROJECT

The vehicular turbine project is composed of three primary sections — design, materials, and testing. Within these primary areas there exist many tasks which must be accomplished in order to achieve the program goal of 200 hours of turbine engine operation over a representative duty cycle at ceramic temperatures up to 2500°F. Each semi-annual report is really a progress report detailing the results of work over a six month time increment, reporting on the individual accomplishments on the tasks which will culminate in the final program objective.

Work is in progress concurrently in areas of turbine engine component design and analysis, ceramic material and process development, material and engine testing, materials technology, and non-destructive evaluation of ceramic engine components. Progress, made in several of these areas in this reporting period, is summarized in this section of the report.

(1) Design and analytical work has continued on the determination of stresses for ceramic rotor designs, and the methods of attaching ceramic rotors to the turbine shaft. The two-dimensional finite element axisymmetric computer program for heat transfer has been improved to accommodate ceramic turbine rotors complete with the output shaft and rotor attachment assembly, including possible cooling schemes. This program is capable of evaluating temperature distributions in the ceramic rotor for various rotor attachment coolant flows by calculating heat transfer coefficients internally. Work on a companion program to determine mechanical stresses in this assembly is in progress. Both of these computer programs will significantly improve the analytical capability for solving complex design problems involving ceramic components, and ceramic-to-metal mounting concepts. Refer to Section 3.1.1 of this report for more detailed information.

(2) Design studies have been completed for coupling the second stage turbine rotor to the shaft, utilizing a curvic coupling of a 15 tooth half-barrel design. Master gauges of the coupling, one in hot-pressed silicon nitride and one in metal, have been fabricated and are within the tight dimensional specifications. Refer to Section 3.1.1 of this report for a more detailed account of this work.

(3) The fabrication of ceramic turbine rotors of high strength — thermal shock resistant ceramics remains the most challenging task to be solved; several approaches are being followed. One approach showing encouraging progress as reported by Energy Research involves fabricating turbine rotors by chemical vapor deposition (CVD) of silicon carbide. The silicon carbide is deposited within tungsten molds of the turbine shape, also formed by CVD. Process parameters have been developed to the point where all 36 blades and most of the rim were formed and replication of the blade shapes was excellent. However, more work remains to be done to improve the quality of the silicon carbide, to increase wall thickness, and to avoid residual stresses in the material. Refer to Section 3.1.2 of this report for more detailed information.

(4) Fabrication of stationary ceramic components — inlet nose cone, turbine stators, and turbine tip shrouds — in reaction sintered silicon nitride continued. As an example, 60 nose cones were formed by injection molding with an expenditure of only a few man-hours. Process work during this reporting period has been concerned with evaluating the silicon nitride produced during nitriding in two distinctly different types of furnaces, and with evaluating the silicon metal powder raw material from several vendors. Characterization of materials in stationary components fired in different furnaces is incomplete. Only one vendor was able to supply silicon powder to meet the requirements specified for injection molding stationary components. Refer to Section 3.3.1 of this report for a more detailed account of this work.

(5) Engine and rig testing of Design 'B' stationary ceramic components has continued. These parts include first and second stage turbine stators, turbine inlet nose cones, and first and second stage turbine shrouds. A number of each of these components has been subjected to three types of test; the first is a cold test using metal turbine rotors (cold dynamic test); the second is a hot test without turbine rotors (hot static test); and the third is a hot test using metal turbine rotors (hot dynamic test). Using these tests, durability of the Design 'B' ceramic components has been encouraging. As an example, a reaction sintered silicon nitride first stage stator has successfully withstood 74 hours of cold dynamic testing; another one has withstood 29 hours of hot static testing, and yet another one 12 hours of hot dynamic testing, all without failure. Another example is a silicon carbide nose cone which, although it developed a crack during initial testing, has been hot static tested for 650 hours, still has only the one crack, and is considered serviceable. Refer to Section 3.3.2 of this report for a more detailed description of work accomplished.

## 2.2 STATIONARY TURBINE PROJECT

The stationary turbine project is a design study of brittle materials in a high temperature gas turbine application, culminating with the demonstration of uncooled ceramic stator vanes in a 30-Mw power turbine operating for 200 hours at 2500°F. This operation will consist of 100 sequences of peaking cycle service. Work is currently in progress in areas of stator vane design and analysis, development of computer programs to be used for rotor blade design, component fabrication, and materials technology. This progress is summarized in this section of the report.

- (1) The first generation 3-piece stator vane design (airfoil and 2 end caps) for static rig testing of hot-pressed silicon nitride was completed. Stress analysis of both the end caps and airfoil revealed that Norton HS-130 material should withstand the mechanical and thermal stresses generated during turbine operation. Refer to Section 4.1.1 of this report for more detailed information.
- (2) A section of the 3D finite element stress analysis program being developed for rotor blade design was completed. This section allows the analysis of isotropic elastic stress in 3D solids. A reliability verification is being made by comparing the output from this program with that from the 2D finite element and finite difference programs used to determine the transient stress in the stator vane airfoil. Refer to Section 4.2 of this report for a more detailed account of this work.
- (3) The Norton Company has machined 20 airfoils from 40 certified billets of hot-pressed HS-130 silicon nitride. End caps are being machined to design specifications. These will complete the stator vane assemblies for the first static rig tests. Refer to Section 4.1.3 of this report for more detailed information.
- (4) Energy Research Corporation produced flexure specimens for the evaluation of chemically vapor deposited silicon carbide. Room temperature strength averaged 60,000 psi with considerable scatter in the data. High temperature strength was more impressive with values as high as 100,000 psi recorded at 2300°F. Attempts to deposit hollow airfoil shapes were unsuccessful. Refer to Section 4.1.3 for more detailed information.

## 2.3 MATERIALS TECHNOLOGY -- VEHICULAR AND STATIONARY TURBINE PROJECTS

Complete property characterization of the ceramic materials for turbine engine use is an enormous task, which will proceed throughout the life span of the contract. This task is also complicated by the fact that many of the materials being investigated are in the developmental stage and improvements in properties are anticipated, which will require that some, if not all of the physical properties must eventually be re-determined. Progress in materials technology is summarized in this section of the report.

(1) Candidate materials for ceramic turbine rotors are hot-pressed silicon carbide and hot-pressed silicon nitride. Property data, measured during this reporting period, included elastic properties of Norton hot-pressed silicon nitride and silicon carbide at high temperatures. A technique for spin testing ceramic disks to simulate the stress distribution in turbine rotors has been developed. Failure of the disks is recorded photographically, and is being correlated to defects detected by NDT studies. Two disks of hot-pressed silicon nitride were spin-tested and failed at stresses of 63 ksi and 51 ksi. For more information, refer to Section 5.2.2 on elastic property determination, and Sec. 5.1.1 on spin testing.

(2) Bending strength as a function of temperature was determined for Ford's injection molded reaction sintered silicon nitride. The strength level of the as-molded material remained virtually constant at around 22,000 psi up to 2000°F, then decreased gradually to 19,200 psi at 2400°F. Refer to Sec. 5.1.2 for more information.

(3) Extensive thermal and mechanical property data were obtained on certified Norton hot pressed silicon nitride from which vanes are being fabricated. In general, the strength of Norton HS-130 silicon nitride shows significant improvement at high temperatures over the earlier HS-110 material. The strength is temperature dependent, however, particularly above 2200°F. The tensile strength decreases from 60 ksi at RT to 17 ksi at 2500°F. A similar temperature dependence was displayed by both the elastic modulus and flexural strength. Creep was observed at 1800°F; but the stress rupture properties appear quite adequate for stator vane application. Tests reveal that there should be no high cycle fatigue problem with the HS-130 material. Shear strength, thermal expansion, and thermal conductivity were determined. Refer to Section 5.1.3 for more detailed information.

(4) Turbine passage corrosion-erosion tests at 2000°F, extended to 250 hours, continued to show the excellent performance of silicon nitride. Net weight losses of 3 mg/cm<sup>2</sup> were encountered for HS-130 silicon nitride, which did not affect the flexural strength. A better understanding of oxide film formation at the surface was obtained through a detailed characterization study of tested specimens. Static oxidation studies continued to reveal insight into the kinetics of oxide film formation. Refer to Section 5.2.4 for more detailed information.

(5) Reaction-sintered silicon nitride is being used extensively for stationary components. Until recently, the structure of the material has not been studied due to difficulties in etching the material. An acid etching technique has been developed which permits the structure of any form of silicon nitride, regardless of density, to be observed macroscopically. It was found that the etching is rate-controlled by the amount of alpha phase silicon nitride and iron impurity present. Refer to Section 5.2.1 of this report for a more detailed description of work accomplished.

(6) The detrimental features in the microstructure of hot-pressed silicon nitride that are related to process controls have been identified. These include impurities, density gradients, flaws, and metallic inclusions. Physical property anisotropy appears related to these features rather than grain orientation. Calcium impurity concentration has a definite, strong influence on the high temperature strength of silicon nitride. The presence of a glass phase at the grain boundaries is most likely responsible for the strength behavior. Section 5.2.3 of this report gives more detailed information.

### 3. PROGRESS ON THE VEHICULAR TURBINE PROJECT

#### 3.1 CERAMIC ROTOR DEVELOPMENT

##### SUMMARY

Design and analytical work has continued to determine stresses for ceramic rotor design and to determine how to attach ceramic rotors to the turbine shaft. The two-dimensional finite element axisymmetric computer program for heat transfer has been improved to accommodate ceramic turbine rotors complete with the output shaft and rotor attachment assembly including possible cooling schemes. This program is capable of evaluating temperature distributions in the ceramic rotor for various rotor attachment coolant flows by calculating heat transfer coefficients internally. Work on a companion program to determine mechanical stresses in this assembly is in progress. Both of these computer programs will significantly improve the analytical capability for solving complex design problems involving ceramic components, and ceramic-to-metal mounting concepts.

Design studies have been completed for coupling the second stage turbine rotor to the shaft, utilizing a curvic coupling of a 15 tooth half-barrel design. Master gauges of the coupling, one in hot-pressed silicon nitride and one in metal, have been fabricated and are within the tight dimensional specifications.

The fabrication of ceramic turbine rotors remains the most difficult technical problem to solve in the vehicular turbine project, because operating stresses requires high strength, thermal shock-resistant materials which must be formed into a very complex shape. The rotor is less than six inches in diameter and has more than thirty small twisted airfoil blades, which constitutes a formidable fabrication problem. Six separate efforts directed at fabricating ceramic rotors are in progress.

The first of these programs is a Ford in-house effort in which the rotor shapes are injection molded from silicon nitride and densified by a pseudo-isostatic hot pressing method. Some compositional gradients exist within nitrided turbine blades and the magnesium oxide sintering aid adversely affects formation of the desired high alpha crystallographic composition. Distortion of the blades during densification remains a problem.

The second program, conducted by the Norton Company, comprised hot-pressing of separate silicon nitride rotor blades using graphite tooling. A full set of blades were to be assembled and formed into an integral unit by hot-pressing a silicon nitride hub around the blades. While some progress was made, the program was stopped because it appeared that too much time would be needed to successfully develop this approach.

The third program, which appears promising, is fabricating a turbine rotor of dense silicon carbide formed by chemical vapor deposition. This work is being performed by Energy Research Corporation. The silicon carbide is deposited within tungsten molds of the turbine shape, also formed by CVD. Process parameters have been developed to the point

where all 36 blades and most of the rim were formed and replication of the blade shapes were excellent. However, more work remains to be done to improve the quality of the silicon carbide to increase wall thickness, and to avoid residual stresses in the material.

The fourth program, conducted by Joseph Lucas Ltd., is attempting to develop a process to fabricate a silicon nitride rotor by preforming individual blades and a hub, assembling the components, and hot-pressing the assembly encased in a conformable ceramic composite. The feasibility of this process has not yet been established.

Other programs include attempting to develop techniques for machining ceramic turbine rotors from billets of hot-pressed material. Ultrasonic machining of hot-pressed silicon nitride has shown that disk contouring, hub boring and end cutting of approximate blade shapes appear economically feasible, with minimal surface damage. Electric discharge machining of hot-pressed silicon carbide is also being studied. A removal rate of 0.012 cubic inches of SiC per hour is indicated by EDM using copper electrodes.

### 3.1.1 DESIGN AND ANALYSIS

#### Introduction

As discussed in the last report<sup>(1)</sup> the selection was made of a preliminary turbine rotor disk geometry for fully dense silicon nitride ( $Si_3N_4$ ). An attachment concept was also selected that would be compatible with the wide range of engine operating conditions.

In order to fully assess the interaction between the rotor and the attachment hardware, it was necessary to modify existing computer programs for heat transfer and stress analysis. Heat transfer programs were revised to handle multiple coolant flows as required by a folded bolt concept described in the previous report<sup>(1)</sup>, and increased in size to allow more precise modeling of boundary conditions as they exist in the engine. Similar revisions were incorporated into the stress analysis programs.

The mathematical model of the rotor assembly including surrounding hardware was refined to reflect changes introduced on the final design of the rotor attachment.

Concurrently, fabrication studies were conducted to develop curvic coupling face splines for shaft to rotor and rotor to rotor junctions. Curvic couplings feature unique spline characteristics that make them quite attractive for use with ceramics. The most important features are part interchangeability, low contact stresses, and the ability to cope with expansion differentials expected at the rotor-shaft junction.

#### Two Dimensional Computer Programs

The basic analytical codes used in the analysis of the turbine rotors and the rotor attachment assembly were three two-dimensional computer programs; of these two are heat transfer programs — one for finite difference analysis (FDHT), and the other for finite element analysis (FEHT). The stress program performs a finite element analysis (FEST). Other computer programs were also used in conjunction with these three basic codes to aid in preparation of data for the input and interpretation of the resulting output data. Examples of these data handling programs would be the renumbering of the finite element member incidence table for the most economic operation and the display of final temperatures and stress distributions. Some basic features of the three main programs, as they existed at the time of the last report<sup>(1)</sup>, are restated as follows:

**FDHT:** two dimensional heat transfer with coolant streams

**FEHT:** two dimensional heat transfer with two (2) coolant streams with self generation of convection coefficient for flow over a rotating disk in an adiabatic housing.

**FEST:** two dimensional stress and strain.

The two finite element programs were compatible in that the FEHT could generate the temperature field format required by the FEST in order to calculate the thermal stresses and strains. However, the two programs had to be

operated separately. Each finite element program had a different size limitation. Due to the configuration and complexity of the rotors complete with their attachment assembly, the finite difference computer programs had to be modified extensively in order to model the problem. The majority of work in this area during this reporting period was spent updating the analytical codes required to analyze the rotors and the rotor attachment assembly.

The FEHT program was modified to include coolant flows in radial and annular channels. The convective film coefficients were generated internally for the particular flow condition once a flow rate and initial coolant temperature were determined. The assumptions and correlations used were discussed for similar flow conditions in the previous report (1). The number of coolant streams possible was increased to twelve. The capability of modeling coolant flow over a rotating disk within an adiabatic housing was modified to include a nonadiabatic housing. The heat transfer from the housing was assumed to be by conduction through half the boundary layer of the coolant stream on the rotating disk.

Data generation for any model is a laborious and time consuming task. Since the design of ceramic components is often an iterative procedure due to the constant updating of material properties and design techniques, it is desirable to have a method of analysis that is flexible and requires as little time as possible in model design. To facilitate this, the finite element programs were modified to accept the basic grid point data, representing the model, in a form most convenient to the designer. The grid point data may now be digitized electronically and numbered in any convenient manner; much of the data can be numbered automatically by the computer program.

When the entire grid point library and member incidence table (i.e. relationship of grid points to each other and therefore the size of the matrix to be solved) have been determined, the model can be studied on a computer-controlled cathode ray tube (CDC 1700 computer). At this point the model grid point library can be modified by the designer if required, and the member incidence table bandwidth can be minimized.

The size restrictions and limitations of the finite element programs were enlarged and the programs were modified such that the maximum model sizes would be compatible. In order to economize on computer size requirements, the programs were made flexible so that computer requirements matched modeling requirements.

At the current level of development, minimum time is required in data preparation, and minimum computer time and capacity are required in problem solution. Output data can be studied graphically by plotting results on paper or viewing them on the CDC 1700 light tube.

### Design Process

Figure 3.1 is a schematic diagram of the method being used to arrive at a final design for the rotors and the rotor attachment concept. The basic approach is to study a large portion of the engine comprising many components with a relatively rough model. This rough model then provides realistic boundary conditions for a more detailed model. The procedure is carried on to the point where a single component can be studied with a very refined model.

The FDHT program was used to study a rough model of the engine rotors and turbine shaft. The model, Figure 3.2 provided such information as rotor bolt cooling requirements and structure temperatures in the vicinity of the bearings and the turbine shaft. From this data rotor attachment assembly concepts were studied. Three possible concepts were discussed in the previous report(1). The concept chosen to be first analyzed was that of the hollow folded bolt. Based on the first approximation of temperature data available adjacent to the bolt from the FDHT model, bolt requirements were estimated and a bolt design was arrived at for analysis. The rotor bolt assembly to be analyzed is shown in Figure 3.3.

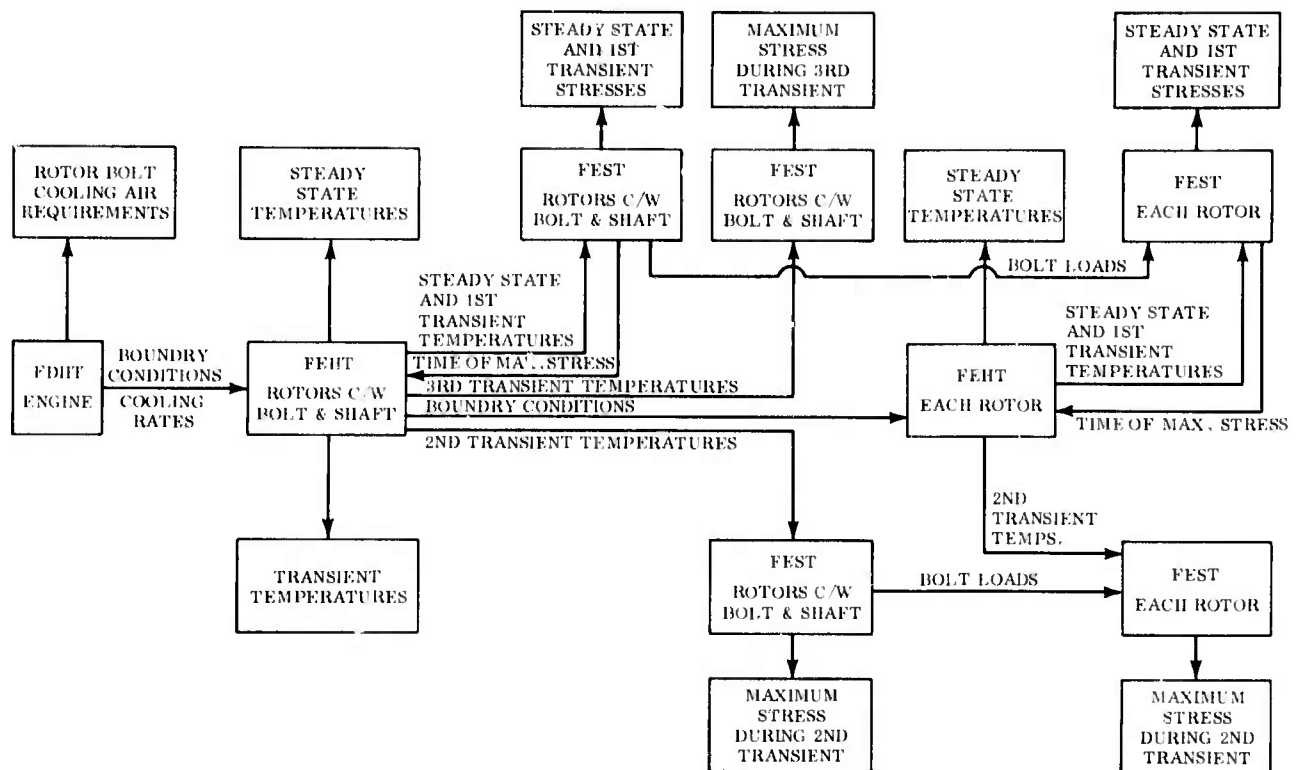


Figure 3.1 — Schematic of the Design Process for Rotors and Attachment

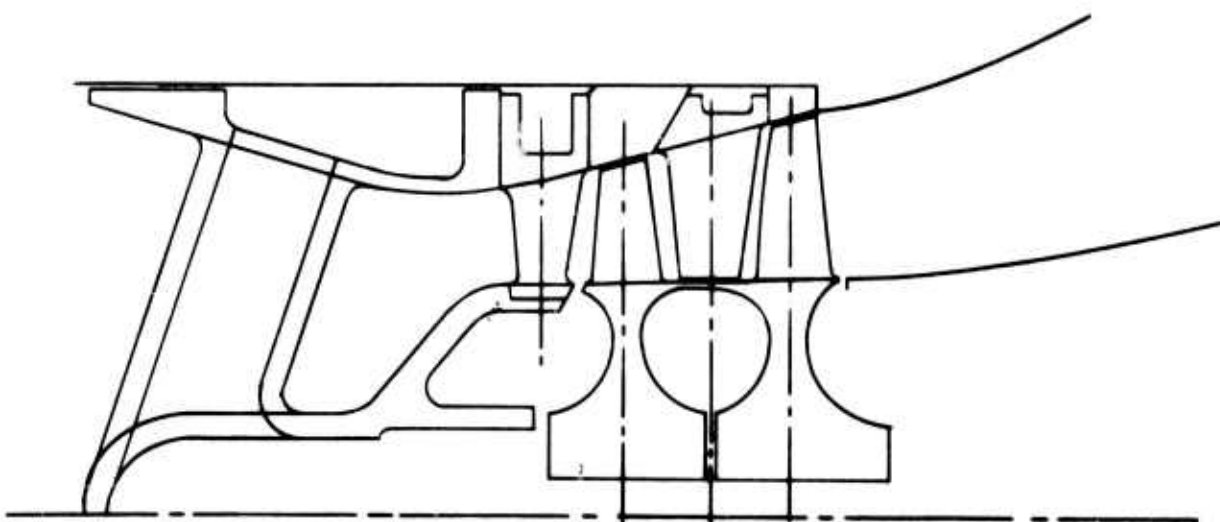


Figure 3.2 — Finite Difference Model of Ceramic Hot Flow Section

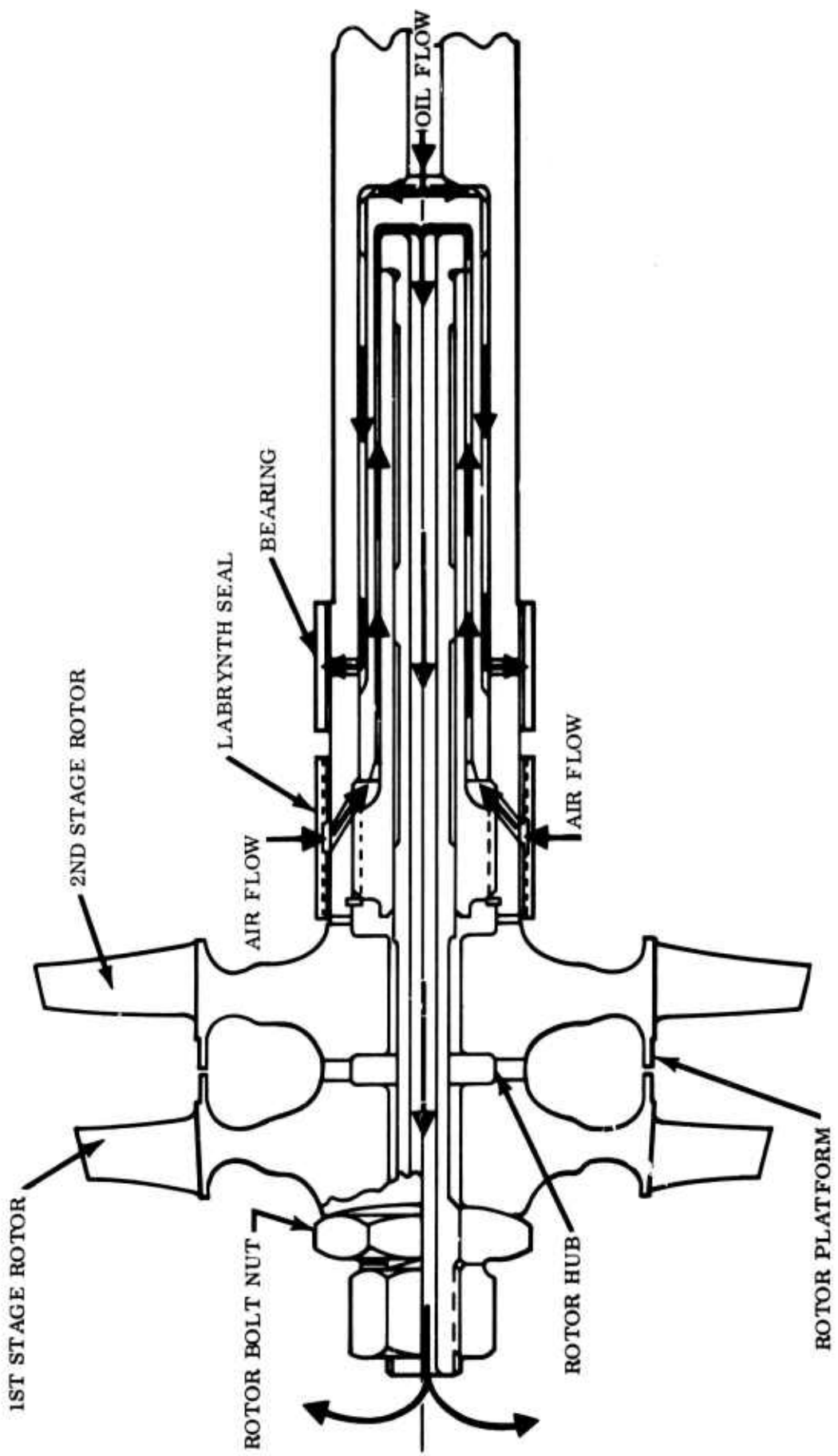


Figure 3.3 — Rotors and Attachment Assembly

The FEHT program can be used to determine the idle and full speed steady state temperature distribution in the attachment assembly model shown in Figure 3.4. A transient heat transfer analysis of the assembly can also be run from time zero to 105 seconds with idle engine conditions being assumed. These runs provide critical bolt temperature data to be used in determining bolt creep characteristics.

Next a FEST analysis of the assembly can be conducted for the same three conditions mentioned above. In all three cases the rotor bolt is allowed to elongate by using pseudo material stiffness properties for those elements connecting the first stage rotor to the rotor bolt nut. From the two steady state runs it is possible to calculate the minimum preload required to offset the thermal bolt load relaxation. A study of the principal rotor stresses as a function of time is used to determine the time of maximum rotor stress. In all cases, blade loading is assumed to be uniformly distributed over the rotor platform; therefore, blades are not shown on the finite element grids. A study of rotor and rotor bolt axial elongation as a function of time is used to determine the time of maximum bolt load. The magnitude of the bolt stress at that time can then be calculated. The bolt load at time of maximum rotor stress is also determined here for later use when analyzing the individual rotors.

When the time of maximum rotor stress is determined, a second transient heat transfer analysis of the assembly is conducted from the time of maximum rotor stress as determined above with engine conditions now assumed to be at full speed and held for 60 seconds. Data from this run is used in a stress analysis to determine the maximum rotor stresses that are expected to occur.

A third transient heat transfer analysis is conducted from idle steady state engine conditions for 20 seconds. Another stress analysis is run to determine the maximum rotor bolt load while the bolt is at its highest temperature.

It should be noted that the grid layouts were selected on the basis of previous studies of rotor stresses, with the finer mesh located in the areas of highest anticipated stresses.

Refined finite element models of the first and second stage rotors are shown in Figures 3.5 and 3.6 respectively. Utilizing the data at time of maximum stress for both the first and second transient cases and the corresponding bolt load data, transient heat transfer and stress analyses of the first and second stage rotors can be conducted. The time period for the transient may be short and the time increment small in order to determine the peak stresses. The rotor profiles can be altered as required in order to minimize stresses in critical areas.

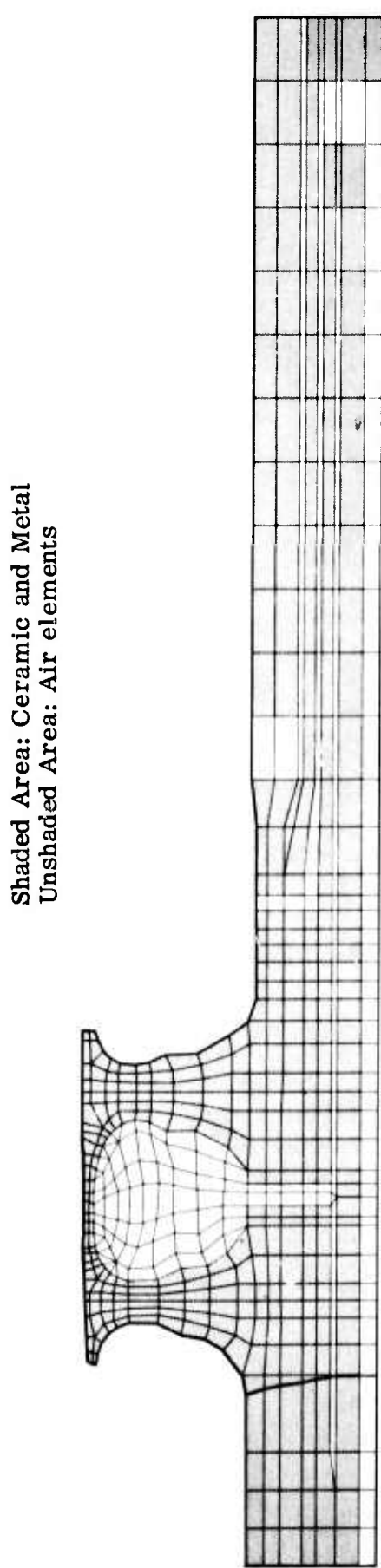
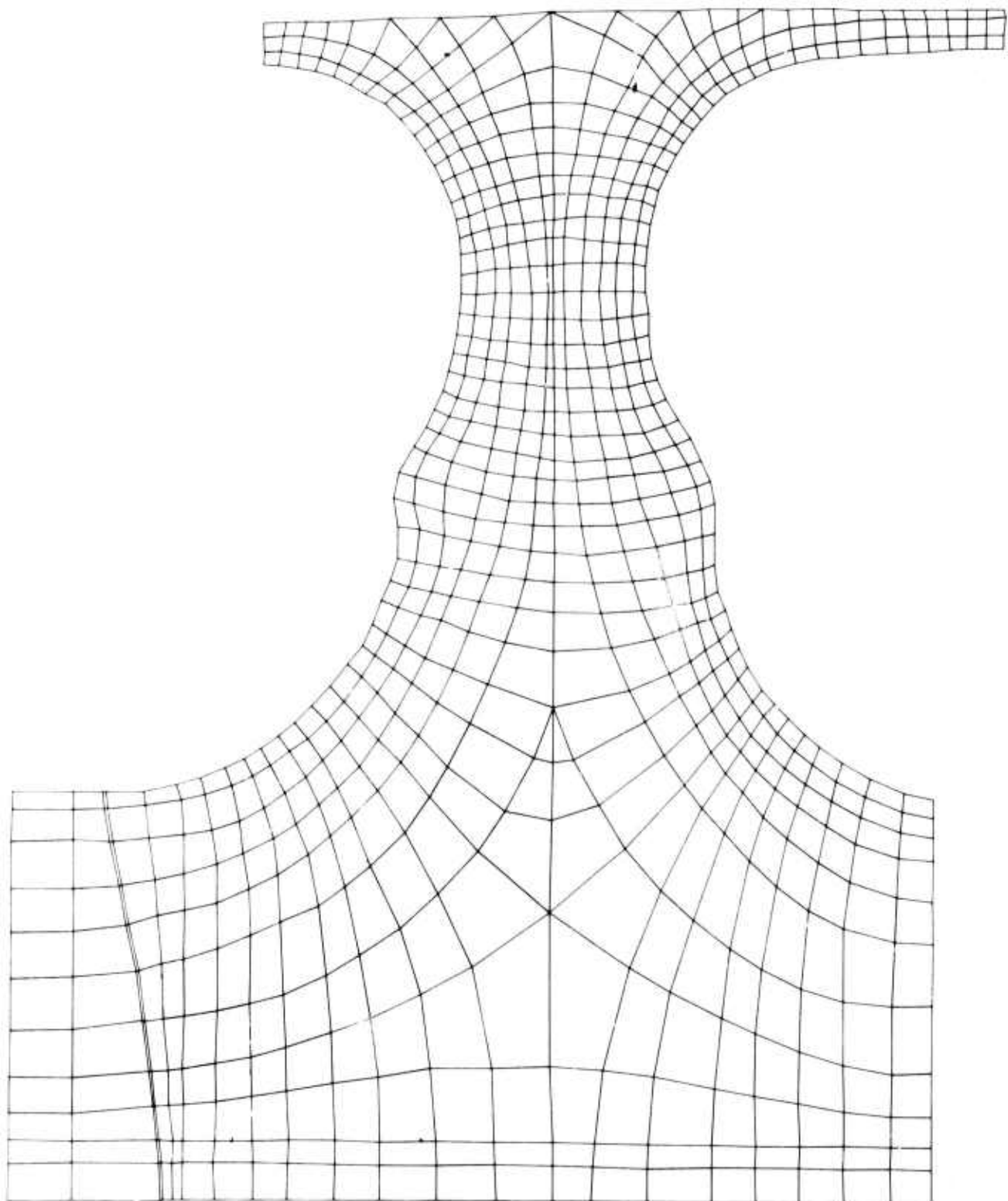


Figure 3.4 — Finite Element Model of Rotor and Attachment Assembly



**Figure 3.5 — Finite Element Model of First Stage Rotor**

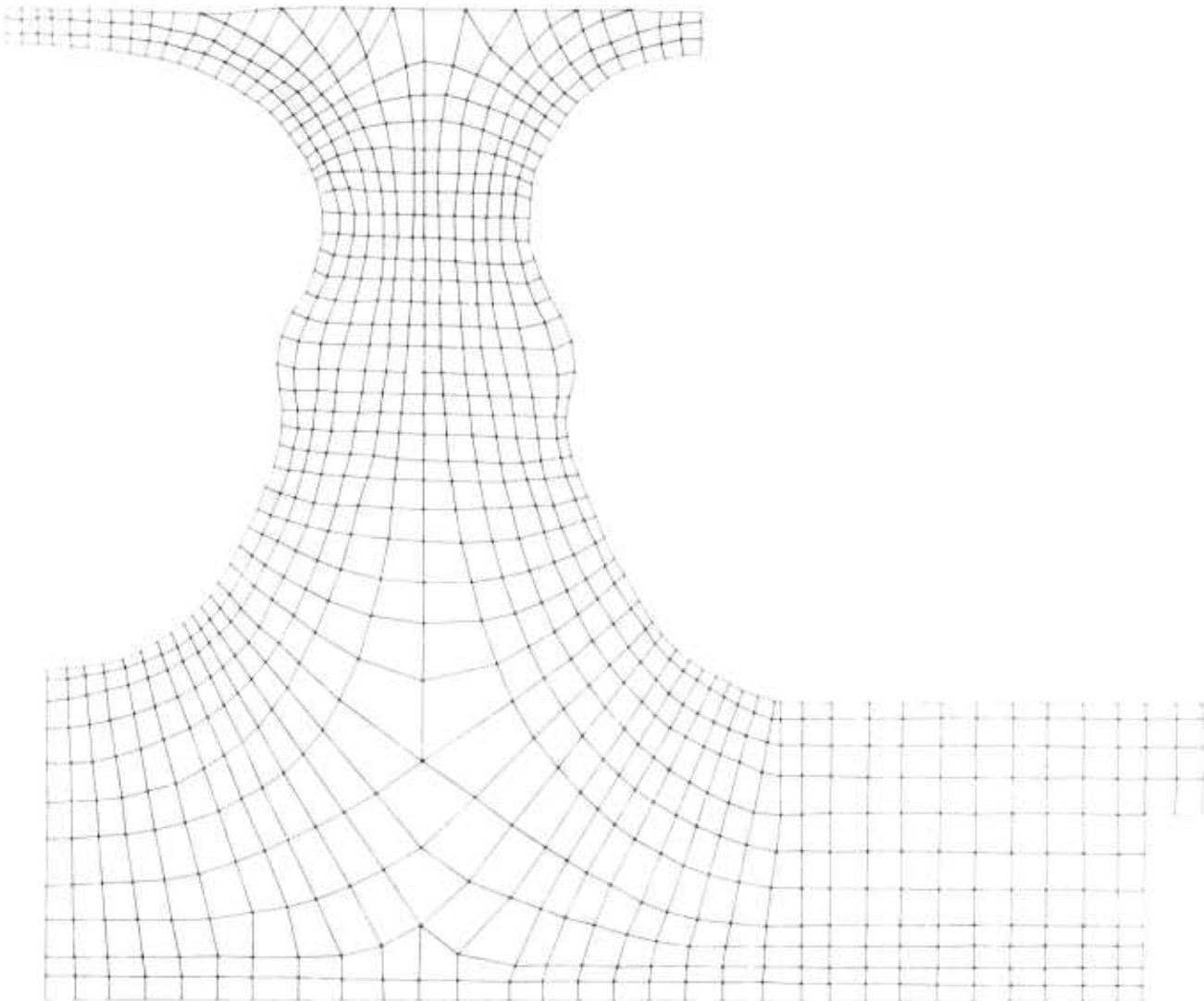


Figure 3.6 — Finite Element Model of Second Stage Rotor

#### Ceramic Rotor Attachment

Another area requiring analysis is the method of torque transfer from the first to the second rotor. Two possibilities are being studied and each study is being conducted as previously described. The first study considers torque transfer through a curvic coupling at the rotor platforms. The second concept has the coupling located at the rotor hubs. The method of machining the couplings at the rotor hub is still in the preliminary stages of design, whereas the platform coupling design has been completed.

The rotors coupled at their platforms react as a rigid body under the prevailing gyroscopic forces. However, increased bolt stress results under transient conditions due to the rotor platforms heating faster than the rotor bolt. Stresses in the rotor disk are also increased with the platform curvic design due to the bending moments resulting from axial loads.

Conversely, rotor disk stresses and rotor bolt stresses are expected to decrease with the hub coupling design relative to the platform coupling. The rotor bolt load will be transmitted in a more direct route back to the turbine shaft coupling. The rotors will act as separate components, however, and as such may subject the rotor bolt to bending stresses. The long overhang of the second stage rotor platform will not be supported by the first stage as in the design with platform coupling.

The transmission of torque from the ceramic rotors to the shaft required a design which would allow for differential thermal expansion between dissimilar materials and still maintaining exacting concentricities. The curvic coupling face spline modified to a half-barrel shape met these requirements and has been proven in gas turbine applications.

The curvic coupling is produced on precision grinding machines. The machine consists of a rotating formed grinding wheel mounted on a shaft which translates into the stationary workpiece. The formed wheel is cupped and grinds two tooth faces simultaneously. It is a functional requirement that curvic couplings be precision ground. Therefore, very precise control settings are built into the curvic grinder. This allows reproducibility of interchangeable parts cut on different machines. In the development of conventional metal curvic couplings, the grinding wheel may be modified and automatically dressed in the grinder. However, since this application required a diamond grinding wheel to machine the silicon nitride part, it was decided to provide all the final adjustments and dressing to the conventional wheel used to cut the metal part. This allowed the use of a formed diamond coated wheel for grinding the ceramic parts resulting in considerable cost savings as compared to fabricating a dressable diamond matrix wheel.

The half-barrel design with a point of tangency at the outer radius allows the convex (metal) tooth to grow radially outward in relation to the concave (ceramic) tooth, while maintaining a uniform contact pressure by elastic deformation of the curvic teeth. The number of teeth was selected at fifteen after several design iterations performed by the Gleason Works. The selection was influenced by consideration of the stress risers in the ceramic component, the minimal number of cuts, and standardization of the design.

Gleason Works was contracted to fabricate one mating set of curvic coupling masters. The hot pressed silicon nitride master was fabricated in-house and diamond ground to the same dimensions specified on the rotor drawing. The final master set is shown on Figure 3.7. The metal part is SAE 4150 with a through hardening of Rockwell C 34-38. Inspection of the masters indicated no runout was present (less than one-ten thousands of an inch) in five arbitrarily selected positions. Parallelism of the mating masters was better than the capability of measurement by standard inspection techniques.

Figure 3.8 illustrates the inspection equipment used to determine the contour and surface texture of the tooth. The curvic specimen is positioned on the inspection block at the 30° pressure angle. A diamond stylus is traversed along the contact face and the excursion of the stylus recorded on the Proficorder. The results of this inspection indicated 0.000125" excursion is present over 0.031" of the tooth with a surface texture of 35  $\mu$  in. arithmetic average. This is acceptable for curvic coupling design. An enlargement (32X) of one ceramic tooth is shown on Figure 3.9. Of interest is the slight curvature of tooth as compared to

the cross-hair of the shadowgraph. While still acceptable, this may be improved. Also of interest is the fin at the bottom of the gable. This is caused by incomplete overlapping of the grinding wheel while cutting adjacent teeth. This does not interfere with the functionality of the face spline, as sufficient clearance is present at the end of each metal tooth. However, this will be corrected either by modifying the diamond wheel or by hand-filing the parts before any testing is performed.

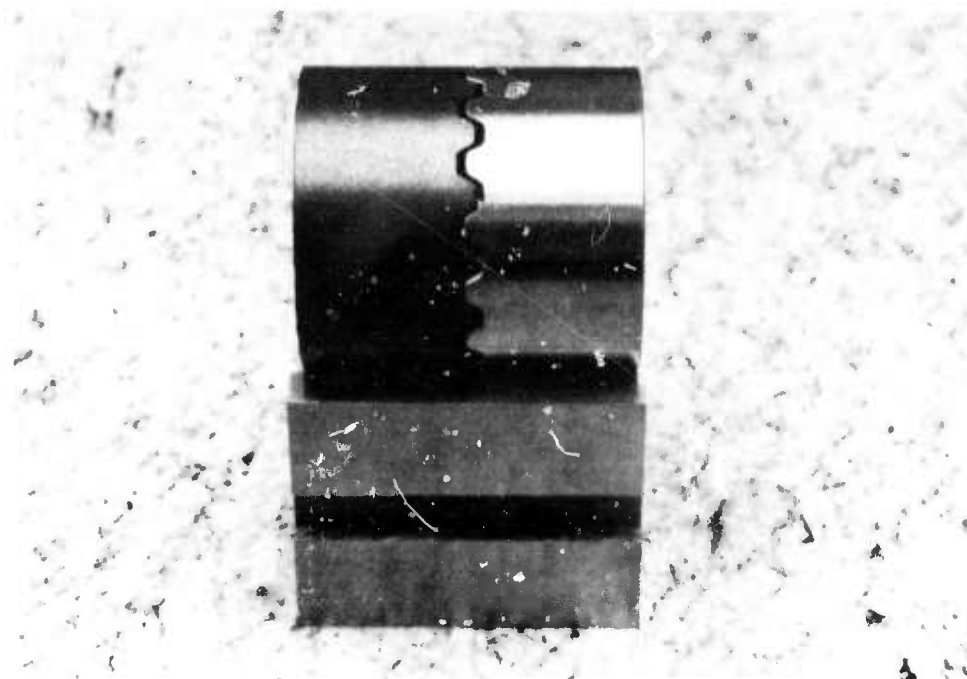


Figure 3.7 — Curvic Coupling Master Set

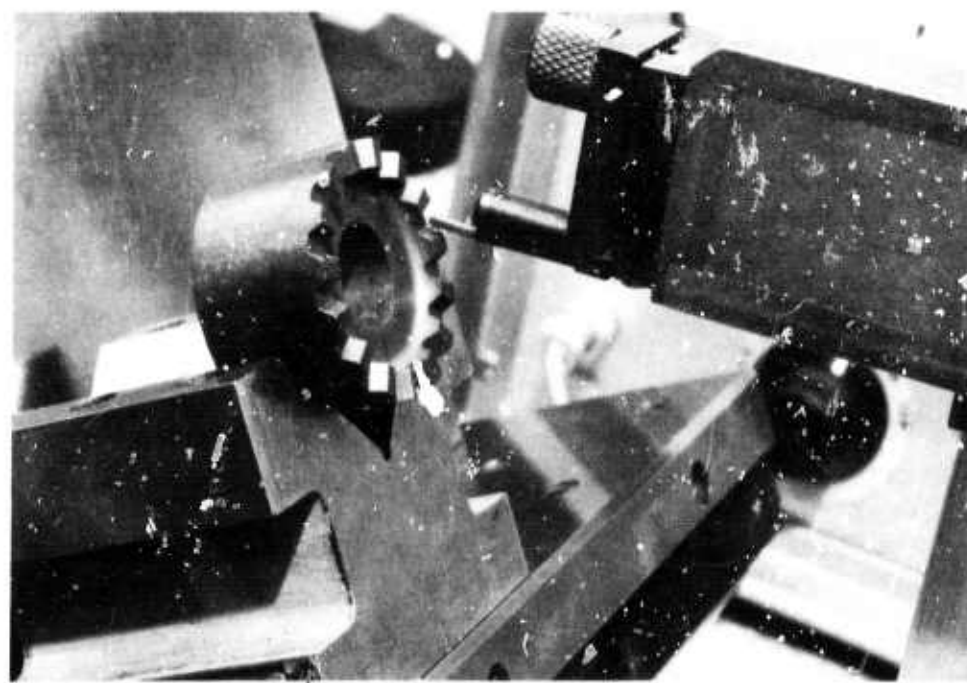


Figure 3.8 — Curvic Coupling Inspection Equipment

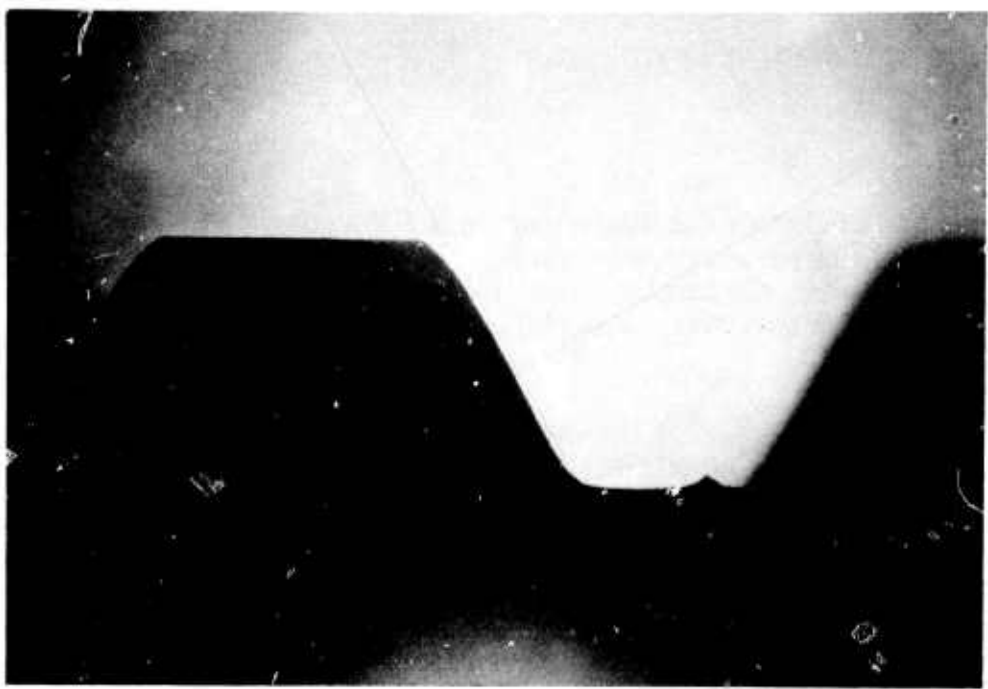


Figure 3.9 — Enlargement of Hot Pressed Silicon Nitride Curvic Coupling Tooth (32X)

### 3.1.2 MATERIALS AND FABRICATION

#### Introduction

Design and materials considerations during the course of the program have shown that few materials have properties capable of withstanding the conditions imposed by the turbine rotor. (1) Two primary candidate materials are being developed, fully dense silicon nitride ( $Si_3N_4$ ) and fully dense silicon carbide (SiC).

Fully dense silicon nitride is almost exclusively formed by hot-pressing. Usually a fine particle size reactive  $Si_3N_4$  powder, mainly composed of the  $\alpha$  form crystallographically, is used as the starting material. A sintering aid such as MgO is added (usually in amounts of 1 to 5 weight %) and intimately mixed. The powder mixture is hot pressed to full density in graphite dies and plungers. Hot-pressing parameters normally used are temperatures of 1700 to 1800°C and pressures of 3000 to 4000 psi for 1 to 2 hours. Several programs are being actively pursued which attempt to fabricate complex shaped turbine rotors by variations of this basic process.

Fully dense silicon carbide can be formed by several methods including hot-pressing, chemical vapor deposition, and reaction sintering. Some of the processes being investigated for the machining of  $Si_3N_4$  could also be applied to SiC, therefore only an electro-discharge machining method unique to the electrically conducting, hot-pressed SiC is being evaluated currently. In addition, a program of growing a rotor molecule by molecule, using the chemical vapor deposition of silicon carbide is described.

#### Ford Pseudo-Isostatic Hot Pressed Method

Ford<sup>(1)</sup> and Lumby and Coe<sup>(2)</sup> have established that the alpha form of silicon nitride is preferred for hot pressing, since fully dense material produced from that form exhibits good mechanical properties. The program approach is to develop the technology to nitride preformed silicon parts into the high alpha silicon nitride form and investigate the techniques of hot-pressing such preforms into dense integral turbine rotors.

The advantage of molding preforms from silicon rather than silicon nitride powder is that the density of the nitrided preformed shapes is high, (approximately 70% of T.D.). This is particularly important for complex shapes such as thin airfoils where the smaller shrinkage experienced during densification yields substantially smaller dimensional distortion.

#### Nitriding Study

Results of nitriding studies from the last report<sup>(1)</sup> indicated that (1) lithium carbonate additions to the silicon metal enhanced alpha silicon nitride formation during nitriding, and (2) the use of static 3 psi nitriding atmosphere resulted in closer control of  $\alpha Si_3N_4$  content than flowing atmosphere. Therefore, efforts this period were directed toward optimizing the lithium content in combination with optimizing the nitriding atmosphere to insure complete nitriding while maintaining a high alpha silicon nitride composition necessary for subsequent hot pressing of high strength material.

The nitriding studies were conducted on small injection molded silicon bars containing lithium carbonate ranging in composition from 0 to 5 w/o lithium oxide based on final silicon nitride content. The silicon metal had an average particle size of approximately  $3\text{ }\mu$  with major impurities being iron and aluminum at 7000 and 10,500 ppm, respectively. The effect of calcium fluoride additions on alpha silicon nitride formation was also evaluated. Past experience has shown approximately 0.67 w/o calcium fluoride additions to silicon metal prior to nitriding improved both the sinterability and strength of reaction sintered silicon nitride. Its effect on alpha formation had not been investigated.

The injection molded bars were baked out at  $300^{\circ}\text{C}$  to remove organics before nitriding. All nitriding experiments were conducted in a small 2-1/2 inch tube furnace under a static, 3 psi atmosphere. The silicon bars were heated at a rate of approximately  $300^{\circ}\text{F}$  per hour to the nitriding temperature, held for 24 hours at this temperature, and allowed to cool overnight. These bars were nitrided at several temperatures in various atmospheres, of  $-85^{\circ}\text{F}$  dew point with a maximum oxygen content of 10 ppm, as follows:

$2300^{\circ}\text{F}$  — cryogenic nitrogen  
 $2450^{\circ}\text{F}$  — cryogenic nitrogen  
 $2450^{\circ}\text{F}$  — nitrogen — 1% carbon dioxide  
 $2450^{\circ}\text{F}$  — nitrogen — 4% hydrogen

After nitriding, the silicon nitride bars were characterized by x-ray diffraction for phase identification of  $\alpha$  and  $\beta$  silicon nitride, silicon oxynitride ( $\text{Si}_2\text{ON}_2$ ), crystobalite ( $\text{SiO}_2$ ) and free silicon metal (Si). All data in this report are in weight percent and may not be directly compared with peak height percent previously reported.(1)

The results of the nitriding studies are summarized in Figure 3.10 showing the effect of both  $\text{Li}_2\text{O}$  and  $\text{CaF}_2$  on the formation of  $\alpha$   $\text{Si}_3\text{N}_4$  and  $\text{Si}_2\text{ON}_2$  under different nitriding conditions. The  $\beta$   $\text{Si}_3\text{N}_4$  concentrations are not shown in the figures, but can be derived by difference.

All results illustrated in Figure 3.10 show that  $\text{CaF}_2$  additions to silicon metal impedes  $\text{Si}_3\text{N}_4$  formation. However, the hindering effect of calcium fluoride is reduced as the  $\text{Li}_2\text{O}$  concentration is increased, and the use of more than 2%  $\text{Li}_2\text{O}$  overrides any effect of calcium fluoride. This effect of  $\text{CaF}_2$  may be related to the silicon-nitrogen exothermic reaction during nitriding, but the exact mechanism is not yet understood.

The results as shown in Figures 3.10A, 3.10B and 3.10C are similar. The formation of  $\alpha$   $\text{Si}_3\text{N}_4$  increases with increasing  $\text{Li}_2\text{O}$  concentrations to a point where excess oxygen in the structure results in  $\text{Si}_2\text{ON}_2$  formation at the expense of  $\alpha$   $\text{Si}_3\text{N}_4$ . This is noted by the corresponding decrease in alpha silicon nitride and increase in silicon oxynitride. Lowering the nitriding temperature  $150^{\circ}\text{F}$  for the cryogenic nitrogen conditions (Figures 3.10A and 3.10B) had no significant effect on the formation of alpha silicon nitride or silicon oxynitride. The lithium content after nitriding was approximately 50 percent greater at the lower temperature ( $2300^{\circ}\text{F}$ ). This is desirable since lithium behaves as a sintering aid during hot pressing.

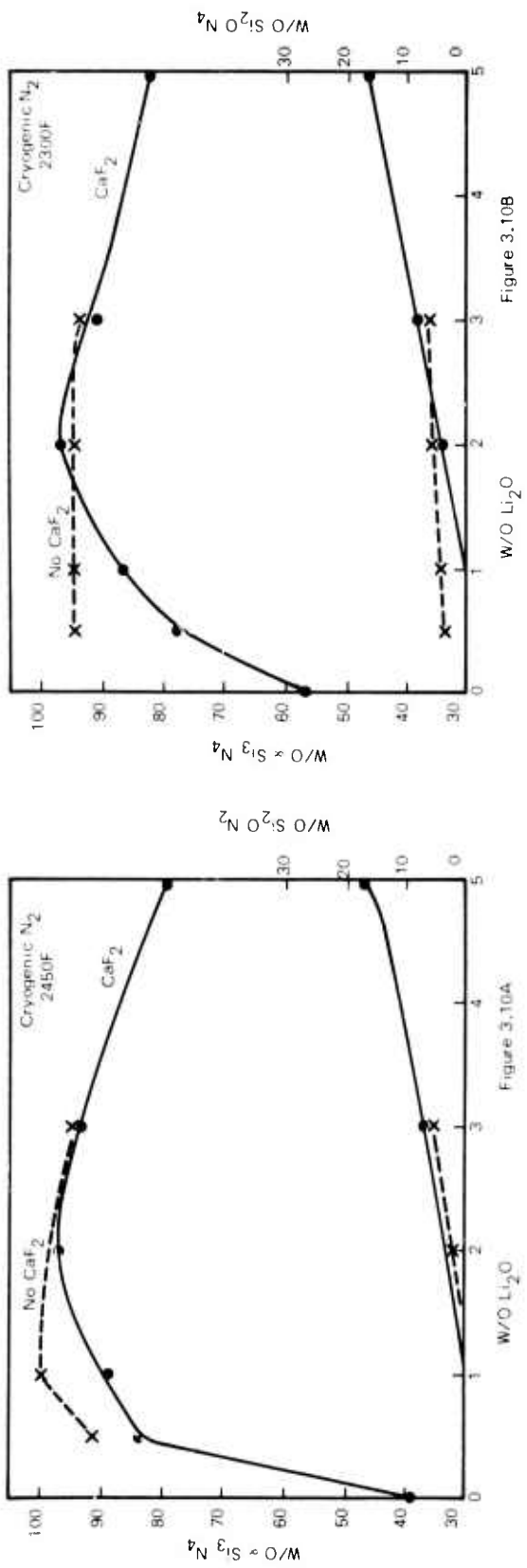


Figure 3.10B

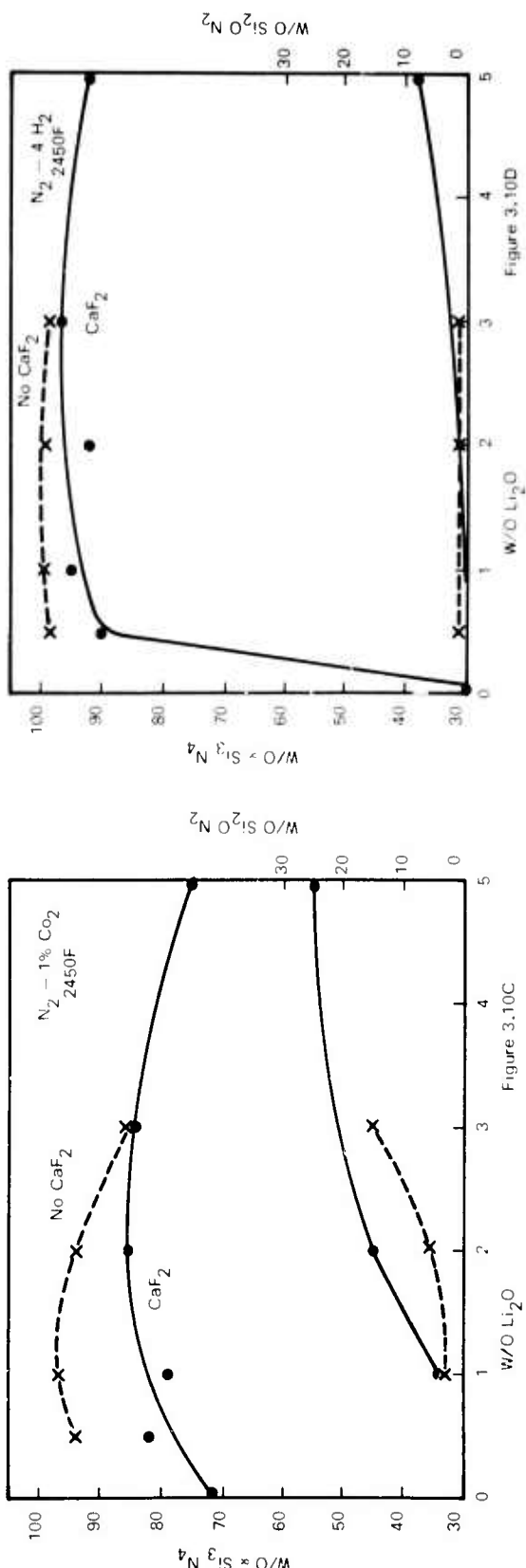


Figure 3.10D

Figure 3.10 — Nitriding Results Under Various Conditions

Figure 3.10D illustrates the results for nitrogen 4% hydrogen at 2450°F showing that all compositions containing lithium oxide nitrided to greater than 90 percent alpha silicon nitride. Two compositions containing  $\text{CaF}_2$  at low  $\text{Li}_2\text{O}$  concentrations (0.5 and 1.0 w/o  $\text{Li}_2\text{O}$  per  $\text{Si}_3\text{N}_4$ ) showed traces of free silicon indicating incomplete nitriding. However, all compositions without calcium fluoride nitrided to completion (no free silicon) with  $\alpha\text{Si}_3\text{N}_4$  contents of 98 to 100 percent.

These results indicate that high alpha silicon nitride (greater than 98 percent) can be prepared by nitriding GT-209(1) silicon at 2450°F in a static, 3 psi nitrogen - 4% hydrogen atmosphere for 24 hours. The alpha silicon nitride content seems to be independent of lithium oxide additions up to 5 w/o. Since high lithium oxide additions do not form silicon oxynitride at the expense of alpha silicon nitride for a nitrogen - 4% hydrogen atmosphere, higher concentrations of lithium oxide may be desirable to enhance densification during subsequent hot-pressing.

Magnesium oxide is normally used as a densification aid during hot-pressing. Its concentration and distribution is critical and must be closely controlled as high concentrations (greater than 2 w/o) may substantially reduce the high-temperature strength of silicon nitride. Past experience has shown the vacuum impregnation technique, using an aqueous magnesium nitrate solution to introduce magnesium into a preformed silicon nitride part, to be unsatisfactory as the  $\text{MgO}$  content was found to vary within the part as well as between parts.

Studies were made to evaluate the behavior of silicon metal containing magnesium oxide during nitriding. These studies were conducted on small injection molded silicon bars containing both magnesium oxide and lithium oxide. Two silicon metal powders were investigated; a coarse high purity grade (GT-22)(1) and the standard silicon powder (GT-209). The GT-22 silicon metal was minus eight mesh and contained 2500 and 1500 ppm iron and aluminum, respectively. The GT-209 silicon metal was finer (approximately  $3\text{ }\mu$ ) and of lower purity, containing 7000 and 10,500 ppm iron and aluminum, respectively. The silicon metal powders containing 2 w/o  $\text{MgO}$  and 1 w/o  $\text{Li}_2\text{O}$  (added as lithium carbonate) were wet ball milled in small plastic jars with tungsten carbide balls and tertiary butyl alcohol for 24 hours. After milling, which reduced the 8 mesh GT-22 to about  $2\text{ }\mu$ , the slurry was dried and screened through a 100 mesh screen. The dried silicon powders were injection molded into bars using a suitable binder, then baked out at 300°C to remove organics. The nitriding experiments were similar to those previously described in which all bars were nitrided under a static, 3 psi atmosphere for 24 hours. The nitrided silicon bars were characterized by x-ray diffraction for phase identification.

The results are summarized in Table 3.1 and Figure 3.11. Comparing these results with data just described show that magnesium substantially retards alpha silicon nitride formation even in the presence of 1 w/o lithium oxide.

Lowering the nitriding temperatures significantly increases the formation of alpha silicon nitride (Figure 3.11) for both GT-22 and GT-209 grade silicon powders. However, caution should be exercised when extrapolating below 2200°F as nitriding to completion becomes more difficult. The GT-22 grade silicon nitrided to slightly higher alpha silicon nitride contents (Figure 3.11) than the GT-209 grade silicon which is probably related to the higher purity of the GT-22 grade silicon.

\* Complete characterization of silicon powders is provided in Ref. (1),  
Page 35

**TABLE 3.1**  
**Nitriding Results For GT-22 and GT-209 Silicon Bars**  
Each Bar Contained 2 w/o MgO and 1 w/o Li<sub>2</sub>O

Run	Silicon Powder	Nitriding Conditions		Phases Present in Si <sub>3</sub> N <sub>4</sub>		
		Temperature °F	Atmosphere	$\alpha$	$\beta$	Si <sub>2</sub> ON <sub>2</sub>
TN-142	GT-209	2450	Cryogenic N <sub>2</sub>	23 w/o	71 w/o	6 w/o
	GT-22	2450	Cryogenic N <sub>2</sub>	27	63	10
TN-144	GT-209	2300	Cryogenic N <sub>2</sub>	37	57	6
	GT-22	2300	Cryogenic N <sub>2</sub>	47	48	5
TN-146	GT-209	2200	Cryogenic N <sub>2</sub>	46	54	—
	GT-22	2200	Cryogenic N <sub>2</sub>	53	47	—
TN-150	GT-209	2300	N <sub>2</sub> - 1% CO <sub>2</sub>	38	60	2
	GT-22	2300	N <sub>2</sub> - 1% CO <sub>2</sub>	51	45	4
TN-172	GT-209	2300	N <sub>2</sub> - 4% H <sub>2</sub>	50	50	—
	GT-22	2300	N <sub>2</sub> - 4% H <sub>2</sub>	56	44	—

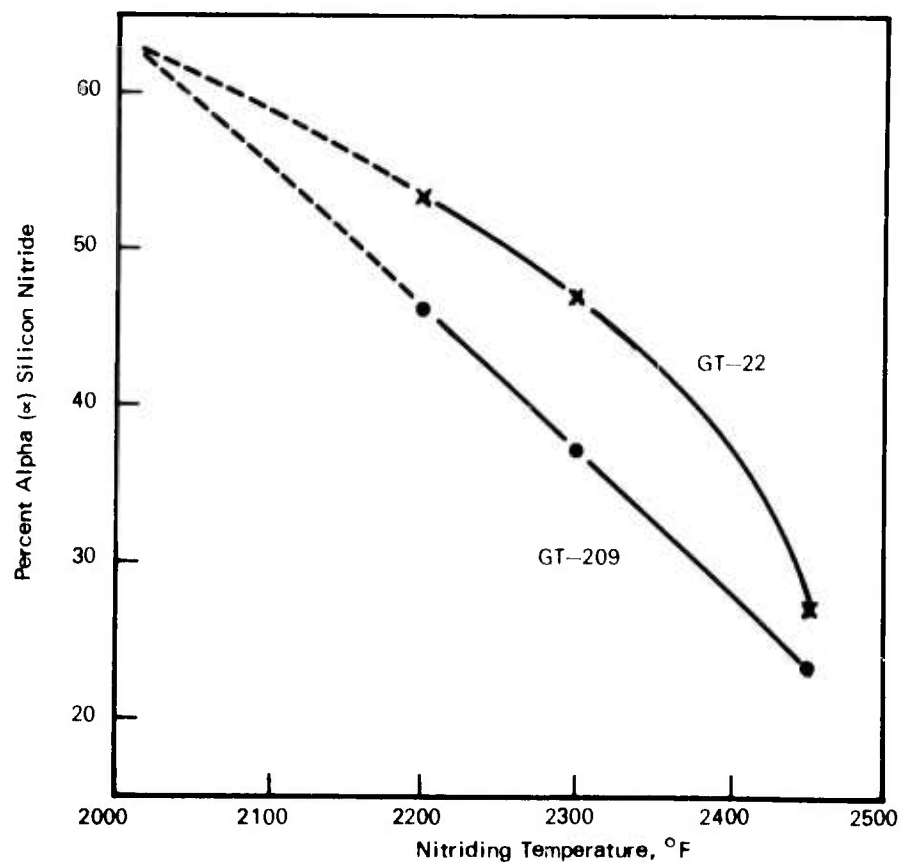


Figure 3.11. — Nitriding Results Using a Static Nitrogen Atmosphere

Chemical characterization has shown that approximately 50 percent of the magnesium oxide volatilized during nitriding, as shown in Figure 3.12. Higher initial MgO concentrations to allow for volatilization during nitriding are being evaluated but this is expected to further hinder alpha silicon nitride formation. Changing the nitriding atmosphere from cryogenic nitrogen to nitrogen - 1% carbon dioxide had little, if any, effect on the phases formed. Nitriding in a nitrogen - 4% hydrogen atmosphere improved the alpha silicon nitride content only slightly. These results indicate that magnesium greatly hinders alpha silicon nitride formation even in the presence of lithium oxide.

### Phase Gradient Study

A phase compositional gradient between the surface and the center of the hub of a turbine rotor preform was reported in the previous report (1). A series of gradient studies were conducted on individually nitrided blades to determine the extent of the problem in smaller cross sections.

Figure 3.13 is a photograph of a blade indicating the portion of the base sliced out for examination. The surface was first examined by x-ray diffraction, then the surface was removed by diamond machining, exposing an interior plane of material at a depth A from the original surface. After x-ray diffraction analysis of the newly exposed plane was complete, the grinding process was repeated to expose a new interior plane at depth B.

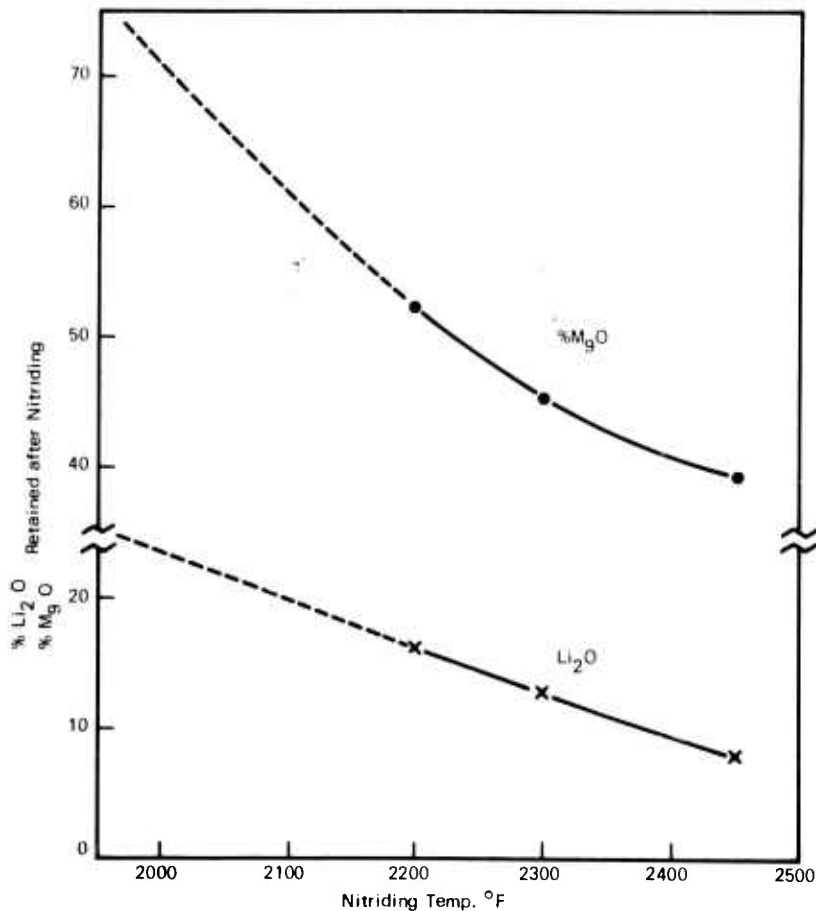


Figure 3.12 — % MgO and % Li<sub>2</sub>O Remaining After Nitriding, as a Function of Temperature

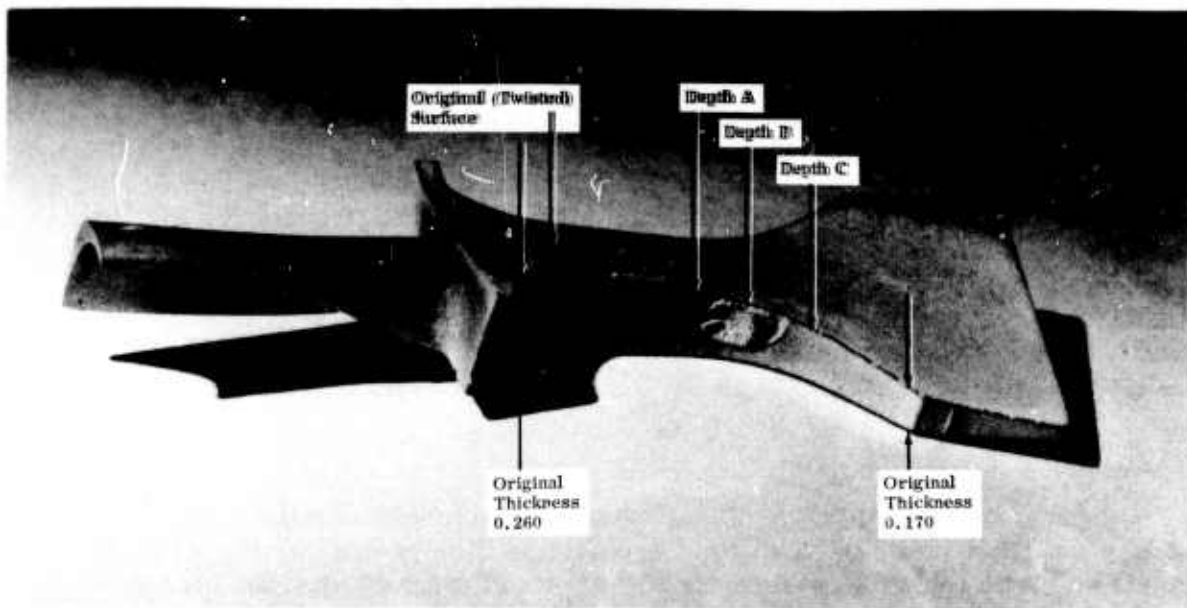


Figure 3.13 — Blade indicating the Portion of the Base Sliced Out

X-ray analysis was obtained on plane B, and, after grinding to expose depth C, an analysis was made of the new surface. Table 3.2 lists the results of the x-ray analysis for all 4 surfaces for 3 blades nitrided by the methods previously discussed. Also listed for comparison purposes are the results of powder diffraction analysis of the remainder of each blade, which represents the average crystallographic composition.

The results for blades No. 1 and No. 2 nitrided in an oxygen rich atmosphere ( $N_2 - 1\% CO_2$ ) show a high concentration of silicon oxynitride on the surface. Directly below the surface, both the alpha and beta phases increase. Further into the blade interior,  $\alpha$  increases while  $\beta$  decreases. The high  $\beta Si_3N_4$  area directly below the surface indicates an oxygen deficient area which is believed to be directly connected with the high  $Si_2ON_2$  adjacent surface layer. The interior analyses are typical of analyses reported earlier under similar nitriding conditions. Nitriding of blade No. 3 in a reducing type atmosphere ( $N_2 - 4\% H_2$ ) resulted in high  $\alpha Si_3N_4$  at the surface with the  $\beta$  phase increasing towards the blade interior.

These results indicate that an oxidizing type atmosphere ( $N_2 - 1\% CO_2$ ) will produce a phase gradient in small silicon nitride turbine blades which could grossly affect properties and performance. The gradient could be larger for more massive sections such as the hub portion of the rotor.

#### Hot Pressing

Hot pressing is the principal method of fully densifying silicon nitride because of its inherent resistance to sintering due to low atomic mobilities and high decomposition pressures at the sintering temperatures. Hot pressing or pressure sintering is the simultaneous application of pressure and temperature to an object usually contained within a graphite die system. Pressure can be transmitted by several methods, the most common being uniaxially

applied pressure to an object in direct contact with the graphite die. Another approach utilizes a powder bed to transmit the pressure to the object at temperature. The powder bed behaves as a first approximation of an isostatic fluid and thus is often referred to as pseudo-isostatic hot pressing. Since complex shapes have been produced by this technique without the need for complex shaped dies, this approach is being pursued for this program.

TABLE 3.2

X-Ray Analyses of Silicon Nitride Blades

Blade 1 — TN 158 N<sub>2</sub> — 1% CO<sub>2</sub> @ 2450°F for 24 Hours

Phase	Average	Surface	Depth From Original Surface		
			A = .052	B = .100	C = .124
α Si <sub>3</sub> N <sub>4</sub>	69.5	12.2	71.8	86.4	84.0
β Si <sub>3</sub> N <sub>4</sub>	9.5	5.8	21.5	8.9	9.0
Si <sub>2</sub> ON <sub>2</sub>	16.1	82.0	5.4	2.8	4.6
Si	—	—	—	—	—
SiO <sub>2</sub>	—	—	—	—	—
SiC	4.9	—	1.3	1.8	2.4

Blade 2 — TN 160 N<sub>2</sub> — 1% CO<sub>2</sub> @ 2450°F for 24 Hours

Phase	Average	Surface	A = .025	B = .048	C = .071
α Si <sub>3</sub> N <sub>4</sub>	90.9	34.3	77.8	94.4	92.7
β Si <sub>3</sub> N <sub>4</sub>	3.3	1.3	18.7	3.9	6.5
Si <sub>2</sub> ON <sub>2</sub>	4.6	64.5	2.6	1.2	0.8
Si	—	—	—	0.2	—
SiO <sub>2</sub>	—	—	—	0.3	—
SiC	1.2	—	0.9	—	—

Blade 3 — TN 162 N<sub>2</sub> — 4% H<sub>2</sub> @ 2450°F for 24 Hours

Phase	Average	Surface	A = .033	B = .053	C = .080
α Si <sub>3</sub> N <sub>4</sub>	88.6	98.0	85.8	80.7	80.9
β Si <sub>3</sub> N <sub>4</sub>	11.2	2.0	14.2	18.6	18.9
Si <sub>2</sub> ON <sub>2</sub>	—	—	—	—	—
Si	0.1	—	—	—	0.3
SiO <sub>2</sub>	—	—	—	0.6	—

Several molded silicon nitride segmented turbine rotors have been pseudo-isostatically hot pressed. Individual silicon turbine blades were first injection molded and then 36 blades were assembled and bonded together by a molded hub section. The assembly was then nitrided to form an integral silicon nitride turbine rotor. The rotor was vacuum impregnated with a saturated aqueous solution of magnesium nitrate. The rotor was placed in an 8 inch thick bed of flake graphite within a 6 inch diameter cavity graphite dies. Both flake graphite and boron nitride have been used as a powder medium for this technique. A transite furnace box encasing the insulation, induction coil, and graphite die system enabled hot pressing under a nitrogen atmosphere.

A major problem encountered during the last reporting period was non-uniform powder flow in the powder bed resulting in fractured parts especially at areas of thin cross section. The hot press has been modified to remedy this by installing a bottom ram to incorporate double pressing action. Two hydraulic flow control valves were installed in the hydraulic lines to maintain equal ram travel.

The graphite dies system was inductively heated without pressure to approximately 1600°C. At 1600°C, approximately 1000 psi pressure was applied employing the double acting rams and heating continued while pressure was increased at 50°C increments until a hot pressing condition of 1750°C and 4000 psi was reached. The temperature and pressure were maintained for one hour after which the system was allowed to cool.

These attempts to hot press a turbine rotor were unsuccessful as the hub portion did not completely densify and the blades closed during pressing, with some fracture occurring at the trailing edges. The average density of the hot pressed rotors was approximately 2.75 g/cm<sup>3</sup> (approximately 87 percent of theoretical).

The two most important factors believed to affect densification are the starting silicon powder and densification additive (MgO). The turbine rotors were prepared from a 8-10  $\mu$  particle size GT-196<sup>(1)</sup> grade silicon powder normally used for reaction sintered parts. Finer silicon powder (Grade GT-209) with particle size of approximately 3  $\mu$  should greatly improve densification during hot pressing. However, problems with the molding tool delayed evaluation. The vacuum impregnation technique used to distribute magnesium oxide throughout the reaction sintered silicon nitride rotor has not been reproducible, since the magnesium content has been found to vary from 0.45 to 1.87 w/o. Variations in both the reaction sintered density (porosity) and the drying rates would greatly affect the magnesium concentration and distribution.

The distortion and cracking of the turbine blades indicates that the powder media is not flowing through the blade openings during pressing. Solid graphite tooling is therefore required that will support blade trailing edges during hot pressing, yet allow densification. Graphite supports have been designed and are presently being fabricated.

Another approach to fabricating complex shaped silicon nitride parts by hot pressing was investigated. The effort involves hot pressing a shaped turbine rotor blank from silicon nitride powder, purchased from Advanced Materials Engineering Ltd. (AME), directly in complex shaped graphite dies. This blank

resembles a standard turbine rotor except it does not have individual blades. The object is to fabricate a theoretically dense part on which turbine blades can be machines, requiring minimum contour machining of remaining section. Efforts to establish machining techniques for silicon nitride are described later in this section.

Processing parameters of AME  $\text{Si}_3\text{N}_4$  powder were evaluated by hot pressing small 2 inch diameter specimens. Chemical characterization indicated that two lots of AME  $\text{Si}_3\text{N}_4$  powder were essentially identical. X-ray diffraction showed the phases present were respectively 89 w/o and 87 w/o alpha silicon nitride; 8 w/o and 12 w/o beta silicon nitride; and 2/o silicon oxynitride (one lot only). Spectrographic analysis showed iron, calcium, and aluminum were the major impurities at the 5000 to 8000 ppm level with no significant difference between the two lots. Particle size measurements were not made on the as-received AME silicon nitride powders as they were reported by the supplier to be minus 325 and minus 100 mesh respectively.

The AME powders were wet ball milled in a rubber lined mill with tungsten carbide balls and tertiary butyl alcohol for various times ranging from 20 to 70 hours. Two percent magnesium oxide was added before milling to aid densification during hot pressing. After milling the powders were dried and screened through a 100 mesh screen. The milled powders were characterized with respect to particle size and chemistry. There was essentially no difference in the particle size of the milled powders, as particle size averaged  $2\text{-}4 \mu$ . Spectrographic analysis showed no significant change in the impurity content resulting from milling. The tungsten and cobalt concentrations remained unchanged at  $< 0.01$  and  $< 0.02$  percent indicating negligible contamination from the grinding balls. The carbon content increased from approximately 0.2 to 0.5 w/o resulting from contamination from the rubber lined ball mill. The carbon impurity will form silicon carbide during hot pressing and therefore should have little effect on the silicon nitride properties.

Samples of milled AME  $\text{Si}_3\text{N}_4$  powder were hot pressed at various temperatures and pressures in 2 inch diameter graphite die to produce a specimen approximately one inch thick. Graphite cloth and boron nitride were used at the graphite interfaces to minimize the silicon-carbon reaction at elevated temperatures. Graphite dies were inductively heated under a nitrogen atmosphere using the same furnace and hot pressing procedure described earlier. Table 3.3 summarizes the results of the hot pressed specimens relating hot pressing conditions, density, grain size, strength, and chemistry.

As expected, the density of the silicon nitride specimens increased with both temperature and pressure, and densities greater than 99 percent of theoretical were readily attained. The microstructure and chemistry were very similar for all the silicon nitride specimens. Hot pressing temperatures in excess of  $1800^{\circ}\text{C}$  for long times may cause slight decomposition of silicon nitride as indicated by the free silicon in specimens HP-87 and HP-88.

Flexural strength measurements at room temperature were determined in 3-point loading on a 0.75 inch span on three test bars ( $1/8'' \times 1/8'' \times 1 1/8''$  long) from each hot-pressed silicon nitride specimen. The average flexural strength for all five specimens was fairly consistent and no correlation with density, microstructure, and chemistry could be made. However, a relatively high

TABLE 3.3

Results of Hot-Pressed AME Silicon Nitride,  
Relating Hot-Pressing Conditions,  
Density, Grain Size, Chemistry, and Strength

Hot-Press Sample	Hot-Pressing Conditions			Density		Chemistry			Flexural Strength psi	
	Temp. °C	Pres. psi	Time at Temp. & Pres. in min.	g/cm <sup>3</sup>	percent of T.D. (1)	grain size $\mu$	Mg w/o	$\beta$ Si <sub>3</sub> N <sub>4</sub> w/o	Free Si w/o	
HP-85	1675	2500	150	2.69	84.6	(2)	ND	100	-0-	ND
HP-86	1750	2500	120	2.92	91.8	(2)	0.91	100	-0-	98000
HP-87	1800	2500	120	3.13	98.4	1.6	0.96	99.3	0.7	106000
HP-88	1850	2500	120	3.16	99.4	1.6	0.99	98.8	1.2	103000
HP-89	1810	4000	80	3.15	99.1	1.1	ND	100	-0-	99000
HP-92	1760	4000	60	3.16	99.4	ND	0.99	ND	ND	97000

(1) Based on a theoretical density of 3.18 g/cm<sup>3</sup>.

(2) Density too low for accurate measurement

ND = not determined

flexural strength of 98,000 psi was attained for specimen HP-86 whose density was only 2.92 g/cm<sup>3</sup> (91.8 percent of theoretical). These results are encouraging because they indicate that strength requirements necessary for the silicon nitride turbine rotor may be achieved at lower densities. Relaxed density requirements for silicon nitride rotor parts may enable lower magnesium oxide concentrations which in turn would improve the high-temperature strength of silicon nitride.

Based on the results of the 2 inch diameter specimens, two shaped turbine rotor blanks were fabricated from powder and procedures similar to that used for specimens HP-85-89 and 92. The two blanks (HP-95 and HP-98) were hot pressed at 4000 psi and 1725 and 1800°C for 130 and 120 minutes respectively. The hot pressed density of the two blanks, HP-95 and HP-98, were 3.14 and 3.19 g/cm<sup>3</sup> respectively. Characterization of the two blanks is in progress. A photograph of a hot pressed rotor blank with a cutaway view is shown in Figure 3.14. Visual examination indicated poor densification at the exterior of the hub extension area of the first blank; however, this was overcome by shortening the hub extension. These results demonstrated that shaped rotor blanks can be fabricated by hot pressing silicon nitride powder to theoretical density in shaped graphite dies. Further refinement of contour tolerances will minimize or possibly eliminate contour machining.

#### Ford/Norton Hot Pressed Rotor Program

A development program was started by the Norton Company, under subcontract to Ford, in September 1971 with two objectives. The primary objective was to hot press individual turbine rotor blades, as close to finished

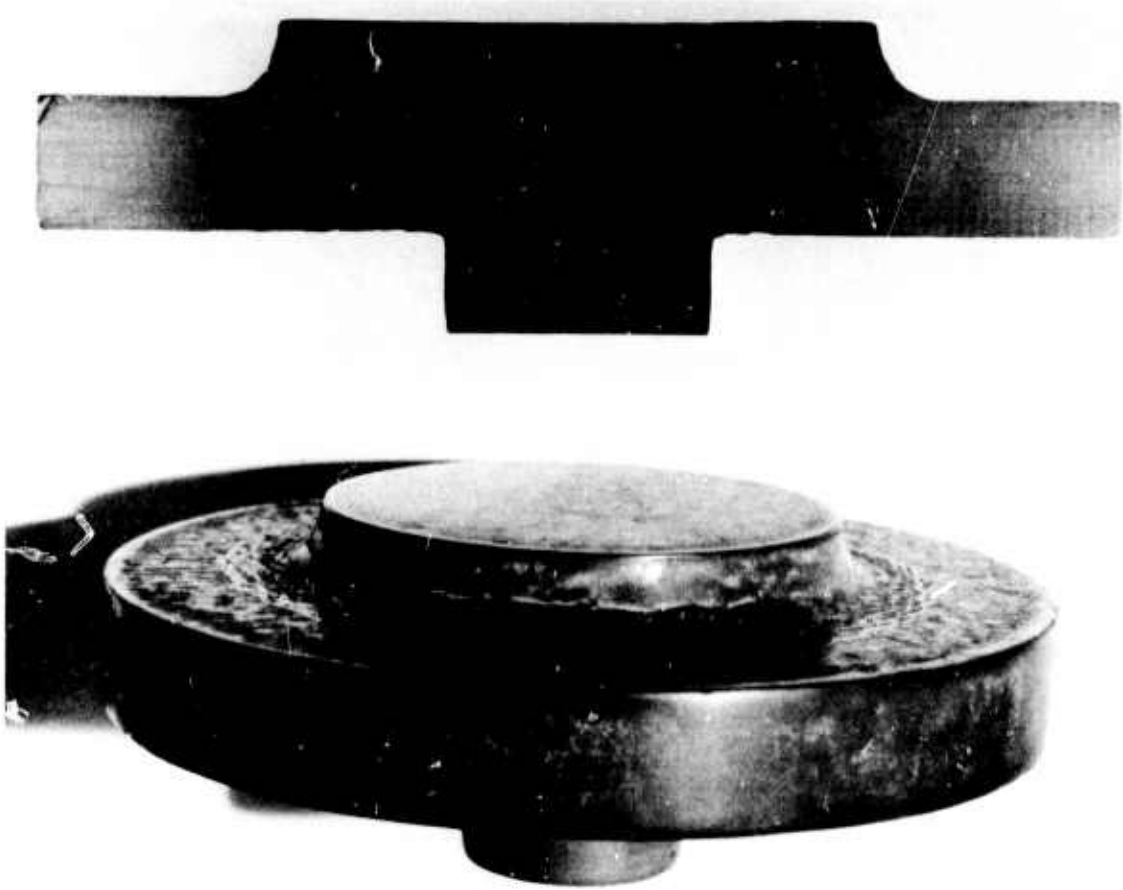


Figure 3.14 — Hot Pressed Rotor Blank

dimension as possible, followed by a second hot pressing which will form the rotor hub around the blade roots and "weld" all of the assembled blades into a monolithic rotor. The secondary objective was to explore the feasibility of directly hot pressing, in one step, a simplified rotor with straight sided but angled blades.

A process has been developed for producing individual blades consisting of several steps. Well characterized reactive silicon nitride powder, high in the alpha ( $\alpha$ ) phase of  $\text{Si}_3\text{N}_4$ , is blended into an injection moldable temporary binder system. The mixture is injected into a molding die producing a pre-formed blade with a simple wedge shaped root. After a heat treatment to remove the temporary binder this preform is hot pressed using tooling proprietary to Norton. A blade produced by this process is shown in Figure 3.15. The airfoil shape is not within tolerance, and the leading and trailing edges and the tip of each blade must be diamond ground to meet specifications. Density of one blade delivered to Ford for evaluation is 3.125 g/cc.

The second part of the two step process consists of forming the rotor hub by hot pressing fresh reactive powder against the assembled blade roots, bonding or "welding" all components into a monolithic rotor. Norton reports that a treatment of the surfaces to be welded is necessary. This treatment, requiring a finite thickness, must be on each side of the root, or tang, of each of the 36 blades.



Figure 3.15 — Hot Pressed Silicon Nitride Turbine Blade

For evaluation purpose 36 simulated blade roots were fabricated and assembled in a simulated welding fixture as shown in Figure 3.16. The space left is the amount of thickness that will be taken up by the surface preparation. Because of the need to machine all blade surfaces and the potential blade stacking/alignment problems encountered, this approach has been de-emphasized until potential solutions to the problems can be found.

#### Ford/Energy Research CVD Silicon Carbide

It was reported in the first interim report that Energy Research Corporation, under subcontract to Ford, was developing a process to form silicon carbide turbine rotors by a chemical vapor deposition (CVD) technique. Feasibility had been demonstrated by the fabrication of a single turbine blade and fixtures were being obtained to fabricate complete first stage turbine rotors. The first phase of the program has now been completed with the demonstration that an approximate turbine rotor shape can be made and released from the mold in which it was deposited.

The turbine rotor is fabricated by depositing silicon carbide inside a mold. Two type of molds were selected for evaluation. One type was fabricated by CVD of tungsten on a beryllium copper mandrel; and other is a ceramic mold formed by conventional investment mold techniques on a wax pattern.



Figure 3.16 — Simulated Blade Welding Assembly Fixture

The mandrel for the CVD tungsten molds was formed by two different methods. The first was by casting individual blades of beryllium copper in conventional investment cavities and then assembling these individual airfoils into a ring to form a turbine rotor. Figure 3.17 shows two such individual blades. The second mandrel technique was to cast an integral beryllium copper rotor, also shown in Figure 3.17, in a conventional investment mold made on a wax pattern produced by bonding together individual wax airfoil sections similar to the beryllium copper pieces shown in Figure 3.17. It was found that this had the additional advantage that two or more stages could be cast simultaneously. The conventional ceramic investment molds cast on wax patterns were available for evaluation first. Early experiments indicated that silicon carbide deposited directly in the silica-zirconia mold was severely weakened, apparently by oxygen contamination from the mold. Attempts to remove the mold resulted in destruction of the silicon carbide rotor. Several molds were therefore coated with tungsten as a thin barrier layer before attempting the deposition of SiC. Such a mold is shown in Figure 3.18. The quality of five rotors fabricated in silica-zirconia molds coated internally with tungsten were better than those deposited without the tungsten coating, but were still poor and unacceptable. The tips of the airfoils filled before the roots, leaving the hoop area open at the end of the run. Figure 3.19 is the result of one of these runs showing the formation of some of the airfoil after much of the mold had been removed, with but little hoop to support the blades.

The development of CVD tungsten molds had proceeded by this time to the point that deposition within them could now be evaluated. Such a mold, with the beryllium copper mandrel removed, is shown in Figure 3.20. The greatly reduced mass of the thin tungsten shell and the higher thermal conductivity of tungsten are probably principle reasons why silicon carbide may be deposited more uniformly within the type of mold, i. e., temperature gradients are more

easily reduced allowing more uniform deposition. Figure 3.21 is a photograph of a full size turbine rotor after removal of the tungsten shell from the silicon carbide shape. This rotor, while far from ideal because of poor material quality, lack of complete filling of the blades, too thin a hoop region, and incomplete removal of stresses formed during deposition, is considered a demonstration of the feasibility of fabricating a full turbine rotor shape from CVD silicon carbide. Figure 3.22 is a close up view of a portion of that rotor showing good dimensional reproduction of the desired aerodynamic shape, as well as the openings at the tips of the blades responsible for the low strength due to the hollow, egg shell-thin structure. Further refinement in deposition techniques is required to develop essentially complete blade filling, and bridging of the slot at the base of the blades forming a complete hoop or platform ring sufficiently thick (about 0.20 inches) and strong to permit attaching it.

#### Ford/Lucas Program

The Joseph Lucas Company, under subcontract to Ford Motor Company, has recently begun a program to produce ceramic turbine rotors from hot pressed silicon nitride.

Their approach is to start with well characterized, high alpha phase, reactive silicon nitride powder and pre-form the complex blade shapes individually by injection molding the powder with a suitable vehicle. These will be assembled and densified by a conformable tool method.

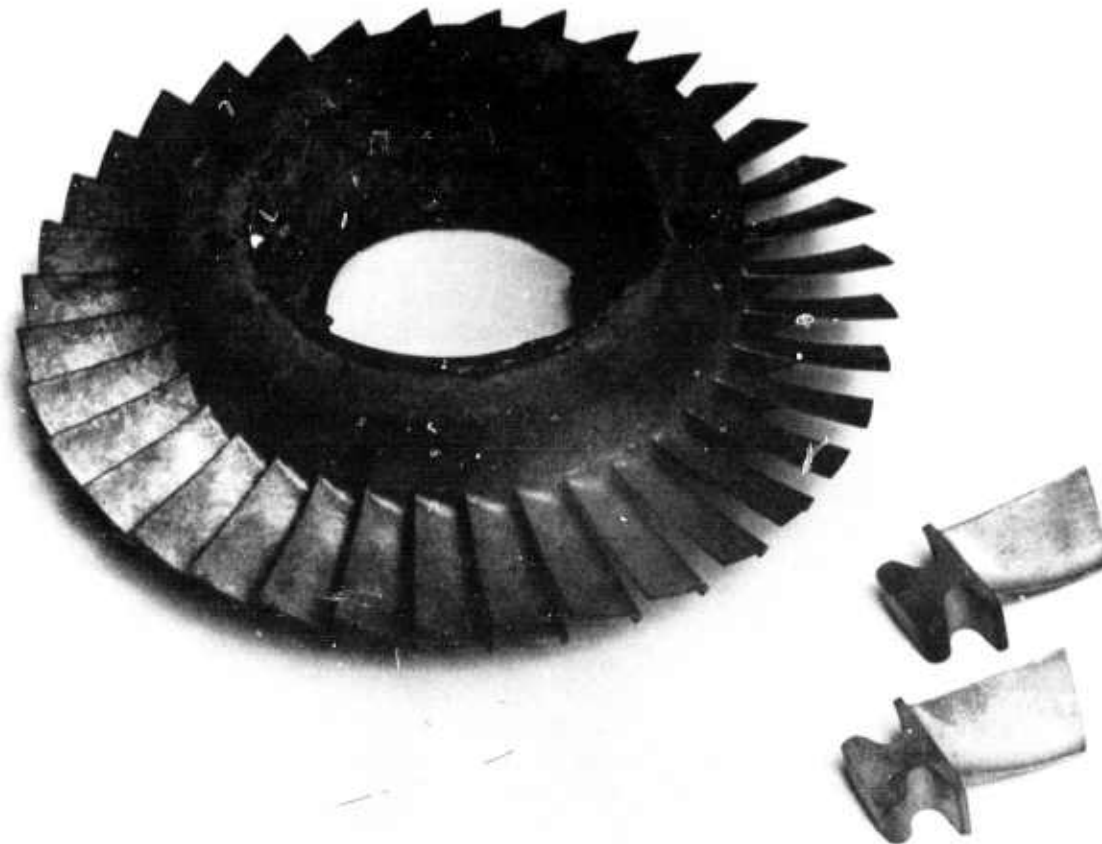


Figure 3.17 — Cast Blades and Integral Rotor Mandrel



Figure 3.18 — Ceramic Mold with Tungsten Barrier Layer

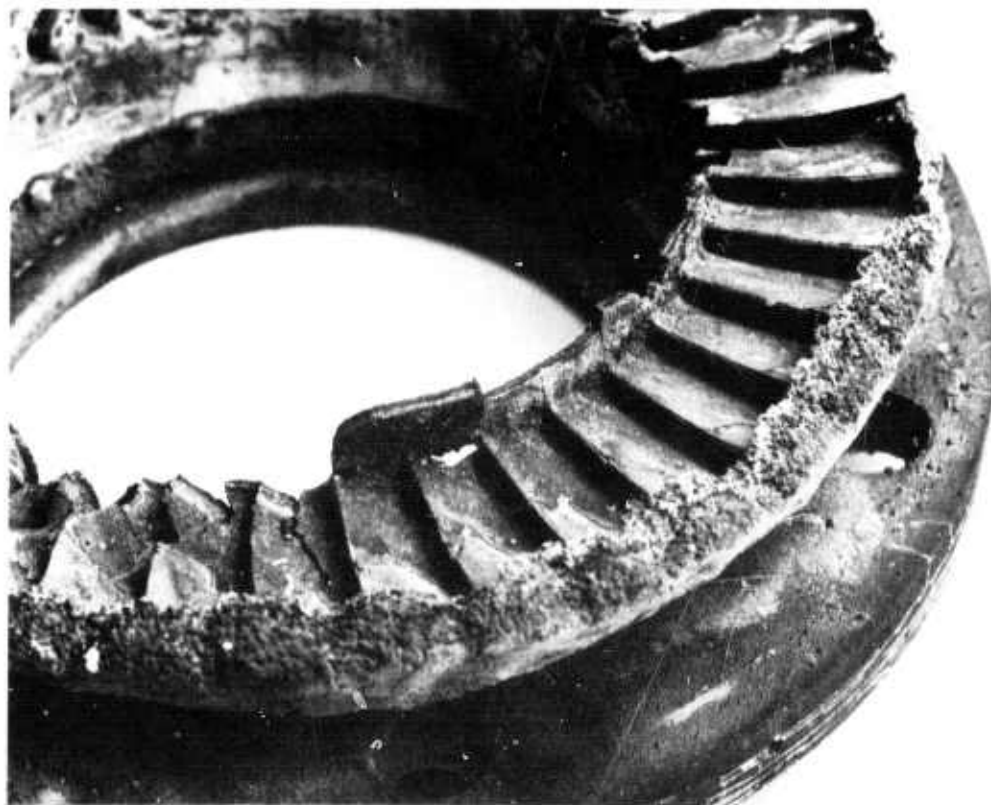


Figure 3.19 — Silicon Carbide Airfoil Segments in Ceramic Mold

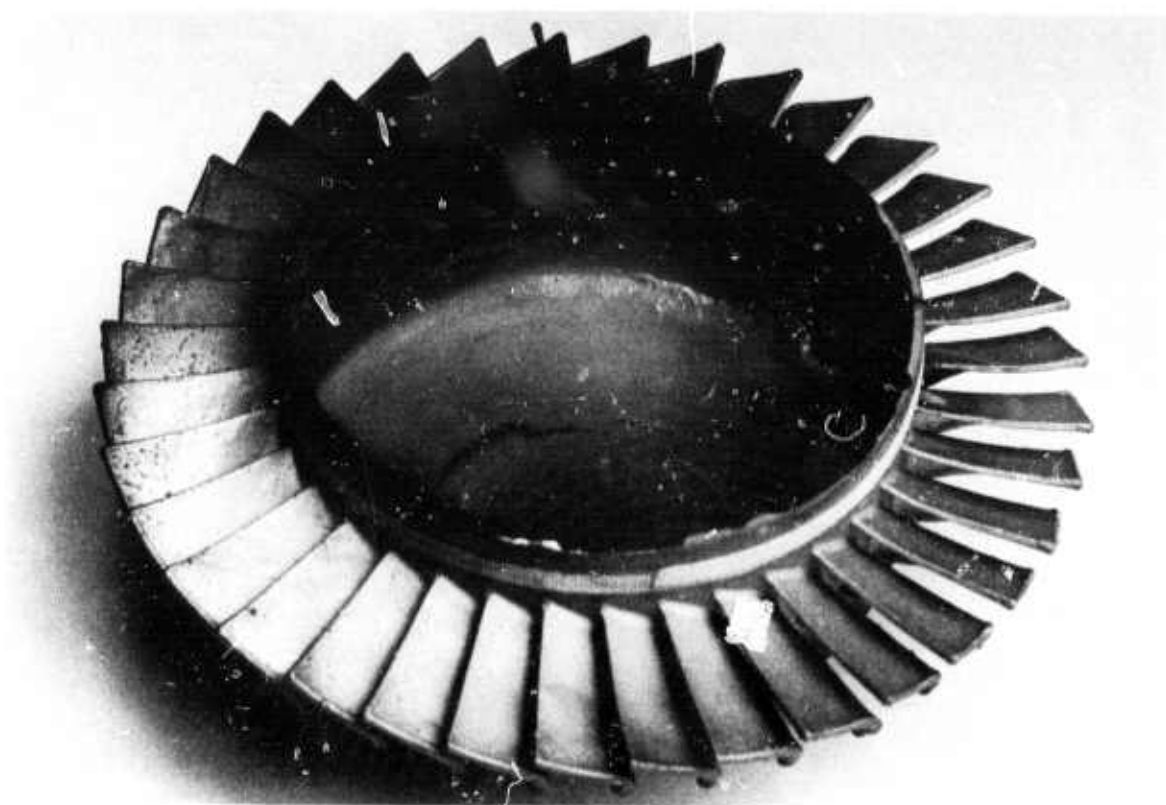


Figure 3.20 — Tungsten Mold After Removing Beryllium Copper Mandrel

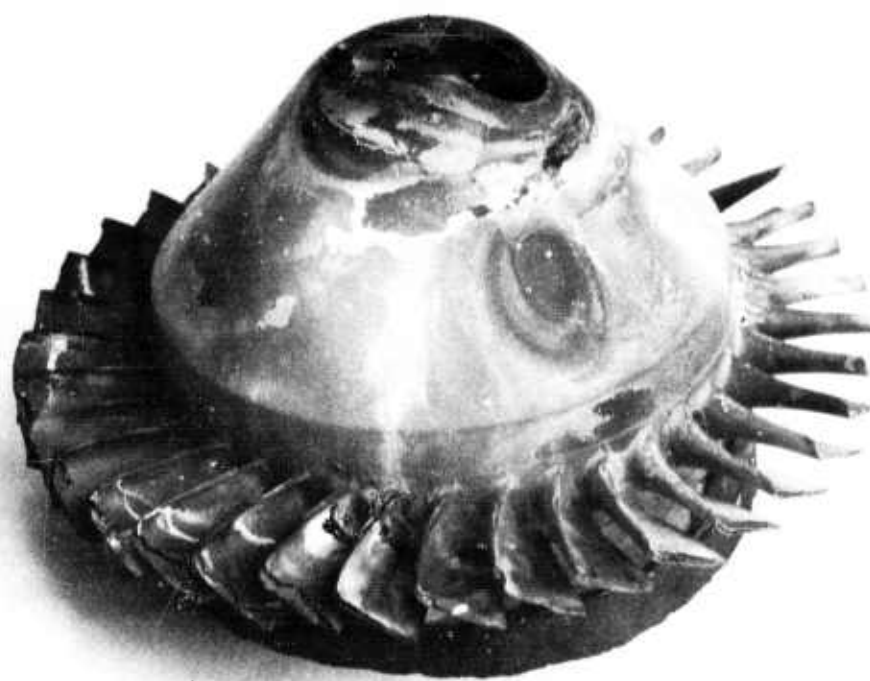


Figure 3.21 — Chemically Vapor Deposited Integral Silicon Carbide Rotor

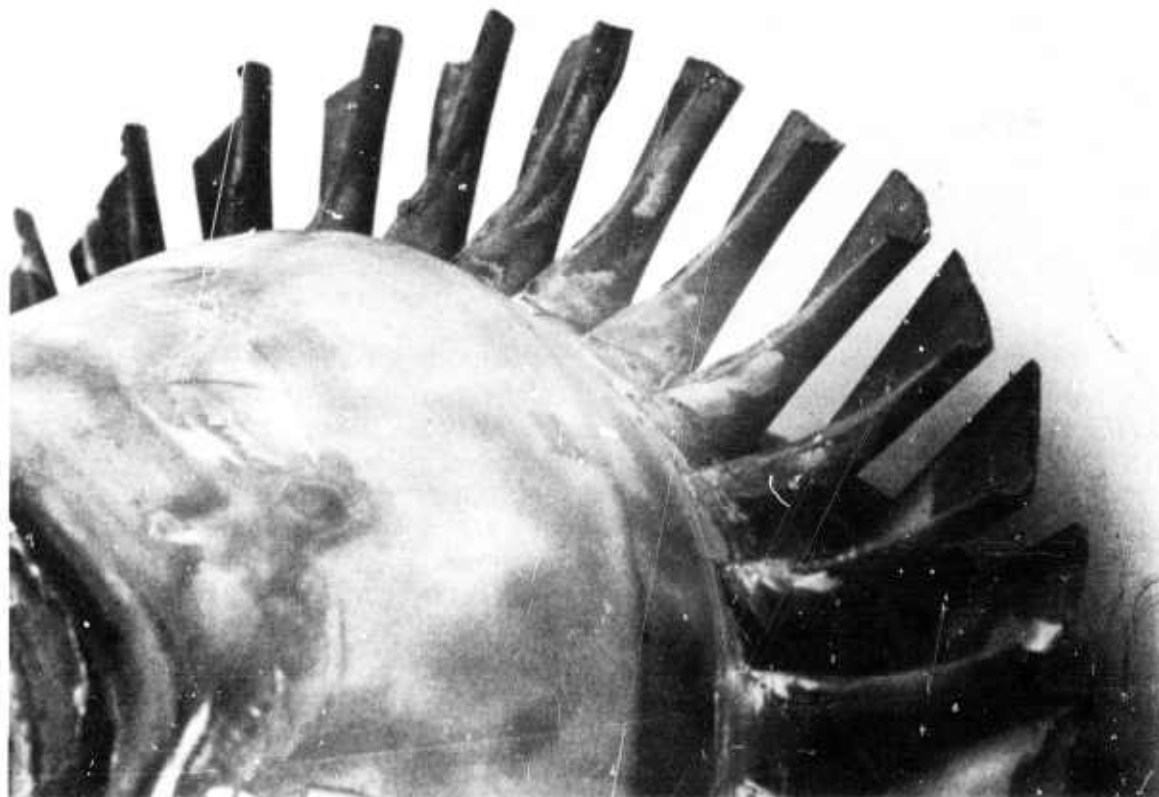


Figure 3.22 — Airfoil Detail in CVD SiC Rotor

#### Ultrasonic Machining

Because of the long lead time anticipated in the development of fabricated ceramic turbine rotors, work was initiated aimed at machining of rotors from hot pressed silicon nitride blanks.

Several machining concepts were evaluated, including laser, electron beam, diamond grinding, and ultrasonic machining. Ultrasonic impact grinding appeared most feasible economically and technically for this application. As was stated in the first report<sup>(1)</sup> preliminary ultrasonic machining of hot pressed silicon nitride indicated a cutting rate of 0.300 inches per minute with a tool wear of 0.002 inches. The configuration machined was a half-inch trepanned core 0.500 inches thick. The results of this preliminary investigation led to a feasibility study of machining rotor blade and disk contours.

Ultrasonic impact grinding as used in the hot pressed silicon nitride machined turbine rotor program employs a non-rotating tool oscillating at high frequencies (20 KHZ) and small amplitudes (0.002 in). The tool is sprayed with an abrasive slurry so that the abrasive particles (200-600 mesh) are forced into the workpiece at high velocities resulting in erosion in the form of the vibrating tool.

The energy source for ultrasonic machining is provided by converting 60 HZ electrical power into 20 KHZ mechanical vibrations through a magnetostriuctive transducer. The electronic generator provides high-frequency alternating current which runs through a coil around the transducer causing a changing magnetic field. This change in flux density causes a change in length of the laminated nickel-iron

core. The change in core length is optimal for certain values of flux density, provided by a D-C current superimposed on the coil. By varying the relative intensity and frequency of the A-C current and intensity of the D-C current, the mechanical amplitudes of the core and thus the tool may be varied. Normally this amplitude is insufficient for ultrasonic machining, and a mechanical amplified (horn) is attached between the core and the tool. The horn will amplify the vibrations as the ratio of the surface area of its ends. The tool is brazed onto the horn. The overall length of the transducer, horn, and tool assembly is approximately one wave length.

Tool wear is of concern in ultrasonic machining as it is in most machining operations. The tool must be soft and resiliant in order to withstand the continual impact of the abrasive particles. For preliminary ultrasonic machining of hot pressed silicon nitride, beryllium copper was selected for the rotor blade contouring. This material showed good resistance to wear and is readily cast in the intricate rotor blade configuration. Such a tool is shown in Figure 3.23. The tools were investment cast using the lost wax technique. The blade contour dies were fabricated by duplicating the airfoil surface of an existing metal turbine rotor using a Kellering machine and hand finishing. One die was fabricated for each side of the rotor blade. Twenty-five of each of the pressure side and suction side tools were cast of beryllium-copper. Low carbon steel was selected for initial work on the disk contouring portion of the program.

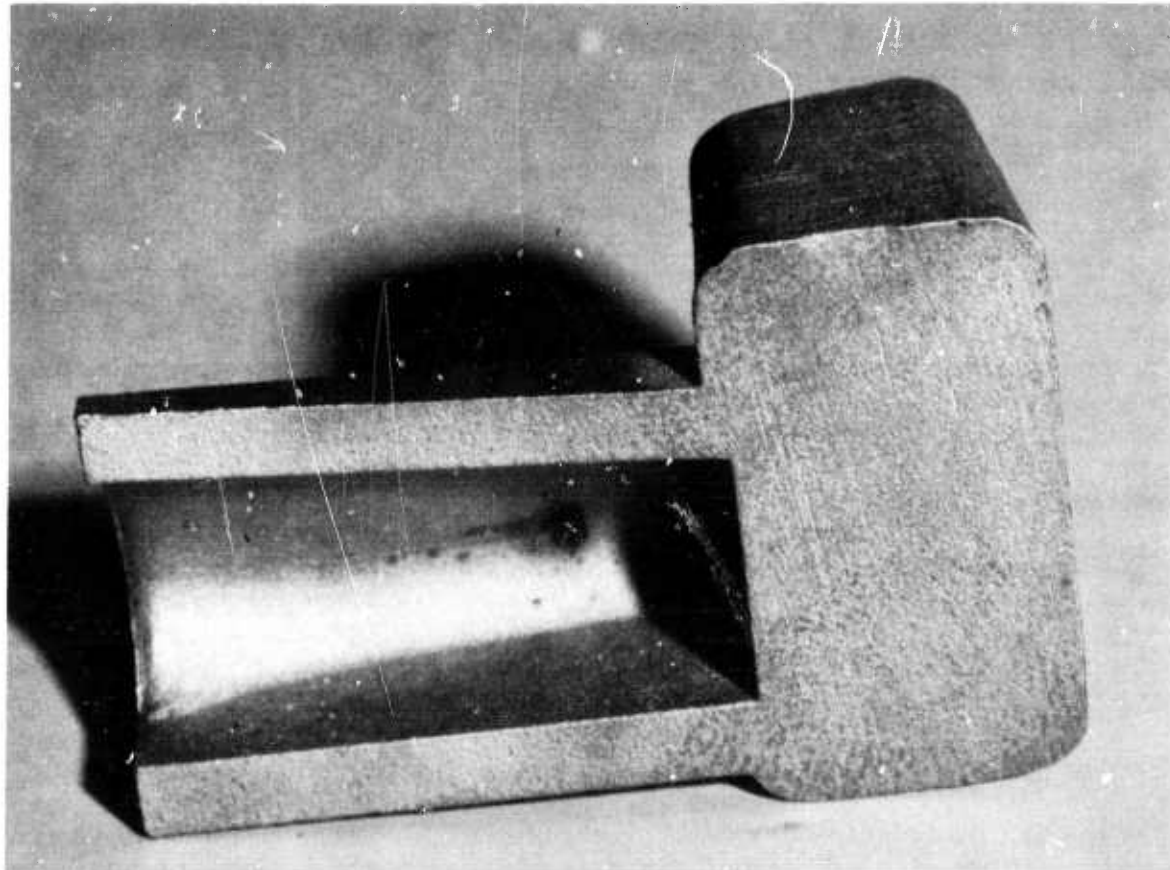


Figure 3.23 — Ultrasonic Machining Tool

The concept of machining the complex geometry of the rotor blade has not yet been proven. The rotor blades are designed to provide optimal aerodynamic performance which required a twisted, tapered airfoil. This presented particular difficulties for ultrasonic machining because the optimum tool configuration is in an end-cutting mode. Airfoil machining required both end-cutting and side-cutting modes. Preliminary attempts in this configuration were unsuccessful due to excessive cutting time and tool wear. Figure 3.24 shows airfoil-shaped slots machined in this fashion. The next approach was to slot the blade cavity, using a conventional end-cutting tool, and then feed the blade tool into the workpiece such that the full length of the tool was end-cutting. However, the tool was not rigid enough to withstand the lateral vibrations and rapidly fatigued. The tool was redesigned to withstand the lateral vibrations and new tools are currently being fabricated.

Disk contouring and core drilling of the center bore were successful and economically feasible. The half-inch diameter bore was machined to  $\pm 0.005$  inches. The disk was contoured in the regions of the blade leading edge, trailing edge and tip. Low carbon steel tools were gravity fed into the rotating disk. A 200 mesh abrasive was used in this roughing operation and fed into the workpiece using the slurry pump pressure and assisted by shop air.

One advantage of ultrasonic machining appears to be apparent lack of surface damage as compared to other ceramic machining techniques. The residual stresses in the machined disks have not been investigated, although electron scanning micrographs were taken of the machined surface. These micrographs indicate surface damage to be less on the ultrasonically machined surface (Figure 3.25) than a diamond ground surface (Figure 3.26) on the same disk. 240 grit boron carbide was used for the ultrasonically machined surface, while a 220 grit diamond wheel produced the ground surface.

#### Electric Discharge Machining of Hot Pressed Silicon Carbide

A program was initiated to investigate the feasibility of electric discharge machining a turbine rotor from a hot pressed disk of dense silicon carbide. Electric discharge machining (EDM) involves creating a spark discharge from an electrode to a workpiece in a dielectric fluid, which erodes material from the workpiece creating a contour that conforms to the shaped electrode. This process can produce intricately shaped parts, with tolerances of  $\pm 0.0005$  inch not uncommon.

The current investigation is aimed at optimizing the electric discharge machining parameters to achieve maximum machining rates. The important parameters are type of power supply (pulsed D. C. or capacitor discharge) open



Figure 3.24 — Airfoil Slots Machined in  $\text{Si}_3\text{N}_4$  Disk

circuit gap voltage, peak current settings, average machining current, frequency, dielectric medium, and electrode material. Some electrode materials considered are silver tungsten, copper tungsten, beryllium copper, brass (60-40), naval brass, muntz metal, copper-graphite, sintered copper, hard drawn copper, and annealed copper.

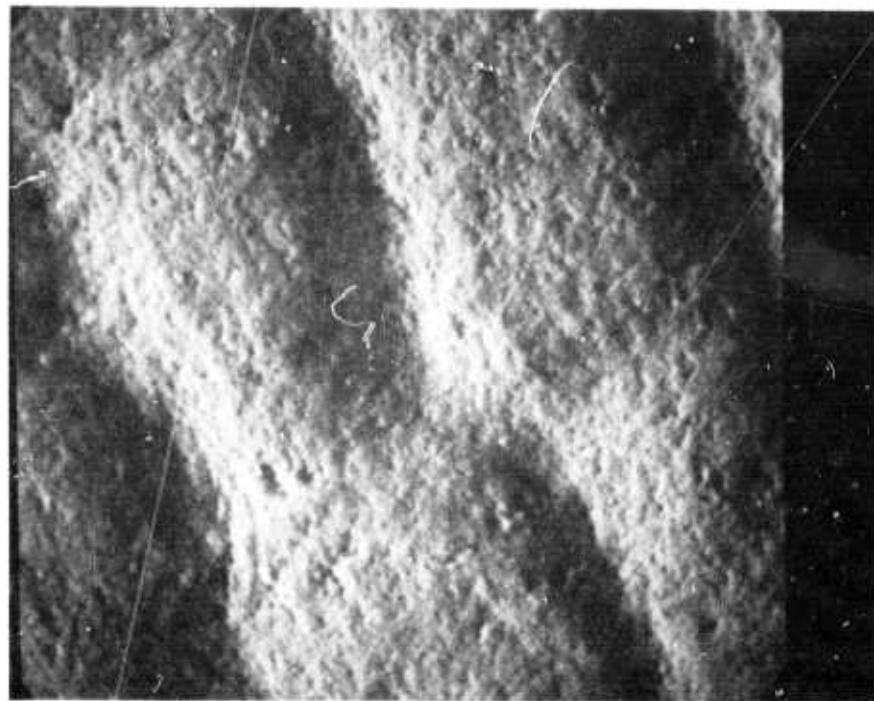


Figure 3.25 — Ultrasonically Machined Surface (540X)

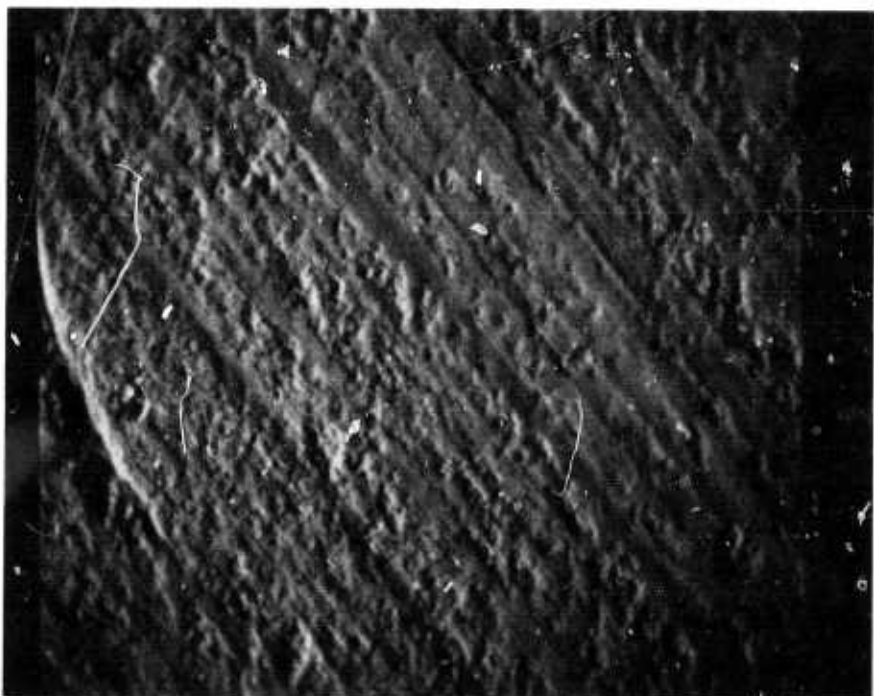


Figure 3.26 — Diamond Ground Surface (540X)

Preliminary machining tests were made on dense silicon carbide using a Sparcotron Model Mark III Capacitor discharge unit. A removal rate of 0.012 cubic inches per hour was attained with copper electrodes with negligible electrode wear.

#### Other Approaches

Two other methods offering potential for fabricating rotors for the small turbine engine are being explored. The first of them, termed the "duo-density" rotor, consists of blades of molded reaction-sintered  $\text{Si}_3\text{N}_4$ , bonded with a hub section of hot-pressed  $\text{Si}_3\text{N}_4$ , into an integral component. The principal advantages of this concept are the use of known technology (molding) for forming the complex airfoils, combined with the use of reaction sintered  $\text{Si}_3\text{N}_4$  of relatively low strength but good retention of this strength at temperature (Section 5.1.2 of this report) for blades which operate at low stresses but high temperatures. Conversely, the properties of hot-pressed  $\text{Si}_3\text{N}_4$  are best used to advantage in the hub area, where stresses are highest but operating temperatures are low. Design studies and experimental work on hot-pressing  $\text{Si}_3\text{N}_4$  around reaction-sintered  $\text{Si}_3\text{N}_4$  are in progress in order to further evaluate this concept.

The second method involves the development of a new class of materials, composed primarily of silicon, aluminum, oxygen, and nitrogen. While little is known of the properties of combinations of these materials, they appear capable of high strength, good high temperature properties, excellent corrosion resistance, and are sinterable.<sup>(3)</sup> Work is currently in progress on compositional and process development.

### 3.2 METAL ROTOR DEVELOPMENT

#### SUMMARY

A considerable amount of meaningful engine testing is being conducted with metal rotors, pending the development of ceramic rotors. While turbine inlet gas temperature must be limited to 2000°F or below to avoid destruction of the metal, much valuable information about stationary ceramic components is being determined. Several metal rotor failures have been encountered, with the most likely cause of failure being high cycle fatigue.

#### Introduction

The development of ceramic turbine rotors is the most formidable task in the development of the small ceramic gas turbine engine, due to the high strength required plus the complex shape. In order that the development and testing of the balance of the engine be allowed to continue in parallel, metal turbine rotors are used for dynamic testing. While this limits the inlet gas temperature to a maximum of 2000°F, a considerable amount of meaningful thermal and aerodynamic testing can be done in order to confirm the design concepts of the other ceramic components. When ceramic rotors are available, they will be substituted for the metal ones.

#### Test Results

Metal turbine rotors are fabricated by investment casting techniques, using a nickel-base super-alloy developed by Ford before the start of this contract. This alloy is similar in composition to Mar - M-246. During this reporting period, several failures of metal rotors were encountered.

The first indication of a problem was a second stage turbine rotor burst, which occurred after 8 hours and 4 minutes of hot running. This failure, shown on Figure 3.27, resulted in the destruction of the ceramic turbine components but was contained within the main engine casing. The fracture surfaces were severely mutilated during the failure, making it difficult to determine the mode of failure. Mechanical properties of the material as measured from two test bars machined from the failed rotor are shown in Table 3.4.

Several other second stage rotor failures subsequently occurred, less severe in nature in that they consisted of platform rubs against the second stage ceramic stator, as shown in Figure 3.28. These failures prompted the theory that the rotor burst was the result of a severe platform rub which overheated the disk locally, which produced high thermal stresses and caused premature rupture of the disk. Subsequent testing produced a long (approximately 180°) hub crack which was located in the same circumferential area as a severe platform hub, which is shown in Figure 3.29.



Figure 3.27 — Rotor Failure After 8 Hours, 4 min. of Hot Running

TABLE 3.4

Mechanical Properties of Rotor Material

	U. T. S. PSI	.2% Y. S. PSI	Elongation %	Reduction of Area %
Bar 1	133,000	131,000	4.5	8.9
Bar 2	120,000	117,000	4.0	11.1
Minimum Expected	113,000	108,000	4.0	—



Figure 3.28 — Rotor Showing Rubbed Area of Rim

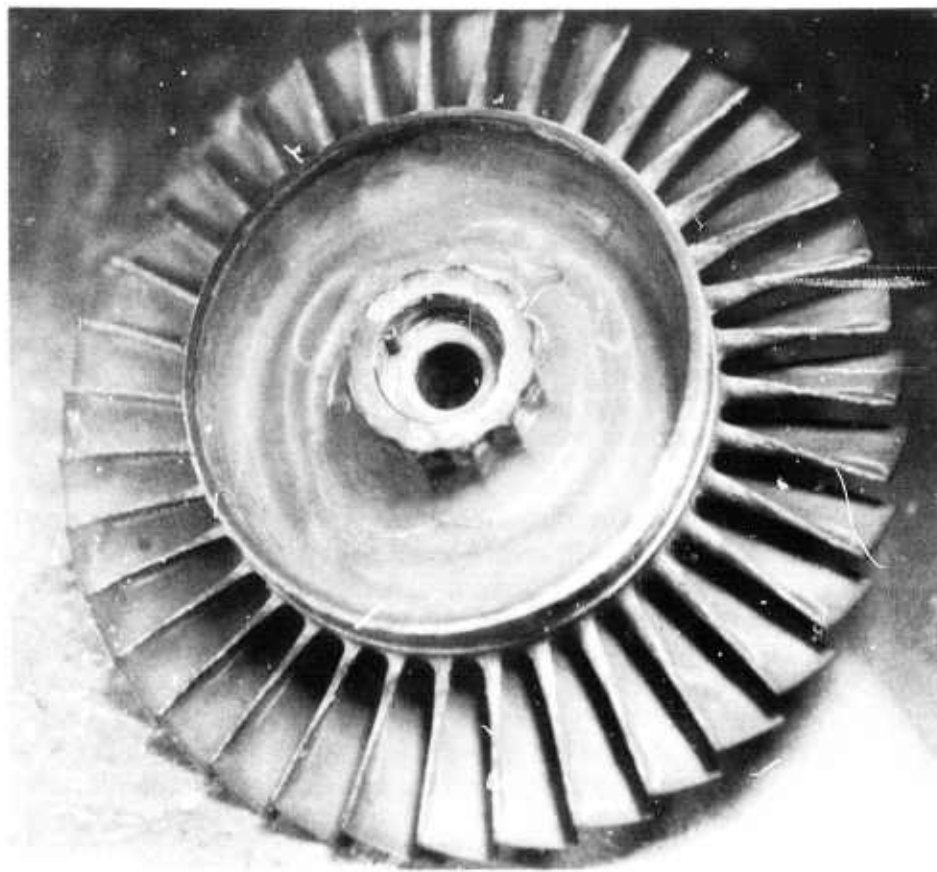


Figure 3.29 — Failed Rotor with Crack in Hub

In order to confirm the sequence of failure, another test was initiated whereby the second stage stator vanes were completely machined away, thus completely eliminating any possibility of platform rub. This rotor was run and inspected after 5 minutes, 35 minutes, 1-1/2 hours, 2-1/2 hours, 3-1/2 hours and 4 hours and 39 minutes. The final inspection revealed a small (approximately 1/4" long), tight circumferential crack in the hub region in the same area as previous cracks and rotor fracture. In addition a small radial crack (approximately .1" long), was detected in the balance ring area.

The second stage rotor failures are summarized in Table 3.5.

TABLE 3.5  
Second Stage Turbine Rotor Failures

<u>Serial Number</u>	<u>Hot Time Hrs.</u>	<u>Failure Indication</u>
9	8:04	Burst — 2 pieces
12	2:05	Platform Rub
16	2:44	Platform Rub — Hub Crack
19	:40	Platform Rub
22	4:39	Hub & Balance Ring Craeks

This test indicated that failure could occur in the absence of a platform rub. The potential causes of this rotor cracking and subsequent burst are listed as follows:

- Stress rupture
- Tensile overstress
- Low cycle fatigue
- High cycle fatigue
- Deficient material properties producing one of the above

Stress rupture was eliminated, since no evidence of associated creep deformation could be found. Tensile overstress was also not probable since these rotors cracked at only 55% speed, while another rotor from the same material batch ran at full speed and was not cracked. Low and high cycle fatigue as possible causes were evaluated by examination of the cracked surface of rotor number 16 which showed evidence of high cycle fatigue under binocular examination. Further examination at higher magnification using a scanning electron microscope is in progress. Work is also in progress to check grain size, microstructure, mechanical and fatigue properties of the material. Rig and engine tests are being run to determine the critical rotor frequencies and sources of excitation.

### 3.3 CERAMIC STATORS, SHROUDS, AND NOSE CONES

#### SUMMARY

The stationary ceramic components in the hot flow path of the vehicular turbine engine are the inlet nose cone which directs the hot gases from the combustor to the first stage stator, two stator stages to direct these gases to the turbine rotors, and shroud rings which form the tip shrouds for each of the two rotors.

Fabrication of stationary ceramic components in reaction sintered silicon nitride continued. As an example, 60 nose cones were formed by injection molding with an expenditure of only a few man-hours. Process work during this reporting period has been concerned with evaluating the silicon nitride produced during nitriding in two distinctly different types of furnaces, and with evaluating the silicon metal powder raw material from several vendors. Characterization of materials in stationary components fired in different furnaces is incomplete. Only one vendor was able to supply silicon powder to meet the requirements specified for injection molding stationary components.

Engine testing has concentrated on evaluating the new design (Design "B") stationary components. Although some failures have been encountered, testing so far indicates that the Design "B" stators are much more durable than were their Design "A" counterparts. Some cracking of silicon nitride nose cones was encountered during hot testing; axial cracking of the outer shroud appears harmless, but circumferential cracking of the inner body is harmful.

A number of each of the stationary components has been subjected to three types of test; the first is a cold test using metal turbine wheels (cold dynamic test); the second is a hot test without turbine wheels (hot static test); and the third is a hot test using metal turbine wheels (hot dynamic test). Using these tests, durability of the Design "B" ceramic components has been encouraging. For example, a reaction sintered silicon nitride first stage stator has successfully withstood 74 hours of cold dynamic testing; another one has withstood 29 hours of hot static testing, and yet another one 12 hours of hot dynamic testing, all without failure. One test run, during which the second stage stator accidentally rubbed the metal rotor rim, was particularly encouraging in that no ceramic vanes were broken, yet the metal was worn away. Another example is a silicon carbide nose cone which, although it developed a crack during initial testing, has been hot static tested for 650 hours, still has only the one crack, and is considered serviceable. Two design modifications are in process to eliminate the inner body cracking of nose cones. Also, improved ceramic stator fabrication techniques are being evaluated.

### 3.31 MATERIALS AND FABRICATION

During this reporting period, progress was made in several areas relative to improving the processing of reaction sintered silicon nitride. The principal areas studied were the use of different types of furnaces for nitriding and work on improving raw materials.

One other aspect of the work on fabrication of ceramic structural components worth mentioning is the use of the injection molding process to fabricate considerable quantities of parts. In this program on the development of brittle materials for gas turbine engines, much testing work is proceeding in parallel with materials development. Several engines and test rigs require ceramic parts, and one soon learns that to repeat and diagnose failures, it becomes vitally important to have a reliable source for supplying quantities of any given ceramic component. An excellent example of this capability was demonstrated during this report period. Using the equipment and process discussed in the last report<sup>(1)</sup>, 60 nose cones were formed by injection-molding with an expenditure of only a few man-hours. By the use of this type of process, it is a relatively simple matter to assure that enough ceramic components are available to avoid costly delays in the engine testing and development process.

#### Effect of Furnace Design Upon Reaction-Sintered $\text{Si}_3\text{N}_4$

Two distinctly different types of furnaces were used for this study, one with a conventional refractory lining, and the other a cold-wall vacuum-type furnace.

During a normal silicon nitride firing, the brick-lined furnace is loaded with silicon preformed parts and the door sealed. A flow rate of thirty  $\text{ft}^3/\text{hr}$  is used to purge the furnace for two hours prior to heating. A firing curve of 24 hours at  $2350^\circ\text{F}$  followed by 24 hours at  $2660^\circ\text{F}$  is utilized. Cooldown is natural furnace cooling, requiring approximately 36 hours, with a total time for firing cycle of 80 hours. The coldwall furnace is fired on a more rapid cycle. The furnace is loaded, sealed and evacuated to 100 microns pressure. Over a period of four hours the silicon parts are heated to  $1000^\circ\text{F}$  in vacuum, which aids in removal of traces of volatile organics from the parts. Nitrogen is introduced at  $1000^\circ\text{F}$  and is maintained at a flow rate of  $10 \text{ ft}^3/\text{hr}$ . An oil bubble trap is used to seal the nitrogen exit tube. A temperature of  $2150^\circ\text{F}$  is reached after 4 hours of gradual heating in nitrogen which is maintained for 8 hours, and then raised to  $2660^\circ\text{F}$  in 4 hours. This temperature is maintained for 24 hours, then the furnace is cooled to ambient in 8 hours. Total firing time for the complete cycle is 48 hours.

Characterization of the materials fired in these two different types of furnace is incomplete. The phase composition of the resulting silicon nitride is discussed in detail in Section 5.3.1 of this report. These results may be summarized here by stating that the material nitrided in the cold-wall metal furnace is higher in the alpha phase and is more consistent in composition from firing to firing. The strength and elastic properties of the silicon nitride was the same in either furnace.

One concern was the possibility that the carbon and graphite components present in the cold-wall metal furnace could result in some silicon carbide in the silicon nitride. After checking several firings by x-ray diffraction, no evidence of silicon carbide was found.

#### Raw Material Studies

To facilitate the injection molding of silicon nitride turbine engine components certain parameters must be met by the silicon raw material. Nitriding studies have shown that to obtain complete nitriding of a silicon compact, the starting particle size must be less than 200 Mesh ( $74 \mu$ ) in diameter. Impurities contained in the silicon metal must also be minimized. Aluminum and iron impurities normally encountered have been investigated and found to be detrimental to strength when in excess of 1%. Traces of other impurities in the range of .01 to .09% have shown no effects on final silicon nitride produced as long as their cumulative total is below 1%.

Four suppliers of silicon metal have supplied samples of their materials for evaluation. Only one was able to supply an injection moldable silicon metal powder within the specified -325 mesh particle size and having no material in excess of 200 mesh.

One vendor's material was contaminated with large particles of silicon, some as large as 1 cm. They were unable to change their production process to eliminate these large particles.

Another vendor's material was found to have 8% of particles over 325 mesh and 2% over 200 mesh. Average particle size was 13 microns. This average material demonstrated good molding properties, but impurity levels proved to be periodically unacceptable. Levels of aluminum contamination at times reached 4% and copper at time reached 2%. The vendor found it impossible to remove these contaminants on a consistent basis, and the large particles of silicon metal (over 200 mesh) appeared as unreacted silicon metal in the finished silicon nitride components.

Another vendor supplied two powders for evaluation, one having a -325 mesh distribution and the second having a -200 mesh particle distribution. The -325 mesh, although chemically 98% silicon, with impurities of 1.27% Al, 0.70% Fe, and 0.05% Ca, was too fine to mold properly with the established thermoplastic binder level. 30% additional binder were required to obtain satisfactory injection molding characteristics. The -200 mesh material, of similar chemical composition to the -325 mesh material had very few + 200 mesh particles, but was unsatisfactory for injection molding, apparently due to its particle size distribution.

The material from the fourth vendor proved acceptable, and is in current use. The material is chemically 98.5% silicon with 0.5% aluminum and 0.75% iron. The maximum particle size is below 200 mesh with an average particle size of 10 microns. The overall particle size distribution proved satisfactory for injection molding of turbine components.

### 3.3.2 TESTING

#### Structural Component Testing of Stator Mounting Concepts

The original design of the first stage shroud/second stage stator interface (see Figure 3.30a) consisted of  $30^{\circ}$  cone angle mating surface, for purposes of centering the second stage stator assembly. Since the first stage shroud is slotted, it will expand thermally in a circumferential direction, and therefore must slide within the support structure. The unrestrained thermal growth of the second stage stator assembly can only take place if slippage occurs on the  $30^{\circ}$  cone angle interface. This interface is subjected to an axial load from the aerodynamic pressure drop across the nose cone, first stage stator and first stage shroud, which acts to further impede this slippage. Engine tests results showed that this required sliding action may not have occurred. Therefore, rig tests were performed to determine the effect of reducing the cone angle.

Assemblies with  $15^{\circ}$  and  $0^{\circ}$  cone angles were evaluated. The  $15^{\circ}$  configuration gave unsatisfactory results. The  $0^{\circ}$  configuration indicated acceptable loading of the support structure and demonstrated two things:

- (1) The split shroud design will slide circumferentially in the support structure when the axial mating surfaces are flat.
- (2) The flat stator-shroud interface will allow radial slippage when subjected to a load 25% greater than the maximum operating load.

All of the ceramic turbine components are now made with the flat sided configuration, as shown in Figure 3.32b, in order to eliminate unnecessary loading of the main support structure.

#### Cold Dynamic Testing of Ceramic Stators

To evaluate the turbine aerodynamic performance, cold testing was carried out using metal turbine rotors. A turbine test rig was constructed using engine parts where possible, including two stages of ceramic stators. Relatively cold air was used to investigate the aerodynamic performance characteristics of the two stage axial turbine. A wide variety of loading conditions on the stators resulted during this testing.

During this aerodynamic evaluation of the design B turbines, various ceramic stators were installed, accumulating a total of 177 hours of test rig time under the conditions described previously. Of this total time, a second stage stator has run for 111 hours, and a first stage stator for 74 hours. No stator failures of any nature occurred throughout the cold test program.

The second stage stator which accumulated 111 hours was initially installed with several root cracks at the trailing edge of various vanes. These cracks did not appear to have propagated during the tests and the stator will be used for further testing. Surface erosion probably due to dirt particles in the air delivery system was noticed although the vanes

Figure 3.30a — Original Design B

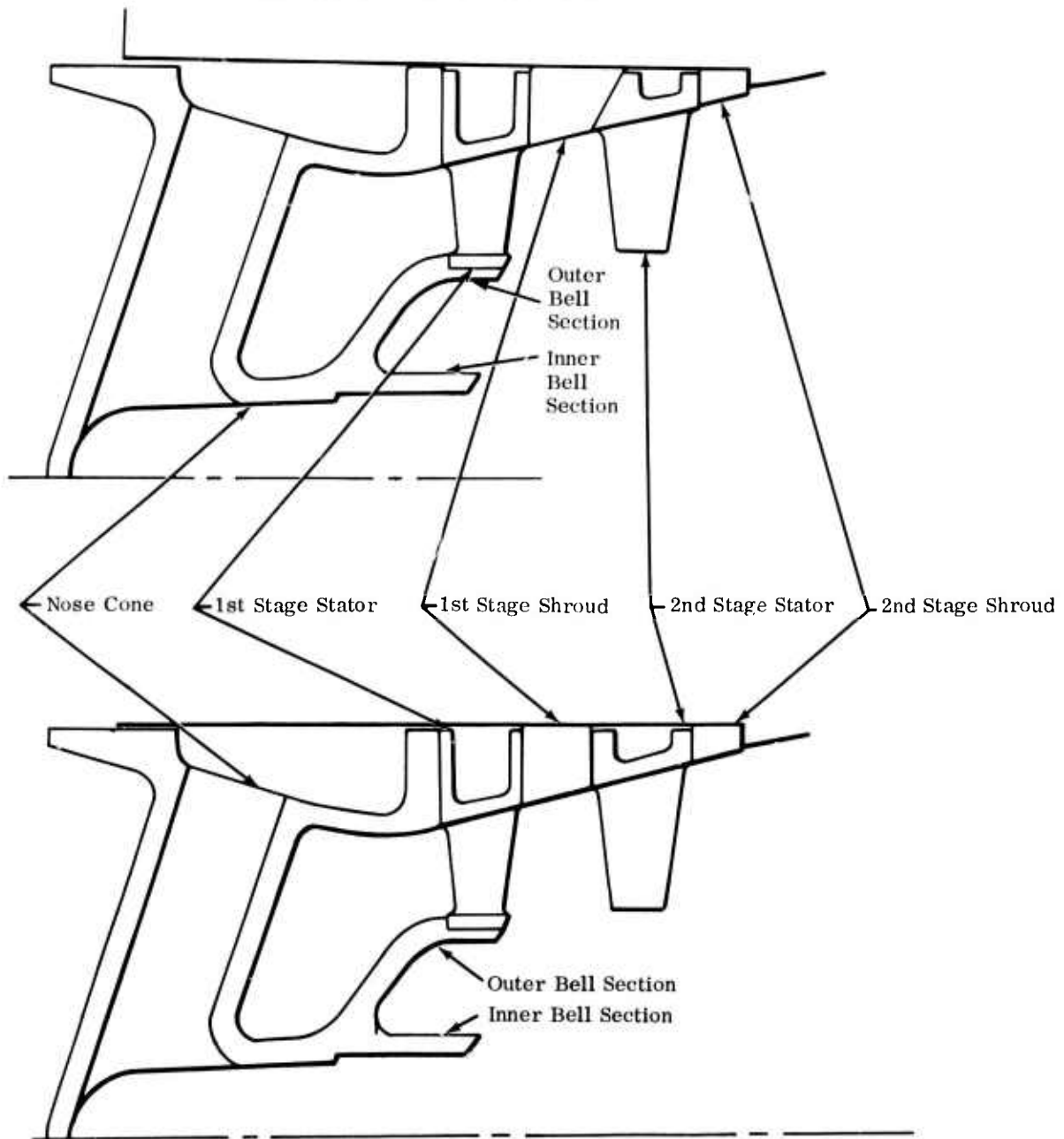


Figure 3.30b — Modified Design B

Figure 3.30 — Design B Hot Flow Path Configuration

remained serviceable. The surface erosion should be much reduced in an engine environment due to the filtering system at the inlet.

The first stage stator has survived the 74 hours of testing in very good condition. No cracks are apparent and surface erosion is minimal.

#### Hot Static and Dynamic Testing of Ceramic Stators, Shrouds and Nose Cones

The inlet nose cone, stators, and shrouds are classified as the hot gas flow path stationary components. These components, located directly downstream from the combustor, must be developed to withstand (a) thermal shock upon start up and shut down, (b) aerodynamic loading at engine operating conditions and (c) mechanical and vibratory loads transmitted from the surrounding structure. Prior to incorporating these components in a complete engine for testing, the ceramic components are qualified in an engine test rig.

Component qualification consists of the following:

- (a) 25 static light cycles
- (b) 3 hours of static testing, and
- (c) 25 hours of dynamic testing

Testing without rotors is referred to as static testing whereas testing with rotors is referred to as dynamic testing. The various test conditions under which the ceramic stators, nose cones, and shrouds are qualified are as follows:

- Static testing — 55% engine speed with turbine inlet temperature limited to 1800°F.
- Dynamic testing — 55% speed with turbine inlet temperature limited to 2000°F
- Cyclic testing (static or dynamic) — a sequence of (1) light-off and acceleration to 55% speed. (2) Shut down (zero fuel) and speed reduction back to light-off condition. This condition is held until the indicated temperature falls to 1200°F, whereupon the sequence is repeated for the desired number of cycles. One of these cycles is termed the one light test.

The evaluation of design 'B' nose cones, stators, and shrouds was carried out in engine test rigs, and the results are summarized in Table 3.6. In each case the component was manufactured from reaction-sintered silicon nitride, except for nose cone serial number G4, which was made of Norton "Crystar" silicon carbide.

TABLE 3.6  
SUMMARY OF TESTING OF CERAMIC NOSE CONES, STATORS, AND SHROUDS

Component	Component Serial Number												Totals
	208	214	215	216	219	232	234	244	247	248	250	259	
First Stage Stator													
• Cold Dynamic Hrs.	5	3	3	3	29	3	74	3	3	3	10	3	177
• Hot Static Hrs.	12	17	3	3	5	1	4	4.5	3	11	10	3	66
• Hot Dynamic Hrs.	25	50	25	25	25	4	74	4.5	3	3	25	3	19.5
• Total Hours													262.5
Total Lites													325
Status <sup>1</sup>	F,X	S	S	S	S	F,X	A	F,C	S	S	A	S	A
Second Stage Stator													
• Cold Dynamic Hrs.	222	271	274	275	276	288	292	295	298	301	303		28
• Hot Static Hrs.	17	5	5	24	5	3	2	3	3	8	3		49
• Hot Dynamic Hrs.	3	8	5	5	5	24.5	111	5	2	3	3		20.5
• Total Hours	25	8	5	25	25	111	25	25	25	25	25		197.5
Total Lites													200
Status <sup>1</sup>	F,X	F,X	F,C	S	A	F,X	F,X	S	S	S	S		
First Stage Shroud													
• Cold Dynamic Hrs.	2	4	5	6	8								
• Hot Static Hrs.													
• Hot Dynamic Hrs.	10	38	4.5	2	2	3							41
• Total Hours	10	42.5	42.5	2	2	2	3						18.5
Total Lites													59.5
Status <sup>1</sup>	F,X	F,X	F,X	S	F,X	F,X	S						150
Second Stage Shroud													
• Cold Dynamic Hrs.	1	2	3	6	9	10							
• Hot Static Hrs.													
• Hot Dynamic Hrs.	29	29	2	10	6	14							49
• Total Hours	2	29	2	10	6	14							18.5
Total Lites													67.5
Status <sup>1</sup>	F,X	F,X	F,X	S	F,X	F,X	S						150
Nose Cones													
• Cold Dynamic Hrs.	G42	4	14	15	16	17	19	23					
• Hot Static Hrs.													
• Hot Dynamic Hrs.	650	212	12	30	7	6	2	3					920
• Total Hours	650	212	1.5	13.5	30	7	10.5	2	3				8
Total Lites													928
Status <sup>1</sup>	S	S	S	S	S	F,C	S	S	S	S			275

1 Status Legend

A - Ok, Special Dimensions — Used for Cold Dynamic Test  
F - Failed  
,B - Bonding  
,C - Crack (s)  
,X - Result of Other Component Failure

S - Serviceable; At Present Nose Cones are Classified as Serviceable if Outer Shroud has (1) Axial Crack — Ceramic Stators are Classified as Serviceable if Vane Cracks Exist but have not Propagated the Complete Vane Span

2 Silicon Carbide Material

Table 3.6 shows that 12 out of 15 first stage stators are still useful after the particular sequence of testing used. Of the three which failed, two of these were caused by failure of another component. The remaining one had blade cracks. Others still serviceable had some blade cracks resulting from fabrication problems. Improved fabrication and inspection process are being established to eliminate cracks.

Table 3.6 also shows that second stage stators had a higher rate of failure — 6 out of 11 are still serviceable, although three failures were caused by other component failures. The remaining two failures were primarily caused by cracks in the bonding material. Improved bonding is expected when new assembly tooling, now on order, is received.

Table 3.6 shows shrouds performed satisfactorily. All noted failures were caused by other component failures.

In the above comments, it is noted that a majority of the failures were caused by other component failures. The other components were predominately metal turbine rotors and their failures are discussed in Section 3.2.

One very interesting result of the hot dynamic testing occurred with a silicon nitride second stage stator. During a dynamic test at approximately 40% maximum engine speed, the platform of the metal second stage rotor rubbed against the tips of the ceramic stator vanes. Although the rotor was ruined, the stator was not damaged. This accident revealed an encouraging degree of resistance to very severe flexural fatigue on the part of the reaction bonded silicon nitride stators. Figure 3.31 shows this stator with metal deposits from the rotor on the vane tips. Figure 3.28 in Section 3.2 of this report, shows the rubbed second stage rotor.

Hot static and dynamic testing of ceramic nose cones has pointed out the following:

Axial cracking of the outer nose cone shroud occurs consistently but does not render the part inoperable.

Under severe but typical thermal conditions, the nose cone inner body may develop a circumferential crack which does render the part inoperable. These two problems are being investigated.

A nose cone with a pre-notched outer shroud will be tested in an attempt to eliminate the random nature of the consistent axial crack. A design modification to the bell section (See Figure 3.30) will also be tested. This modification should reduce thermal stresses in this area, thus eliminating the circumferential cracking.



Figure 3.31 — Ceramic Stator Showing Metal Deposits on Vane Tips

## 4. PROGRESS ON THE STATIONARY TURBINE PROJECT

### 4.1 STATOR VANES

#### SUMMARY

In order to avoid the large stress concentrations normally encountered with the transition zones in an integral vane design, a simply supported 3-piece ceramic stator vane assembly was selected for the large stationary gas turbine. Furthermore, the vane size was reduced to one-half (chord and thickness) that of the metal vane used originally in the 30 MW machine as a result of computer analyses of the transient thermal stress occurring during emergency shut down conditions and steady state stresses.

All of the basic components of the 3-piece vane design, established during the first contract year, are the result of a more complete stress analysis. Currently, hardware is being fabricated to permit initial static rig testing in early 1973. The first generation silicon nitride vane assembly consists of an untwisted, non-tapered airfoil section and two end caps. The support structure for this 3-piece vane element includes an appropriate spring clamping mechanism which assures positive locking of end cap pairs.

During the report period, generalized computer codes were prepared to describe the position and magnitude of maximum combined stresses. Thermal shock tests were performed to confirm the 2-dimensional stress analyses. Maximum contact stresses at the airfoil-to-end cap interface reach 11,700 psi, compressive; 6100 psi, tensile; and 4500 psi, shear. All of these stresses fall within the strength capability of commercially available  $\text{Si}_3\text{N}_4$  and SiC.

The effect of airfoil geometry on transient thermal stress was also considered. Blunting of the leading edge of half size vanes by increasing the radius 47% does not reduce the maximum thermal stresses of 31,000 and 28,000 psi which develop in  $\text{Si}_3\text{N}_4$  and SiC airfoils, respectively, under emergency shut down conditions from 2500°F. Stresses at the trailing edge are reduced by increasing the section thickness but this result is not considered critical to airfoil performance because the maximum stress occurs at the leading edge.

The Norton Company has machined silicon nitride airfoil blanks to meet the first generation vane specification. End caps and the airfoil tenon geometry will be completed well before static rig testing is scheduled to begin. Energy Research Corporation produced flexure specimens for the evaluation of chemically vapor deposited silicon nitride. Room temperature strength averaged 60,000 psi with considerable scatter in the data. High temperature strength was more impressive with values as high as 100,000 psi recorded at 2300°F. Attempts to deposit hollow airfoil shapes were unsuccessful.

In order to accomodate the 3-piece ceramic vane assembly, specifications were established for modifying the Westinghouse static rig. Preliminary design work is in progress.

#### 4.1.1 DESIGN

##### Introduction

The 30 MW test turbine that will be used in the demonstration utilizing 1st row ceramic vanes is shown in Fig. 4.1. The circled area highlights the 1st row vanes. Three design iterations, based on a 3-piece vane concept (airfoil and two end caps) were reported previously. A fourth design iteration of this concept has emerged from a more complete stress analysis of the previous three. The Norton Company is fabricating silicon nitride airfoil sections and end caps to the first generation vane assembly specification.

The basic element of the design is the 3-piece ceramic stator vane assembly represented in Fig. 4.2. A concave seat in the end cap is used with a convex vane tenon of compound curvature; this provides the contact surfaces that are ellipsoidal.

##### Design

The vane assemblies are paired for use with associated support hardware. Two vanes and two end caps are supported at either end by a single insulator and a single metal shoe. The outer metal shoe has a single pivot, plunger, and spring, while the inner mechanism is made up of the metal shoe with two pivots and plunger. This arrangement gives 3-point circumferential stability to the entire structure. The spring assembly, which is contained by the outer support ring maintains the position of the vane assembly with the clamping force provided by the spring.

A woven mesh of fiber material is being considered as a thin cushion to distribute load between the insulator and the metal shoe. This material will serve as a seal between the insulator and ring housing. A number of experimental fiber products have been ordered for evaluation.

A linear steady state heat transfer study was made of the airfoil, end caps, insulator, cushion and metal shoe assembly. The radial space limitations that exist in the turbine, the temperature extremes, and the prescribed limits for thermal stresses in the end caps, require that the insulator can support compressive loads at a hot face temperature of 2200°F while maintaining a thermal gradient of 1000°F across less than an inch thickness. Since this requirement could exceed the capability of most commercially available insulating materials, such alternatives as film cooling the end cap or increasing the metal shoe maximum allowable temperatures are being considered.

A complete mechanical model of the vane assembly and supporting structure has been designed to evaluate the kinematics of the initial design. This will be built from plastic and metal parts.

The Norton Company was furnished with detailed design drawings for the machining of silicon nitride end caps and airfoils. Twenty 3-piece stator vane assemblies will be completed by September 15, 1972. Static rig testing is scheduled to begin in 1973.

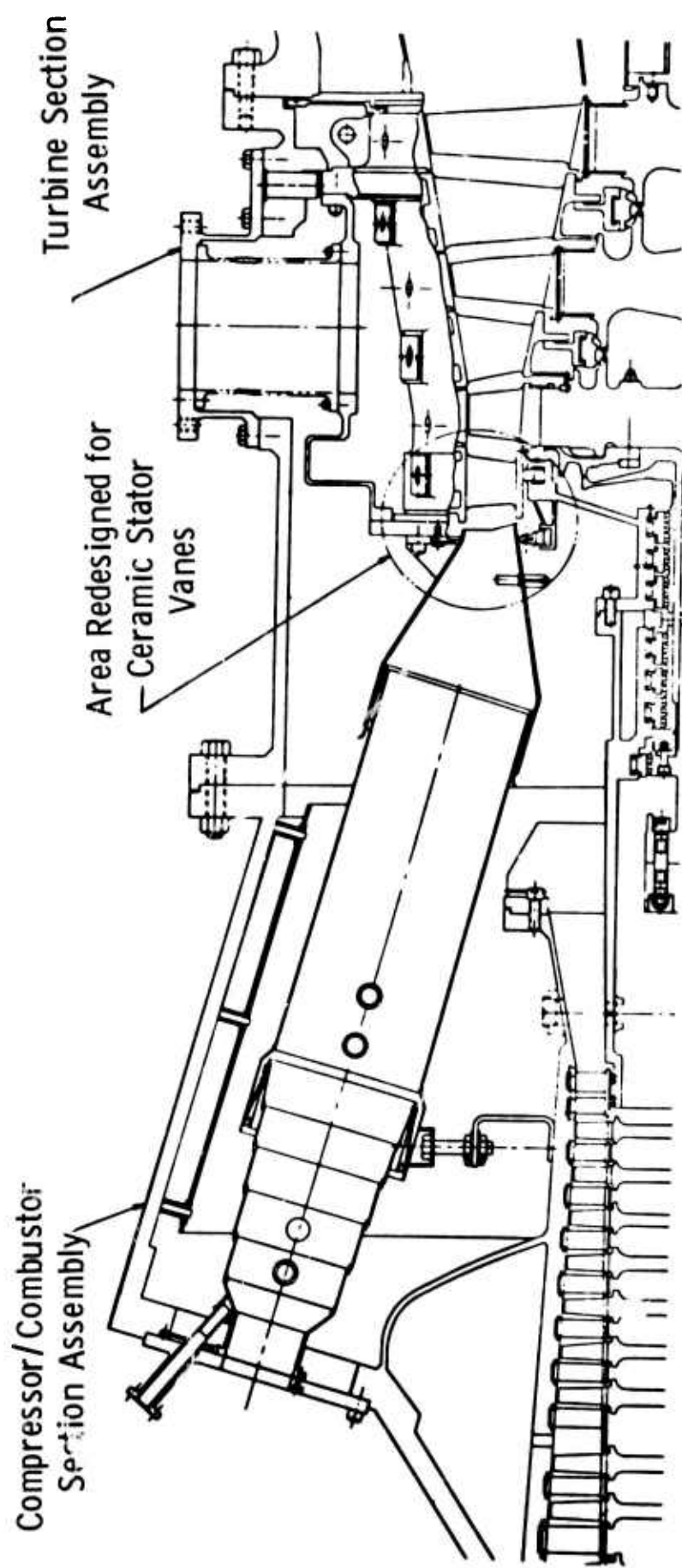


Figure 4.1 — Schematic of 30 Mw Test Turbine Flow Path

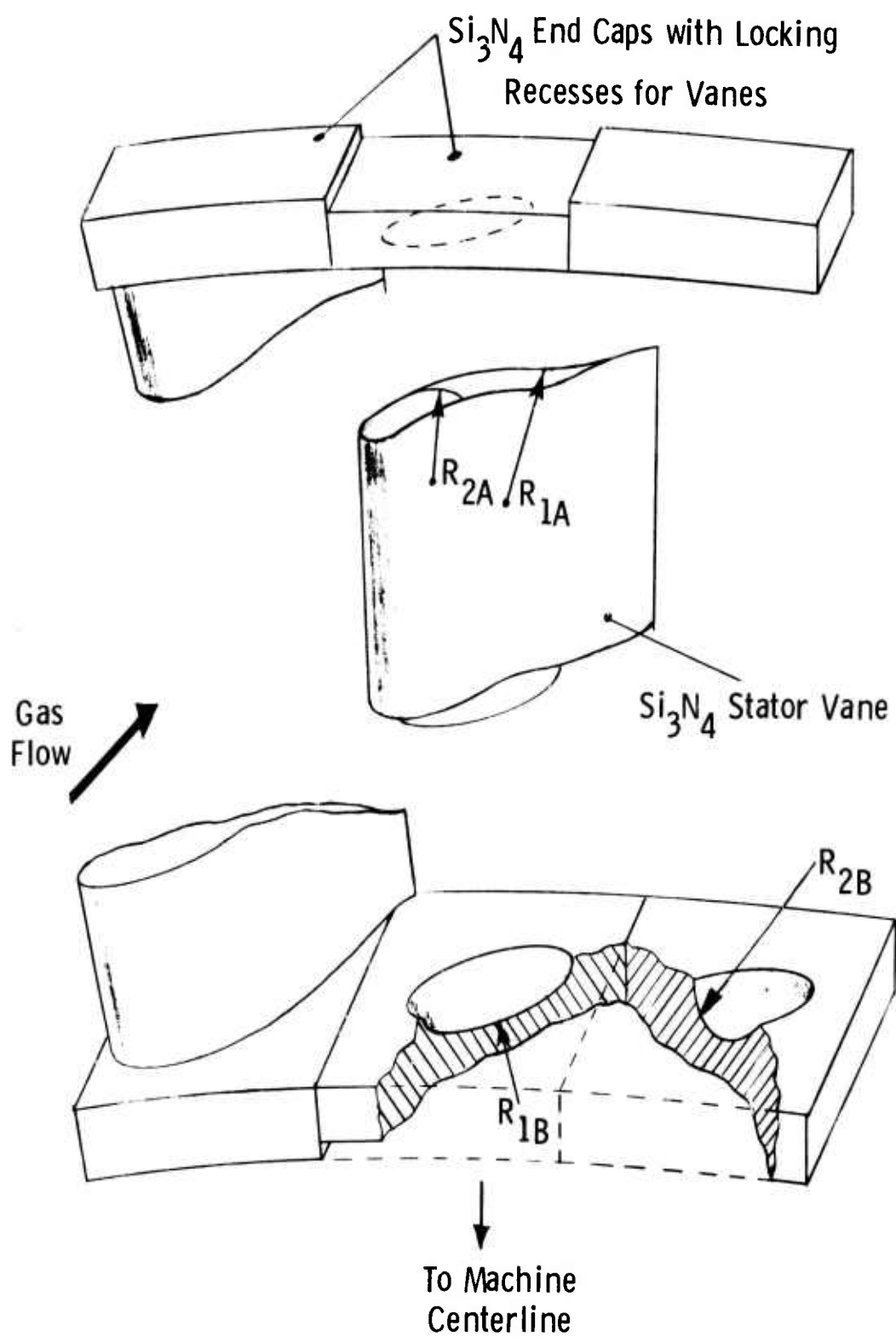


Figure 4.2 — Schematic of Vanes and End Caps Cut Away to Show Tenon Design

#### 4.1.2 STRESS ANALYSIS

##### Vane/End Cap Contact Stress Analysis

The 3-piece vane assembly design was selected to avoid the areas of large stress concentration normally associated with transition zones in integral vanes or blades. Each element (airfoil or end cap) was designed as small as possible and with relatively uniform cross sections to minimize stress from thermal gradients.

In designing the 3-piece vane assembly, an airfoil-to-end cap interface of compound curvature was chosen in order to provide a locking mechanism that will prevent ratcheting of the airfoil end support out of the end cap groove. Although a spherical surface would allow the vane to pivot freely, it would neither preclude airfoil twisting under potentially light spring loads nor provide for airfoil-end cap-insulator-shoe linkage stability.

The airfoil face is characterized by major and minor radii,  $R_{1A}$  and  $R_{2A}$ , respectively (Fig. 4.2). Similarly, the end cap seat is designated  $R_{1B}$  and  $R_{2B}$ . The contact area is elliptical in perimeter, and the pressure surface that is due only to the normal load is semi-ellipsoidal. Elasticity theory yields explicit formulae for the size of the contact area and the maximum compressive, tensile, and shear stresses due to normal loads. However, the airfoil-to-end cap interface must also support a considerable tangential (measured with respect to the airfoil Y-Y axis) gas load. Stresses due to tangential loads may be found using the method of Poritsky. (4)

This analysis may be extended to the more general case by sectioning the normal load pressure surface in line with the tangential load and matching the semi-ellipse with the appropriate cylindrical case (Fig. 4.3). A different cylindrical model must be used for each section of the elliptical contact surface. Using the notation of Fig. 4.4, it is necessary to choose  $L$  such that  $B = b$  and  $Q_0 = q_0$ . Thus, the stresses along the minor axis LM due to tangential load only, are identical to those along line NP. Generalized computer codes indicating location and maximum stress components due to combined loading were prepared for use in parametric optimization.

For the geometry under consideration, analysis showed that the maximum stresses at the airfoil-to-end cap interface are:

Compressive stress,  $\sigma_{Cmax}$ , is 11,700 psi  
Tensile stress,  $\sigma_{Tmax}$ , is 6,100 psi  
Shear stress,  $\sigma_{Smax}$ , is 4,500 psi

The state of stress due to this contact must be superimposed upon the maximum transient and steady state thermal stresses acting on the airfoil tenon and end cap. This analysis is in progress using axisymmetric and 2-D finite element codes.

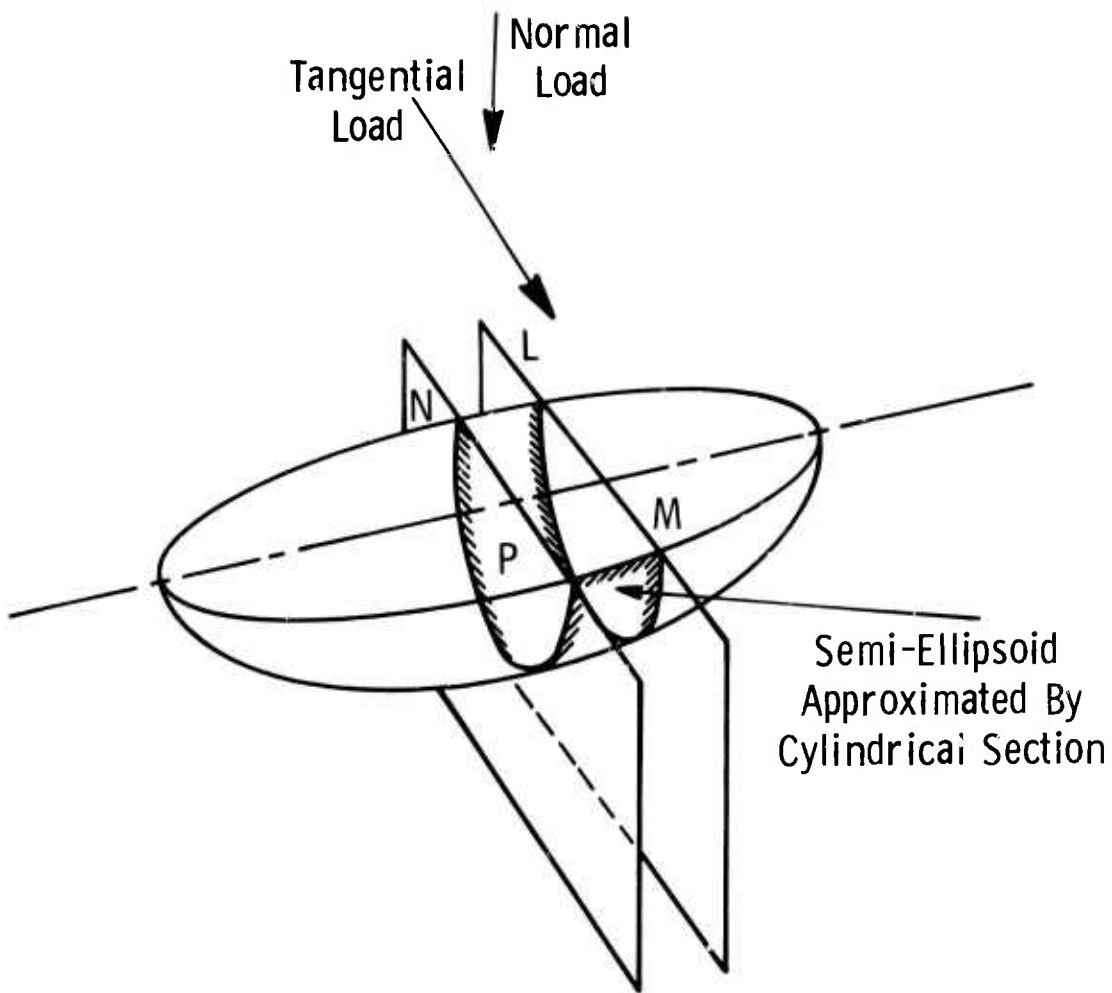


Figure 4.3 — End Cap Recess Showing Cylindrical Approximation for Load Analysis

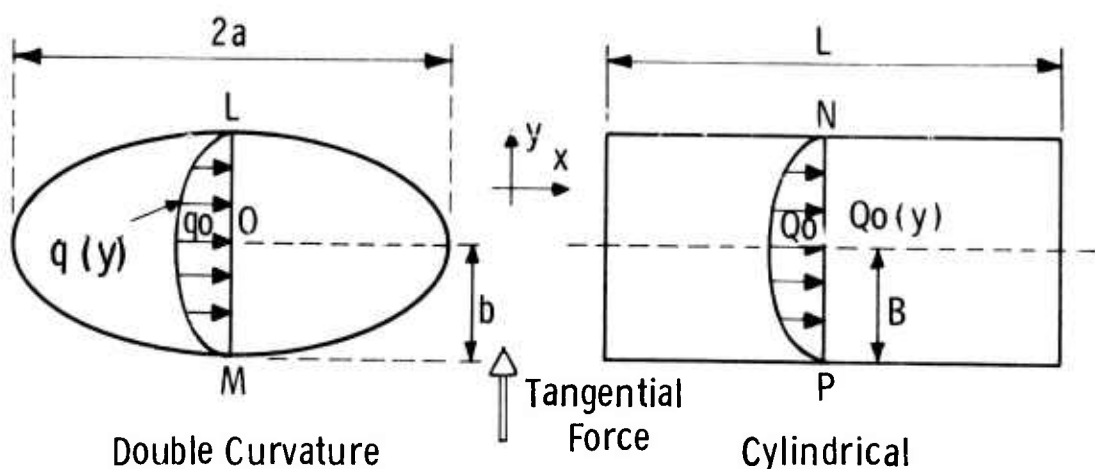


Figure 4.4 — Elliptical Contact Surface and the Cylindrical Section Analog Used to Calculate Maximum Stresses Under Combined Compressive and Tangential Loads

### The Effect of Geometry on Transient Thermal Stress

Calculations of maximum transient thermal stresses developed in the airfoil section under emergency shut down conditions previously led to the selection of a half size vane. (1) Finite difference and numerical integration techniques were used to determine if any simple changes in geometry would further lower the peak stresses in the leading and trailing edges.

The effect of blunting the leading and trailing edges of the half size vane was studied for both silicon carbide and silicon nitride (Fig. 4.5). An increase of 47% in leading edge radius produced negligible results. If the trailing edge radius and thickness were increased by 56%, the transient thermal stress would decrease 12 and 21% in SiC and  $\text{Si}_3\text{N}_4$ , respectively.

No change in the airfoil profile is planned, however, since the maximum stress occurs in the leading edge where the effect of blunting is insignificant. Furthermore an increase in the trailing edge thickness would adversely affect gas flow because of increased turbulence.

### Correlation of Design Analysis Codes with Experiment

The programs used to analyze stresses in vanes have been correlated with each other and with turbine passage experiments in order to establish their validity. A transient axisymmetric finite element computer program has been developed and used to calculate stresses in cylinders subjected to a uniform gas cooling from above  $1600^{\circ}\text{F}$  down to  $600^{\circ}\text{F}$ . This axisymmetric program gives the complete state of stress, both in plane 1 and plane 2 in Fig. 4.6. The results of this axisymmetric program correlate well with the existing computational method using a finite difference heat transfer program and a numerical integration of stresses when applied to a uniformly quenched cylinder. The correlation increases the confidence of applying the existing programs to thermal shock tests in the turbine gas passage and to vane analysis itself.

Tests on silicon carbide were performed in the turbine passage. When the fuel was shut off, the gas temperature dropped from  $2000^{\circ}\text{F}$  (for example) to  $600^{\circ}\text{F}$  in a few seconds. Large thermal gradients were measured by thermocouples in a second SiC cylinder located beside the test cylinder. The stresses induced by differential thermal expansion caused cracking in the axial direction. Both computer methods predicted that axial stresses should be larger than circumferential stresses, and that circumferential cracks should appear.

Experiments indicated that quenching is uniform around the cylinder to within 10 to  $15^{\circ}\text{F}$  (Fig. 4.7) and that the axisymmetric finite element program could be used in plane 1, Fig. 4.6. Since the physical properties such as coefficient of thermal expansion, thermal conductivity, elastic modulus and Poisson's ratio of the SiC are not precisely known, and since the heat flux and loads at the ends imposed by the fixture are not well controlled, the discrepancy between analysis and experiment is not unexpected. Figure 4.8 shows some typical results for the thermal quench of medium strength hot pressed SiC.

To improve the experiment, silicon nitride cylinders with accurately measured thermal diffusivity and coefficient of expansion are being introduced into the passage. Thermocouples are placed in wells such that both axial and radial temperature gradients may be measured. By rotating this cylinder, the vari-

ation in temperature around the circumference can also be monitored. These improvements will not only provide a better check for the computer results, but will provide additional experience on the fixturing and instrumentation of ceramics in a turbine environment.

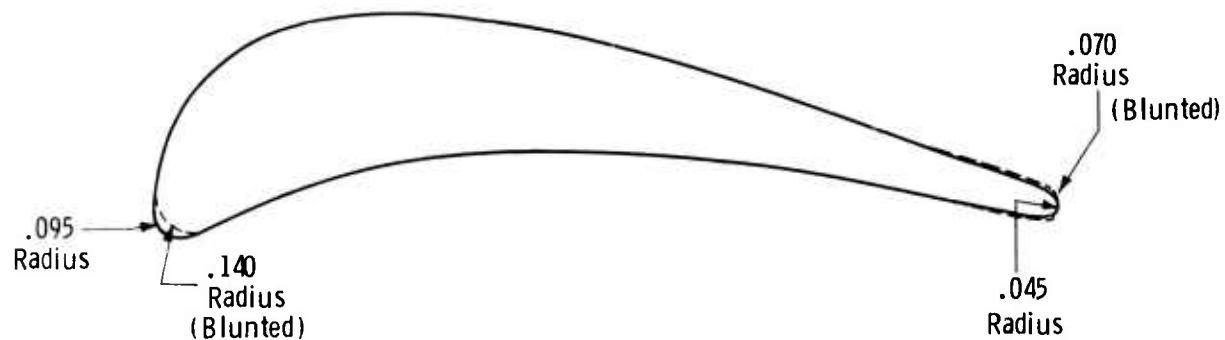


Figure 4.5 — Dimensions of Blunted Leading and Trailing Edges of Ceramic Vane

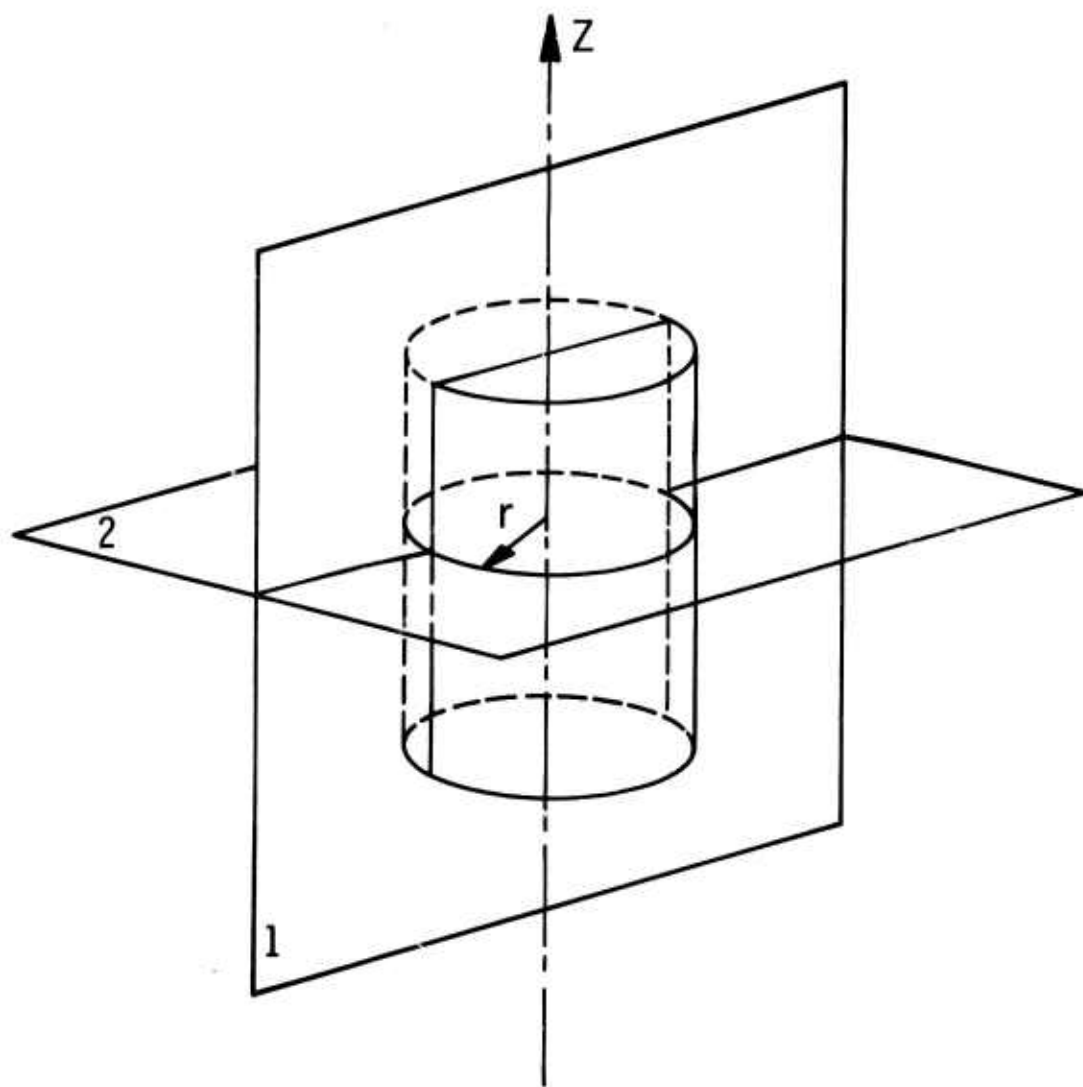


Figure 4.6 — Thermal Quench Cylinder Coordinate System

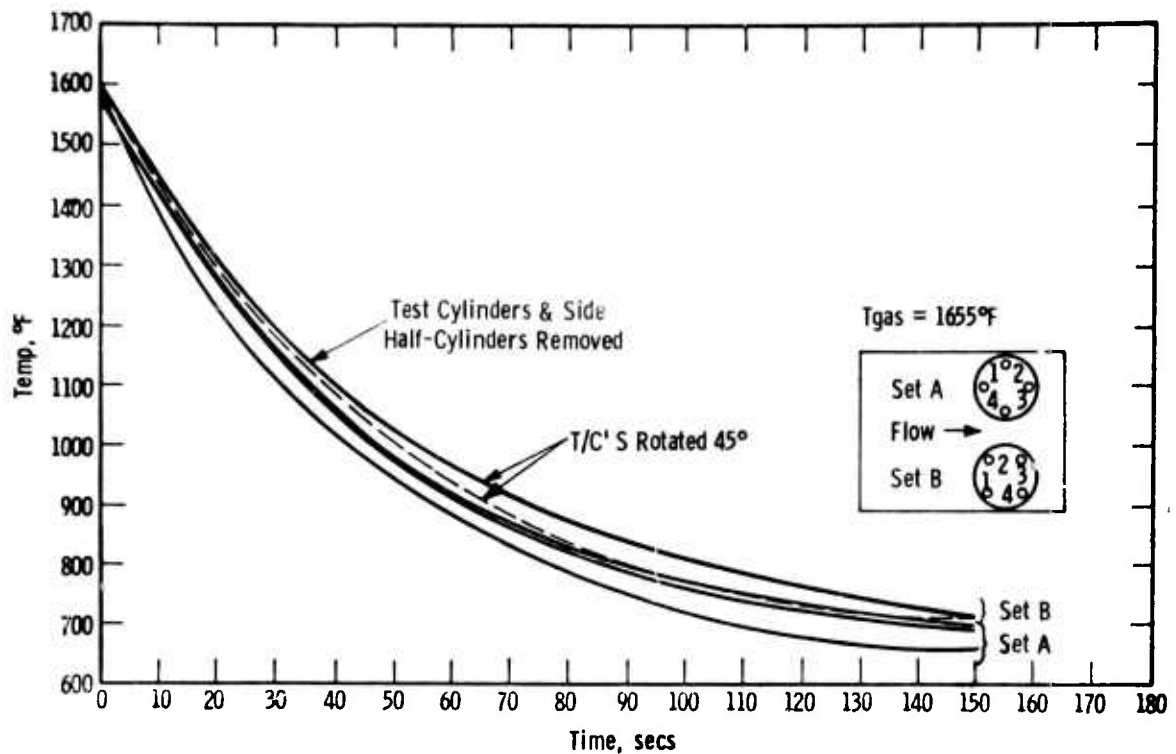


Figure 4.7 — Temperature Decay for a Thermocouple at Position #3 in Thermally Quenched Cylinders of SiC

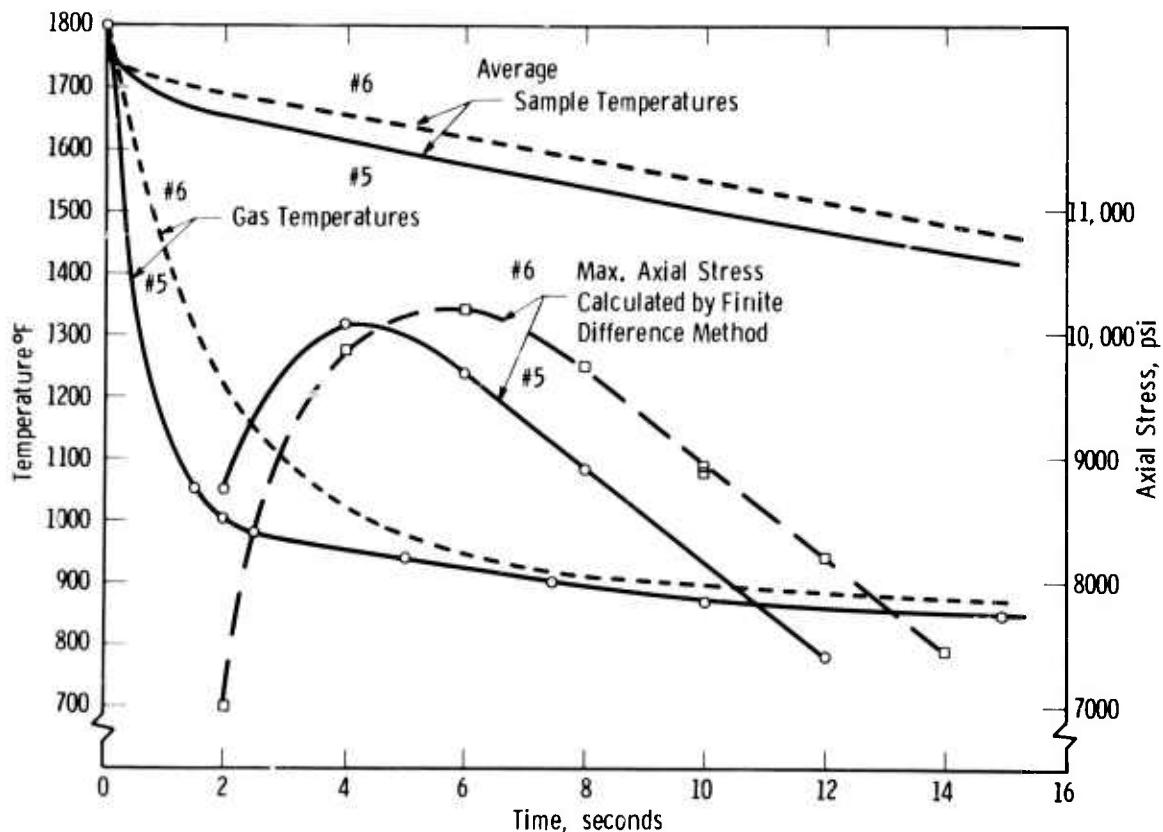


Figure 4.8 — Temperature Decay and Maximum Transient Tensile Stress in the Axial Direction for Silicon Carbide Cylinders Cooled in Test Passage

#### 4.1.3 MATERIALS FABRICATION

##### Introduction

The Norton Company was selected to manufacture stator vane assemblies of high-strength, hot-pressed silicon nitride while Energy Research Corporation was contracted to furnish hollow silicon carbide vanes produced by chemical vapor deposition.

In addition to the hardware requirements both Norton and Energy Research were required to supply representative room temperature property data and sufficient quantities of their respective materials for evaluation and statistical property characterization. Norton's high-density, hot-pressed silicon carbide has been purchased for initial evaluation as a candidate turbine material.

##### Norton Silicon Nitride

The Norton Company was required to prepare 200 lbs of high purity alpha silicon nitride powder for the hot pressing of 40-6.3" x 6.3" x 1.3" thick billets. Ten billets were set aside for material characterization studies at Westinghouse. Twenty stator vane assemblies, consisting of an airfoil section with 2 end caps, were to be machined from the 30 billets remaining. All billets were certified by room-temperature density and flexural strength measurements.

Norton data serving to certify the first 20 silicon nitride billets (Norton HS-130 material) is reported in Table 4.1. Densities range from 3.15 to 3.21 gm/cc, well above the minimum 3.10 gm/cc specified. The results of the bend tests (3 point loading over a 3/4 inch span) indicate that the material meets the specification that modulus of rupture (less two standard deviations) must exceed 90,000 psi. Billet to billet variation as well as the scatter of data within individual billets is much higher than that representative of a uniformly processed material, however.

The reason for this high standard deviation is not known with certainty because the vendor did not record either the location of fracture or evidence for edge defects, etc., which could influence the scatter in results. Because, of this uncertainty in the Norton data, a meaningful Weibull modulus cannot be calculated from the data in Table 4.1.

Billets 1-3, 9 and 10 were delivered to Westinghouse for material characterization. Billets 4-8 and 11-16 were sliced in half and used by Norton to machine 20 airfoil blanks 6 in. long x 3 in. chord. Four of these airfoils are pictured in Fig. 4.9. Remnant material from the airfoil machining operation was sent to Westinghouse for physical property verification.

Norton received modified stator vane assembly drawings on May 31, 1972. Necessary tooling has been procured, and the finish grinding that is needed to produce the tenon geometry at the ends of the airfoils is in progress. The FY 1972 subcontract has been extended through August to permit the final grinding of the end cap sets. These 3-piece stator vane assemblies represent the first generation hardware to be tested in the static rig starting in 1973.

TABLE 4.1

## Properties of Norton HS-130 Silicon Nitride

<u>Billet Number</u>	<u>Density gm/cc</u>	<u>Average MOR psi</u>	<u>Standard Deviation psi</u>	<u>Range psi</u>	<u>No. of Tests</u>
1. 121471	3.18	123,200	7,300	135,900 108,300	20
2. 123071	3.20	140,300	10,600	160,800 120,500	20
3. 031772	3.15	121,200	15,100	146,600 84,900	20
4. 031072	3.21	140,800	13,900	162,700 119,300	20
5. 032272A	3.18	117,700	10,300	135,200 96,800	20
6. 032772A	3.16	114,400	8,100	131,800 100,300	20
7. 032872A	3.15	121,600	7,700	135,400 100,900	20
8. 032872B	3.17	131,700	11,500	153,600 111,700	20
9. 040472A	3.16	127,600	16,000	152,800 95,800	20
10. 050372A	3.19	135,900	19,200	163,600 91,200	20
11. 051772A	3.17	141,100	6,000	150,000 128,800	20
12. 051872A1	3.18	134,000	11,300	150,500 108,300	20
13. 051872A2	3.16	122,500	7,900	134,700 107,100	20
14. 052672A	3.18	123,200	8,800	134,800 101,600	20
15. 050972A	3.16	118,900	5,000	125,900 105,100	20
16. 050872A	3.17	152,000	13,900	167,000 114,000	20
17. 051572A	3.18	124,400	12,300	145,500 102,100	25
18. 043172A	3.18	116,000	8,600	127,700 87,800	21
19. 060172A	3.20	122,700	9,800	139,000 100,500	23
20. 060272A	3.21	131,100	15,600	149,200 96,600	21

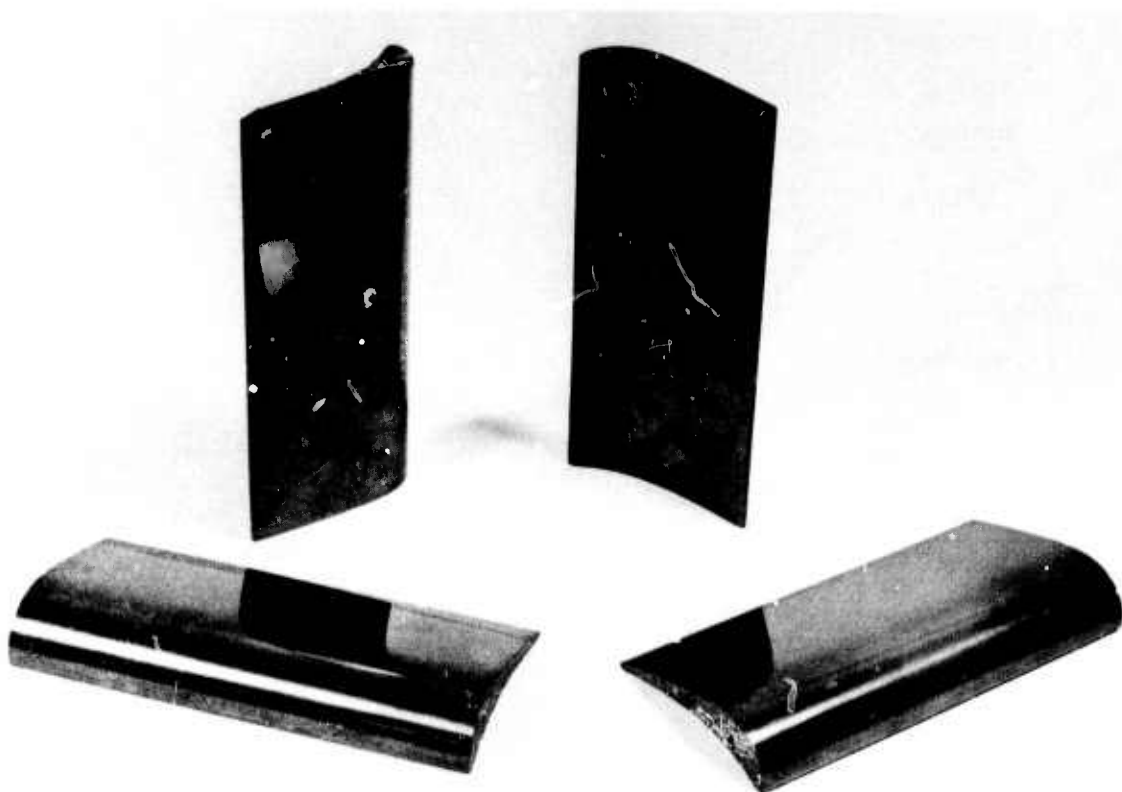


Figure 4.9 — Airfoils Machined From HS-130  $\text{Si}_3\text{N}_4$  by the Norton Company

#### Norton Silicon Carbide

A high strength, hot pressed silicon carbide has been developed by the Norton Company. Its strength at room temperature is comparable to hot pressed silicon nitride but limited tests indicate improved high temperature properties. The flexural strength of the material was reported by Norton to be 75,000 psi at  $2192^{\circ}\text{F}$ , 63,000 psi at  $2507^{\circ}\text{F}$  and 45,000 psi at  $2732^{\circ}\text{F}$ . The thermal conductivity decreases from 555 BTU in/hr  $\text{ft}^2\text{F}$  at  $150^{\circ}\text{F}$  to 265 BTU in/hr  $\text{ft}^2\text{F}$  at  $2500^{\circ}\text{F}$ .

Five 3" x 3" x 1/2" billets and 20 test bars 1/4" x 1/8" x 2" were purchased for initial evaluation of the hot pressed silicon carbide. Preliminary results are presented in Section 5.1.3. of this report.

#### Energy Research CVD Silicon Carbide

The Energy Research Corporation attempted to establish the feasibility of using CVD silicon carbide as a gas turbine material. They were required to submit tensile and flexural strength specimens, tensile and flexural strength specimens cut from hollow airfoil sections, and 5 hollow airfoils according to the subcontract agreement.

Westinghouse received and tested 10 flexural strength specimens nominally  $1\frac{1}{8}'' \times 1\frac{1}{4}'' \times 3\frac{3}{4}''$ . The data supplied by Energy Research (Table 4.2) is representative of the material produced to date. Room temperature flexural strength (4 point loading over inner and outer spans of  $1\frac{1}{8}$  inches and  $3\frac{3}{8}$  inches) range from 29,400 to 89,100 psi. The average for the specimens tested was  $58,300 \pm 9,200$  psi. Efforts to improve the strength of the deposited silicon carbide or reduce the scatter have been unsuccessful. The high temperature strength of the material is promising, however. These data are presented in Section 5.1.3. of this report.

Initial efforts to deposit hollow vane shapes were only partially successful. Thermal gradients caused local buckling and distortion of the tungsten mandrel. Poor circulation of the flowing gases restricted deposition of the silicon carbide in both the leading and trailing edge areas as shown in Fig. 4.10. The use of lances which direct gas flow into limited access areas would be expected to improve the uniformity of deposition leading to the complete formation of leading and trailing edges. The current effort has been terminated, however, to enable Energy Research to concentrate on CVD fabrication development for the small turbine rotor for the vehicular gas turbine project. (See Section 3.1.2 of this report.)

Until CVD silicon carbide is developed and available in a useful, as-deposited form, it cannot be accepted or rejected as a candidate stator vane material for the large gas turbine.

TABLE 4.2  
Energy Research CVD SiC  
Specimen Grown Internal to Mandrel  
MOR Test Results Using Four Point Bending Fixture

CVD Run No.	Specimen Width-b Inches	Specimen Thickness-d Inches	Breaking Load Pounds	4 Point MOR Strength psi
<b>C-71-10-24</b>				
A	.245	.155	105	60,200
B	.222	.156	72	45,000
C	.251	.157	54	29,400
<b>C-71-11-7</b>				
X	.255	.125	72	61,000
Y	.231	.117	65	69,400
<b>C-71-11-10</b>				
1	.260	.164	136	65,600
2	.237	.173	137	65,200
3	.258	.173	96	42,000
<b>C-71-11-11</b>				
1	.259	.164	184	89,100
2	.251	.163	146	73,900
<b>C-71-11-12</b>				
1	.260	.174	110	47,100
2	.257	.125	52	48,700
3	.246	.144	70	46,300

TABLE 4.2 — Continued

CVD Run No.	Specimen Width-b Inches	Specimen Thickness-d Inches	Breaking Load Pounds	4 Point MOR Strength psi
C-71-11-13				
1	.257	.136	95	67,500
2	.257	.143	126	80,900
3	.256	.123	86	74,900
4	.246	.146	104	66,900
5	.249	.138	96	68,300
6	.247	.143	95	63,500
C-71-11-16				
1	.247	.130	59	48,000
2	.251	.135	68.5	50,000
C-71-12-7				
1	.257	.140	90	60,500
2	.244	.124	63	56,500
3	.251	.130	76	60,000
C-71-12-9				
1	.252	.120	77.5	72,000
2	.252	.124	75	65,000
3	.248	.137	60	40,000
C-71-12-10				
1	.246	.131	85.5	68,000
2	.245	.130	85.5	69,500
3	.248	.125	69	60,000
C-71-12-12				
1	.246	.137	58.5	51,000
2	.245	.138	61	48,000
3	.248	.131	60.5	48,000
C-71-12-14				
1	.248	.130	56.5	45,000
2	.247	.123	54.5	49,000
C-721-13				
1	.247	.125	69.5	61,000
2	.246	.122	75	69,000
3	.248	.124	75	66,000
C-72-1-4				
1	.246	.124	72.5	64,500
2	.250	.158	111	60,000
C-72-1-7				
1	.250	.165	106	52,500
2	.259	.166	130	61,500
C-72-1-8				
1	.251	.179	160	67,000
2	.249	.166	114	58,000
C-72-2-2				
1	.251	.156	96	53,000
2	.249	.162	113	59,000
3	.246	.157	95	53,000

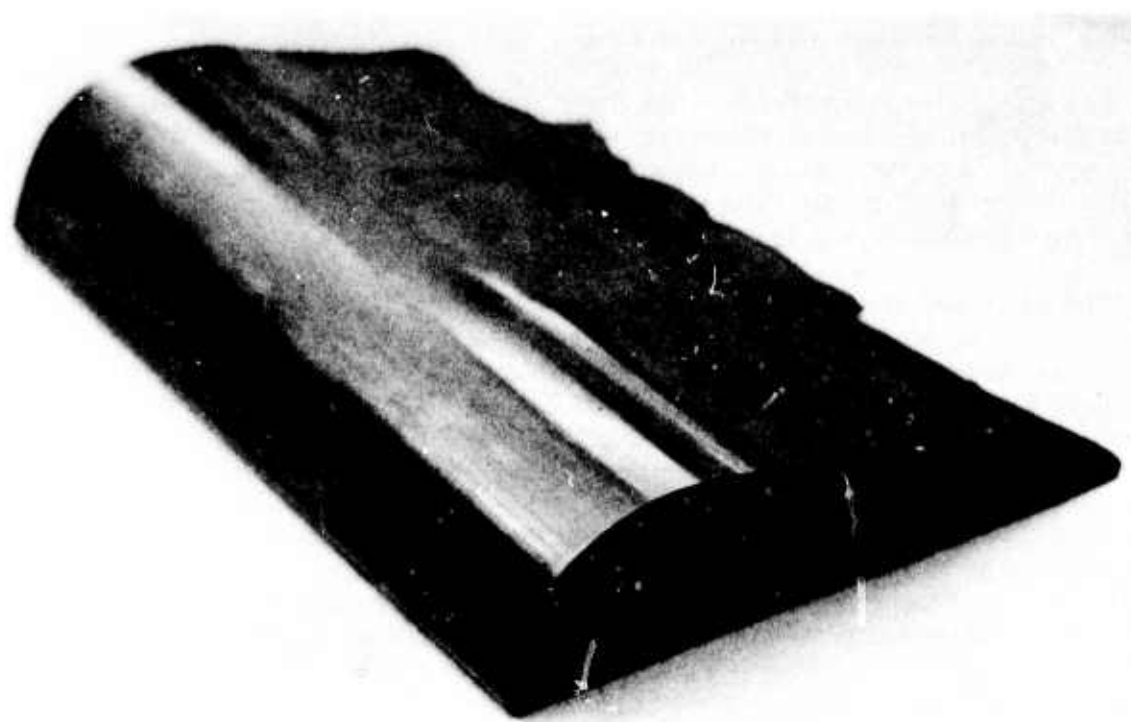


Figure 4.10 — Energy Research CVD Silicon Carbide Hollow Vane

#### 4.1.4 STATIC TEST RIG MODIFICATION

The static test rig at the Westinghouse Gas Turbine Systems Division Laboratory has been primarily devoted to the testing of combustors and metal components. For this reason, a major redesign is now required to accommodate the ceramic stator vane tests and to increase the rig's maximum operating capability from  $1950^{\circ}\text{F}$  to  $2500^{\circ}\text{F}$ .

The proposed static rig modification is illustrated schematically in Fig. 4.11. The ceramic stator vanes in this test are used to turn the combustion gases exiting from the transition piece at an angle of  $116.5^{\circ}$ . In order to utilize the existing exhaust system, the instrumentation shell will be mitered to accommodate the drastic change in flow direction. Gases exiting from the vanes will pass through an instrumentation duct containing temperature profile rakes,\* total pressure rakes, and static pressure taps. The duct will either be lined with a high density castable refractory that exhibits excellent resistance to flame wash and erosion at  $3000^{\circ}\text{F}$ , or it will be metal with a water jacket. Flow continues downstream into a mixer section where the average operating temperature is measured at an exhaust spool piece. The current insulation requirement for the rig sections are also being changed to maintain a safe metal shell temperature when operating at  $2500^{\circ}\text{F}$ .

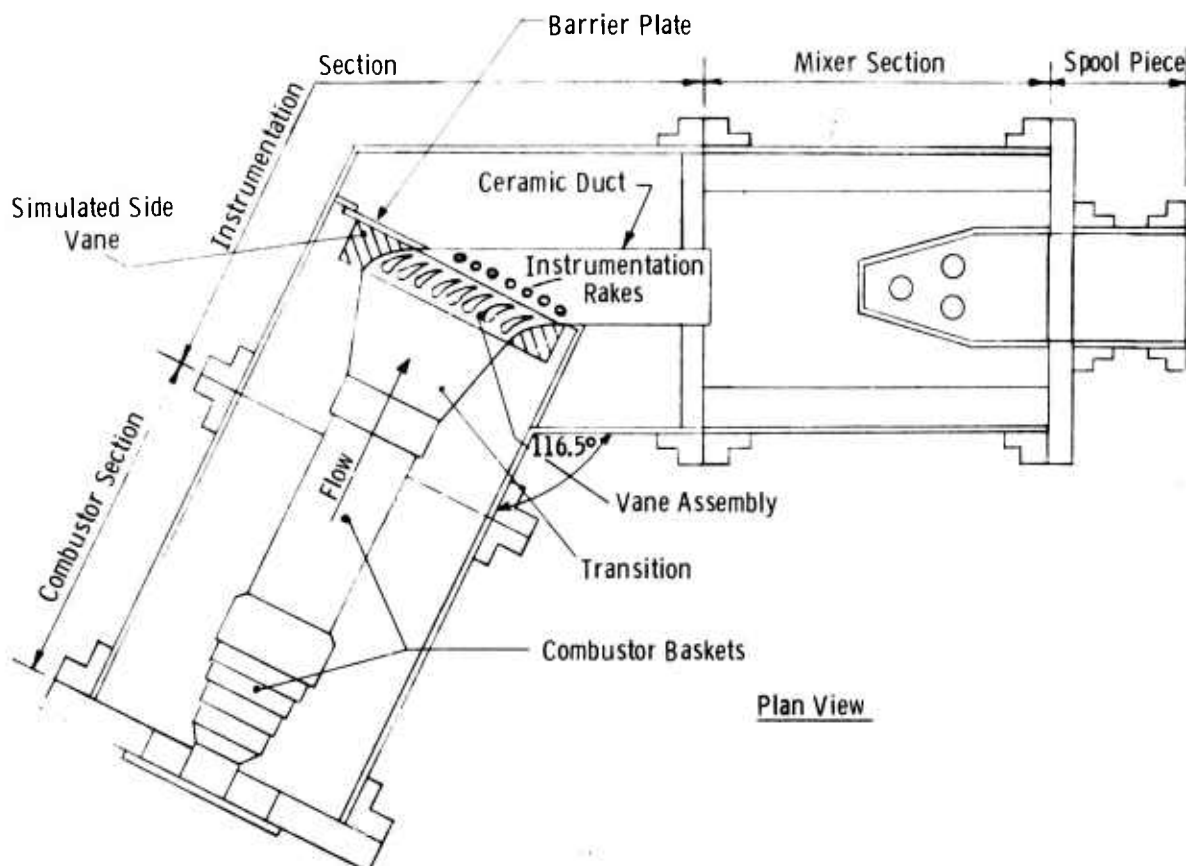


Figure 4.11 — Modified Static Test Rig for  $2500^{\circ}\text{F}$  Test of Ceramic Vanes

\* The term *rake* is used to describe a multiple unit with up to seven thermo-couple junctions or pressure taps positioned to obtain a line profile of the gas duct. Several rakes at intervals across a duct allow the full area profile to be measured.

The actual vane assembly will consist of eight half size vanes (or four assemblies of dual vanes and support hardware) and two simulated side vanes. This assembly will be attached to a barrier plate, the rig counterpart of the gas turbine blade ring. One set of full size combustor hardware (primary basket, secondary basket, transition piece) and a nozzle assembly will be used to generate the hot gases. Internal baffles will be used in the combustor shell to simulate the actual machine geometry about the baskets. Sight glasses will be provided for visual inspection of the vane assembly during rig operation.

At the operating temperatures planned, it may be impossible to instrument the vane assemblies directly with strain gauges and thermocouples. Initial attempts to install this type of instrumentation using flame sprayed alumina or a variety of refractory cements proved unsuccessful. Surface roughening and the use of intermediate materials, such as nickel aluminide or silicon metal, failed to improve adhesion significantly.

## 4.2 ROTOR BLADE DEVELOPMENT

### SUMMARY

A finite element program for isotropic elastic analysis of three dimensional solids has been completed. This technique is being tested on simple problems with known solutions before it is applied to rotor blade airfoil design.

#### 4.2.1 THREE DIMENSIONAL FINITE ELEMENT STRESS ANALYSIS

##### Introduction

The rotor blade development work has been confined specifically to the development of a 3D finite element stress analysis. Rotor blade design studies will begin during the 1973 fiscal year program.

The Westinghouse three dimensional finite element program is based upon a higher order isoparametric element not presently available in a program like NASTRAN. In addition to complex curved-sided elements and variable strain capability, this unique program will have the capacity of analyzing elastic-plastic-creep problems having contact faces between several parts. The program is expected to meet the most exacting requirement of analytical blade design and also be available to confirm the analysis upon which the vane designs are based.

##### Finite Element Program

The finite element program for isotropic elastic analysis of three dimensional solids has been completed. This program consists of a system of subroutines including a wave-front equation solver and stiffness and load vector routines for three dimensional isoparametric elements. The current version is based on a cartesian coordinate system. The accuracy of the program has been verified on a number of problems for which known solutions exist. These problems are of a simple nature compared to practical design problems, since no exact solutions for complicated geometries are known.

The equation solver is based on the Gaussian elimination method which uses a wave-front technique. With this method, large systems of equations can be solved provided the wave-front does not exceed certain limits which depend on the configuration of the computer system. In general, the wave-front technique allows larger systems to be solved efficiently.

The following types of displacement boundary conditions were incorporated into the program:

1. Prescribed displacements.
2. Group of nodal points having equal but unknown displacements in a specified coordinate direction.
3. Displacements restricted to a prescribed direction.
4. General linear constraint displacement.

Displacement boundary condition 4 is the most general one that can be handled with a linear system of equations. Boundary conditions 1 to 3 are special cases of 4.

Four different types of three-dimensional isoparametric elements were incorporated into the program:

1. Eight mode element (linear displacements), Fig. 4.12.
2. Twenty node element (quadratic displacements), Fig. 4.13.
3. Thirty-two node element (cubic displacements), Fig. 4.14.
4. Mixed element, Fig. 4.15.

The last element is the most versatile because it allows the user to vary the number of nodes. It also facilitates the generation of graduated element networks to properly account for regions where large stress gradients are anticipated, e.g., these regions are represented by 24 or 32 node elements while others are only represented by 8 node elements.

The following loading cases can be handled by the program:

1. Surface tractions.
2. Static uniform pressures.
3. Centrifugal force loads.
4. Thermal loads.

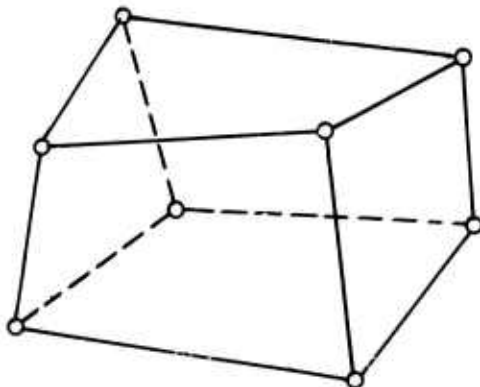


Figure 4.12 — Eight Node Isoparametric Element  
(Linear Displacements)

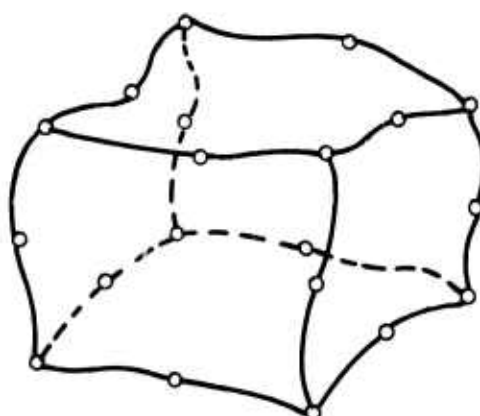


Figure 4.13 — Twenty Node Isoparametric Element  
(Quadratic Displacements)

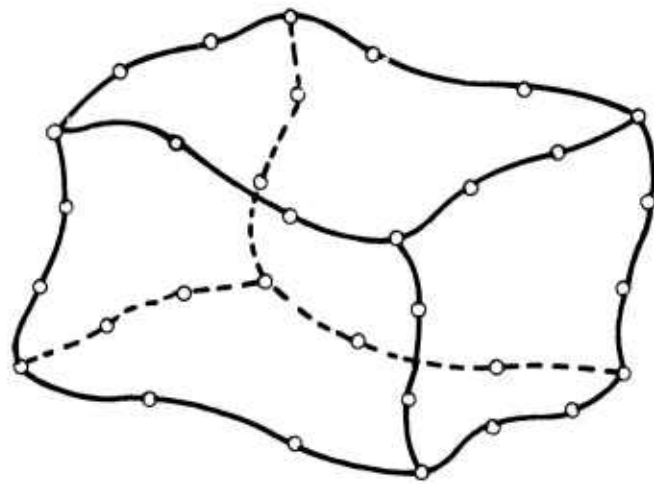


Figure 4.14 — Thirty-two Node Isoparametric Element  
(Cubic Displacement)

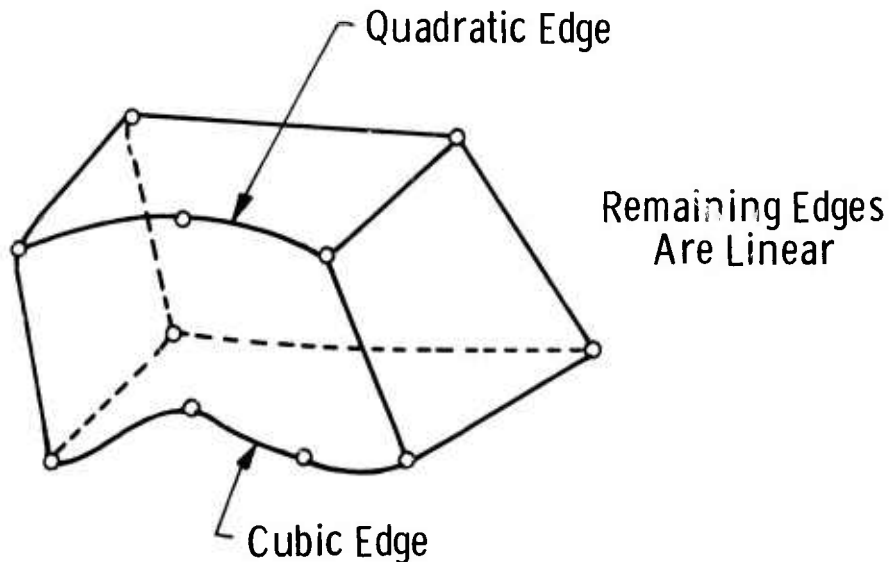


Figure 4.15 — Mixed Isoparametric Element

The computer program consists of three overlays. An overlay is a portion of the program that is written on files and is loaded into the computer at the time it is needed for execution. In the first overlay the input data are read in, internally processed, and stored in auxiliary storage. The bookkeeping for the wave-front equation solver is done in the second overlay. In the third overlay, the element stiffness matrices are computed and the total system of equations are solved, the stresses are obtained, and the output is produced.

5. PROGRESS ON MATERIALS TECHNOLOGY — VEHICULAR AND STATIONARY TURBINE PROJECTS

SUMMARY

Design technology is highly dependent upon physical properties of the materials being used. This section deals with work performed during the reporting period on the acquisition of physical property information. Complete property characterization of the ceramic materials for turbine engine use is an enormous task, which will proceed throughout the life span of the contract. This task is also complicated by the fact that many of the materials being investigated are in the developmental stage and improvements in properties are anticipated, which will require that some, if not all, of the physical properties must eventually be re-determined.

Spin testing of ceramic materials is a relatively new method for determining material strength which simulates closely the stresses encountered in turbine rotors. Samples of lithium-aluminum-silicate material were spin-tested, and found to have an average tensile strength of 8930 psi, which compares very closely to the bending strength of this material. Two disks of hot-pressed silicon nitride were spin-tested and failed at stresses of 63 Kpsi and 51 Kpsi. This compares closely with strengths established by tensile tests which were about half of the strength in bending. Work is shown relating defects, as determined ultrasonically, to the fracture patterns.

Bending strength as a function of temperature was determined for Ford's injection molded reaction sintered silicon nitride. The strength level of the as-molded material remained virtually constant at around 22,000 psi up to 2000°F, then decreased gradually to 19,200 psi at 2400°F. This is not expected to have an adverse effect upon the use of this material for stator application.

Extensive property data was generated on Norton HS-130 hot-pressed silicon nitride. In general the strength of this material decreases with temperature, particularly above 2000°F. Tensile strength drops from 60 ksi at RT to 17 ksi at 2500°F. The flexural strength in the strong direction is reduced to 50 ksi at 2500°F from a value of 98.6 ksi at RT and 2000°F. Weibull parameters were established from flexural data and it was possible to predict the effect of size and strain rate, as well as the properties for other modes of testing. Fatigue limits are 30 ksi at 2350°F and 40 ksi at 2200°F. Stress rupture life at 10 ksi and 2300°F is greater than 100 hours. The elastic modulus drops sharply above 2000°F; room temperature values were  $44.5 \times 10^6$  psi whereas at 2500°F the modulus fell to  $11.5 \times 10^6$  psi. Thermal expansion and thermal conductivity data determined by Battelle is reported. Friction and damping behavior is also discussed.

Flexure strength testing of Norton hot-pressed silicon carbide and Energy Research chemically vapor deposited silicon carbide were determined at various temperatures. The hot-pressed material had a room temperature strength of 72,000 psi, decreasing somewhat to 52,000 psi at 2500°F. The Energy Research material maintained an average strength of 75,000 psi up to 2500°F.

No high cycle fatigue problem is anticipated with  $\text{Si}_3\text{N}_4$  at a use temperature of up to  $2200^{\circ}\text{F}$ . The stress-rupture behavior of Norton HS-130 silicon nitride appears quite adequate for vane applications since the loads imposed under steady state operating conditions in the turbine do not exceed 3300 psi. The preliminary properties of hot-pressed SiC appear very promising for turbine components under  $2200^{\circ}\text{F}$ , and will be further evaluated for use at  $2500^{\circ}\text{F}$ .

Dynamic corrosion-erosion tests were extended to 250 hours. Corrosion of Norton HS-130  $\text{Si}_3\text{N}_4$  in simulated gas turbine environments at  $2000^{\circ}\text{F}$  results in a weight loss of  $3.5 \text{ mg/cm}^2$  after 250 hours. This represents a surface recession of less than 0.0004 inches when the data is plotted in terms of oxide penetration. Preliminary results suggest that the strength of the material is not affected by the gas turbine environment.

Comparable weight loss data for superalloys like Udimet 500 or X45 at  $1650^{\circ}\text{F}$  are 130 and  $80 \text{ mg/cm}^2$ , respectively. These values reflect surface recessions of 0.006 inches (Udimet 500) and 0.004 inches (X45), an order of magnitude greater than the ceramic.

## 5.1 MATERIALS ENGINEERING DATA

### 5.1.1 SPIN TESTING OF CERAMIC MATERIALS

#### Introduction

Spin testing has been selected, along with other fracture tests, as a destructive means of evaluating the strength of ceramic materials. The advantage of spin testing is the ability to test samples in a biaxial loading mode closely simulating the mechanical loads imposed on the turbine rotor. Test samples may be readily prepared, since they consist of simple right-cylindrical disks of the approximate size of the rotor.

The materials evaluated by spinning to destruction, thus far, are lithium aluminum silicate and hot-pressed silicon nitride.

#### Procedure

The spin pit used for testing ceramic disks consists of a Barbour-Stockwell Model 1307 two-inch air turbine which powers the ceramic disk mounted on an arbor and suspended on a 3/16" spindle. This turbine is capable of 100,000 RPM. A magnetic pick-up, built into the turbine housing is fed to an electronic counter mounted on the operator's control panel. The catcher assemblies were removed for these tests so that photographs may be taken of the spinning disks. The spin pit was evacuated to reduce heating due to friction.

The inside of the spin pit was lined with three inch oak and two inches of clay. The clay reduced fragmentation of the ruptured disk. The bottom of the spin pit was covered with plate glass which allowed photographs to be taken during the tests, and at the moment of failure of the disks.

The photographic triggering mechanism was made from reaction sintered silicon nitride, fabricated in-house. This thin stationary ring was located such that there was an air gap of about 0.030 inches between the ring and the rotating disk. A schematic drawing of the triggering and photographic technique used is shown in Fig. 5.1. An epoxy conducting paint was applied to the outside of the ceramic ring and a current fed through the ring into the triggering circuit. This circuit was broken when hit by the portion of the disk where fracture occurred, which fired two strobelights exposing the photographic plate.

Prior to assembly, the ceramic disks were inspected dimensionally and by ultrasonic c-scan. The disks were mounted on the arbor with a slip fit and retained in position by a hand-tightened nut. The assemblies were balanced to 0.005 oz-inches prior to spinning. The 3/16" spindle was inserted into the arbor assembly and the runout of the spindle checked and straightened, if required, prior to each run. However, even though much care was taken in preparing the assemblies, there was always a low critical frequency encountered in the spin pit tests. Therefore, it was standard procedure in all tests to rapidly accelerate through the low critical into a dynamically stable frequency range. At this point the assembly was slowly accelerated until a burst speed was obtained. The electronic counter was equipped with a delay which allowed the operator to record the maximum RPM obtained.

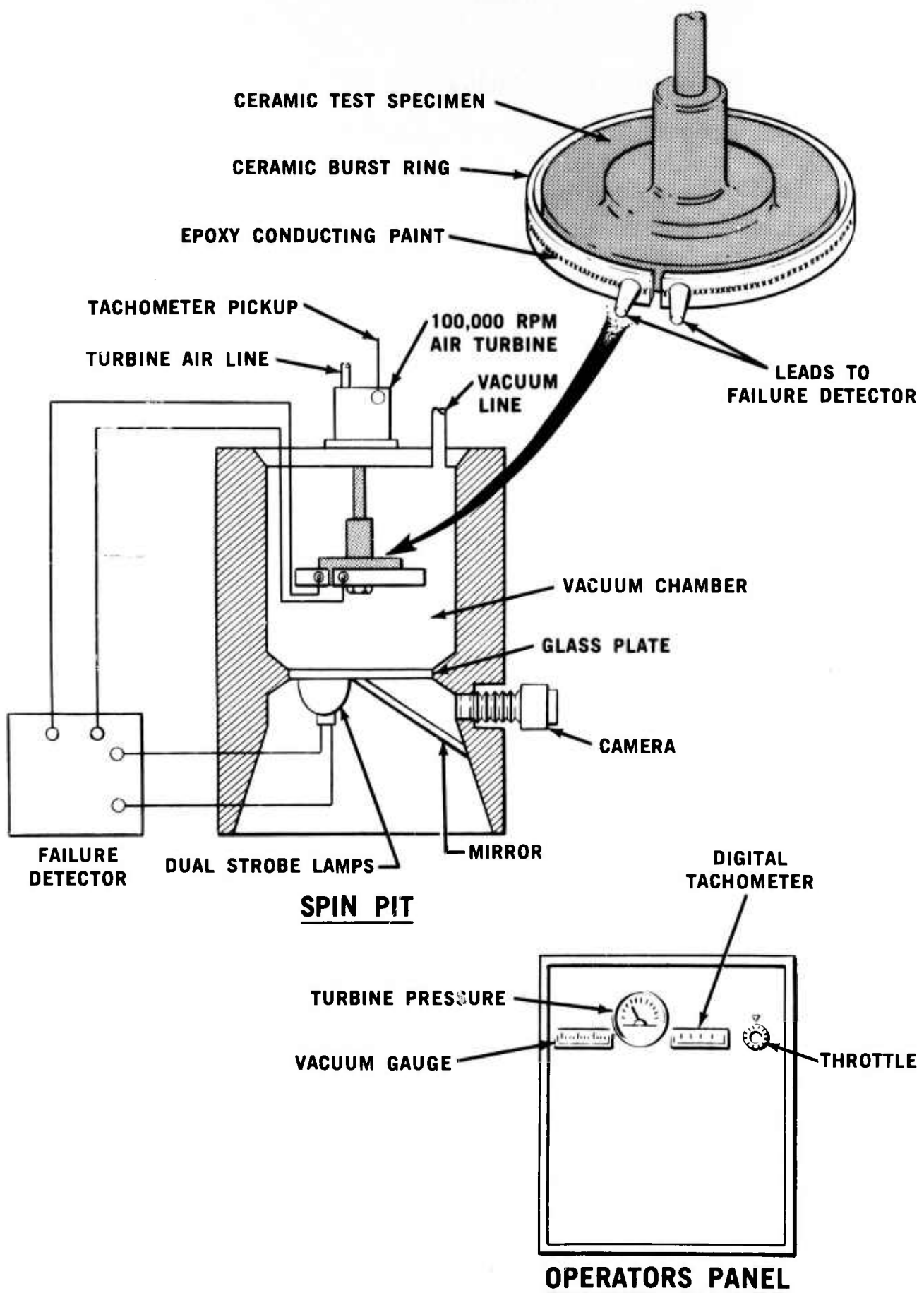


Figure 5.1 — Schematic of Method for Spin Testing of Ceramic Disks

## Test Results

Eight samples of lithium aluminum silicate (LAS) were spin tested to determine the maximum tensile strength and to correlate fracture patterns with the ultrasonic c-scan flaw patterns previously obtained. The specimens were diamond ground from material supplied by Corning Glass Works. The tensile strength was calculated and found to be  $8930 \pm 1030$  psi for the eight samples. This was found to be nearly equal to the modulus of rupture, which was 8600-8950 psi of this material taken from four-point bend samples. The bending test samples, 1-1/4" x 1-1/4" x 7", were cut from large blocks of the material. The bars were broken using an Instron test machine with a cross head speed of 0.10 in/min.

Figure 5.2 shows the c-scans of 3 disks, with the fracture pattern (drawn by hand) superimposed. The fracture pattern was established using the photographs taken at rupture along with the reassembled pieces. Inspection of these three disks indicate there is little or no correlation between the number of flaws present and the maximum tensile strength as determined by spin testing. Shown in Figure 5.2c, disk number thirteen had the largest number of flaws present and the second highest strength. This is possible since the highest stressed point in the disk is at the hub. It appears that the type of flaw and the location has more effect on the burst strength than the gross number of flaws. There is some evidence from Figure 5.2c that the fracture will follow a region of flaws (line A). However, much more work must be carried out to determine if this is a valid correlation.

Two hot pressed silicon nitride disks made from Norton HS-110 material were spin tested to destruction. These disks, which were six inches in diameter, were diamond ground to a surface finish of  $7-11 \mu$  in, arithmetic average. Disk number one burst at 51,280 RPM, with a corresponding maximum tensile stress at the bore of 62,980 psi. This disk is shown in Figure 5.3 at the time of rupture. Unlike the LAS material disks, gross fragmentation is evident. However, examination of the fragments around the bore indicated the fundamental failure occurred at three equally spaced planes. This is typical of disk failure and it is assumed that this is the point of crack initiation. Ultrasonic c-scan traces of the number one disk indicated three flaws were present. Because of the gross fragmentation, the fracture pattern could not be superimposed on the c-scan traces. However, it is felt the flaws, located at near mid-radius, did not influence the fracture.

Disk number two had considerably more flaws, which are shown on the ultrasonic c-scan traces in Figure 5.4. These flaws, some of which are located near the bore, may have influenced the burst speed of this disk which occurred at 46,900 RPM. The maximum tensile stress at this speed was 50,995 psi. In this test the triggering mechanism failed to fire the strobe-lights so no picture at failure is available.

The low failure strength may be due in part to the fact that the disk was made from Norton's HS-110 material, representative of early manufacture of silicon nitride. As reported in the first interim report(1) the strength in bending of HS-110 was found to vary with sample size and test procedure. Small samples (1/8" x 1/8" x 1") in 3 point load yielded strengths of 123 Kpsi while larger samples (1/4" x 1/4" x 4") in 4 point bending yielded only 90 Kpsi average. Individual values as low as 99,000 and 70,000 psi were found in these tests of bars all cut from a billet having a density of 3.11 g/cc. The second

spin disk, which exhibited a density of 3.07 g/cc, would be expected to have a larger number of voids, flaws or porous regions as was shown in Fig. 5.4. The lower density, greater number of defects, and the much larger sample area stressed during spinning would be expected to contribute to lower strength.

A third hot pressed HS-110 disk was prepared for spin testing; however, a large density gradient, visible to the eye as a color gradient and also depicted by ultrasonic c-scan, made balancing of the disk impossible.

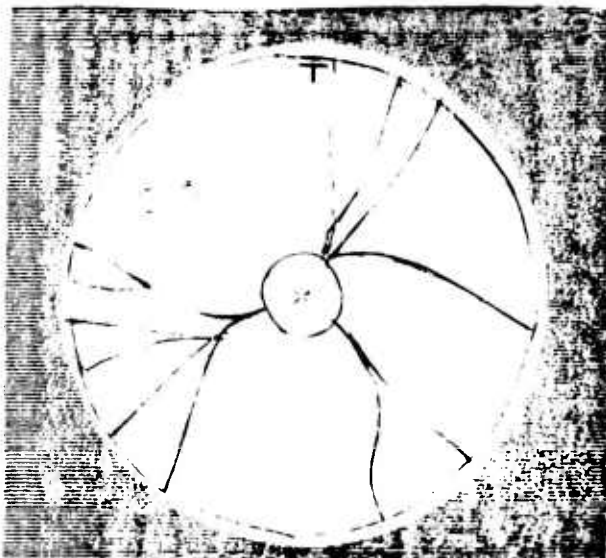


Figure 5.2a — Disc #5

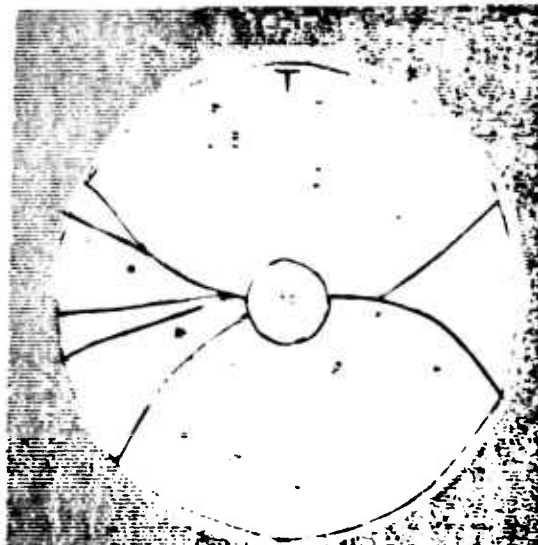


Figure 5.2b — Disc #7

Tensile Strength of 10,518 psi

Tensile Strength of 6926 psi

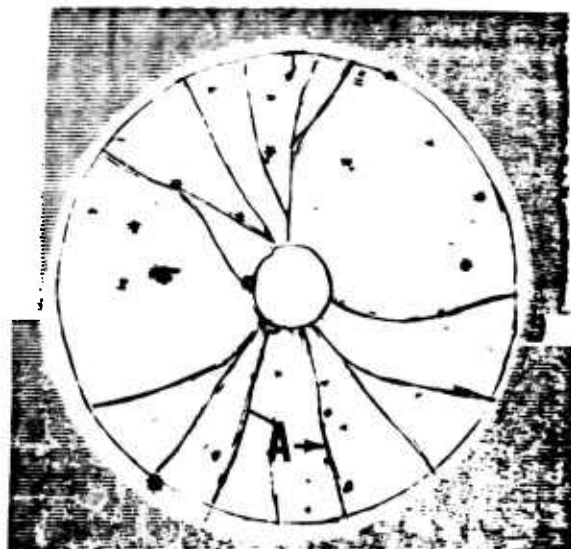


Figure 5.2c — Disc #13

Tensile Strength of 9930 psi

Figure 5.2 — Ultrasonic C-Scans of LAS Disks, with Fracture Lines Superimposed

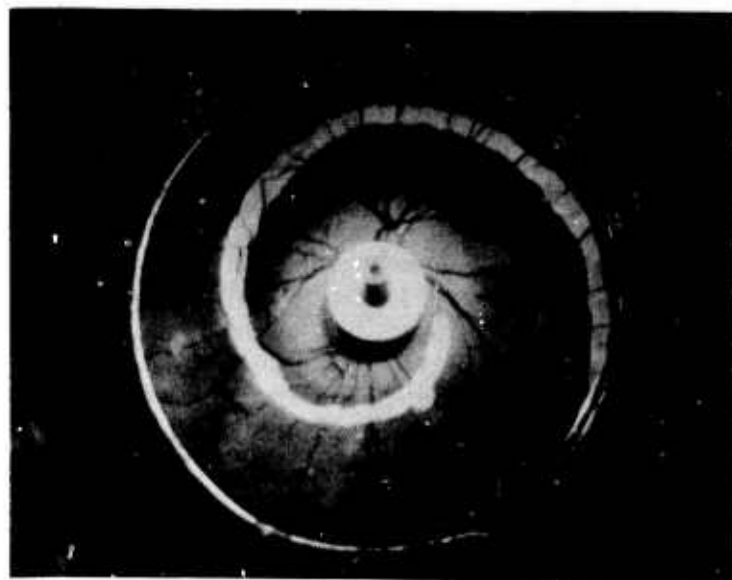
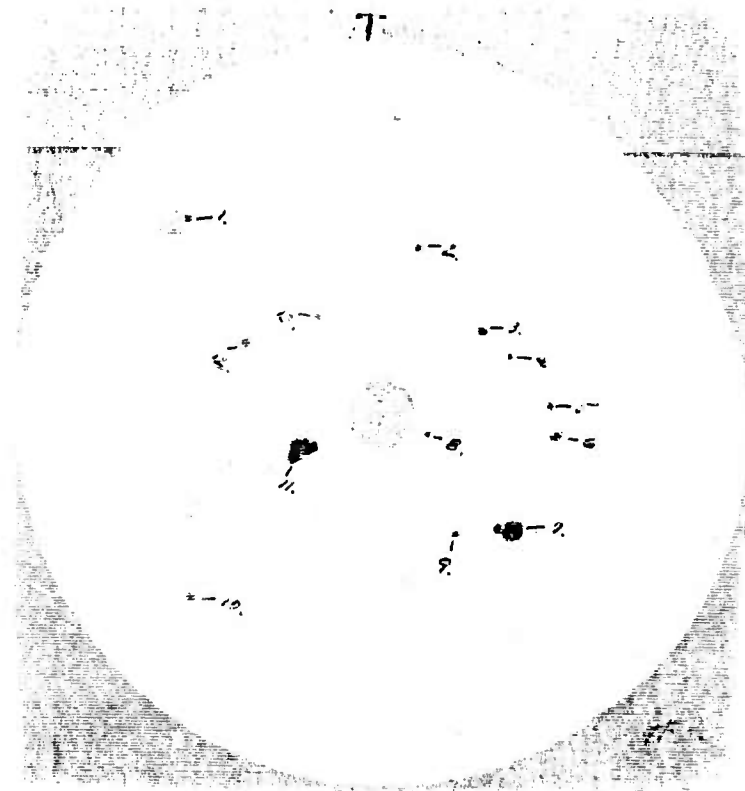


Figure 5.3 — Spin Test of  $\text{Si}_3\text{N}_4$  at Point of Fracture



Flaw No.	Depth (In.)	Flaw No.	Depth (In.)
1.	.33	8.	.44
2.	.26	9.	.33
3.	.25	10.	.33
4.	.39	11.	.33
5.	.33	12.	.33
6.	.39	13.	.33
7.	.39		

Figure 5.4 — Ultrasonic C-Scan of  $\text{Si}_3\text{N}_4$  Disk No. 2

### 5.1.2 HOT MOR OF REACTION-SINTERED $\text{Si}_3\text{N}_4$

The hot strength of injection-molded reaction-sintered silicon nitride fabricated by Ford was measured utilizing a refractory three point loading fixture, hydraulically loaded, and heated in a resistance heated furnace. Loading capacity of the system is 100 pounds. A silicon carbide block with silicon carbide knife edges on 3 inch centers is used. The loading ram is silicon carbide and is guided by bearings located in the cool portion of the furnace. Air cooling is used to further protect the bearings and the hydraulic system. A silicon carbide knife edge attached to a pivoted self-aligning plate is fastened to the loading ram. Alumina rods are used to manipulate samples. Round samples are rolled down an inclined ramp and the alumina rods separate the samples and load them individually onto the knife edges. Temperature capability of the furnace is  $2400^{\circ}\text{F}$ .

The test samples were unmachined, injection molded silicon nitride rods, 1/4 inch diameter by 4 inches long. Test rods were fired at  $2100^{\circ}\text{F}$  for 24 hours followed by  $2660^{\circ}\text{F}$  for 24 hours, and had a sintered density of 2.2 grains/cc. Thirty rods each were tested at  $67^{\circ}\text{F}$ ,  $940^{\circ}\text{F}$ ,  $1760^{\circ}\text{F}$ , and nine rods were tested at  $2400^{\circ}\text{F}$ . A malfunction in the loading mechanism caused this latter test to be terminated at this point.

The average strength values at each temperature level are shown in Figure 5.5. At  $67^{\circ}\text{F}$  strength was 22,459 psi with a standard deviation of 2665 psi. At  $940^{\circ}\text{F}$  the mean strength was 22,216 psi with a standard deviation of 2459 psi. For  $1760^{\circ}\text{F}$  the mean strength was 24,000 psi with standard deviation 2130 psi.

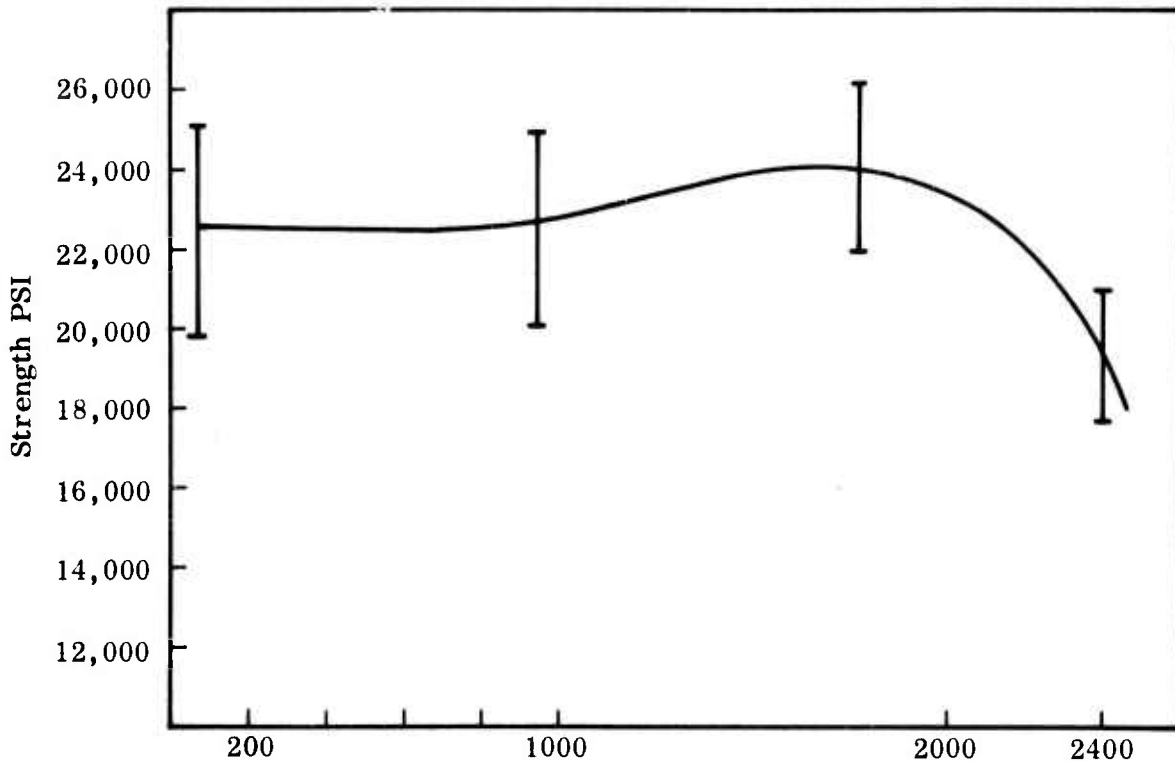


Figure 5.5 — Strength vs Temperature for Reaction Sintered  $\text{Si}_3\text{N}_4$

Finally, at 2400°F the strength had a mean value of 19,281 psi with a standard deviation of 1578 psi. These values are plotted on Figure 5.5 with error bars of one standard deviation.

All mean values represented on the curve were tested for significance using a statistical "T" test, and were found statistically valid.

The statistical "T" test was employed to verify the changes of mean value observed at each data point in the hot MOR test. Ambient strength values were used as the control data point. A slight increase in strength was noted at 1000°F; however, when statistically tested the increase proved insignificant. The increase in strength at 2000°F and the decrease in strength at 2400°F both proved significant when tested for significance. Since the strength increased at the 1000°F point was found insignificant, the point was plotted at the base line value.

There are several factors which may lead to the decrease in strength observed at 2400°F. The furnace is under-powered and takes 24 hours to reach 2400°F. The time of soak of the silicon nitride bars in air may cause oxidation effects to become apparent. Also the intergranular impurities present in the silicon nitride such as calcium impurities and FeSi compounds may cause weakening of the material above the melting point of the impurity phases. This subject will be discussed in more detail in Section 5.2.1 of this report.

### 5.1.3 PHYSICAL PROPERTIES OF HOT-PRESSED SILICON NITRIDE

#### Introduction

In the stationary turbine project, commercially-produced silicon nitride and silicon carbide that meets specified standards will be used to fabricate stator vanes. All of the pertinent mechanical and thermal properties of these materials are being determined such that statistically significant design values from RT to 2500°F will be available for the final vane design. In addition, since a final design must usually incorporate a corrosion allowance, dynamic corrosion tests are being conducted in a pressurized test passage that reproduces the operational environment of a large stationary gas turbine.

Two grades of hot-pressed silicon nitride from Norton were produced during the first year of this project. These are designated HS-110 and HS-130; the difference is essentially in the impurity content where HS-130 is the most pure and shows superior mechanical and thermal properties at high temperatures. The HS-130 grade is a material certified by Westinghouse that meets density and strength measurements as described in Section 4.1.3. While most of this section is concerned with determining the properties of  $\text{Si}_3\text{N}_4$ , some data is presented on silicon carbide.

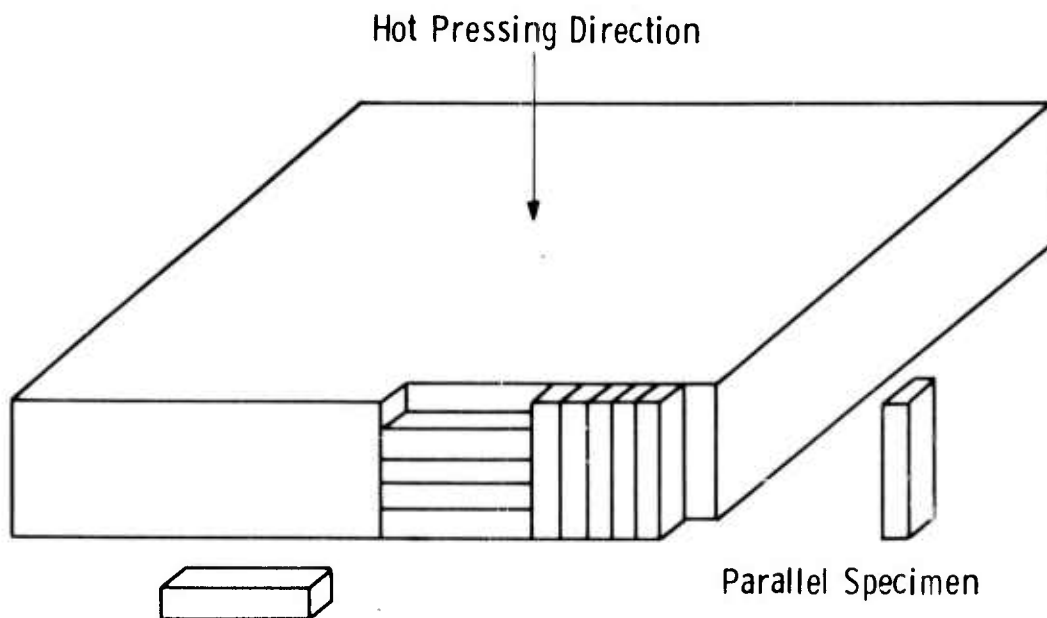
In the following sections on properties, there will be reference made also to strong and weak directions in the hot-pressed silicon nitride. These refer to directions that are perpendicular and parallel to the hot pressing direction, respectively. A clear illustration of these directions is provided in Figure 5.6.

#### Tensile Strength

The strength of a ceramic under pure tension is usually the most desirable for reliable engineering design. But tensile strength, particularly at high temperatures, is also the most difficult and expensive to obtain. Complex high temperature grips, extremely precise machining accuracy, and difficulty with accurate alignment, generally preclude large numbers of tension tests.

This dilemma can be resolved by supplementing tension data with reliable flexural data through the use of Weibull's (5) statistical characterization of brittle materials. Weibull's theory attributes the failure of brittle materials to flaws that are randomly distributed throughout the material. Thus, the larger the volume under high stress, the more likely a flaw will be included that causes a failure. A bend specimen with only the outer fibers under the maximum stress might be expected to survive a higher load than a tensile specimen having the entire gauge volume under maximum stress. The risk of failure was experimentally found to be proportional to

$$\int_v \left(\frac{\sigma}{\sigma_0}\right)^m dV$$



Perpendicular Specimen	Westinghouse	<u>73,000</u> $\pm$ 11,000 psi
Westinghouse	Norton	<u>107,000</u> $\pm$ 17,000 psi
Norton *		<u>125,000</u> $\pm$ 16,000 psi

\*Norton data was obtained in 3-point bending

Figure 5.6 -- Illustrations of Specimen Direction and Strength Values With Respect to Hot Pressing Direction

for a number of materials. Stress is given by  $\sigma$  and volume by  $V$ . The Weibull modulus  $m$  and normal stress  $\sigma_0$  are characteristic of the material tested. In some cases

$$\int_V^{\infty} \left( \frac{\sigma - \sigma_u}{\sigma_0} \right)^m dV$$

was found to be more appropriate where  $\sigma_u$  is the third material parameter.

Twenty-four values of RT fracture strength obtained in three-point bending by the Norton Company were used to calculate values of  $m$ ,  $\sigma_u$ , and  $\sigma_0$  for hot-pressed silicon nitride (strong direction). Results gave  $m = 9.1$ ,  $\sigma_u = \text{zero}$ , and  $\sigma_0 = 57,800$  psi. With these values, the average fracture strength in both four-point bending and tensile loading were predicted and compared with test values obtained at Westinghouse. These values are compared in Fig. 5.7. As may be seen, the agreement between predicted and measured data is very good.

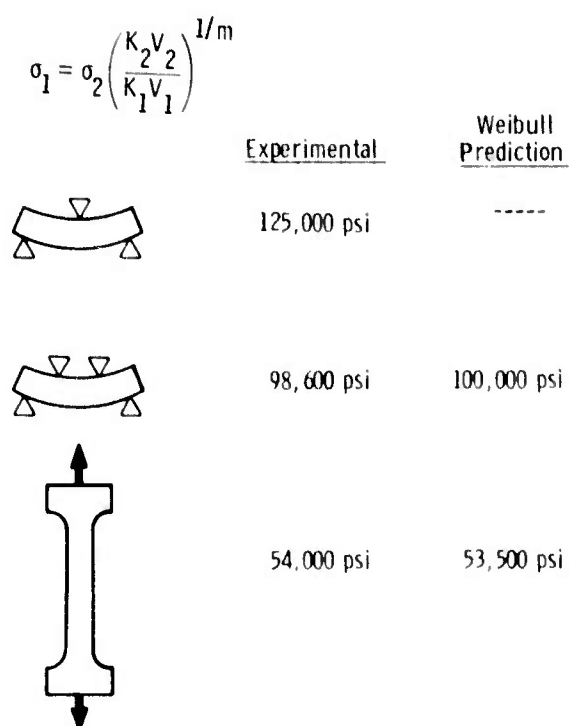


Figure 5.7 — Effects of Mode of Testing on the Strength of  $\text{Si}_3\text{N}_4$

The Weibull parameters were also determined for hot-pressed silicon nitride in the weak direction at  $2350^{\circ}\text{F}$ . In this case  $m = 8.7$  and  $\sigma_0 = 29,200$ . By regressive curve fitting, these data were combined with flexural data that show a strain rate dependence at high temperature to produce the following expression relating temperature, strain rate and volume to tensile strength:

$$\sigma_T = \frac{28,600 \dot{\epsilon}}{V \cdot 11} \cdot \left( \frac{27.5}{2920-T} \right)^{27.5} \pm 12\%$$

T in degrees F

V in cubic inches

$\dot{\epsilon}$  in inch/inch-minute

The results of using this expression to predict tensile strength for several volumes are shown in Figs. 5.8 through 5.10.

An extensive tensile test program for two sizes of specimens is underway to confirm or improve these predictions. The tensile specimens are taken in the strong direction and hence strength should be  $\sim 15\%$  to  $25\%$  higher. Preliminary results from inert gas tensile tests indicate that the actual strong direction data are predicted by the above weak direction expression for temperatures of  $2300^{\circ}\text{F}$  and below (Table 5.1). A further Weibull determination at high temperature and strong direction is currently in progress. As more complete tensile data become available, the Weibull parameters will be adjusted accordingly.

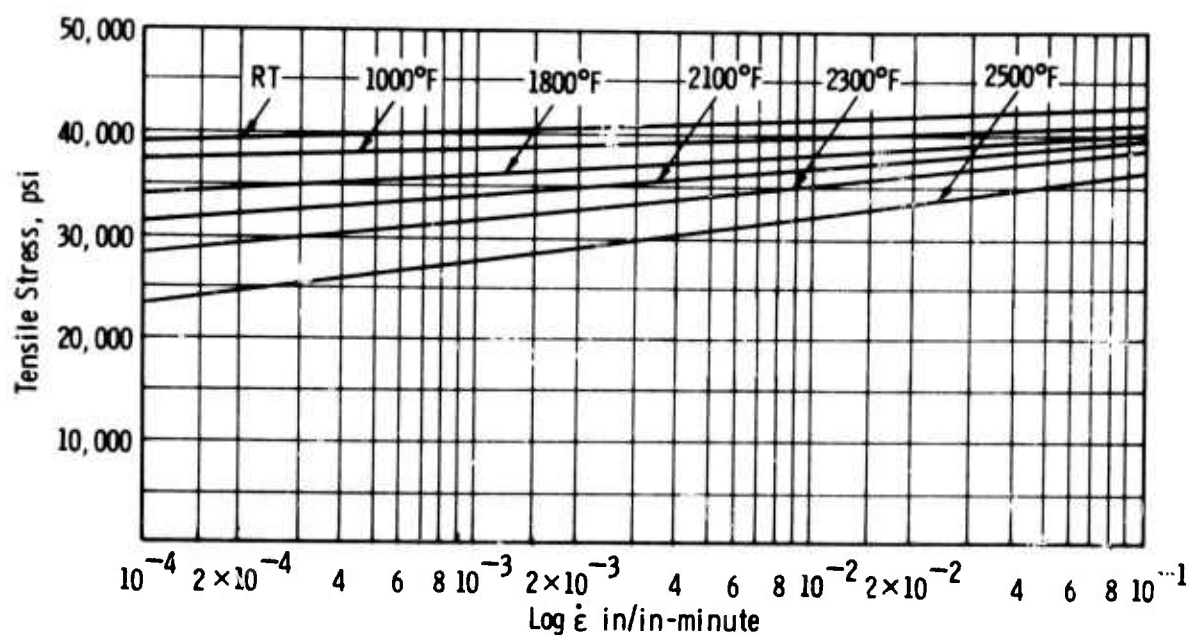


Figure 5.8 — Predicted Tensile Strength of Hot Pressed  $\text{Si}_3\text{N}_4$  vs Temperature and Strain Rate

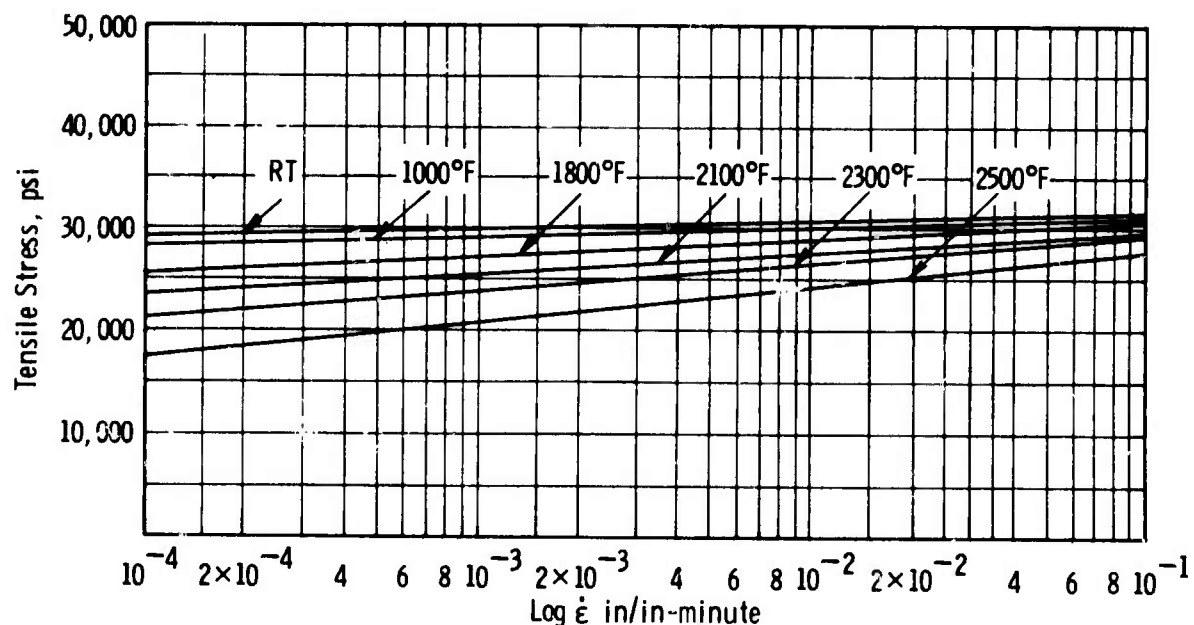


Figure 5.9 — Predicted Tensile Strength for Hot Pressed  $\text{Si}_3\text{N}_4$  vs Temperature and Strain Rate

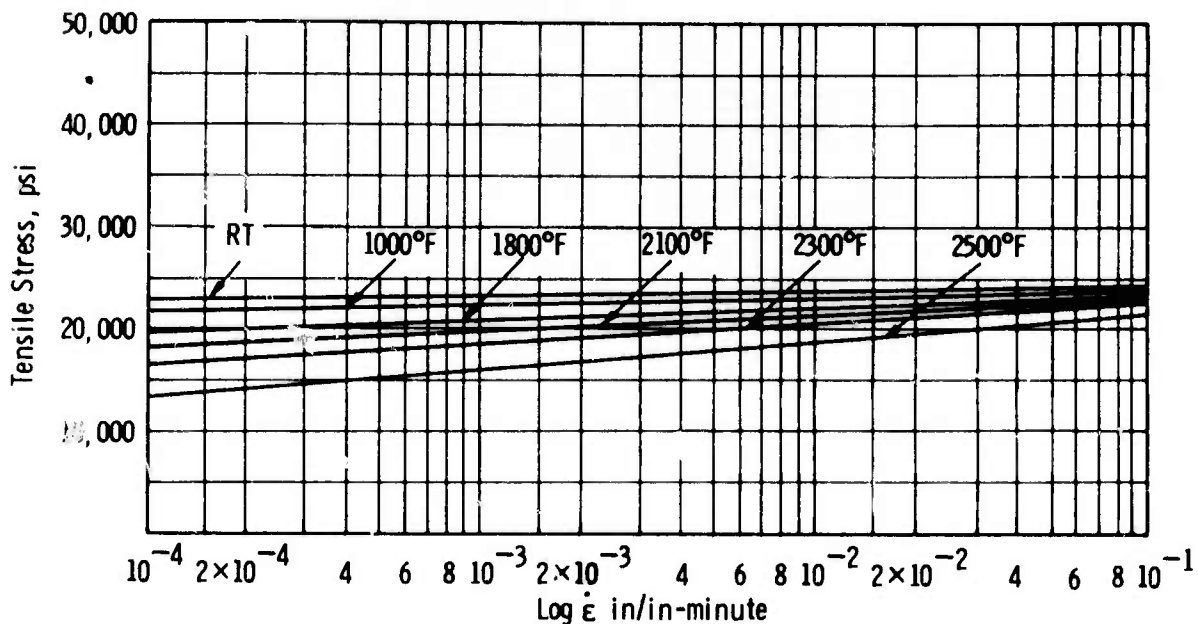


Figure 5.10 — Predicted Tensile Strength of Hot Pressed  $\text{Si}_3\text{N}_4$  vs Temperature and Strain Rate

Table 5.1  
Tensile Test Data for Silicon Nitride

Temperature °F	1800	2100	2300	2500
Strain Rate				
.01 in/in-min	43.0 ksi*			
.001 in/in-min	49.2 ksi	35.8 ksi	31.5 ksi	17.1 ksi
.00018 in/in-min	41.6 ksi*			

\*Indicates specimen was used for modulus determinations up to 2500°F where some damage may have occurred. Test will be repeated for 1800°F only.

For extremely brittle materials surface flaws control the strength and hence the Weibull integral is performed as a surface integral rather than a volume integral. At present the data indicate that a volume integral is appropriate, although polishing the sample surfaces and eliminating scratches perpendicular to the tension direction can markedly improve the strength. When larger samples are tested in air, a more complete analysis of tensile strength as a function of strain rate, volume, surface finish, and temperature will be made. The ultimate use of Weibull statistics is to predict safety factors for engineering use.

Preliminary modulus of elasticity data were obtained from the tensile tests. Strain was measured optically to 10 micro-inch accuracy using a Physitech Extensometer. The values range from  $44.5 \times 10^6$  psi at room temperature to  $11 \times 10^6$  psi at 2500°F as shown in Fig. 5.11.

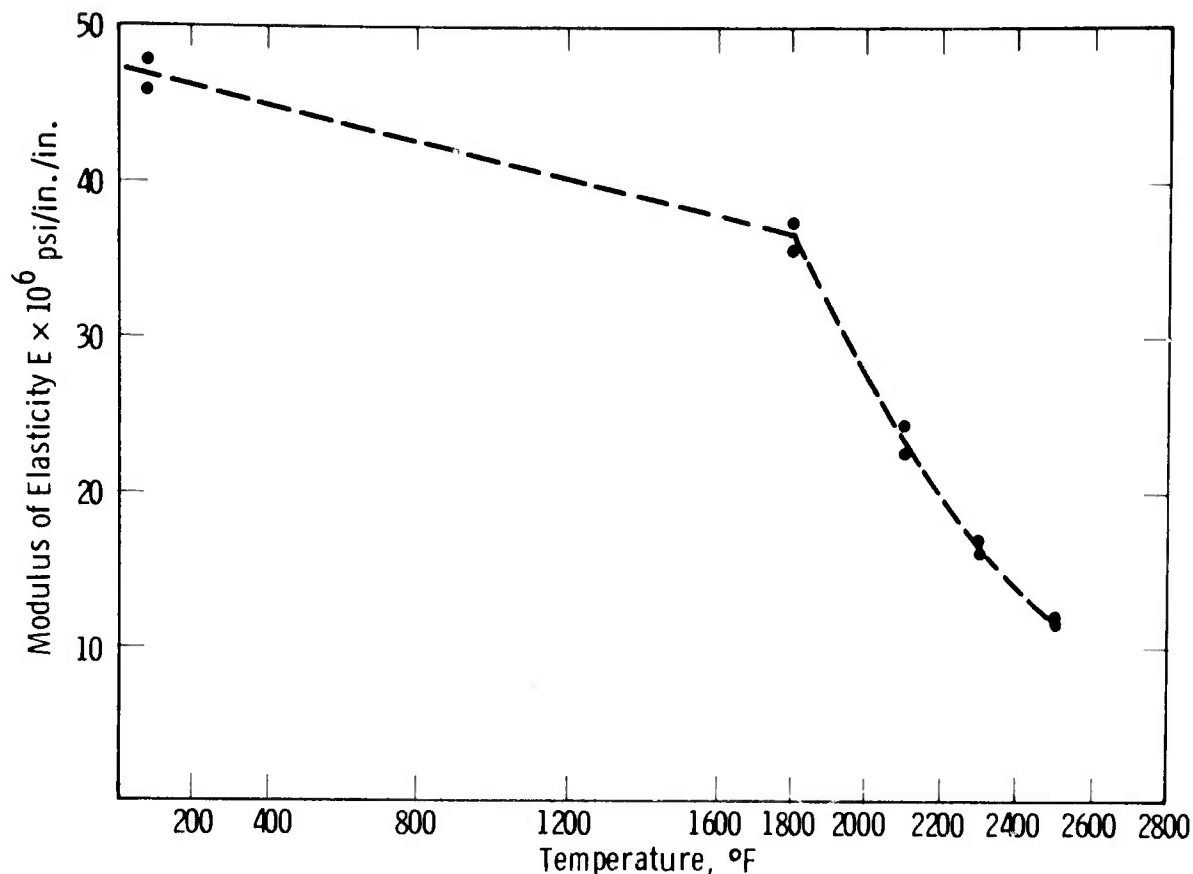


Figure 5.11 — Modulus of Elasticity of Hot Pressed Silicon Nitride  
vs Temperature (Inert Atmosphere)

### Stress Rupture

One specimen prepared from the HS-110 grade material was tested in air, at 1800°F and 20,000 psi. This particular specimen survived for 200 hrs, with final elongation of 0.16%. The steady state creep rate was  $3.5 \times 10^{-6}$ /hr.

A more systematic investigation of the creep behavior of  $\text{Si}_3\text{N}_4$  is being conducted on the HS-130 material. Cylindrical specimens, 2-3/4" long, with 1/4" gauge diameter and 1-3/4" gauge length (Fig. 5.12) were tested in a He atmosphere. Gripping is accomplished by the ball-and-socket arrangement, where all parts are made of graphite. The specimens are placed in an induction furnace capable of providing a uniform 3" hot zone at the maximum test temperature of 2500°F. The furnace and specimen assembly are placed in an Instron machine, where a constant load is maintained automatically. Specimen elongation is measured by an LVDT attached to the bottom ram on the machine. In all specimens tested, good agreement was obtained between the elongations measured on the machine and those measured from the fractured specimens.

A summary of the creep results on the first batch of specimens is given in Table 5.2. A typical creep curve, selected for the 10,000 psi, 2300°F test condition, is shown in Fig. 5.13. It is interesting to note that the curve displays the classical three stages of creep phenomenon.

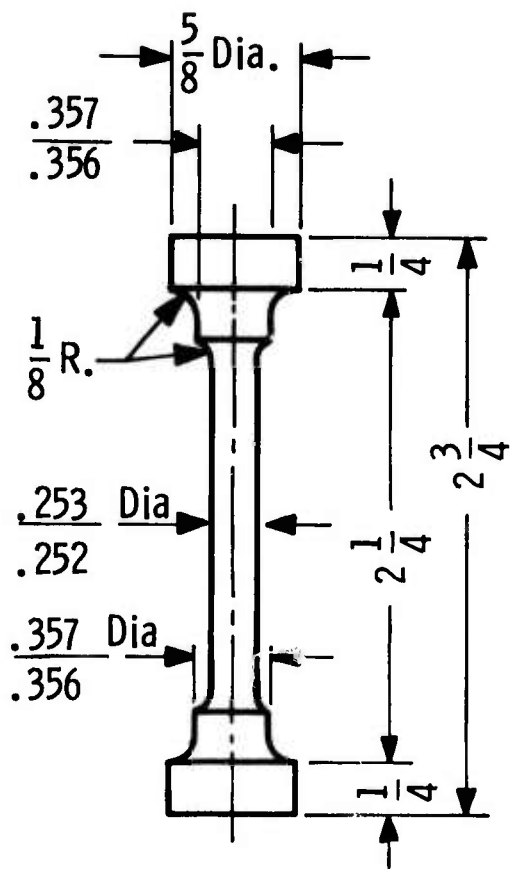


Figure 5.12 — Creep Specimen

TABLE 5.2

Creep Results, Helium Atmosphere, Specimens Machined From Norton Billet 011072B1

Sample #	Temperature °F	Stress 1000 psi	Time to Failure	Steady State Creep Rate	Elongation %
3	2500	15	0.8 min.	$3 \times 10^{-2}$	0.32
4	2500	10	24 hours	$2 \times 10^{-3}$	0.71
6	2300	10	129 hrs. (no failure)	$1.9 \times 10^{-5}$	1.30
11	2300	10	600 hrs.	$1.8 \times 10^{-5}$	0.58
7	2300	14	42.7 hrs.	$3.6 \times 10^{-5}$	0.51
8	2300	14	17.2 hrs.	$9.3 \times 10^{-5}$	0.53
9	2300	12	45.0 hrs.	$1.8 \times 10^{-5}$	0.46
10	2300	12	86.8 hrs.	$2.5 \times 10^{-5}$	—

The data are replotted in terms of stress-life time in Fig. 5.14. Also shown in this figure are stress-rupture data obtained from the Norton Company for specimens tested in a three-point bending mode, at 2200°F in air. The effect of the testing mode is quite apparent. It is also noteworthy that the slopes of the two curves are similar.

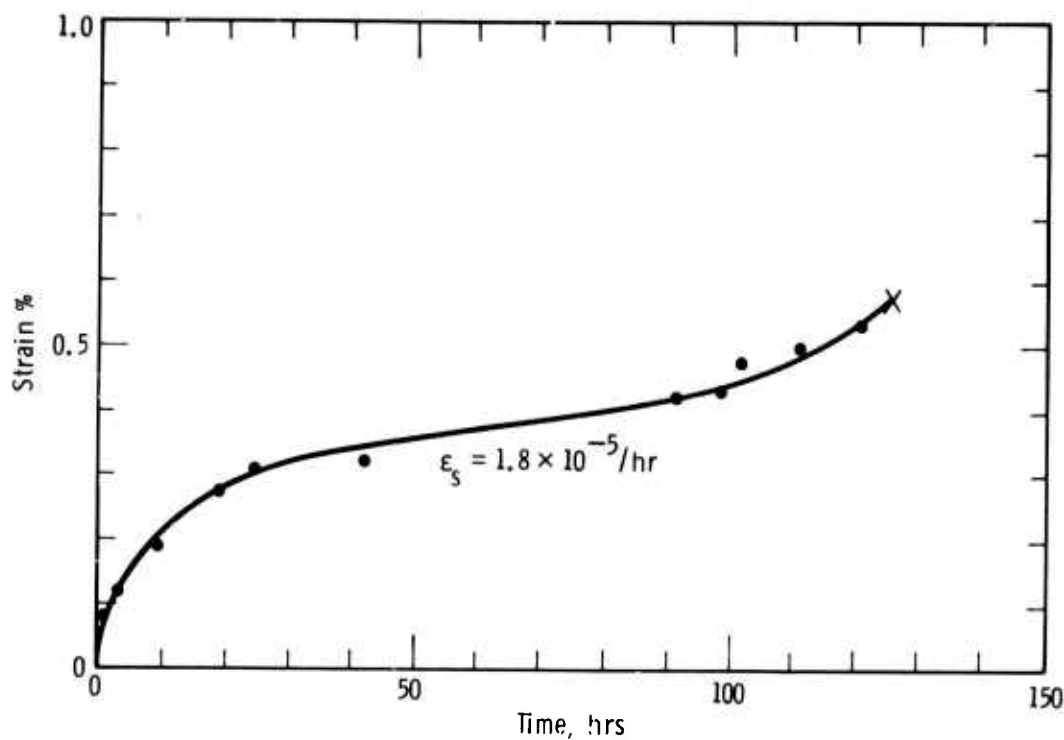


Figure 5.13 — Creep Curve, 10,000 psi,  $2300^{\circ}\text{F}$

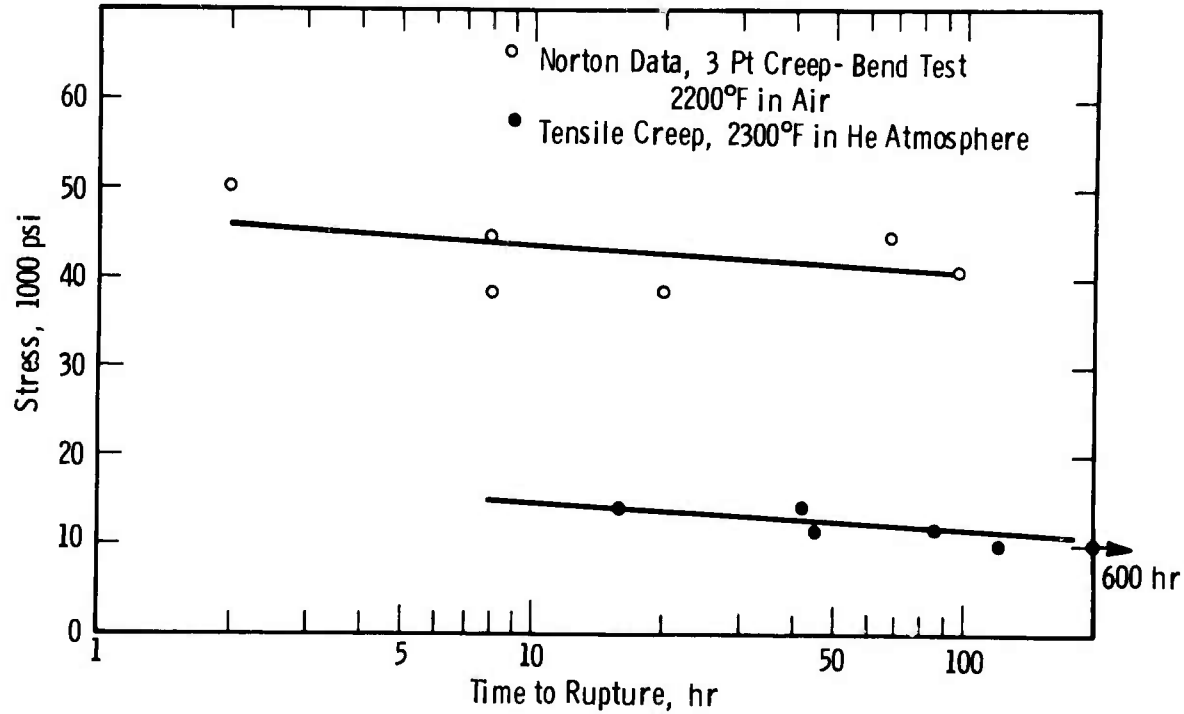


Figure 5.14 — Stress Rupture Properties of  $\text{Si}_3\text{N}_4$

The available data are not sufficient for mechanism analysis. However, when plotted in terms of steady state strain rate vs log stress (Fig. 5.15), the data indicate a low exponent in the relation  $\dot{\epsilon} = \sigma^n$ . An exponent of  $n < 2$  usually indicates a visco-elastic mechanism, i. e., a Nabarro-Herring diffusional creep or a grain boundary sliding. Preliminary transmission electron microscopy data indicate that grain boundary sliding may indeed be the rate controlling mechanism during creep deformation.

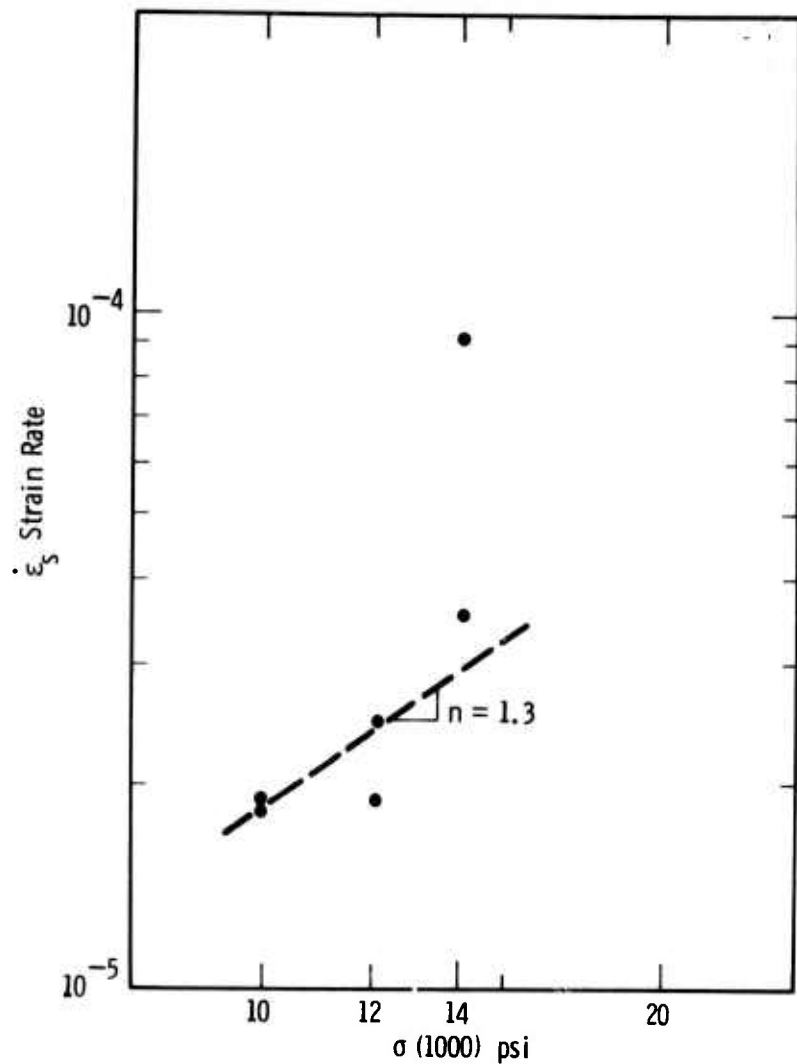


Figure 5.15 — Strain Rate vs Stress, 2300°F in Helium Atmosphere

### Flexural Testing

#### Hot-Pressed Silicon Nitride

The flexural strength of HS-130 hot-pressed silicon nitride was measured as a function of temperature. At temperatures  $> 1800^{\circ}\text{F}$ , the flexural strength was measured as a function of loading rate. Although most of these measurements were performed on the weak direction (parallel specimens), the strength of the strong direction (perpendicular specimens) was also investigated as a function of temperature.

The flexural strength was measured in four-point loading (distance between outer span = 0.875 in, inner span = 0.375 in) with a fixture made of hot-pressed silicon nitride. The approximate specimen dimensions were 0.125 x 0.250 x 1.25 inches. Four specimens were tested for each condition. All specimens were ground parallel to length on three sides (tensile and 2 adjacent side surfaces) with a 220 grit diamond wheel to insure a uniform surface finish. Except for one set of specimens, all strength measurements were conducted in air.

The majority of test specimens were machined from the first two  $1.3 \times 6.3 \times 6.3$  ineh billets of Norton HS-130 silicon nitride. A limited number of specimens were made from block #3. The strength of Norton HS-110 silicon nitride is reported for comparative purposes.

The strength of HS-130 silicon nitride is compared with HS-110 in Fig. 5.16, for the weak direction specimens tested at a cross head speed of 0.02 in/min.\* The strengths of both materials are similar at room temperature. The significant difference is exhibited at elevated temperatures where strength degradation occurs at  $\sim 1800^{\circ}\text{F}$  and  $\sim 2200^{\circ}\text{F}$  in HS-110 and HS-130, respectively. The change may be attributed to the Ca impurity concentration as discussed in Section 5.2.3.

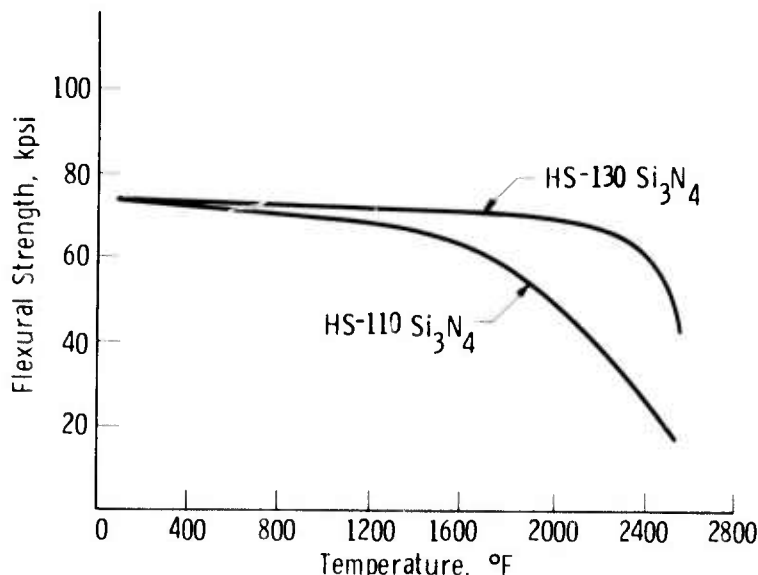


Figure 5.16 — Strength vs Temperature for Two Forms of  $\text{Si}_3\text{N}_4$  (HS-110 and HS-130) Fabricated by Norton Co.

The anisotropy in the strength of hot pressed silicon nitride is apparent in Fig. 5.17 where strength in both directions of HS-130 material is plotted as a function of temperature. A difference of 25% is maintained to  $\sim 2200^{\circ}\text{F}$ , the threshold of strength degradation.

The strain rate sensitivity of silicon nitride is shown in Fig. 5.18. At temperatures above  $1800^{\circ}\text{F}$  the flexural strength varies directly with loading rate.

Since the high-temperature strength of hot-pressed silicon nitride may be a limiting factor in the engineering use of this material, experiments were performed to determine the phenomenon responsible for its high temperature strength behavior. At temperatures  $< 2300^{\circ}\text{F}$ , the load-deflection (or stress-strain) curves were linear (or elastic) to fracture. At temperatures  $> 2300^{\circ}\text{F}$  significant deflection was observed just prior to fracture. The amount of deflec-

\*A cross head rate of 0.02 in/min corresponds to a loading rate of approximately  $7.2 \times 10^5$  psi/min and a strain rate of  $1.61 \times 10^{-6}$  in/in/min.

tion increased with decreasing strain rate and increasing impurity levels in the material tested, i.e., it was much more significant in the HS-110 material relative to the HS-130 material.

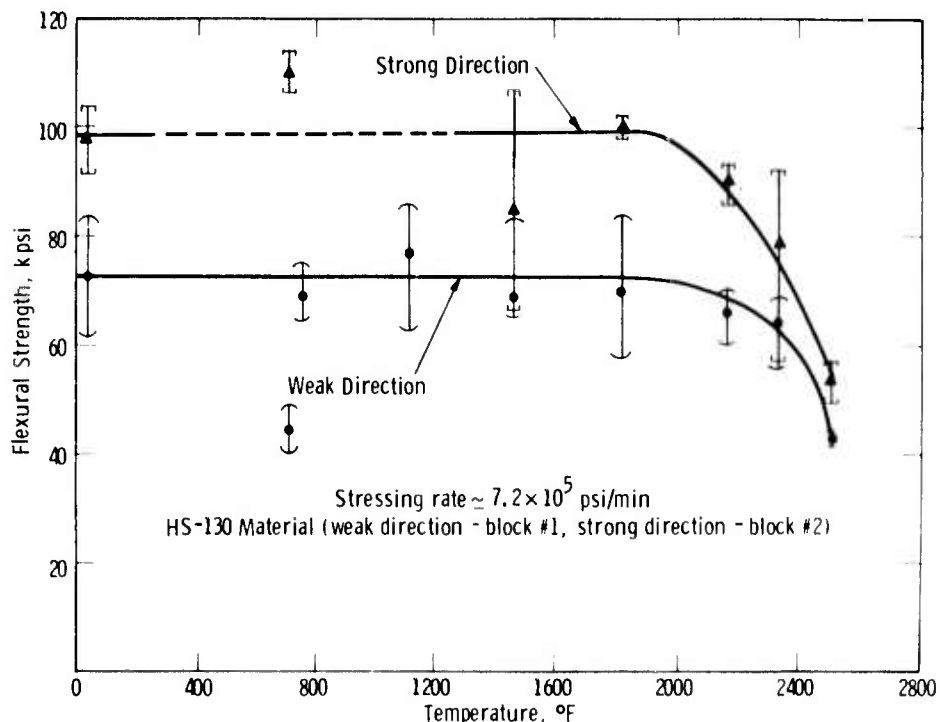


Figure 5.17 – Strength vs Temperature for the Weak and Strong Directions of HS-130  $\text{Si}_3\text{N}_4$

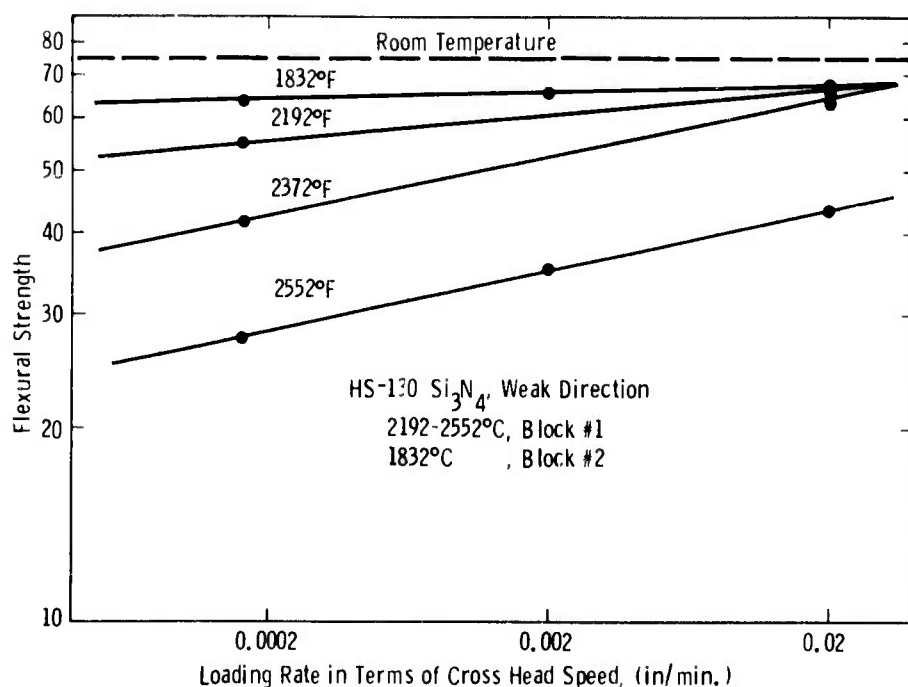


Figure 5.18 – Log Plot of Strength vs Loading Rate at Different Temperatures for HS-130  $\text{Si}_3\text{N}_4$

At first, the non-linear stress-strain behavior was attributed to some sort of plastic yielding phenomenon, but examination of the fracture surfaces disclosed a rough area the shape of a crack adjacent to the tensile surfaces of the specimens (Fig. 5.19). Additional experiments were performed to correlate this unusual fracture surface topography with the non-linear stress-strain behavior.

Specimens were loaded into the "plastic" range, then unloaded prior to failure. Examination of the tensile surfaces revealed lines of oxidation resembling surface cracks which had not propagated completely through the specimen. An oil dye penetrant was used to confirm the presence of a surface crack in one specimen of HS-110  $\text{Si}_3\text{N}_4$ . Since slow crack growth occurs prior to fracture, the non-linear portion of the stress-strain curve may be explained as a change of the specimen's compliance as the crack grows.

Static fatigue (stress, corrosion, propagation of cracks due to atom transport, etc.) in brittle materials is characterized by slow crack propagation prior to fracture and strength dependence on loading rate. At high loading rates crack growth is minimal prior to catastrophic fracture. The result is high strength. Conversely, at low loading rates, crack growth is substantial and low strength results. The data indicated that the high temperature strength of hot-pressed silicon nitride is governed by a static fatigue mechanism and that its susceptibility to static fatigue increases with temperature above 1800°F.

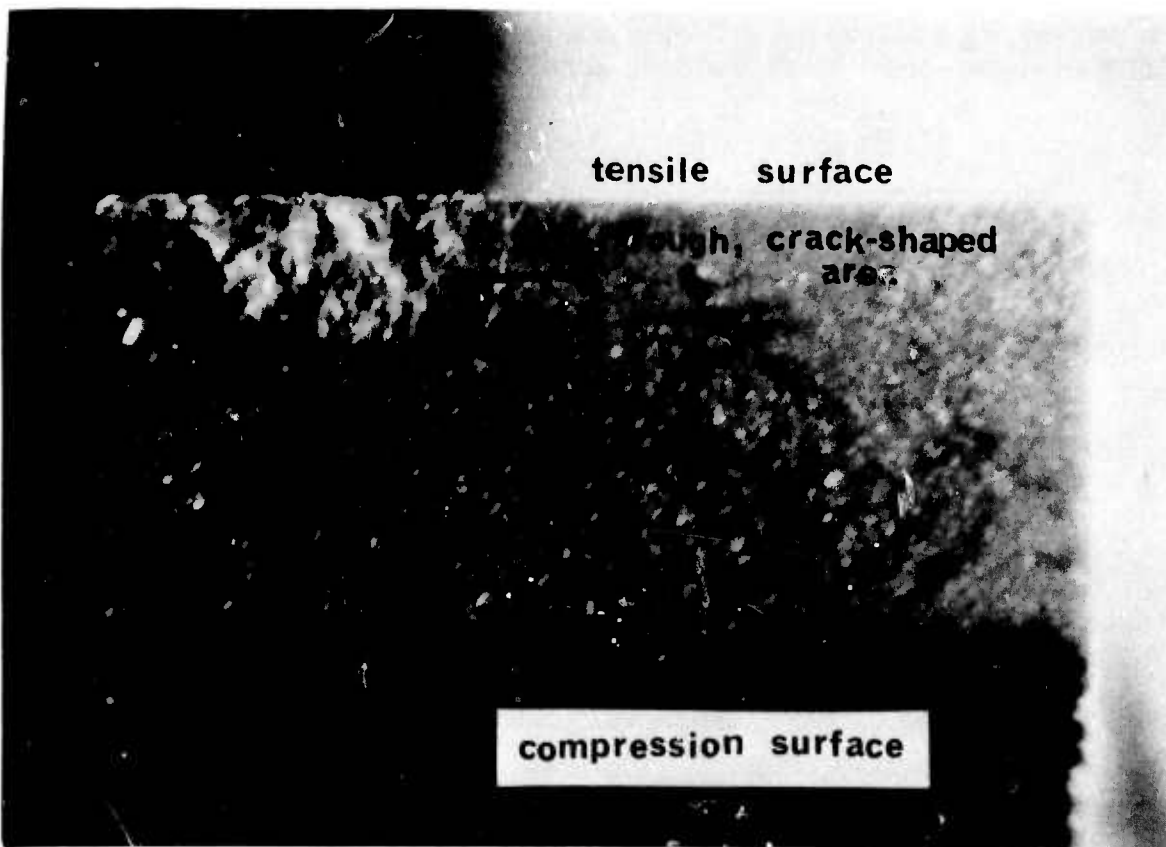


Figure 5.19 — Fracture Surface Topography of HS-130  $\text{Si}_3\text{N}_4$  Fractured at 2550°F. Note Rough, Crack-Shaped Surface Area Adjacent to the Tensile Surface (Approximate Fracture Area Dimensions: 0.125 x 0.250 Inches)

## Silicon Carbide

The flexural strength of hot pressed silicon carbide recently received from the Norton Company is now under investigation. Specimens were prepared and tested in the same manner as that discussed for silicon nitride. The bulk of the  $0.125 \times 0.250 \times 2$  inch flexural specimens were prepared from  $0.5 \times 3.0 \times 3.0$  inch blocks. A number of finished flexural specimens were also purchased from Norton to compare the effects of machining.

The average strength of Norton prepared specimens (320 grit diamond ground) tested at Westinghouse in 4-point bending was  $100,900 \text{ psi} \pm 12\%$  psi (4 tests) as compared to  $72,000 \pm 13\%$  (4 tests) for Westinghouse prepared specimens (220 grit diamond ground). These preliminary data indicated that the strength of silicon carbide is sensitive to surface finish.

The flexural strength of silicon carbide as a function of temperature is presented in Fig. 5.20. Too few tests have been performed to comment upon the minimum strength occurring at  $\sim 800^{\circ}\text{F}$ . The decrease in strength observed at temperatures above  $1800^{\circ}\text{F}$  is significant.

No strain rate sensitivity was detected in single specimen tests at  $2300^{\circ}\text{F}$  in the range  $0.2 - 0.0002$  in/min cross head speed.

Weibull statistical parameters were determined at  $2372^{\circ}\text{F}$  at a cross head rate of 0.002 in/min for 20 specimens. A Weibull modulus,  $m = 12.6$  with normal stress,  $\sigma_0 = 33,200$  psi indicates that the silicon carbide tested is somewhat less volume sensitive than silicon nitride.

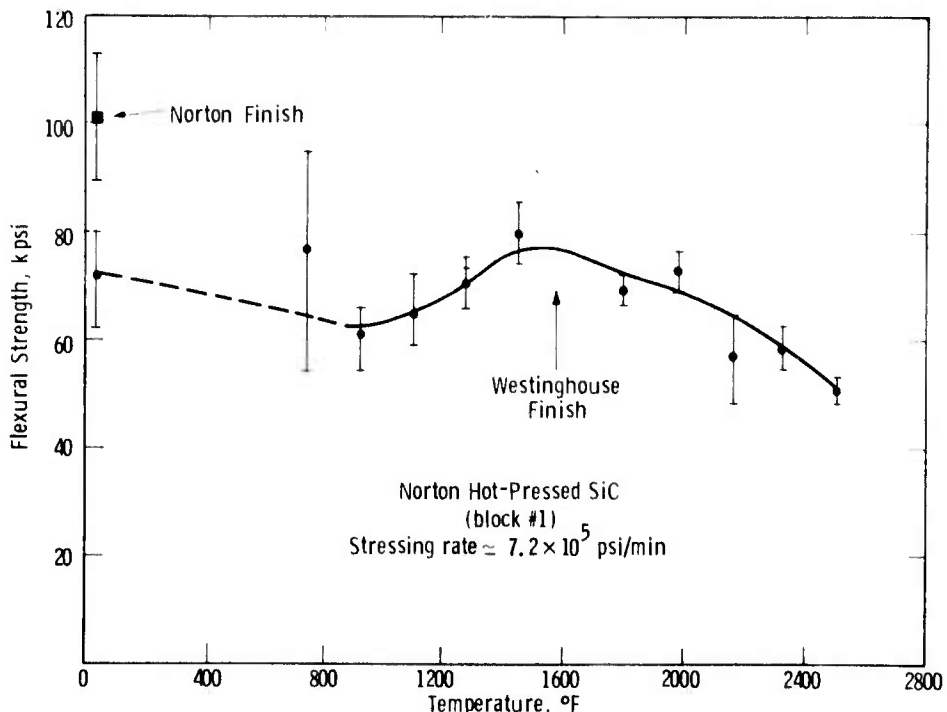


Figure 5.20 — Flexural Strength vs Temperature for Hot-Pressed SiC Fabricated by Norton Company

### CVD Silicon Carbide

The flexural strength of Energy Research Corporation chemical vapor deposited silicon carbide was determined under conditions of 4-point loading (outer span = 0.875 in, inner span = 0.375 in) from room temperature to 2500°F. Specimen size was nominally 0.125 x 0.250 x 1.125 inches, and most specimens were tested at a cross head strain rate of 0.001 in/in/min. Although a few tests were made at strain rates of 0.01 and 0.0005 in/in/min, a strain rate sensitivity could not be detected because of the large scatter in the data.

The results of testing a total of 28 specimens of this material are shown in Fig. 5.21. Even though the scatter in these data is very great, the strength of the material appears to increase with temperature to an impressive average value of 75,000 psi at temperatures above 1800°F.

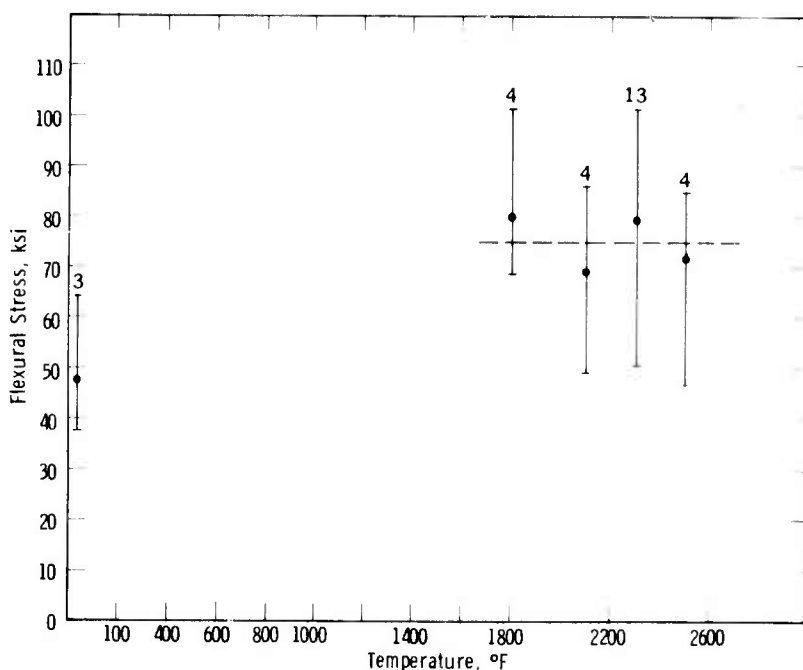


Figure 5.21 — Flexural Failure Stress of Energy Research Chemical Vapor Deposition Silicon Carbide as a Function of Temperature. Numbers indicate the number of samples tested.

### Shear Testing of Silicon Nitride

Preliminary shear modulus and fracture strength measurements were made at room temperature on one sample HS-130 silicon nitride at a strain rate of  $8 \times 10^{-4}$  in/in/minute. A shear modulus of  $18 \times 10^6$  psi and fracture stress of 68,600 psi were determined. The specimen was loaded to about 60,000 psi then unloaded and reloaded to failure. No hysteresis was observed. As samples became available, high temperature tests will be conducted..

### Fatigue Testing

The fatigue characteristics of Norton HS-110 and HS-130 silicon nitride were determined using the high cycle fatigue machine shown schematically in Fig. 5.22. A flat specimen 5-1/2 in long x 1" wide is clamped at one end,

while load is applied at the other end by an eccentric driver rotating at 1800 rpm. The maximum outer fiber tensile or compressive stress along the center line of the gauge section is obtained by applying the classical cantilever-beam formula

$$\sigma = \frac{6P l}{bh^2}$$

where  $P$  is the applied load,  $l$  is the distance from the load end to the center of the gauge section,  $b$  is the minimal width of the specimen at the gauge section and  $h$  is the specimen thickness. The glo-bar furnace, which is open to the atmosphere, is capable of providing stable temperatures up to 2350°F with variations of no more than  $\pm 18^{\circ}\text{F}$  along the gauge section. An optical pyrometer placed above the furnace is connected to a trigger mechanism that would shut off the test if a sudden temperature change of more than  $\pm 45^{\circ}\text{F}$  were to occur. A microswitch placed inside the machine terminates the test at the moment of a specimen failure.

Fracture surfaces were examined by scanning electron microscopy (SEM) and replica transmission microscopy, using standard two-stage plastic-carbon replication techniques. The flat surfaces near the fractured edge were examined by replica and thin foil transmission electron microscopy. Grain morphology was revealed by etching the specimen at 1380°F for 1 minute in a molten salt consisting of a mixture of 95 parts  $\text{K}_2\text{CO}_3$  and 15 parts  $\text{NaF}$ .

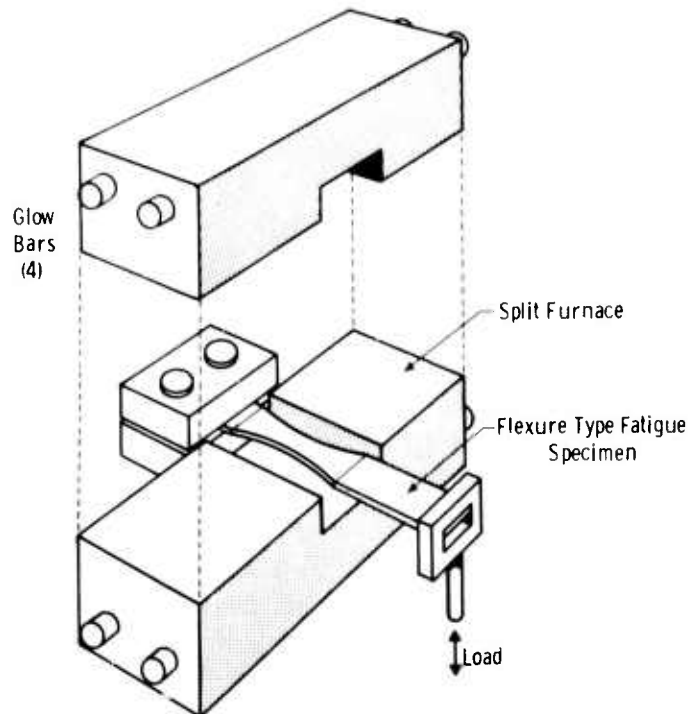


Figure 5.22 — Fatigue Test

The results of testing at 482, 1800, 2200 and 2350°F are shown in Figs. 5.23 and 5.24 for HS-130 and HS-110 materials respectively. The dispersion of results around the best fit straight line is very small. The few data points that fell far off the curves (marked a and b) were associated with large inclusions found on the fractured surfaces.

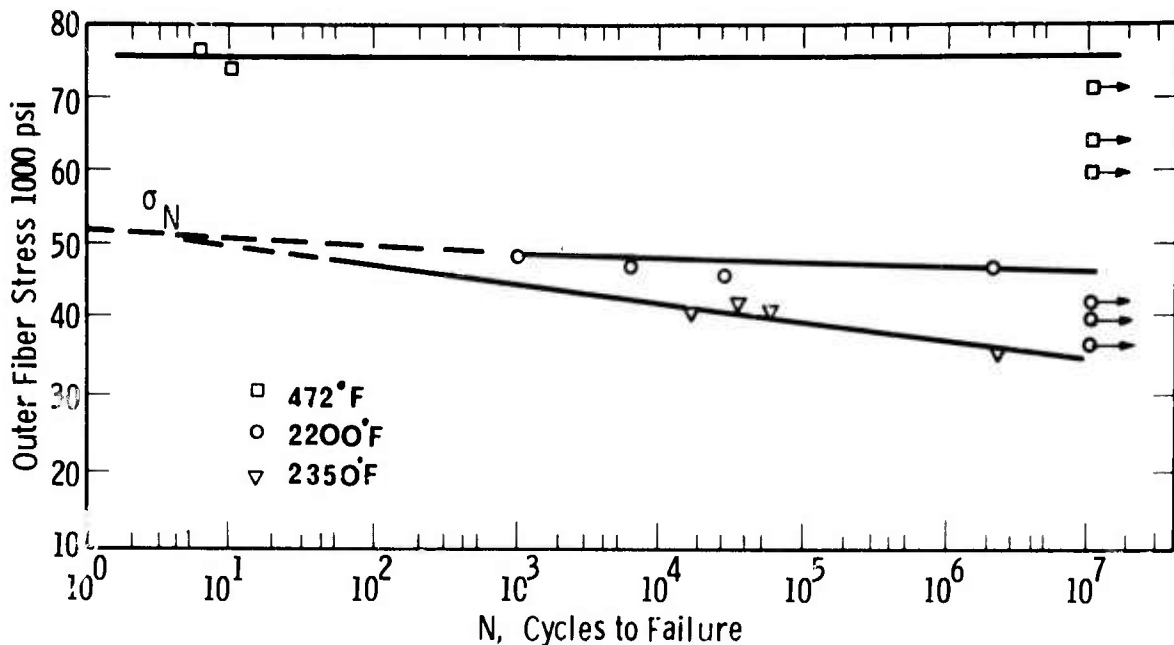


Figure 5.23 — Cyclic Fatigue Behavior of Norton HS-130 Hot Pressed  $\text{Si}_3\text{N}_4$  at 1800 cpm

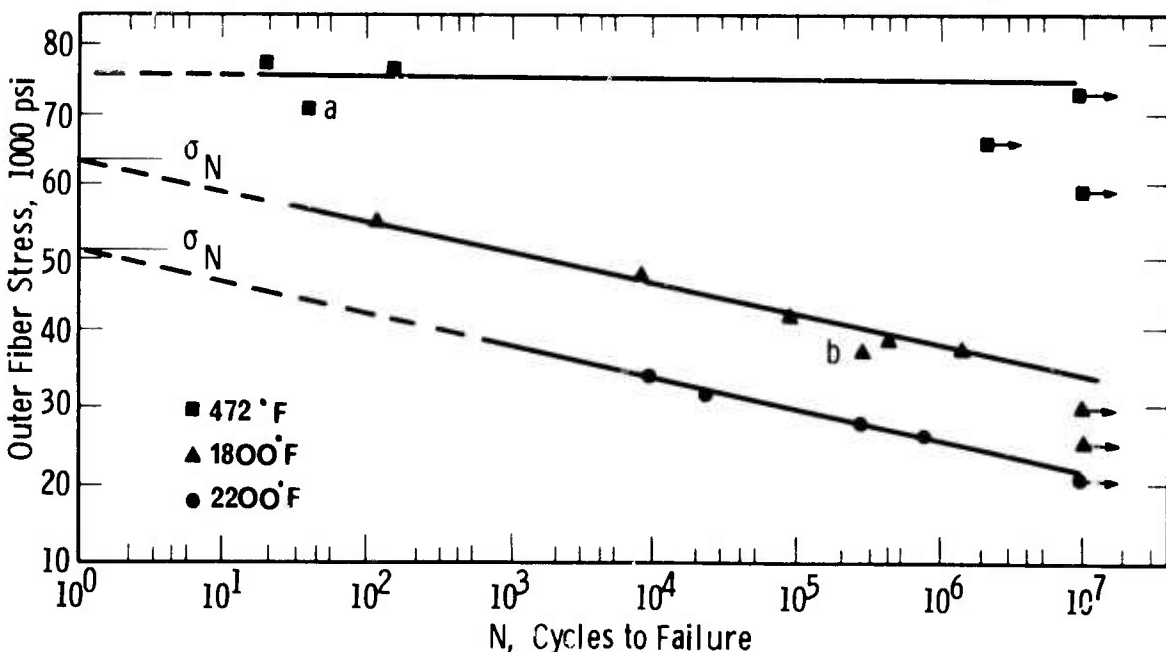


Figure 5.24 — Cyclic Fatigue Behavior of Norton HS-110 Hot Pressed  $\text{Si}_3\text{N}_4$  at 1800 cpm

The straight line extrapolations of the 2200 and 2350°F data to one cycle converge at a stress level of 51,000 psi. This is interpreted to indicate that the intrinsic, time independent strengths are the same. The higher purity material, HS-130, does not exhibit time dependent fatigue behavior at 2200°F. Neither material displays the phenomenon at 482°F.

Typical fracture surfaces of specimens fatigued at 482°F and 2200°F are shown in Fig. 5.25a and Fig. 5.25b respectively. The sharp facets and the

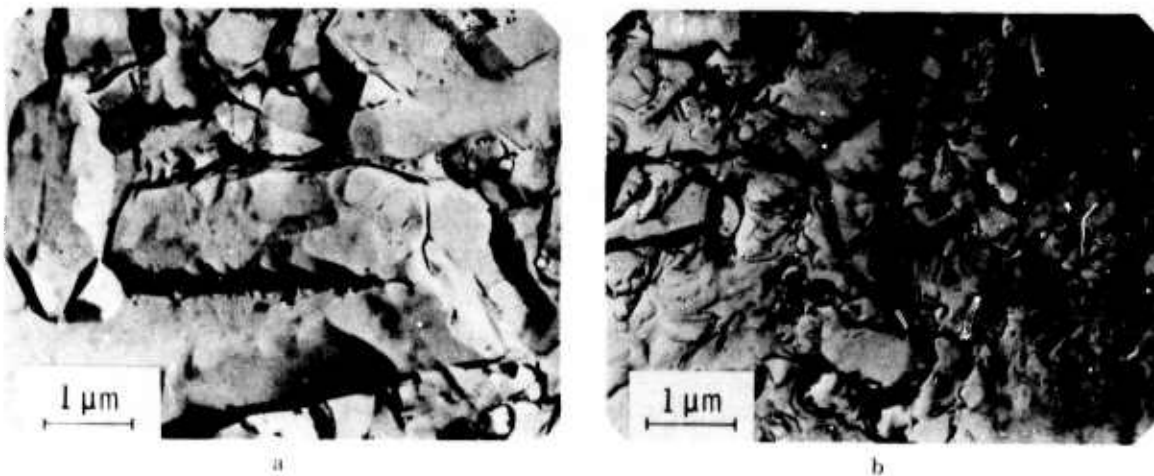


Figure 5.25 — Fracture Surfaces, Fatigue Specimen, HS-110 Material  
a)  $472^{\circ}\text{F}$  b)  $2200^{\circ}\text{F}$

numerous secondary cracks (dark lines on the replica) indicate that, at both temperatures, failure occurs by intergranular cracking. The less sharp appearance of Fig. 5.25b is due to a thin layer of oxide that must have formed on the newly fractured surface during the few minutes it took to remove the specimen from the furnace. Similar features were observed on the fractured surfaces of specimens tested at  $1800^{\circ}\text{F}$  (HS-110) and  $2350^{\circ}\text{F}$  (HS-130).

Dislocation structures near the outermost stressed surfaces of specimens tested at  $1800$  and  $2200^{\circ}\text{F}$  are shown in Figs. 5.26a and 5.26b respectively. It should be emphasized that the features shown in these two micrographs represent selected areas of highly localized deformation. The majority of the grains showed no evidence of a build up of dislocations over the original low density, typical of the as-received material (see Fig. 5.27a). Helices and stacking faults are seen in Fig. 5.26a, center and top right respectively. A high density of tangled dislocations are shown in Fig. 5.26b. The helical dislocations and the tangles are not found in the as-received material and must have formed as a result of the fatigue deformation. Similar observations were recently reported (6) on deformed reaction sintered  $\text{Si}_3\text{N}_4$ .

A different mode of deformation was observed in specimens fatigued at  $2350^{\circ}\text{F}$ . Although evidence of localized dislocation motion was found, the more prominent features are shown in Fig. 5.26c. The foil for this particular micrograph was cut from the interior of the specimen in an area of high stress concentration near a large inclusion, Fig. 5.26d, where failure must have originated.

Triple point cavitations and grain boundary separations are indicative of grain boundary sliding as shown, for example, in alumina. (7)

A clear cut case cannot be made for the application of an elastic stress corrosion model for the fatigue behavior of  $\text{Si}_3\text{N}_4$  at high temperatures. Although massive dislocation motion is not likely to occur in this material at temperatures below  $3100^{\circ}\text{F}$ , (8) the microstructures shown in Fig. 5.26 indicate that one cannot rule out localized contributions from either dislocation motion, grain boundary sliding, or diffusional creep. (9) The latter viscoelastic mechanisms are probable since the high strength and high density of  $\text{Si}_3\text{N}_4$  are obtained by hot pressing in the presence of a liquid phase.

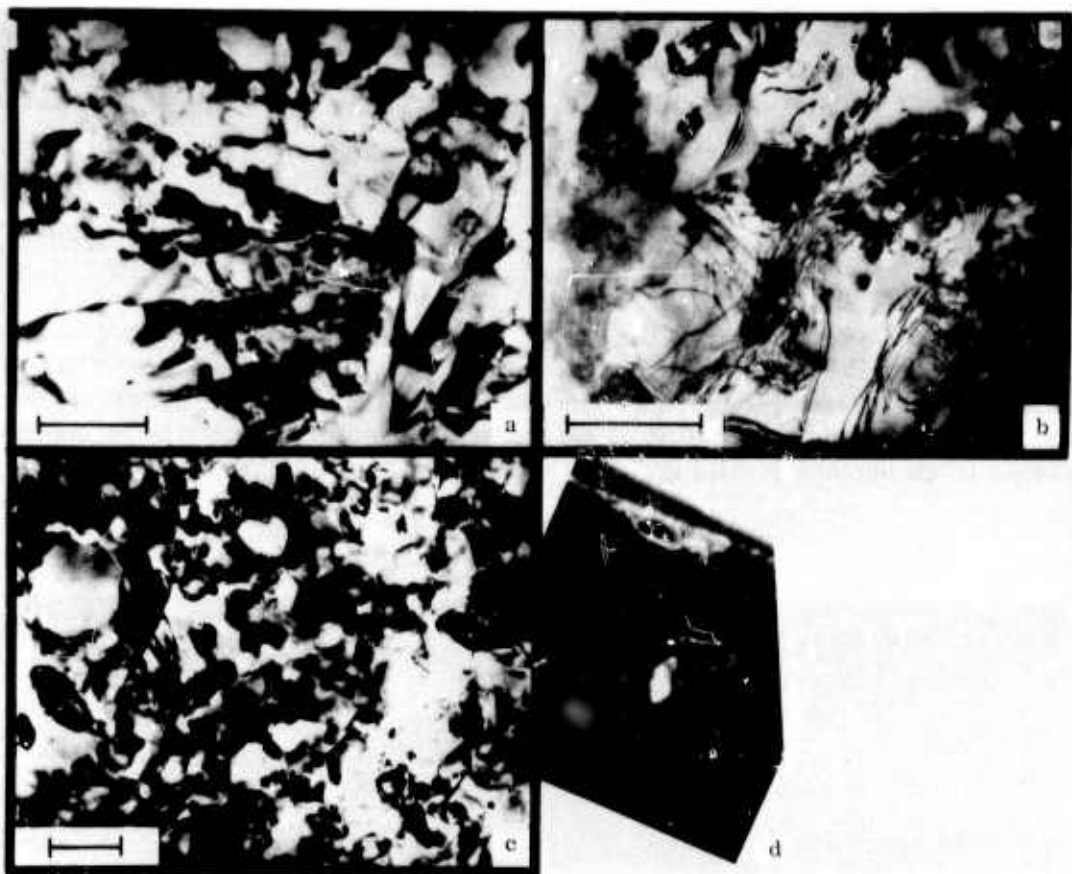


Figure 5.26 — Thin Foil Transmission Micrographs of Fatigue Specimens .1 $\mu$ m Scale Bars

- a. Helices and stacking faults. Specimen tested at 1800°F and 20,000 psi. HS-110 material.
- b. Localized deformation in a large grain. Specimen tested at 2200°F and 25,000 psi. HS-110 material.
- c. Grain boundary sliding in specimen tested at 2350°F, and 40,000 psi. HS-130 material.
- d. Failure which originated at an inclusion in c.

Tensile creep and bend creep tests were conducted to examine these possibilities. It was considered necessary to introduce the static test, since viscoelastic mechanisms are rate sensitive, and may be affected by the high rates of straining realized in the cyclic fatigue test.

A flat specimen, 2" long, 1/4" wide and 1/8" thick, prepared from the HS-110  $\text{Si}_3\text{N}_4$  was placed in a four-point bend fixture and subjected to a static load of 38,000 psi at 2200°F for 4 hours. A permanent set corresponding to a plastic strain of 0.001 on the outer surface was measured. Thin foils were prepared from both the tensile and the compressive surfaces, and the typical microstructures are shown in Figs. 5.27c and 5.27d. Also shown in Fig. 5.27b is a micrograph taken from a foil prepared from the tensile-creep specimen. This particular specimen was 6" long, with a 1/4" diameter and 1" long gauge section. It failed at 1800°F under 20,000 psi stress after plastic strain of 0.0025 inches had occurred. Figure 5.27b shows that limited dislocation motions had occurred also during creep deformation as evidenced by the helices

and the dislocation loops present in the large grain. Also note triple point cavitation and grain boundary separations. The latter are quite dominant in the bend creep specimen, and quite significantly, occur on both the tensile (Fig. 5.27c) and compressive (Fig. 5.27d) surfaces.

Applying the formula (Ref. 10)

$$\epsilon = \rho bx \quad (1)$$

where  $\epsilon$  is the plastic strain;  $\rho$  the dislocation density;  $b$  the Burger's vector and  $x$  the average distance a dislocation moved, the dislocation's contribution to the measured plastic strain was found to be less than  $10^{-5}$ . Therefore, it seems that the major contribution to the permanent deformation during creep is derived from boundary sliding.

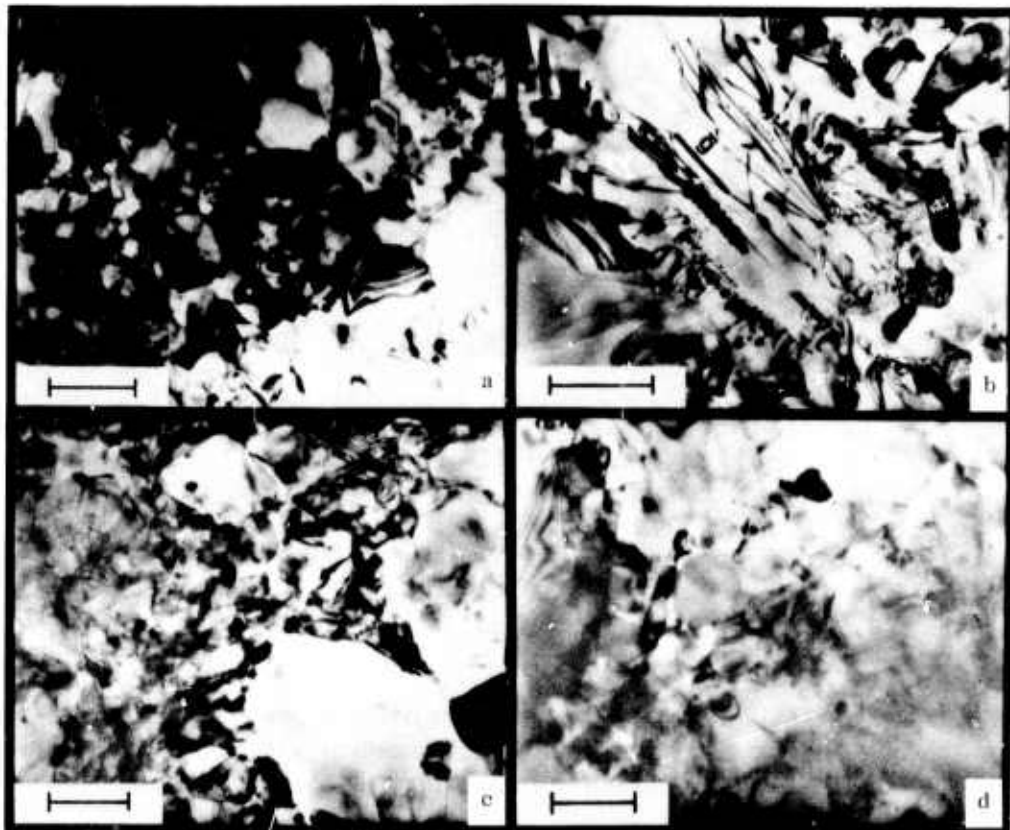


Figure 5.27 - Thin Foil Transmission Micrographs of Creep Specimen, HS-110 Material .1 $\mu$  Scale Bars

- a. As received, not tested material, for comparison
- b. Dislocation loops and helices occasionally observed in large grains. Tensile creep specimen, 1800°F, 20,000 psi
- c. Tensile surface of a bend-creep specimen. 4 hours at 2200°F, 38,000 psi. Note grain boundary sliding and separation
- d. Same specimen as in c. Compressive surface. Note triple-point cavitations and boundary sliding.

Boundary sliding will probably be inhibited in the cyclic fatigue tests, where the average strain rate was 3 in/in/min., or about six orders of magnitude higher than the average strain rate in the creep tests. This is certainly the case for temperatures up to 2200°F.

Hillig and Charles (11) considered the fatigue failure of a brittle material as an elastic medium. The time dependent failure of the material is attributed to a slow growth of pre-existing flaws as a result of a corrosion process under load. Charles and Shaw (12) showed that the local rate of growth of the flaw can be expressed as:

$$V = V_0 \exp - [Q - V^* \sigma + B] / RT \quad (2)$$

where  $Q$  is the activation energy of the process,  $V^*$  is the activation volume,  $\sigma$  the applied stress and  $B$  is related to the geometry of the crack tip. Developing Eq. (2) further, Charles and Shaw obtained

$$\frac{d(\sigma/\sigma_N)}{d \ln t} = - \frac{RT}{V^* \sigma_{th}} \quad (3)$$

where the left hand side of Eq. (3) is the slope of the line in a plot of  $\sigma/\sigma_N$  as a function of life time,  $\sigma$  is the applied stress for a given fatigue test,  $t$  is the time to failure,  $\sigma_N$  and  $\sigma_{th}$  are the time dependent and the theoretical strengths of the material, respectively.

The fatigue data of Fig. 5.24 is replotted in terms of  $\sigma/\sigma_N$  as a function of life time in Fig. 5.28. The time independent strength,  $\sigma_N$ , for the particular

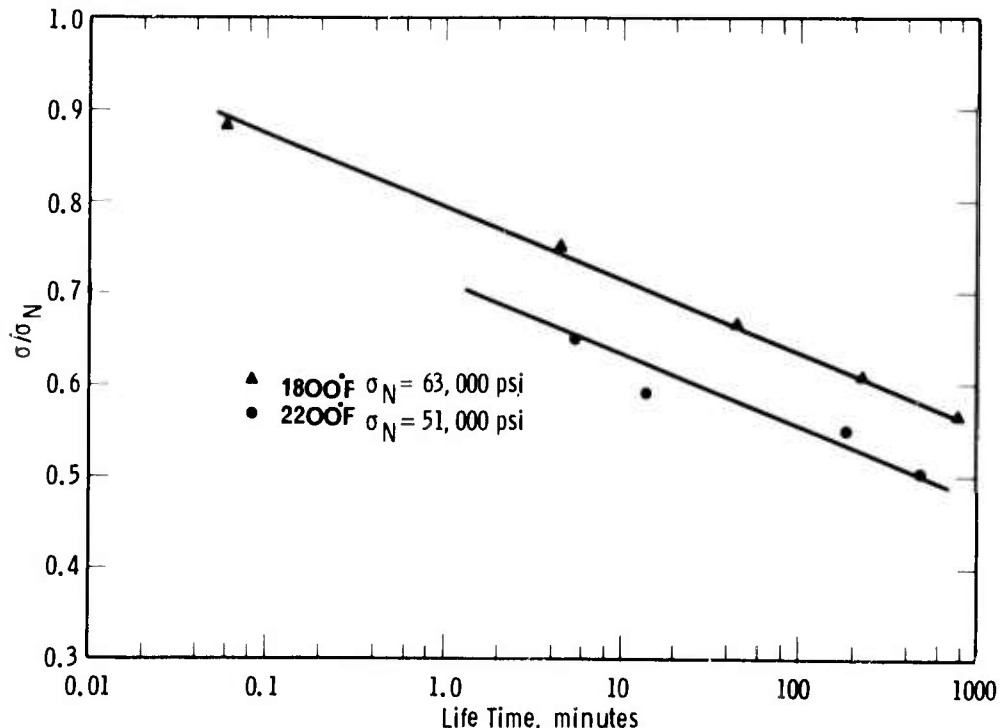


Figure 5.28 — Normalized Stress as a Function of Life Time HS-110 Grade  $\text{Si}_3\text{N}_4$

mode of bending employed in the tests, was taken as the extrapolated value of  $\sigma$  at one cycle. At  $1800^{\circ}\text{F}$ ,  $\sigma_N = 63,000$  psi and at  $2200^{\circ}\text{F}$ ,  $\sigma_N = 51,000$  psi.

Taking  $\sigma_{\text{th}} = E/5$  we obtain  $9 \times 10^6$  psi for the theoretical strength of  $\text{Si}_3\text{N}_4$ . From Fig. 5.28 we measure  $d(\sigma/\sigma_N)/d\ln t = -0.08$ . Inserting the appropriate values into Eq. (3) we obtain for the activation volume:

$$V^* (1800^{\circ}\text{F}) \approx 4.6 \text{ cc/mole}$$

$$V^* (2200^{\circ}\text{F}) \approx 5.5 \text{ cc/mole.}$$

These results compare favorably with the value of 4.0 cc/mole which is the activation volume for alkali metal ion diffusion in silicate glasses. (12)

The corrosion results, Figs. 5.29 and 5.30 indicate that diffusion of Ca and Mg occurs, forming magnesium-calcium-silicates on the surface which have much lower melting points than pure silicates. (13) It is quite plausible that in the absence of a plastic mechanism, the lifetime of a fatigue specimen is controlled by the slow crack growth that occurs as a result of the formation of low melting glasses, through a corrosion mechanism in air.

Using Eq. (2) it is possible to obtain an estimate of the activation energy from Fig. 5.28. If we assume that the term B in Eq. (2) is independent of stress and temperature and note that  $V^*\sigma$  is less than 0.5 kcal/mole we obtain:

$$Q \approx \frac{R \Delta \ln t}{\Delta \frac{1}{T}} \quad (4)$$

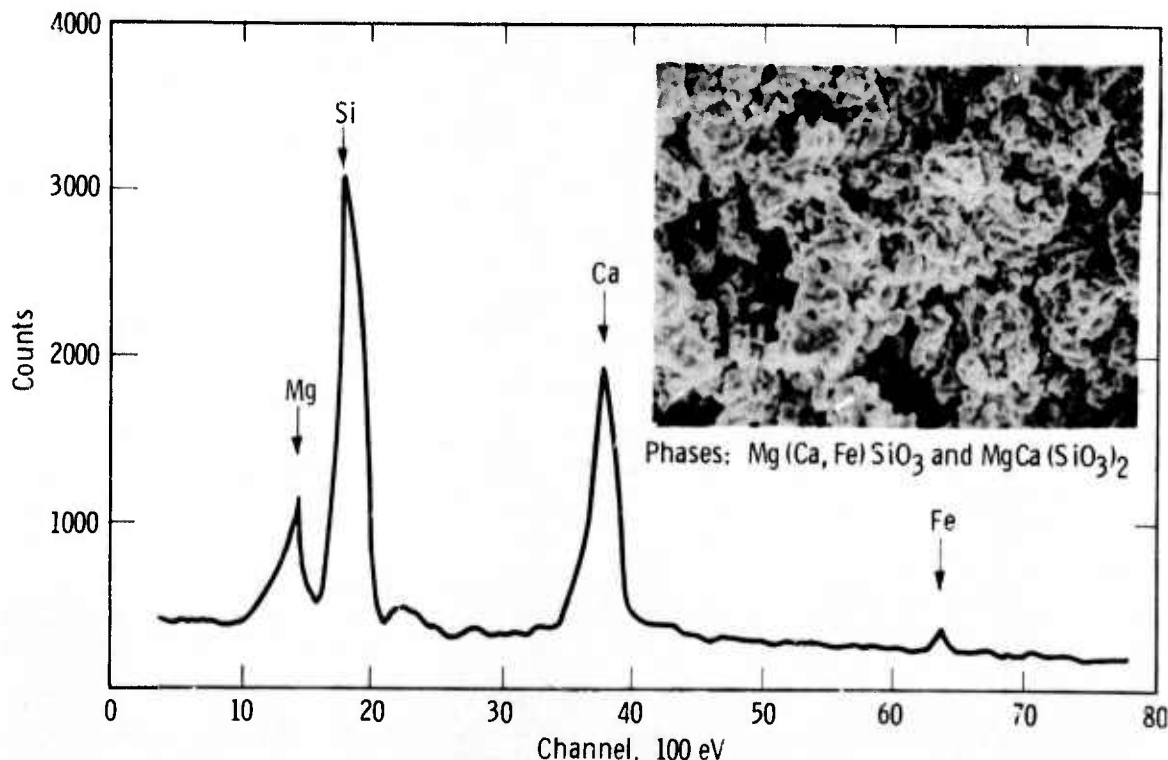


Figure 5.29 — Non-Dispersive X-Ray Analysis of Corrosion Layer, HS-110 Material, 8 Hours at  $2200^{\circ}\text{F}$  in Air

For any given value of  $\sigma / \sigma_N$ ,  $Q \approx 65$  kcal/mole is obtained for the activation energy of the corrosion process. This value compares with 89.5 kcal/mole obtained from studies of the kinetics of oxidation of hot pressed  $\text{Si}_3\text{N}_4$ .

Finally, the time independent fatigue behavior of HS-130 material at  $2200^{\circ}\text{F}$  is noted again (Fig. 5.23). The rate of oxidation of this material is lower by more than an order of magnitude compared to the less pure HS-110 material. Hillig and Charles (11) have shown that conditions of stress corrosion rate may exist, under which the sharpening of the flaws by stress corrosion may just balance the rounding effect of the stress concentration at the flaw tip. Under such conditions, slow crack propagation will not occur, and a time-dependent fatigue behavior will not be observed. It is evident that at room temperature neither oxidation nor plastic deformation occur and therefore no time dependent fatigue behavior is observed in HS-130 silicon nitride.

#### Thermal Property Testing

The thermal properties of Norton HS-130 silicon nitride are being measured by the Battelle Memorial Institute.

Thermal expansion is measured directly by tracking the relative displacement of fiducial marks on the silicon nitride specimens with telemicroscopes fitted with filar eye pieces. The apparatus is illustrated schematically in Fig. 5.31. Suitably marked specimens are supported within a tube furnace which is enclosed in an insulated vacuum/atmosphere chamber. Dilation on heating or cooling is tracked manually with the microscopes. Specimen temperature is measured by either a thermocouple or an optical pyrometer. Dilations of the order of  $7 \times 10^{-6}$  inches can be measured on specimens nominally 2-3/4 inches in length.

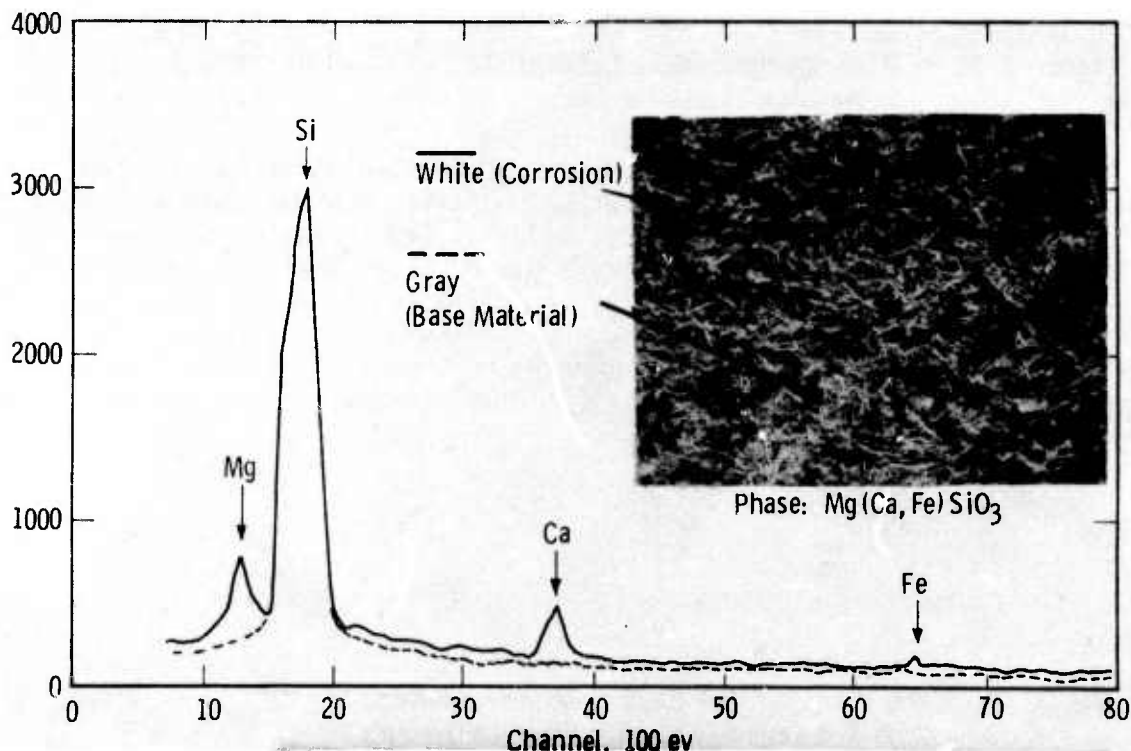


Figure 5.30 — Non-Dispersive X-Ray Analysis of Corrosion Layer, HS-130 Material, 100 Hours at  $2200^{\circ}\text{F}$  in Air

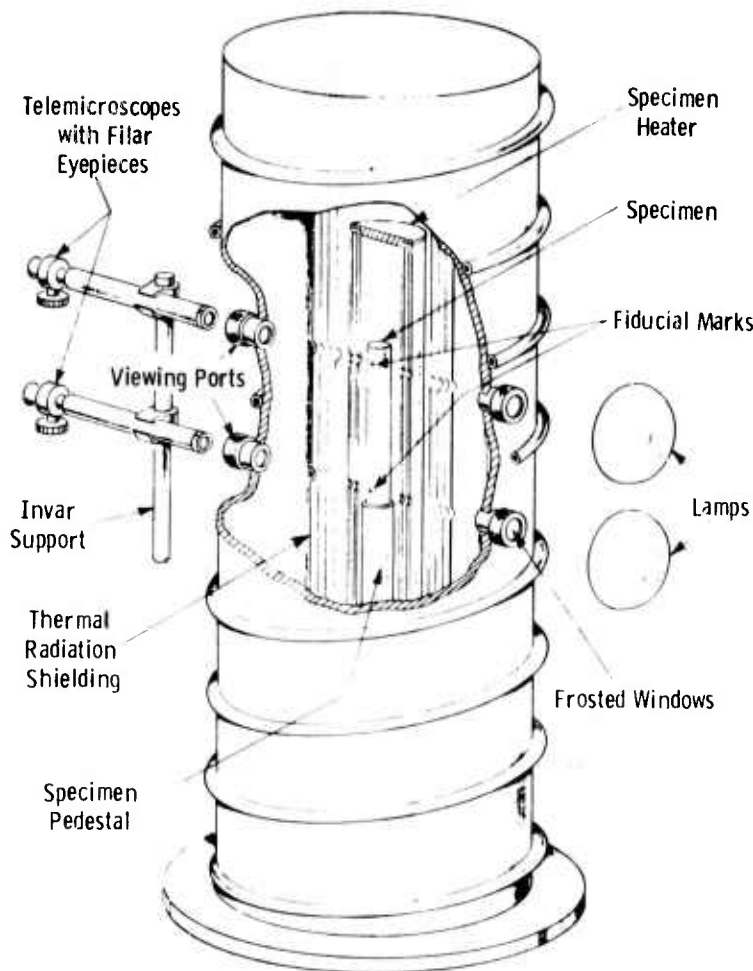


Figure 5.31 — High-Temperature Dilatometer as Used for Direct-View Expansion Measurements

Thermal conductivity is measured by a flash thermal diffusivity method. The diffusivity is determined by the transient behavior of a specimen subjected to a short-time thermal pulse on one of its sides. The apparatus appears in Fig. 5.32. A thin disc-shaped specimen is placed in the isothermal zone of a furnace and irradiated on the front face by a short-duration laser pulse. As the heat pulse travels through the specimen, its back-face temperature rise is recorded as a function of time. The temperature-time history can be related directly to the thermal diffusivity of the specimen according to the equation

$$d = \frac{0.139L^2}{t_{1/2}}$$

where  $d$  = thermal diffusivity

$L$  = specimen thickness

$t_{1/2}$  = time required for back face temperature to reach 1/2 its maximum temperature rise.

Thermal conductivity is derived as the product of thermal diffusivity, density, and specific heat.

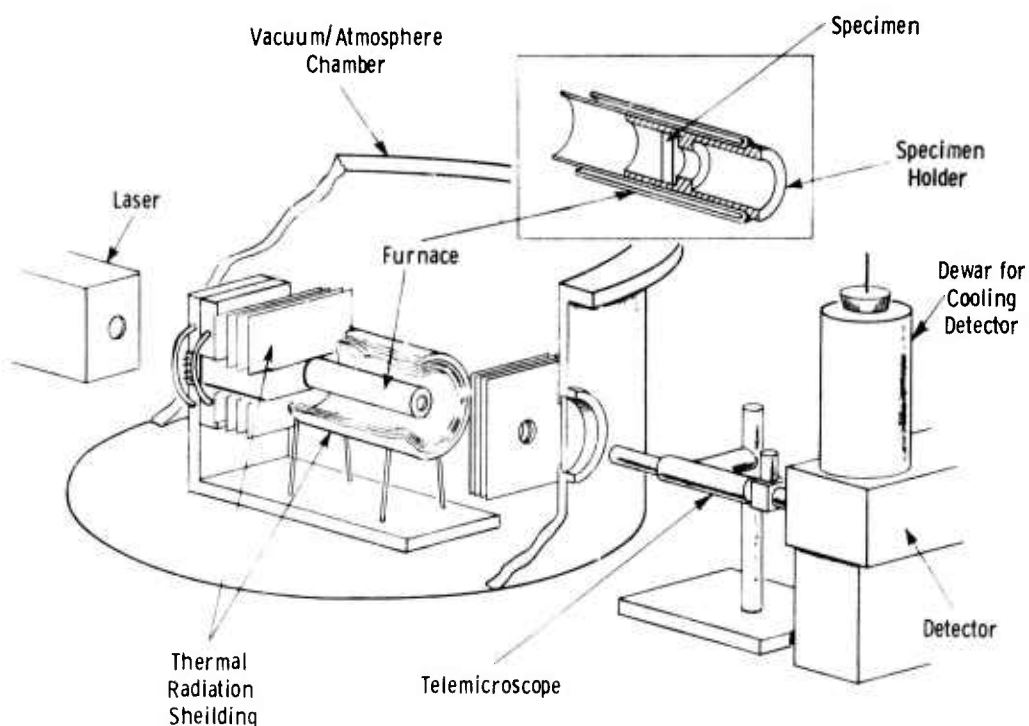


Figure 5.32 — Thermal Diffusivity Apparatus

The initial results are given in Figs. 5.33 through 5.35. Measured values of thermal conductivity are somewhat higher than those used in transient thermal stress calculations to date. The thermal expansion measurements are also somewhat higher than those previously used. The net effect, however, is not expected to change the predicted state of stress significantly.

#### Dynamic Corrosion-Erosion Testing of $\text{Si}_3\text{N}_4$

A test passage which simulates the operational environment of a large stationary gas turbine was used to determine the corrosion-erosion resistance of silicon nitride. The details of the test passage and experimental procedure are given in an earlier report.<sup>(1)</sup> Nine specimens of Norton HS-130 silicon nitride were exposed in the test passage at  $2000^{\circ}\text{F}$  for 250 hours. The gas stream velocity approaching the specimens was 500 feet/second at the passage pressure of 3 atm. The corrosion experiments were carried out with Gulf No. 2 diesel fuel to determine the baseline corrosion behavior of  $\text{Si}_3\text{N}_4$ , and by adding 0.5 weight % sulfur to the fuel in the form of ditertiary butyl disulfide. The Gulf No. 2 diesel fuel contained following impurities:

Barium	4 ppm
Sodium	0.2 ppm
Sulfur	0.06%
Molybdenum	trace amounts
Vanadium	Nil
Ash	< 0.001%
Water and Sediment	Nil

The silicon nitride specimens were cleaned, weighed, and measured before the test. After every 25 hours of exposure in the test passage, each specimen was visually examined and weighed.

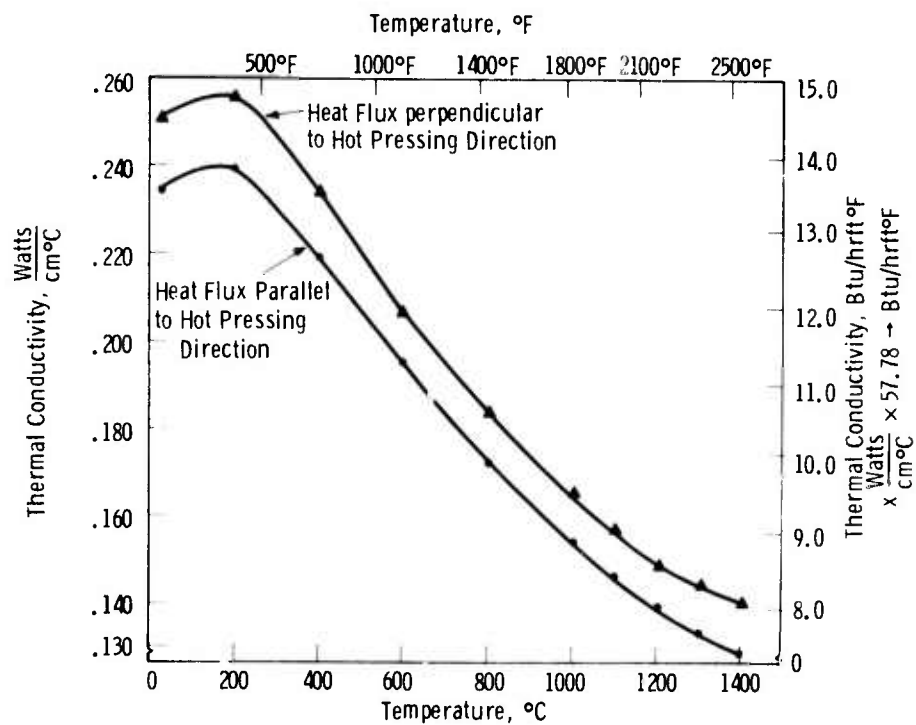


Figure 5.33 — Thermal Conductivity of Hot Pressed  $\text{Si}_3\text{N}_4$  as a Function of Direction and Temperature

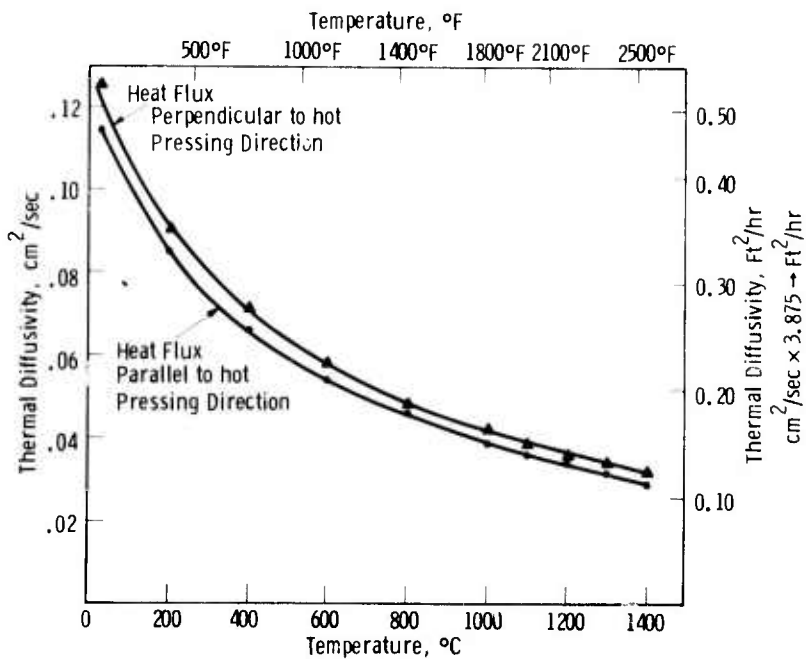


Figure 5.34 — Thermal Diffusivity of Hot Pressed  $\text{Si}_3\text{N}_4$  as a Function of Direction and Temperature

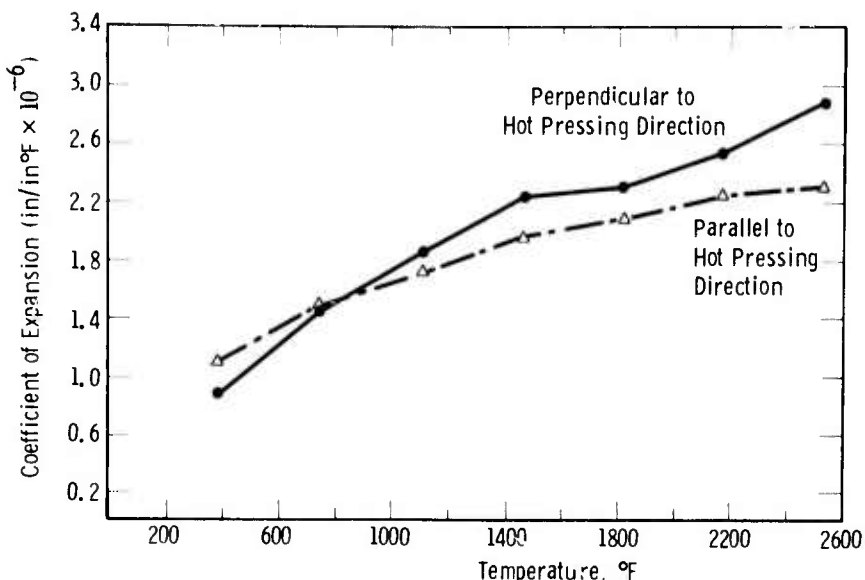


Figure 5.35 — Thermal Expansion of Silicon Nitride as a Function of Temperature and Direction

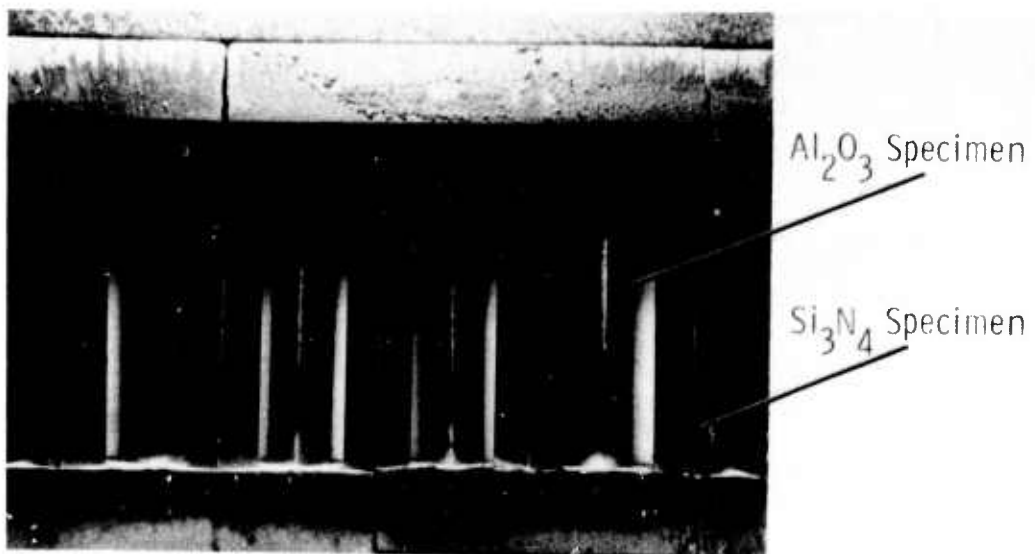
The physical appearance of the front and back surfaces of  $\text{Si}_3\text{N}_4$  samples after 250 hours of corrosion is shown in Fig. 5.36. The front surfaces are relatively clean with only small amounts of uniform surface deposits, but the leading edge on each specimen has undergone some erosion as magnified in Fig. 5.37. The surface deposits and glass formed on front surfaces of the  $\text{Si}_3\text{N}_4$  specimens are swept to the back surfaces by the high velocity of the impinging gas stream. The flow pattern of this glass is also from the scanning electron micrograph in Fig. 5.38.

The back surfaces of the silicon nitride specimens, also shown in Fig. 5.36b, are completely covered with brown glass and other deposits. These surface deposits were analyzed by scanning electron microscopy. Figure 5.38 shows a scanning electron micrograph and non-dispersive x-ray counts in a typical area of the surface deposit. The non-dispersive x-ray analysis shows that the major constituents of the surface deposit are Si, Ba and Fe. (Au and Pd counts in Fig. 5.38 are from the surface film of Au-Pd alloy deposited on  $\text{Si}_3\text{N}_4$  specimen for SEM examination). The emission spectrographic analysis, Table 5.3, also shows that the major elements in the surface deposit on  $\text{Si}_3\text{N}_4$  specimens are Si, Ba, and Fe with small quantities of Ni, Mg, Mn, Al, Ca, V, Mo, Na, etc.

For comparison purposes, two alumina specimens were also exposed in the test passage alongside the silicon nitride. Table 5.3 also gives the chemical analysis of the surface deposits on these samples. As may be seen, the chemical analysis is similar for both silicon nitride and alumina except for the expected higher silicon on  $\text{Si}_3\text{N}_4$ . This similarity of the chemical analysis shows that most of the surface deposits came externally and were formed from the condensation of impurities in the fuel and from the erosion of the stainless steel liner used in the test passage.

The x-ray diffraction analysis of the front surfaces of corroded  $\text{Si}_3\text{N}_4$  specimens revealed that these surfaces are uniformly covered with barium silicate ( $\text{BaSi}_2\text{O}_5$ ). Even though the fuel contains only 4 ppm of barium, most of it

apparently deposits on silicon nitride in the form of barium oxide ( $\text{BaO}$ ) which then reacts with surface silica ( $\text{SiO}_2$ ) to form barium silicate. Other elements like Fe, Ni, Mn, etc., and probably some remaining barium deposited on the surface as oxides, form low melting glass with silica which is swept to the back surfaces. X-ray diffraction analysis of these shiny brown deposits gave an amorphous pattern confirming a glass phase. Relatively high percentages of iron in this glass come from erosion of the steel liner used in the passage.



(a) Front Facing the Gas Stream



(b) Back

Figure 5.36 — Silicon Nitride and Alumina Specimens in the Holding Fixture After 250 Hours of Testing in Turbine Test Passage

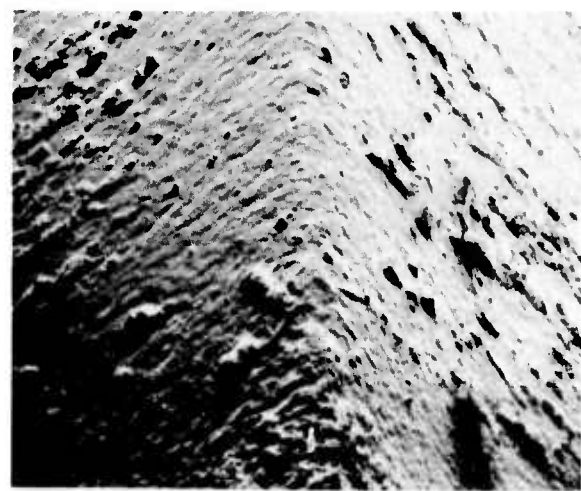


Figure 5.37 — Scanning Electron Micrograph of the Leading Edge on a  $\text{Si}_3\text{N}_4$  Specimen after 250 Hours of Testing in Turbine Test Passage at  $2000^{\circ}\text{F}$  Showing Glass Flow Lines and Erosion on the Surface.

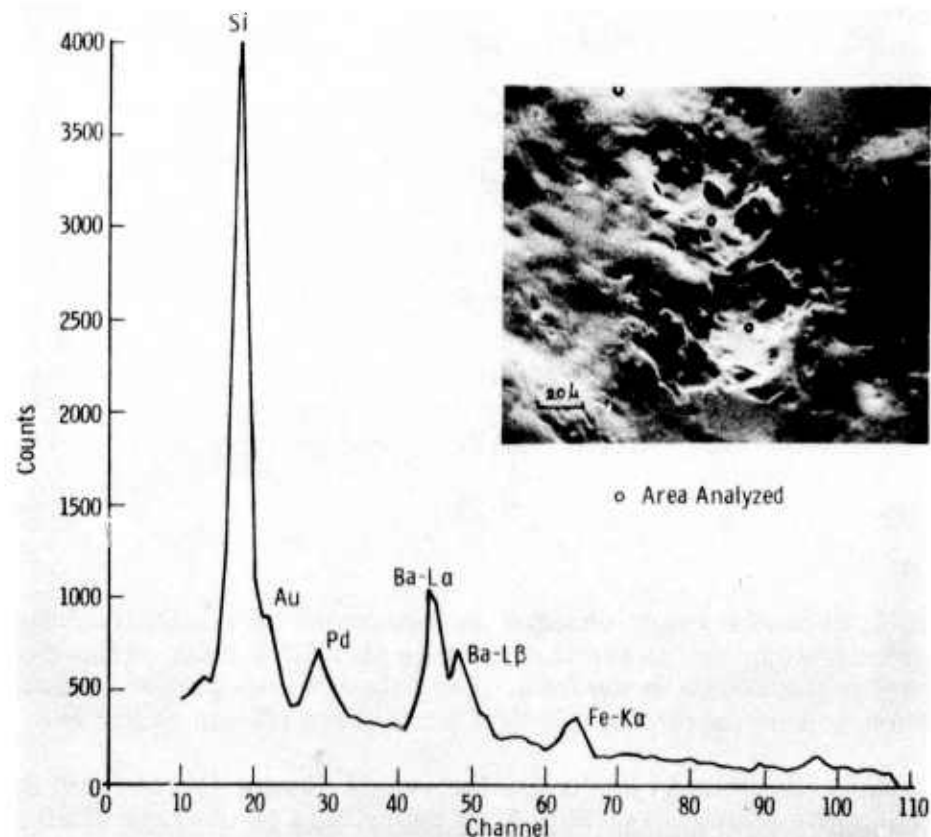


Figure 5.38 — Scanning Electron Micrograph and Non-Dispersive X-Ray Analysis of Surface Deposit on  $\text{Si}_3\text{N}_4$  Specimen After 250 Hours of Exposure in Turbine Test Passage at  $2000^{\circ}\text{F}$ .

TABLE 5.3

Emission Spectrographic Analysis of Surface Deposition On  
 $\text{Si}_3\text{N}_4$  and  $\text{Al}_2\text{O}_3$  Samples Tested in Turbine Test Passage  
in Clean Diesel Fuel at 2000°F and 3 Atmospheres Pressure

<u>Element</u>	<u>% Concentration on <math>\text{Si}_3\text{N}_4</math> Sample</u>	<u>% Concentration on <math>\text{Al}_2\text{O}_3</math> Sample</u>
Silicon	> 20	0.4
Iron	8	10
Barium	5	10
Nickel	1	1
Magnesium	0.5	0.5
Manganese	0.3	0.3
Aluminum	0.3	0.1
Calcium	0.2	< 0.2
Vanadium	0.1	0.3
Molybdenum	0.05	0.05
Titanium	< 0.01	< 0.05
Cobalt	< 0.05	< 0.05
Copper	0.03	< 0.05
Zinc	0.05	< 0.05
Chromium	0.01	0.5

Figure 5.39 shows weight changes as function of corrosion time for silicon nitride specimens exposed in the test passage at 2000°F using clean diesel fuel with 0.5 wt % sulfur added to the fuel. The data are also plotted in terms of penetration to demonstrate how insignificant these effects really are.

There was considerable scatter in the weight change values from specimen to specimen, and each curve in Fig. 5.39 represents an average of nine specimens. In both experiments, silicon nitride gained weight initially. This gain in weight is obtained in two ways: (1) by the surface oxidation of  $\text{Si}_3\text{N}_4$  whereby nitrogen atoms are replaced by heavier oxygen atoms to form silica ( $\text{SiO}_2$ ), and (2) from the condensation of impurities from the gas stream as

discussed above. As the volume of these surface deposits increases the glass is swept away by the high velocity of the oncoming gas stream. The specimens start to lose weight as the test progresses. Some reduction in weight is also caused by erosion of front surfaces and the leading edge of the silicon nitride sample, again due to the high velocity of the gas stream.

The weight loss of silicon nitride specimens tested with sulfur in the fuel is greater than those tested in clean fuel. However, specimens tested with sulfur in the fuel also underwent many more thermal cycles, which caused some edges to chip off, giving some weight loss as the test progressed. Additional weight loss may also be due to the volatile silicon sulfides. The surface deposits are now being completely analyzed to determine the effect of sulfur on the corrosion behavior of silicon nitride. Subsequent experiments will be carried out by adding sodium and vanadium to the fuel to determine their effect on the overall corrosion-erosion behavior of silicon nitride in gas turbines.

After the weight change data were obtained, bend tests were performed to determine what effect the turbine environment had on the strength of silicon nitride. The flexural strength was measured under conditions of 4-point loading (outer span 1.5 inches, inner span 0.75 inch) using a cross head strain rate of 0.0005 in/in/min at RT, 2000°, and 2200°F. The specimen size was 1/4 x 1/4 x 2 inch.

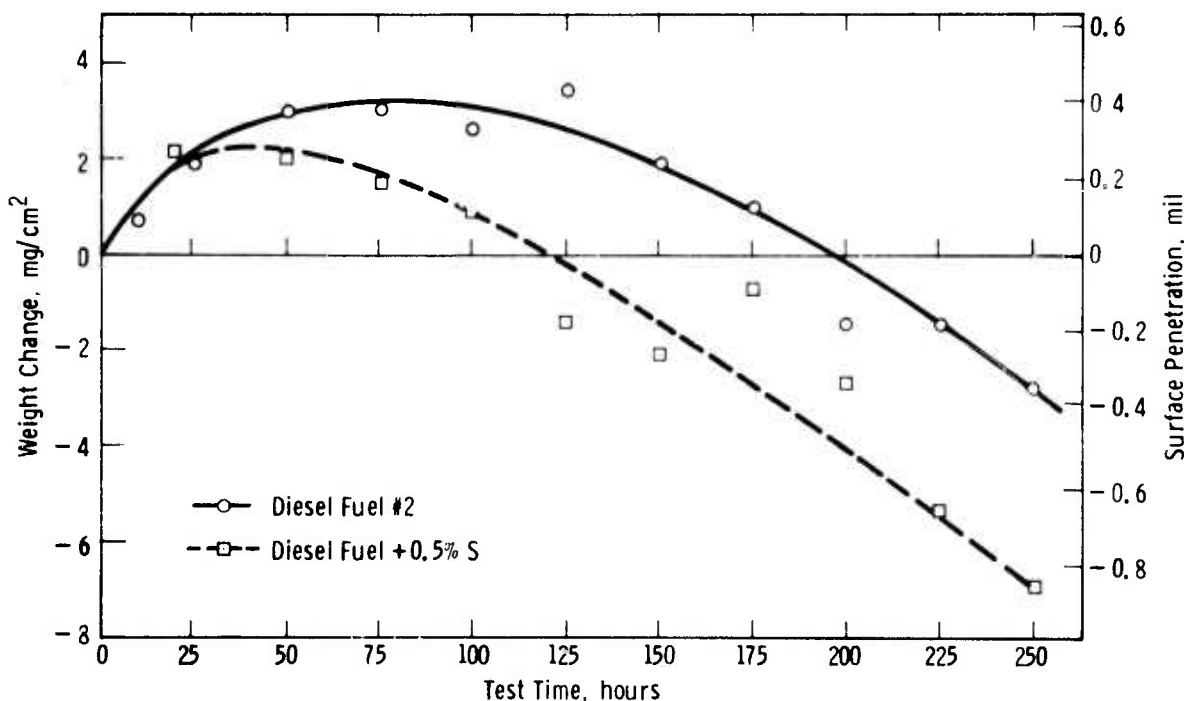


Figure 5.39 — Weight Change Data for Norton HS-130  $\text{Si}_3\text{N}_4$  in Turbine Test Passage at 2000°F and 3 Atmospheres Pressure

Weibull statistics predict a room temperature flexural strength of  $\sim 75,000$  psi for these 1/4 x 1/4 x 2 inch specimens (compared to 98,600 psi for smaller specimens) because of the larger volume under stress. Flexural strengths for non-corroded control specimens were consistent with this predicted flexural strength. Data appearing in Fig. 5.40 indicate that the strength of silicon nitride is not impaired by 250 hour exposure in a turbine atmosphere at 2000°F.

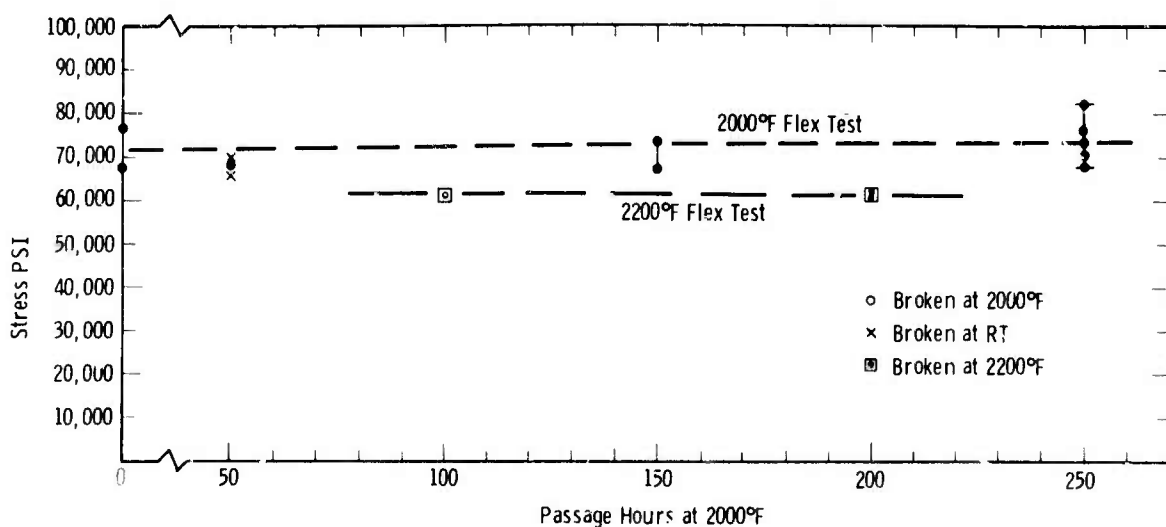


Figure 5.40 — Flexural Failure Stress of  $\text{Si}_3\text{N}_4$  Versus Exposure Time in the Turbine Test Passage at 2000°F. 1/4 x 1/4 x 2 Inch Samples in 4 Point Loading (Strong Direction)

### Special Testing

#### Friction

The three piece vane design for the stationary gas turbine permits some freedom of motion between the stator vane airfoil and its restraining end caps. Because this motion is affected by tenon geometry and friction at that interface, both static and dynamic coefficients of friction as well as the wear characteristics must be measured for high density silicon nitride against itself.

The procedure and apparatus for measuring friction were described in the first semiannual report.<sup>(1)</sup> The friction coefficient of  $\text{Si}_3\text{N}_4$  versus  $\text{Si}_3\text{N}_4$  was determined again with better control of temperature. Figure 5.41 gives the static or breakaway coefficient as a function of temperature. The dynamic coefficients of friction were stick-slip in behavior, except for virgin material at RT where the average measured coefficient was 0.22.

#### Wear and Fret

Besides friction coefficients, wear and fret tests will be made in the test fixture depicted in Fig. 5.42. The construction of this apparatus was recently completed.

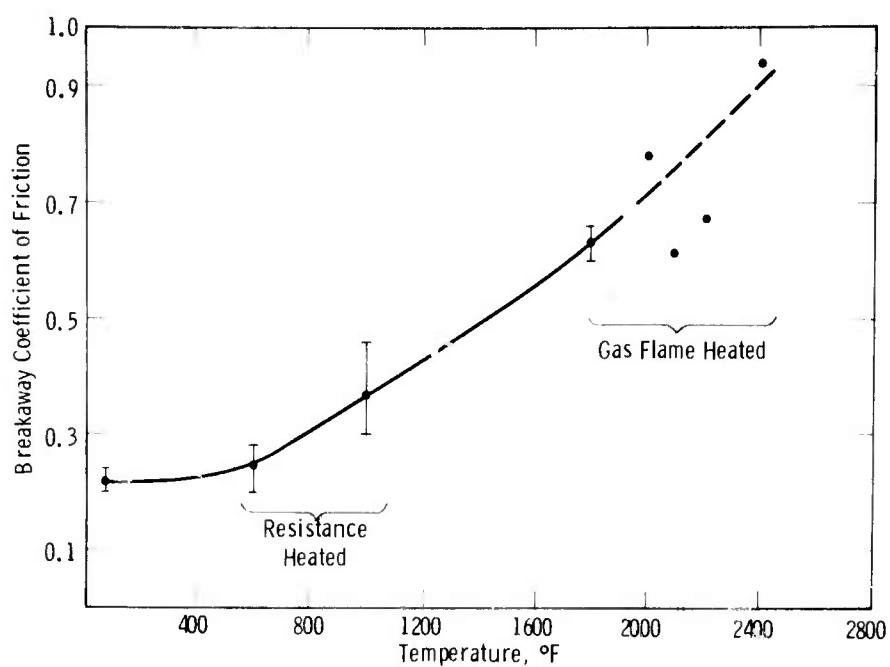


Figure 5.41 — Breakaway Coefficient of Friction of Silicon Nitride vs Silicon Nitride as a Function of Temperature

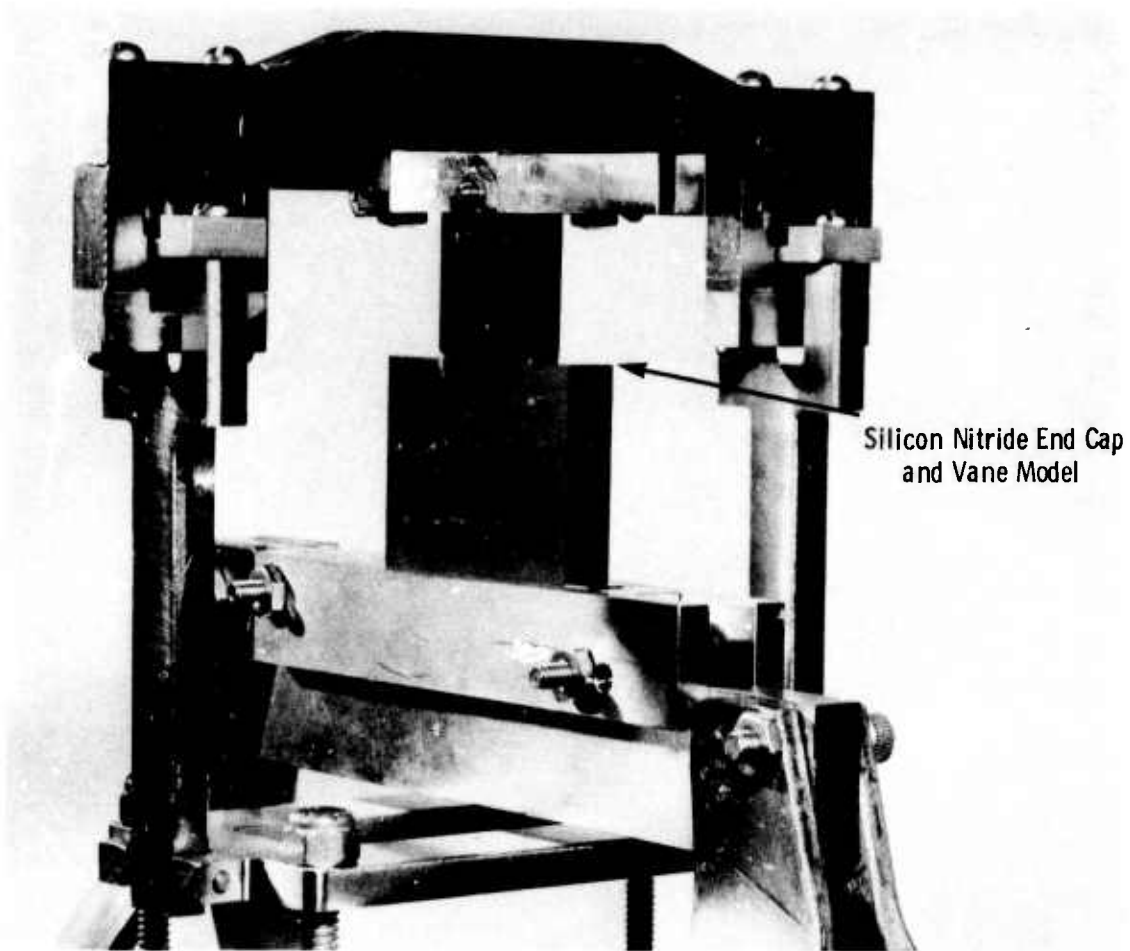


Figure 5.42 — Wear and Fret Test Apparatus

## 5.2 MATERIALS SCIENCES

### SUMMARY

The purpose of detailed investigations into material sciences is to develop an understanding of material behavior which will lead to improved material through better control of composition, processing, and fabrication. This is of particular importance since the ceramic materials being utilized in the turbine engines are relatively new and appear capable of considerable improvement. Various phases of the material sciences investigation will be continued throughout the life of the program. During this reporting period, (1) work was performed on the characterization of reaction-sintered silicon nitride, (2) some elastic properties of hot-pressed silicon nitride and silicon carbide were determined at elevated temperatures, (3) the microstructure of hot-pressed silicon nitride was studied, and (4) static oxidation measurements were performed on hot-pressed silicon nitride.

(1) A technique was developed to perform quantitative x-ray diffraction analysis for the phases present in the  $\text{Si}_3\text{N}_4$  system. Using this technique for a constant time-temperature cycle, the  $\alpha/\beta$  composition could be altered by changing the nitrogen flow. Over a period of time, this proved to be the dominant process variable.

An etching technique has been successfully applied to  $\text{Si}_3\text{N}_4$ . It was found that the etching rate is a function of both percent  $\alpha\text{Si}_3\text{N}_4$  and the amount of Fe impurity, and is independent of density of the material. The etching and microstructural studies strongly indicated that an FeSi phase may be located at the grain boundaries.

(2) Resonance techniques were used to study the elastic properties of hot-pressed  $\text{Si}_3\text{N}_4$  and hot-pressed  $\text{SiC}$ , as a function of temperature. Curves of Young's modulus, shear modulus, and Poisson's ratio vs temperature — were determined.

(3) Anisotropy in properties of hot-pressed silicon nitride is attributed to microscopic defects rather than grain morphology. These defects include density gradients along the hot-pressing direction, favorably oriented flaws, and foreign inclusions, of which silicon is the most common. Clustering of small impurity particles has also been identified by electron microscopy. Direct evidence for a glassy phase, which is believed to exist at grain boundaries and influences the high temperature properties, has eluded detection by the analytical tools used to date.

(4) Thermodynamic considerations show that volatilization of the protective surface oxide ( $\text{SiO}_2$ ) to  $\text{SiO(g)}$  or other volatile species will not occur during the oxidation of  $\text{Si}_3\text{N}_4$ . The oxidation resistance of Norton HS-130 is significantly better than the HS-110 material reported previously. This improvement is attributed to a lower impurity content. The activation energy for static oxidation at 1 atm oxygen pressure in the temperature range  $2000^{\circ}$  to  $2500^{\circ}\text{F}$  is 89.5 kcal/mole which appears to be related to a diffusion controlled process of oxygen ions through a silicate surface film. Magnesium silicates (enstatite and clinoenstatite) are the major crystalline phases developed after oxidation at  $2000^{\circ}$  to  $2500^{\circ}\text{F}$ .

Thermodynamics suggest that a stable, non-volatile silica layer should be maintained on the surface of silicon nitride under the oxygen pressures encountered in gas turbines. If this is the case significant loss of vane material is not expected to occur at turbine inlet temperatures up to 2500<sup>0</sup>F. Since kinetic effects need to be considered, however, efforts will be made to correlate as far as possible the static oxidation phenomena with dynamic turbine results. The cyclic behavior of the protective layers will be determined as part of the dynamic tests.

### 5.2.1 CHARACTERIZATION OF REACTION SINTERED SILICON NITRIDE

#### Introduction

The optimization of the physical properties of a material through process modification should be accompanied by a thorough understanding of the micro-structure and the chemistry of the material. The purpose of this work was to develop the tools necessary to study the structure of reaction-sintered  $\text{Si}_3\text{N}_4$ . The primary areas of investigation included development of quantitative x-ray diffraction methods and characterization of reaction-sintered  $\text{Si}_3\text{N}_4$  using these techniques. Work was then initiated to study the microstructure of typical reaction-sintered  $\text{Si}_3\text{N}_4$ . To perform this task, etching rate studies were first carried out. The use of these tools will assist in the optimization of the physical properties of reaction-sintered  $\text{Si}_3\text{N}_4$ .

#### Quantitative X-Ray Diffraction of $\text{Si}_3\text{N}_4$

In the first interim report<sup>(1)</sup>, much x-ray diffraction data was presented using peak height percents. This type of analysis is acceptable when comparing two materials or groups of materials of the same phase composition. Problems arise when additional phases are introduced, and the comparisons become less meaningful. When attempting to study the microstructure of a material, an accurate phase analysis is necessary.

In order to improve the analytical methods, a study was undertaken to develop the intensity factors ( $K_i$ ) needed to convert peak intensity ( $I_i$ ) to weight fractions ( $W_i$ ) of the phase present. The relation

$$W_i = K_i I_i / \sum_n K_i I_i \quad (1)$$

describes the necessary calculations, where the summation is over all phases present.

The procedure employed was to prepare powdered mechanical mixtures of known percentages of the pure phases present in  $\text{Si}_3\text{N}_4$ . In this study,  $\beta$   $\text{Si}_3\text{N}_4$  was used as the primary reference, with second phases added to it. The diffraction intensities were measured for selected reflections and from these the data counts/second/percent were calculated, the ratio of the latter giving the required intensity factor.

The phases used in this study were those that have been identified in samples of  $\text{Si}_3\text{N}_4$ . Typically these phases are:  $\alpha$ - $\text{Si}_3\text{N}_4$ ,  $\beta$ - $\text{Si}_3\text{N}_4$ ,  $\text{Si}_2\text{ON}_2$ ,  $\text{Si}$ ,  $\alpha$  Cristobalite, and  $\text{SiC}$ . The values of  $K_i$  to be used in equation (1) are listed in Table 5.4 together with data associated with selected reflections of the component phases.<sup>(14)</sup>

#### Characterization of $\text{Si}_3\text{N}_4$ Using X-Ray Diffraction

The development of techniques to perform quantitative phase analysis on  $\text{Si}_3\text{N}_4$  enables phase composition to be used as a quality control parameter in nitriding. The knowledge of the phase composition should give information on the nitriding process; i.e. variability in temperature, oxygen content and water vapor in the nitrogen gas, nitrogen flow rate, and leaks in the furnace.

A history of the phase compositions, along with a history of the controllable variables for each firing, should identify the important process parameters.

TABLE 5.4

K<sub>i</sub> VALUES FOR THE Si<sub>3</sub>N<sub>4</sub> SYSTEM

Phase	Reflections	d(A)	2θ CuKα	K <sub>i</sub>
α Si <sub>3</sub> N <sub>4</sub>	(201)	3.89	31.0	1.72
β Si <sub>3</sub> N <sub>4</sub>	(200)	3.29	27.1	1.0
Si <sub>2</sub> ON <sub>2</sub>	(200)	4.44	20.0	0.57
Si	(111)	3.14	28.4	0.23*
α Cristobalite	(101)	4.04	22.0	0.24
SiC	---	2.51	35.7	0.50

\* Because of interference from a weak SiO<sub>2</sub> line, the intensity of the Si line must first be reduced by 5% of the intensity of the (101) SiO<sub>2</sub> line before multiplying by 0.23 and using equation (1).

Test bars of injection molded silicon were burned out by gradual heating to 600° F in air, and then prefired in nitrogen at 1900° F for 12 hours. Pieces of these test bars were then placed in specific locations within the two production furnaces. (See Section 3.3.1 of this report for a detailed description of these furnaces.) Conventional two stage nitridings (24 hours at 2100° F followed by 24 hours at 2660° F) were performed. The samples were then analyzed for phase composition.

The results for the brick-lined furnace are given in Table 5.5. The results can be broken down into two groups. The firings, H-4 to H-14, have an average of 20 wt% α Si<sub>3</sub>N<sub>4</sub> for the right front position and 30 wt% α Si<sub>3</sub>N<sub>4</sub> for the left front position. This shows that compositional differences were present within the furnace. During the course of these firings many furnace variables were introduced through normal maintenance; the heating elements were replaced, the thermocouples were replaced, and the refractory brick was replaced. All these variables seemingly had no major effect on the resultant phase composition.

The second group, H-15 to H-20, had an average of 64 wt% α Si<sub>3</sub>N<sub>4</sub> for both positions examined. The same furnace maintenance occurred during the course of these firings. Again, no apparent effect was observed.

One variable was changed from the first to the second group. The first group was produced using free flowing nitrogen, 30 cu ft/hr at the inlet and 25 cu ft/hr at the exhaust. The second group was produced with a restricted nitrogen flow; 39 cu ft/hr at the inlet but only 10 cu ft/hr at the exhaust, resulting in a more static condition within the furnace. This effect could explain the gradient observed in the first group of firings. The nitrogen inlet is located at the top right side of the furnace and the exhaust is manifolded across the bottom of the furnace. This would cause the parts on the right side of the furnace to be "washed" with nitrogen to a greater degree than the left side.

The results for the cold-wall metal furnace are given in Table 5.6. The average composition for the two positions was 66 wt% α Si<sub>3</sub>N<sub>4</sub>, 34 wt% β Si<sub>3</sub>N<sub>4</sub>. No SiC was detected. These parts were produced with a reduced and restricted

TABLE 5.5  
X-RAY DIFFRACTION RESULTS FROM THE BRICK-LINED FURNACE

Firing Number	Right Front			Left Front			Other Phases
	% $\alpha$ Si <sub>3</sub> N <sub>4</sub>	% $\beta$ Si <sub>3</sub> N <sub>4</sub>	Other Phases	% $\alpha$ Si <sub>3</sub> N <sub>4</sub>	% $\beta$ Si <sub>3</sub> N <sub>4</sub>	Other Phases	
H-4	20	80	None	25	75	None	Present
H-5	20	80	None	25	75	None	Present
H-9	28	72	None	40	60	None	Present
H-10	25	75	None	28	72	None	Present
H-11	7	93	None	45	55	None	Present
H-12	30	70	None	36	64	None	Present
H-13	0	100	None	7	93	None	Present
H-14	24	76	None	34	66	None	Present
			Present				
H-15	62	38	None	64	36	None	Present
H-16	52	48	None	56	44	None	Present
H-18	68	32	None	65	35	None	Present
H-19	74	26	None	68	32	None	Present
H-20	52	48	None	68	32	None	Present
			Present				

nitrogen flow condition; 10 cu ft/hr at the inlet and 5 cu ft/hr at the exhaust. It should be noted that the phase composition was high in  $\alpha$  Si<sub>3</sub>N<sub>4</sub>, close to the results obtained in the second group of firings done in the brick-lined furnace.

The mechanism for this observed flow rate dependence could be explained by presence of an SiO<sub>(g)</sub> boundary layer on the silicon particles.<sup>(15)</sup> Under flowing nitrogen conditions, this boundary layer would be washed away or drastically reduced. This would lower the oxygen potential at the surface of the silicon particles, leading to the formation of  $\beta$  Si<sub>3</sub>N<sub>4</sub>. Restricting the nitrogen flow and moving toward a more static condition could significantly alter the conditions at the boundary layer. Restricting the flow should allow a greater amount of the SiO<sub>(g)</sub> to remain on the surface of the silicon particles, increasing the oxygen potential and increasing the amount of  $\alpha$  Si<sub>3</sub>N<sub>4</sub> formed.

It can be concluded that for a constant time-temperature cycle, the nitrogen flow is the predominant process variable in the production of reaction-sintered Si<sub>3</sub>N<sub>4</sub>. It has been shown that the  $\alpha$  /  $\beta$  composition can be changed by controlling the nitrogen flow.

**TABLE 5.6**  
**X-RAY DIFFRACTION RESULTS FROM THE**  
**COLD-WALL METAL FURNACE**

Firing Number	Position 1		Other Phases	Position 2		Other Phases
	% $\alpha$ Si <sub>3</sub> N <sub>4</sub>	% $\beta$ Si <sub>3</sub> N <sub>4</sub>		% $\alpha$ Si <sub>3</sub> N <sub>4</sub>	% $\beta$ Si <sub>3</sub> N <sub>4</sub>	
VH-11	72	28	None	67	33	None
VH-13	75	25	Present	73	27	Present
VH-19	71	29	None	75	25	None
VH-21	59	41	Present	61	39	Present
VH-24	54	46	None	60	40	None
			Present			Present

Etching of Si<sub>3</sub>N<sub>4</sub>

The preferred technique to study the structure of a material using the electron microscope involves viewing a replica of a polished and etched surface. Other techniques are available but this method provides the best compromise between ease of sample preparation and ease of interpretation. The major problem with this technique is developing a reproducible etch that works for reaction sintered Si<sub>3</sub>N<sub>4</sub>, a widely variable material.

Two etches have previously been reported; a eutectic mixture of NaOH and KOH at 260°C (16), and a eutectic mixture of K<sub>2</sub>CO<sub>3</sub> and NaF at 740°C (1). Both of these etches were reportedly used for hot-pressed Si<sub>3</sub>N<sub>4</sub>. The latter was tried for reaction sintered Si<sub>3</sub>N<sub>4</sub> and proved unsuccessful, as did thermal etching at various temperatures in air. It was also reported that Si<sub>3</sub>N<sub>4</sub> was attacked by 3% HF plus 10% HNO<sub>3</sub> at 71°C (17). This was the basis for the present etch (30 parts HF, 25 parts H<sub>2</sub>O<sub>2</sub>, 5 parts HNO<sub>3</sub>) reported for hot pressed Si<sub>3</sub>N<sub>4</sub> (1). This etch has since been successfully applied to reaction sintered Si<sub>3</sub>N<sub>4</sub>.

Si<sub>3</sub>N<sub>4</sub> samples of various phase compositions and impurity levels (Table 5.7) were mounted in epoxy, ground, and polished with 0.3 pm CeO paste. The samples were ultrasonically cleaned and etched in a boiling solution of 30 parts 48% HF plus 25 parts Reagent Grade H<sub>2</sub>O<sub>2</sub> plus 5 parts concentrated HNO<sub>3</sub>. A covered platinum crucible was used to hold the solution. Following treatment in the solution for a specified time, the samples were replicated and viewed in an electron microscope to determine the completion of the etching process. The etching process was considered complete when grains and boundaries could be clearly seen.

The results of this study are summarized in Figure 5.43. The etching of Si<sub>3</sub>N<sub>4</sub> is a function of two variables; weight percent  $\alpha$  Si<sub>3</sub>N<sub>4</sub> and weight percent iron present as an impurity. It is shown that this curve can be applied for injection molded ( $\rho = 2.2 - 2.3$  g/cc), slip cast ( $\rho = 2.4 - 2.5$  g/cc) and

hot-pressed ( $\rho = 3.1 - 3.18$  g/cc) silicon nitrides. From this it can be concluded that the etching process is independent of the density of the material.

The fact that iron is an important variable in the etching process implies that the iron impurities are concentrated at the grain boundaries. If the iron was present as a metallic impurity, a solution of  $\text{HNO}_3$  should etch the material. This was not observed. These results could have been predicted if it was assumed that the iron was present as an  $\text{FeSi}$  compound. This assumption is supported by the observation of a single x-ray peak which appears at  $44.9^\circ 2\Theta$ , (2.01A). This peak has been tentatively identified as an  $\text{FeSi}$  compound. A further study to determine the solubility of  $\text{FeSi}$  is in progress.

In summary, a reproducible etch has been developed and applied to both reaction-sintered and hot-pressed silicon nitride. The iron dependence of the etch has been tentatively attributed to the presence of an  $\text{FeSi}$  phase located at the grain boundaries. It is not clear at this time why the amount of  $\alpha \text{Si}_3\text{N}_4$  present effects etching time.

TABLE 5.7  
PHASE COMPOSITION, IMPURITY  
CONCENTRATION, AND ETCH TIMES FOR VARIOUS  
SILICON NITRIDES

Sample No. *	Phases		Major Impurities (wt%)**				Etch Time (Min)
	Wt% $\alpha \text{Si}_3\text{N}_4$	Wt% $\beta \text{Si}_3\text{N}_4$	Fe	Ca	Al	Mg	
228-1	86	14	0.55	0.40	0.60	0.03	19
228-2	74	26	0.50	0.40	0.70	0.03	16
228-4	70	30	0.55	0.40	0.70	0.02	15-1/2
228-5	37	63	0.70	0.40	0.85	0.07	7
237-1	100	0	0.50	0.70	0.90	0.08	25
237-2	93	7	0.25	1.00	0.85	0.08	22
237-4	95	5	0.45	0.50	1.10	0.08	23
237-3	82	18	0.50	0.70	0.85	0.08	18-1/2
238-2	10	90	0.70	0.60	0.50	0.90	3
238-3	0	100	0.08	0.10	0.20	3.00	2
241-2	30	70	0.90	0.30	0.65	0.03	3
241-3	37	63	0.90	0.35	0.65	0.03	3-1/2
241-4	14	86	0.90	0.40	0.55	0.03	1-1/2
241-5	18	82	0.70	0.40	0.60	0.04	2
241-6	23	77	0.80	0.40	0.70	0.02	2-1/2
241-1	40	60	1.10	0.20	.65	0.02	1-3/4
241-7	15	85	1.10	0.40	.75	0.02	3/4

\* 228, 237, 241 Series Reaction-Sintered  $\text{Si}_3\text{N}_4$  (Injection molded)

237-3 Reaction-Sintered  $\text{Si}_3\text{N}_4$  (slip cast)

238 Series — Hot-Pressed  $\text{Si}_3\text{N}_4$

\*\* Emission Spectrographic analysis

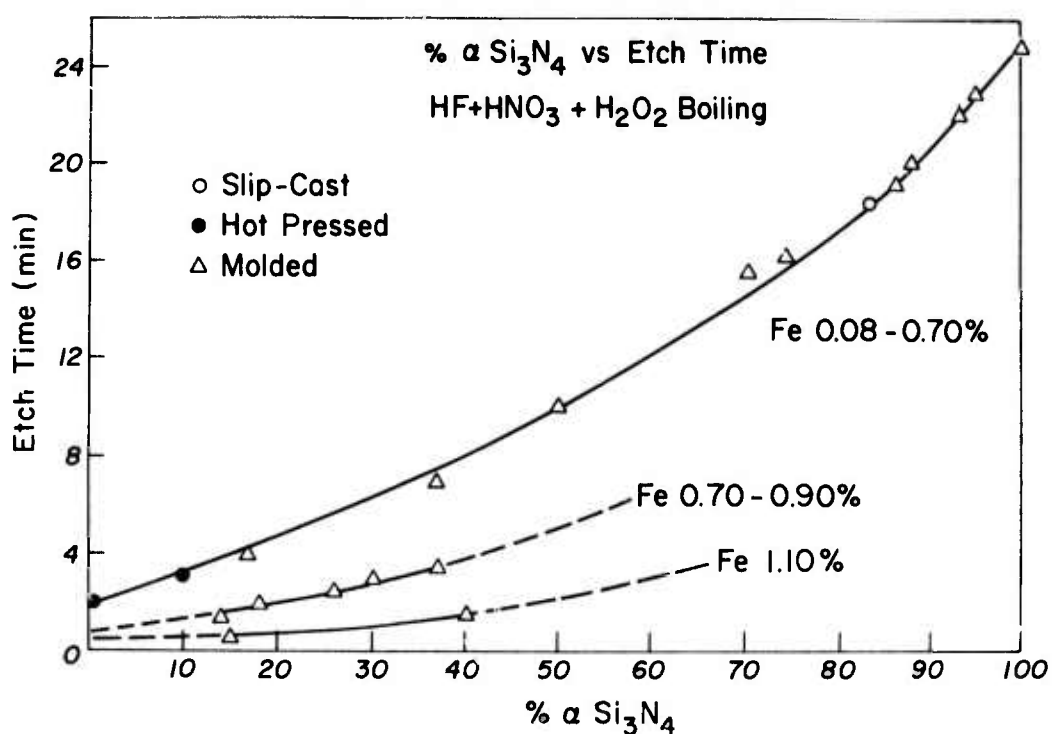


Figure 5.43 — % Alpha  $\text{Si}_3\text{N}_4$  vs Etch Time

#### Microstructure of Reaction-Sintered $\text{Si}_3\text{N}_4$

Three samples of reaction-sintered  $\text{Si}_3\text{N}_4$  were chosen to study the microstructure of the material. The chemistry of the samples, 228-1, 228-5 and 241-5 are described in Table 5.7. These samples were selected as being representative of the range of reaction-sintered  $\text{Si}_3\text{N}_4$  produced.

All samples were made from 98% pure, -325 mesh silicon metal, injection molded into test bars, and fired in a normal two stage process in the brick-lined furnace. The firing consisted of 24 hours at 2150°F and 24 hours at 2660°F with the nitrogen flow as a variable. The samples were prepared for replication using the etching procedures described in the previous section. A negative replication process was then used, which consisted of shadowing at 45° with platinum followed by carbon applied normal to the surface.

The typical structure of samples 228-1 (86%  $\alpha$   $\text{Si}_3\text{N}_4$ , 14%  $\beta$   $\text{Si}_3\text{N}_4$ ), 228-5 (37%  $\alpha$   $\text{Si}_3\text{N}_4$ , 63%  $\beta$   $\text{Si}_3\text{N}_4$ ) and 241-5 (18%  $\alpha$   $\text{Si}_3\text{N}_4$ , 82%  $\beta$   $\text{Si}_3\text{N}_4$ ) are shown in Figures 5.44, 5.45, and 5.46. The structures appear very similar in many respects. The grain size is predominantly submicron, with all samples exhibiting some clusters of 1-2  $\mu\text{m}$  grains. The grain shape is distributed between equiaxed and slightly elongated grains. Porosity is also noted to be evenly distributed, with some porosity concentrated in the center of the large grain clusters (Figures 5.44 through 5.46). The major differences appear to be in the appearance of grain boundaries. Sample 228-1 (Figure 5.44) appears to have some grain boundaries composed of individual etch pits. Etch pits also appear randomly throughout the sample. The grain boundaries for samples 228-5 and 241-5 (Figure 5.45 and 5.46) appear much more well defined, although some of the boundaries in 228-5 still appear to be made up of etch pits.

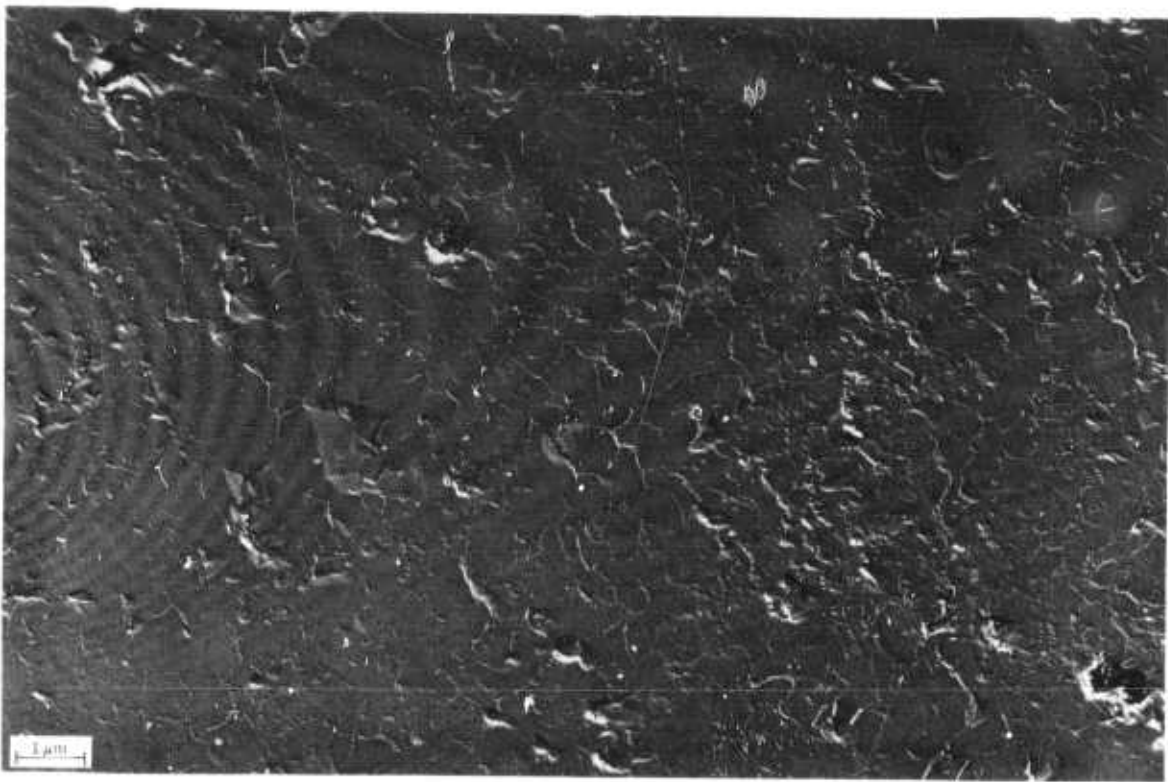


Figure 5.44a — Typical Areas From Sample 228-1 (86%  $\alpha$  , 14%  $\beta$  ) 13,200X

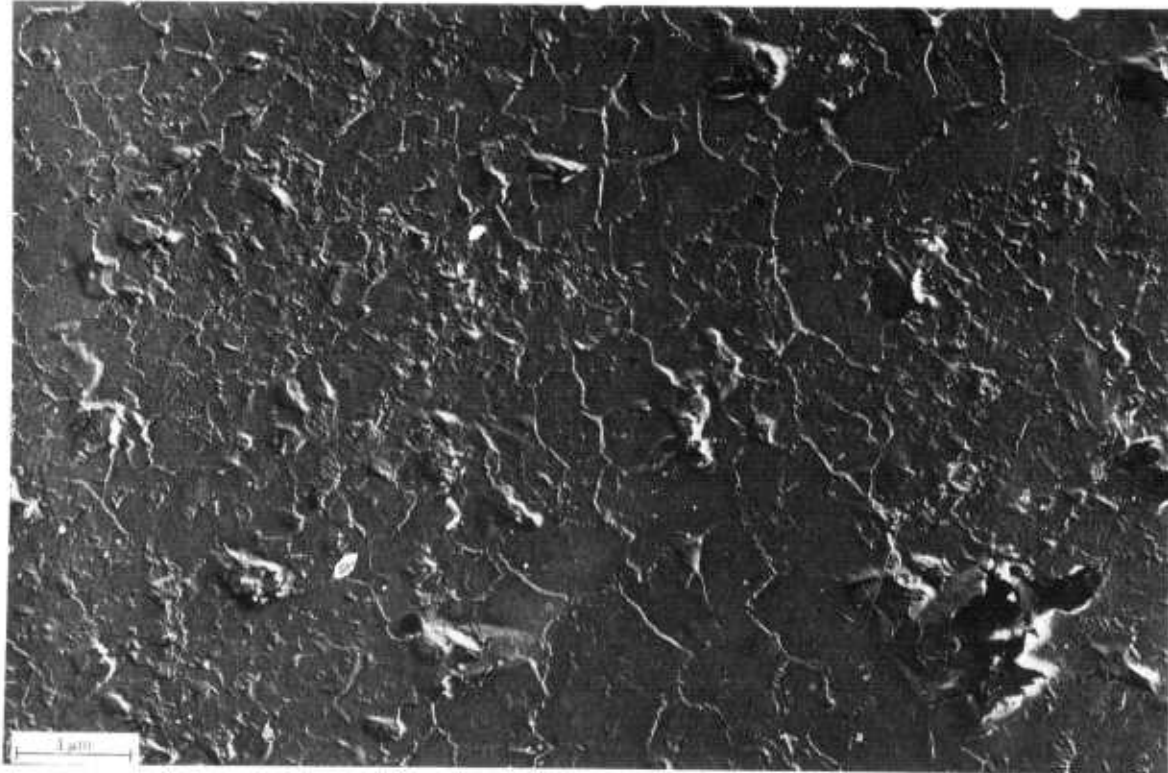


Figure 5.44b — Typical Areas From Sample 228-1 (86%  $\alpha$  , 14%  $\beta$  ) 24,800X

Figure 5.44 — Microstructure of Reaction-Sintered Silicon Nitride

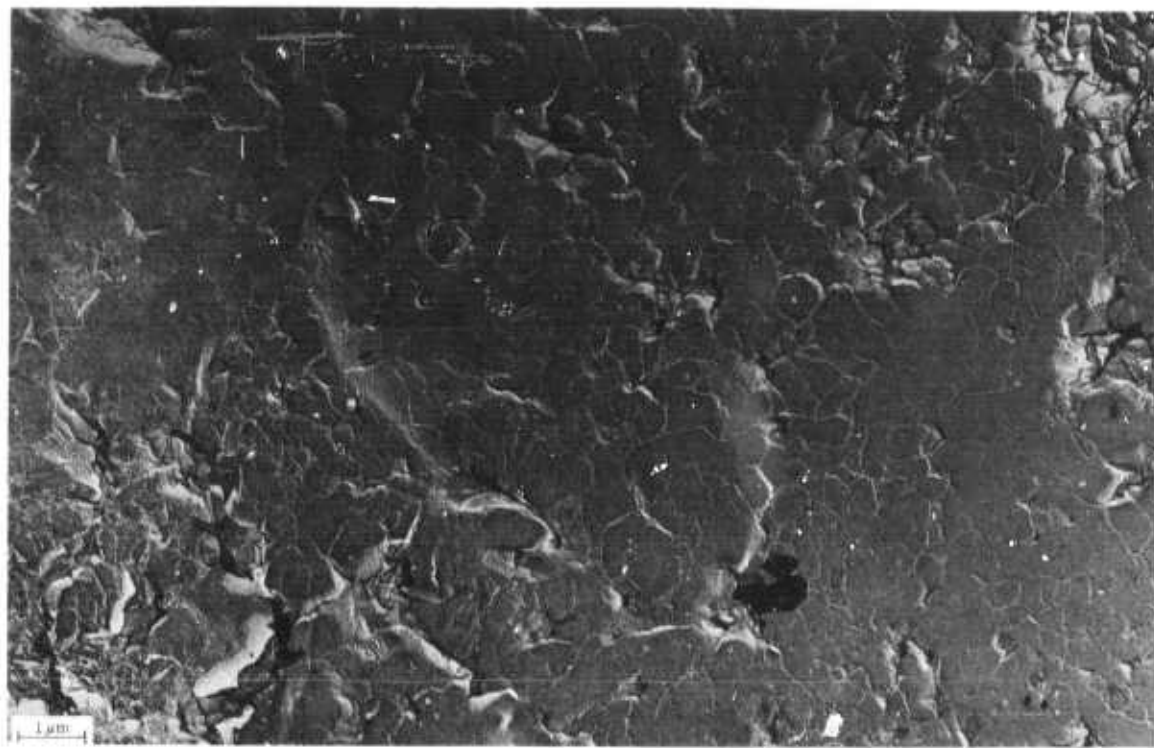


Figure 5.45a — Typical Areas From Sample 228-5 (37%  $\alpha$  , 63%  $\beta$  ) 24,800X

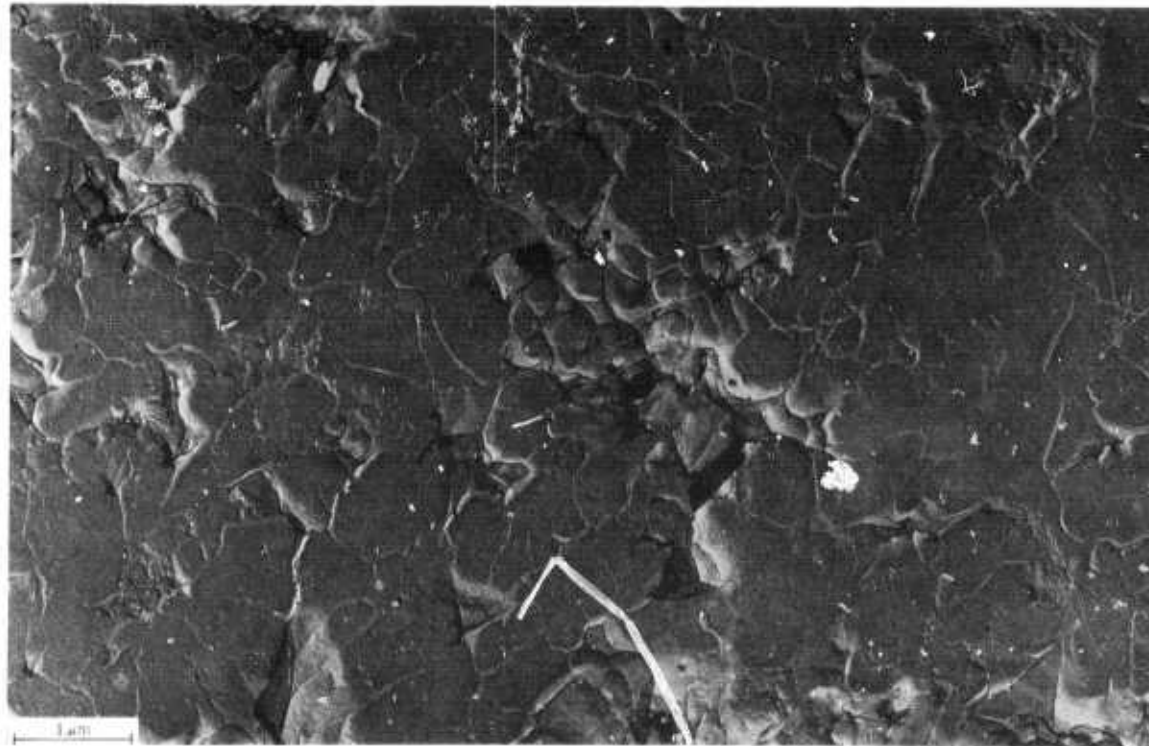


Figure 5.45b — Typical Areas From Sample 228-5 (37%  $\alpha$  , 63%  $\beta$  ) 13,200X

Figure 5.45 — Microstructure of Reaction-Sintered Silicon Nitride

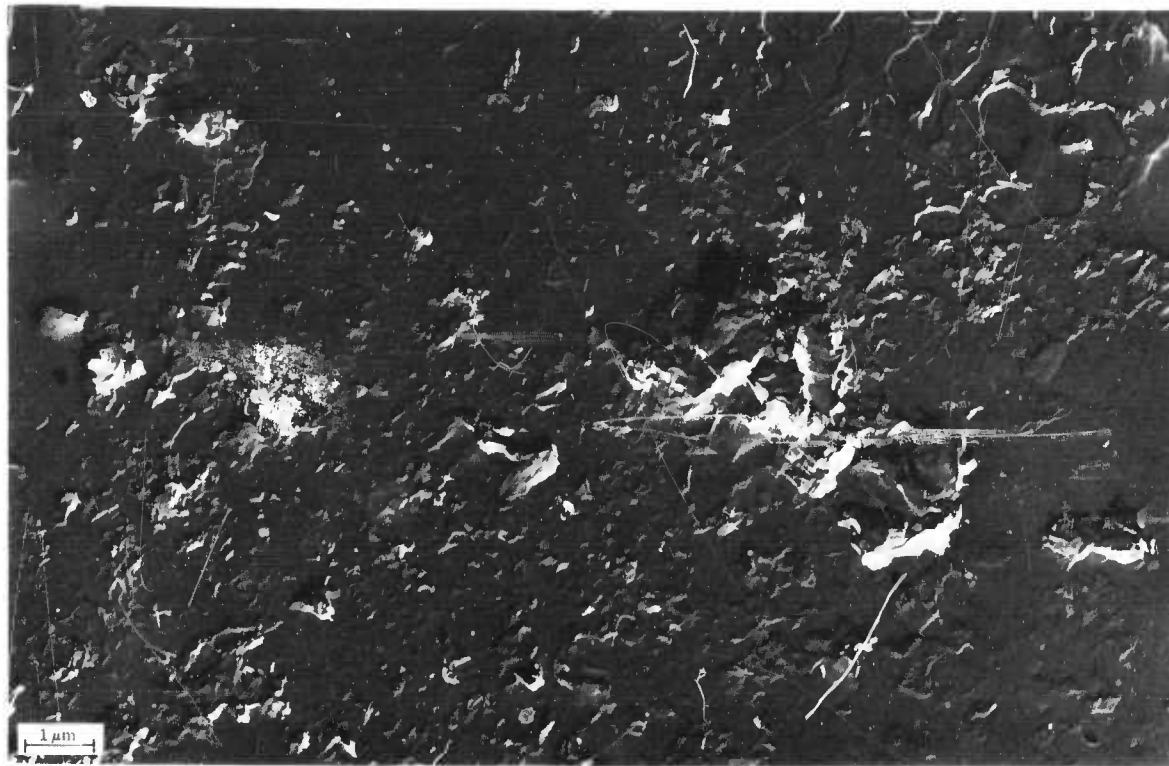


Figure 5.46 — Microstructure of Reaction-Sintered Silicon Nitride  
Typical Areas From Sample 241-5 (18%  $\alpha$ , 82%  $\beta$ ) 13,200X

A fracture surface was studied to insure that the etching technique is bringing out the true microstructure and not impurity concentrations (Figure 5.47). A fracture of injection molded  $\text{Si}_3\text{N}_4$  was replicated and viewed in an electron microscope. The fracture shows a region of large grains surrounded by smaller submicron grains. Because of the general structural similarities observed with these two different techniques, it can be concluded that the etching technique developed is showing the true microstructure of reaction sintered  $\text{Si}_3\text{N}_4$ .

The differences noted in the samples can be explained by x-ray diffraction results. The three samples all contained a trace of  $\text{FeSi}$ , with sample 228-1 having the least amount. This would lead to the poorly resolved grain boundaries that were observed.

The large grain clusters have previously been observed (8) and identified as  $\beta \text{Si}_3\text{N}_4$ . It was explained that these large grains are formed from a liquid-vapor reaction. The porosity associated with these large grains could be formed because of liquid silicon flowing into the surrounding structure. No conclusions can be made at this time concerning the similarities of the observed submicron grain size and shape with respect to  $\alpha/\beta$  ratio. The submicron grains or matt structure have also been previously observed and theories regarding their basic formation have been advanced. (8) (18) The matt structure has been identified as containing both  $\alpha$  and  $\beta \text{Si}_3\text{N}_4$ . Future work will concentrate on grain morphology and identification using electron diffraction.



Figure 5.47 — Fracture Surface of Reaction Sintered  $\text{Si}_3\text{N}_4$

### 5.2.2 ELASTIC PROPERTIES OF SILICON NITRIDE AND SILICON CARBIDE

The elastic properties as a function of temperature of several hot pressed  $\text{Si}_3\text{N}_4$  and SiC samples have been determined by resonance techniques.

The speed of shear and longitudinal sound waves has been measured in several samples of hot pressed silicon nitride.

These materials appear to be elastically isotropic in that the speed of a shear wave does not depend on the direction of its polarization. Thus the speed of longitudinal and shear sound waves (denoted by  $V_L$  and  $V_S$ ) should be related to the Lamé modulus  $\lambda$  and shear modulus  $\mu$  by the usual formulas of isotropic elasticity:

$$\mu = \rho V_S^2, \quad (1)$$

and

$$\lambda + 2\mu = \rho V_L^2 \quad (2)$$

where  $\rho$  is the material density. In terms of  $\lambda$  and  $\mu$  the bulk modulus  $B$ , Young's modulus  $Y$  and Poisson's ratio  $\sigma$  are

$$B = \frac{2}{3} \mu, \quad Y = \frac{\mu(3\lambda + 2\mu)}{\lambda + \mu} \quad \text{and} \quad \sigma = \frac{\lambda}{2(\lambda + \mu)}$$

Sound velocities were measured using a single-ended pulse-echo method shown schematically in Figure 5.48. Pulses of ultrasound of  $2 \mu$  sec pulse width and 10 MHz carrier frequency are generated via a quartz transducer, and the sound is introduced into a fused silica acoustic delay line which is attached to the sample with high temperature cement. The speed of sound propagation is calculated from the known sample length and the transit time of the ultrasonic pulse through the ceramic sample. Errors in the sound velocity measurement, estimated to be at most 2%, are determined mainly by the quality of the high temperature glue joint.

Thus far, reliable high temperature results have been obtained only for shear waves propagating in high density material. Curves of shear modulus vs temperature for three samples of hot pressed  $\text{Si}_3\text{N}_4$  of different densities are shown in Figure 5.49. In order to examine the effect of various densities, these samples were taken from available material from three vendors which exhibited a considerable spread in density. Figure 5.50 shows the variation of shear modulus with sample density at 27°C. Hot-pressed silicon nitride samples taken from the same three billets of material used in Figure 5.49 were used for shear modulus. The low density data for Figure 5.50 was measured from a sample of reaction-sintered  $\text{Si}_3\text{N}_4$  made by Ford by the slip-casting method. The Lamé modulus at 27°C derived from eq. (2) is  $\lambda = 7.6 \times 10^{11}$ ,  $1.2 \times 10^{11}$  and  $4.6 \times 10^{11}$  dyne/cm<sup>2</sup> for  $\rho = 3.05$ , 3.10 and 3.22 gm/cm<sup>3</sup> respectively. In relation to the shear moduli the  $\lambda$  moduli are rather small and show no simple relation to sample density.

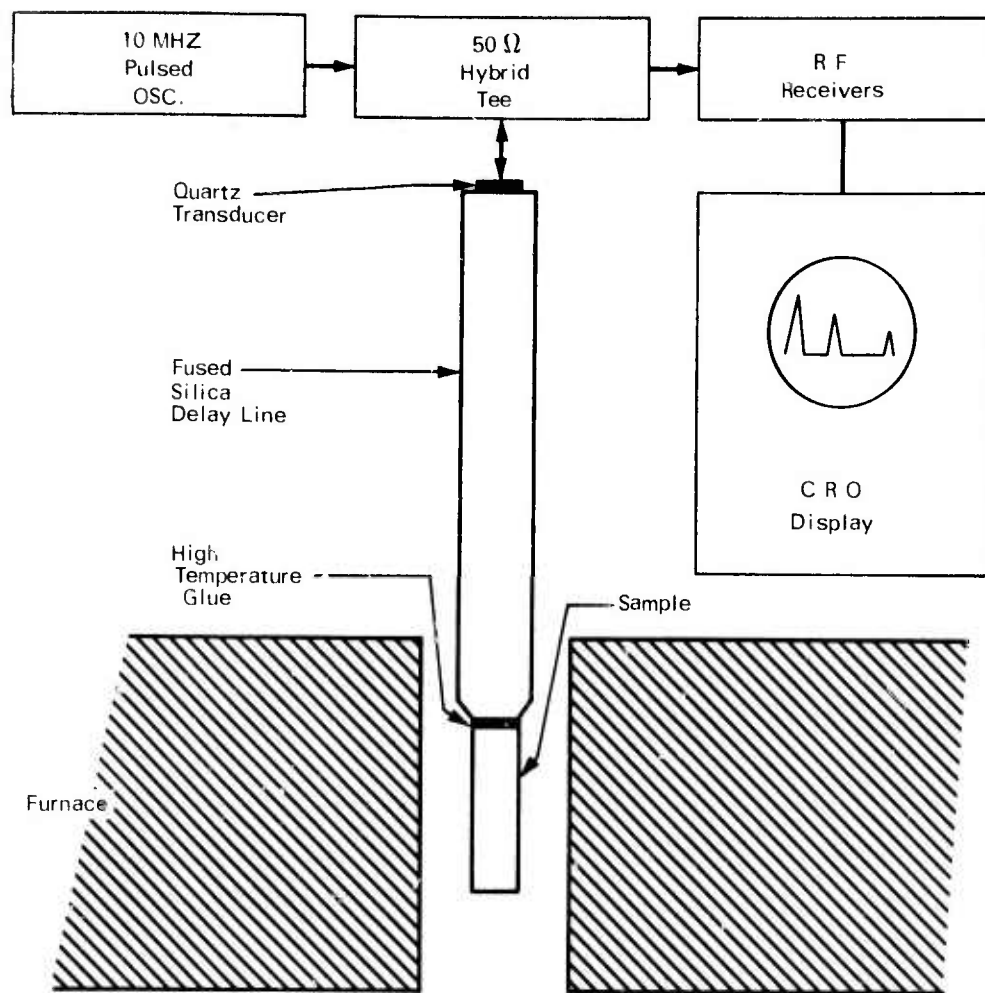


Figure 5.48 — Schematic Diagram of Ultrasonic Equipment

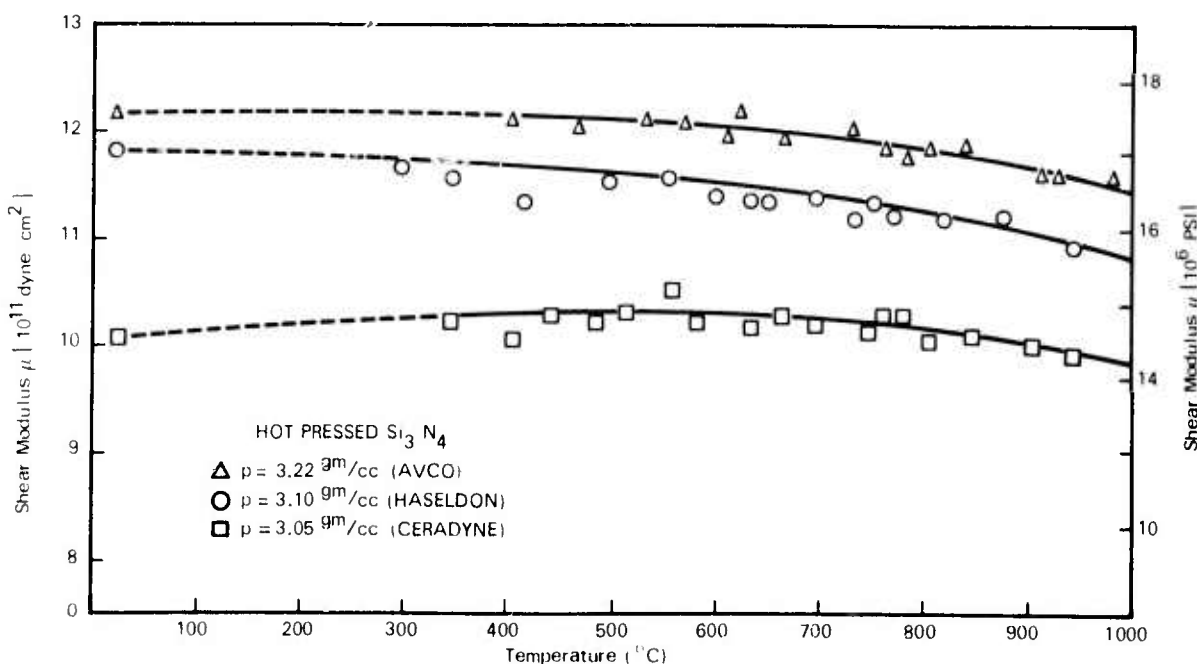


Figure 5.49 — Shear Modulus vs Temperature for Hot-Pressed  $\text{Si}_3\text{N}_4$

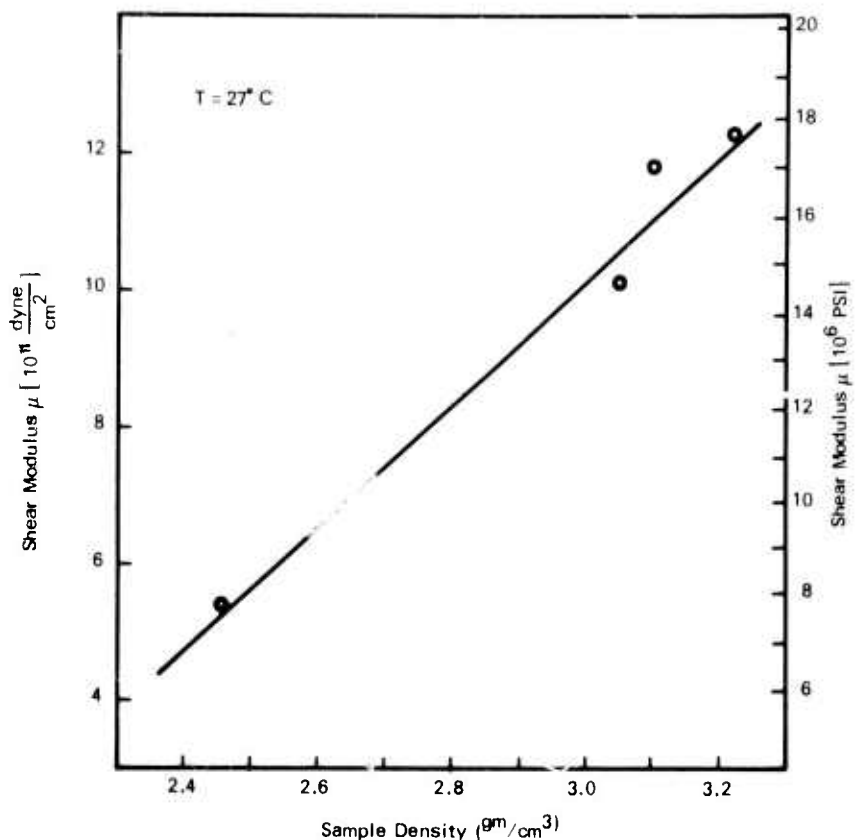


Figure 5.50 — Shear Modulus of  $\text{Si}_3\text{N}_4$  vs Density

Preliminary room temperature measurements in extruded, reaction sintered silicon carbide with  $\rho = 3.10 \text{ gm/cm}^3$  (Refel) have shown that  $V_S = V_L$  to within about 5%. This experimental result requires a negative  $\lambda$  in eq(2) and shows that eqs. (1) and (2) may not provide a valid description of the elastic properties of these materials. Further experimental work as well as an effort to correlate experimental data with existing theories of the average properties of composite materials will be necessary to clarify the results.

Young's modulus, shear modulus and Poisson's ratio, each as a function of temperature, were determined for two of Norton's high strength materials, hot pressed silicon carbide and hot pressed silicon nitride (HS-130). This was done by sonic resonance techniques at the Corning Glass Works Research Center. Curves of these properties as averaged from two samples of hot pressed silicon carbide exhibiting densities of 3.293 and 3.295 g/cc are shown in Figures 5.51, 5.52 and 5.53.

The average Young's modulus values of two samples of silicon nitride having densities of 3.175 and 3.181 g/cc is shown as a function of temperature in Fig. 5.54. Difficulty was encountered in measuring the shear modulus due to failure of the fiber slings at high temperature. However, if a temperature dependence of Poisson's ratio for silicon nitride is assumed to be similar to that measured for silicon carbide the shear modulus can be calculated at 1400°C. The assumed extrapolations of Poisson's ratios and the resulting shear modulus calculated curve are shown in Figures 5.55 and 5.56 respectively. These data agree quite well with data on hot pressed silicon nitride as previously discussed.

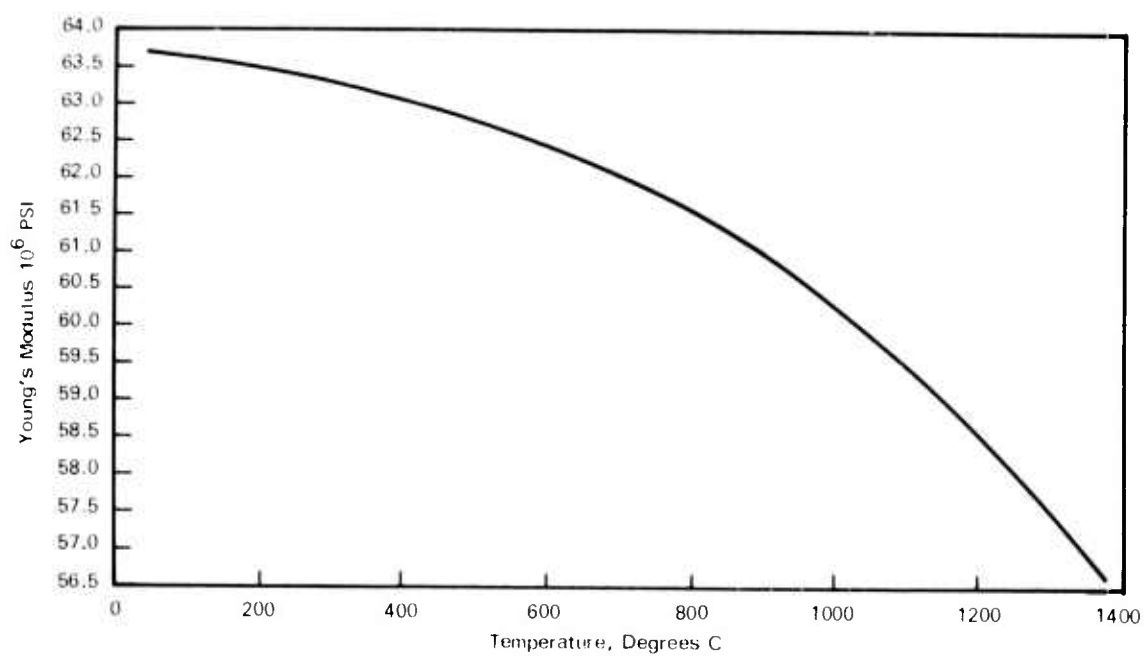


Figure 5.51 — Young's Modulus vs Temperature for Hot-Pressed SiC

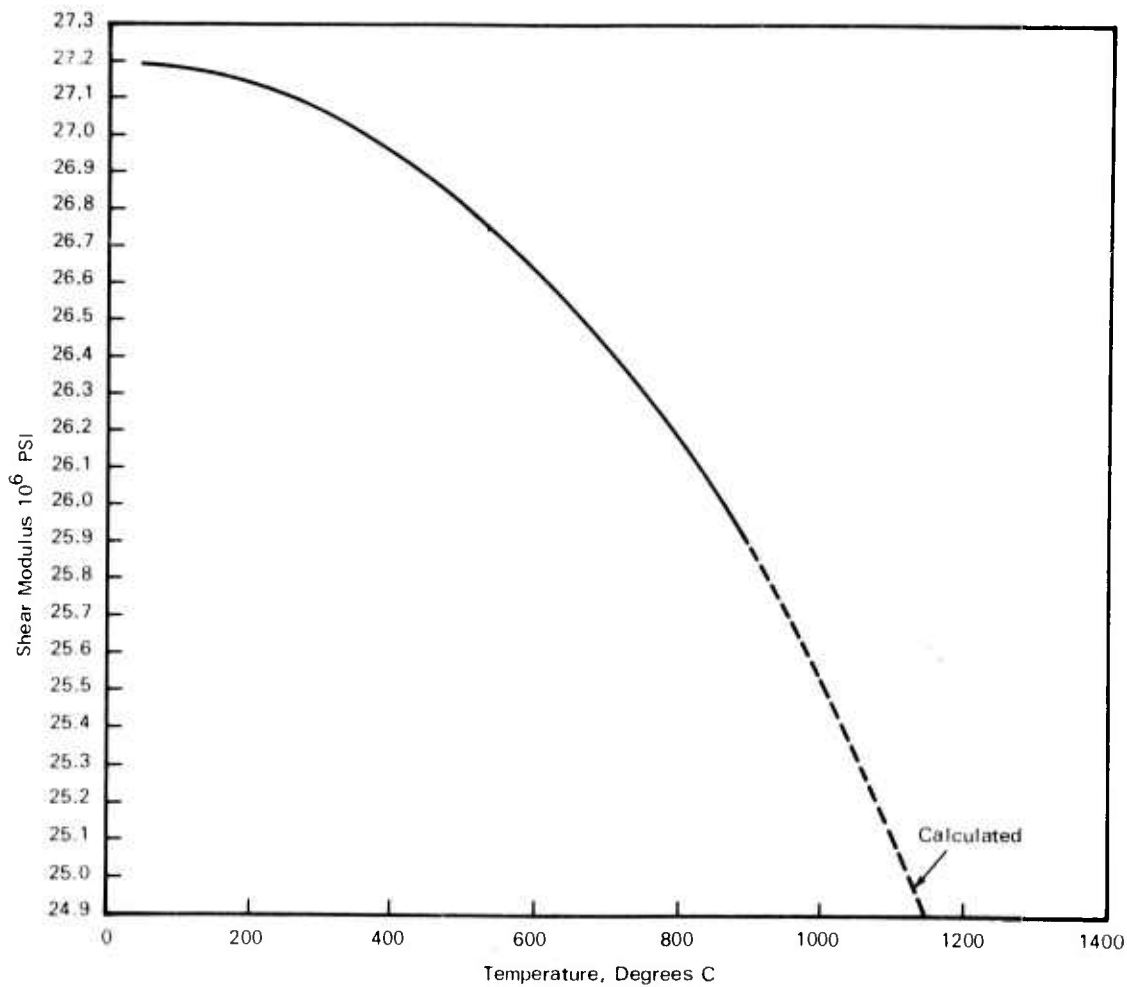


Figure 5.52 — Shear Modulus vs Temperature for Hot-Pressed SiC

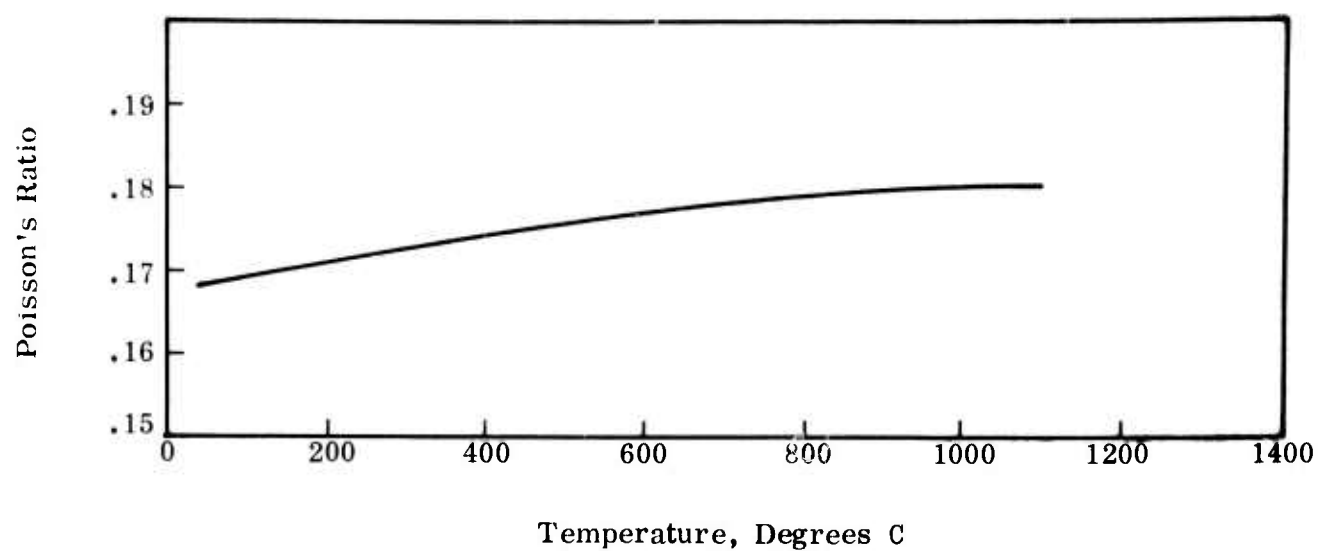


Figure 5.53 — Poisson's Ratio vs Temperature for Hot-Pressed SiC

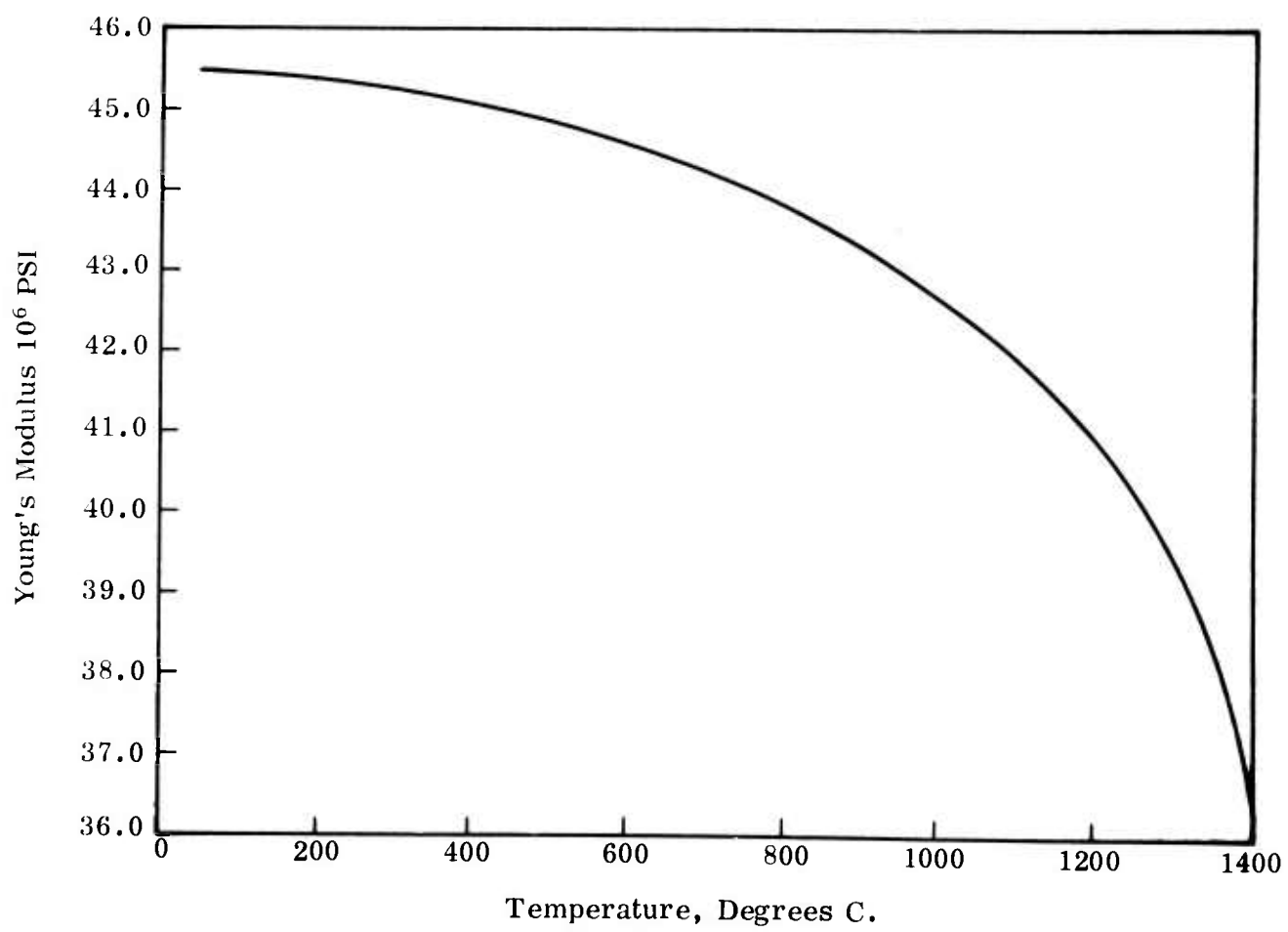


Figure 5.54 — Young's Modulus vs Temperature for Hot-Pressed  $\text{Si}_3\text{N}_4$

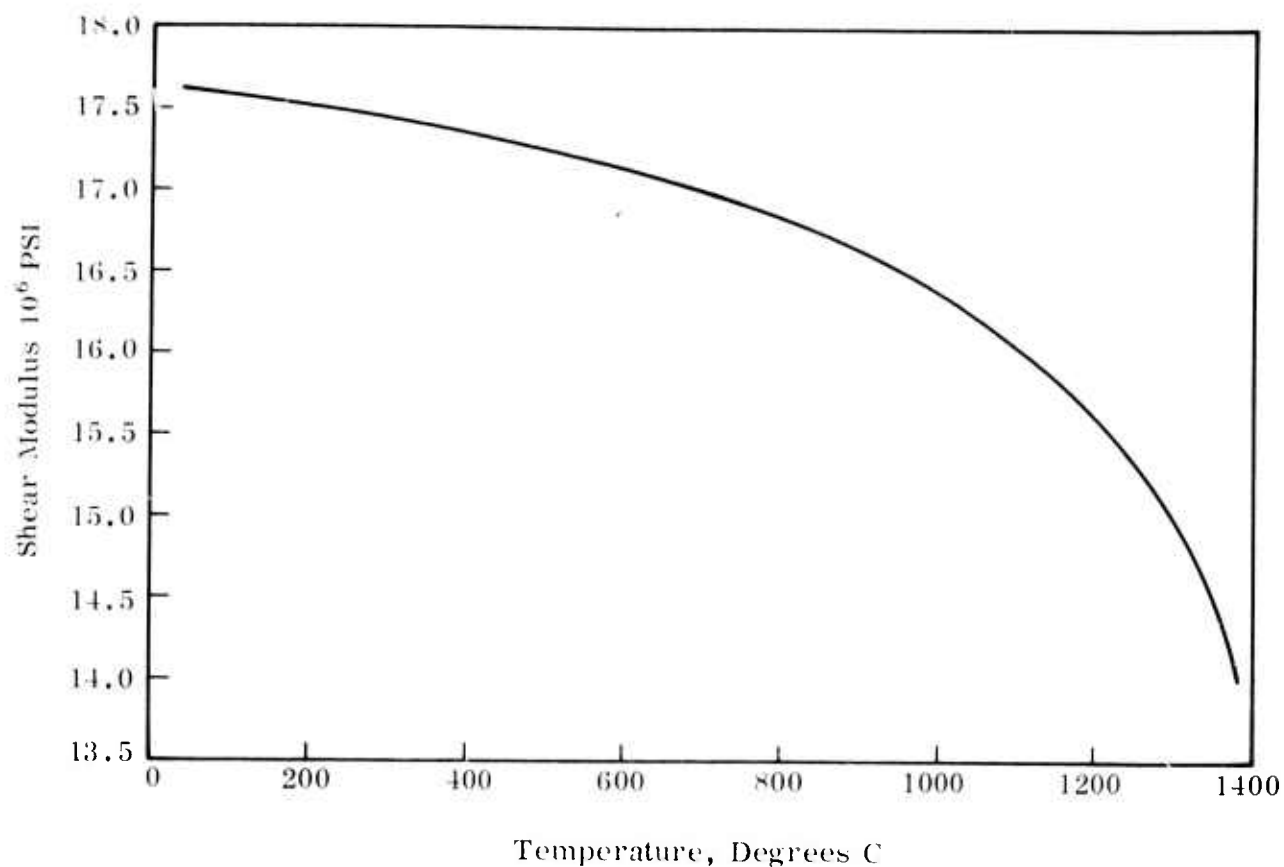


Figure 5.55 — Shear Modulus vs Temperature for Hot Pressed  $\text{Si}_3\text{N}_4$   
Calculated from Young's Modulus Curve and Assumed  
Poisson's Ratio Curve

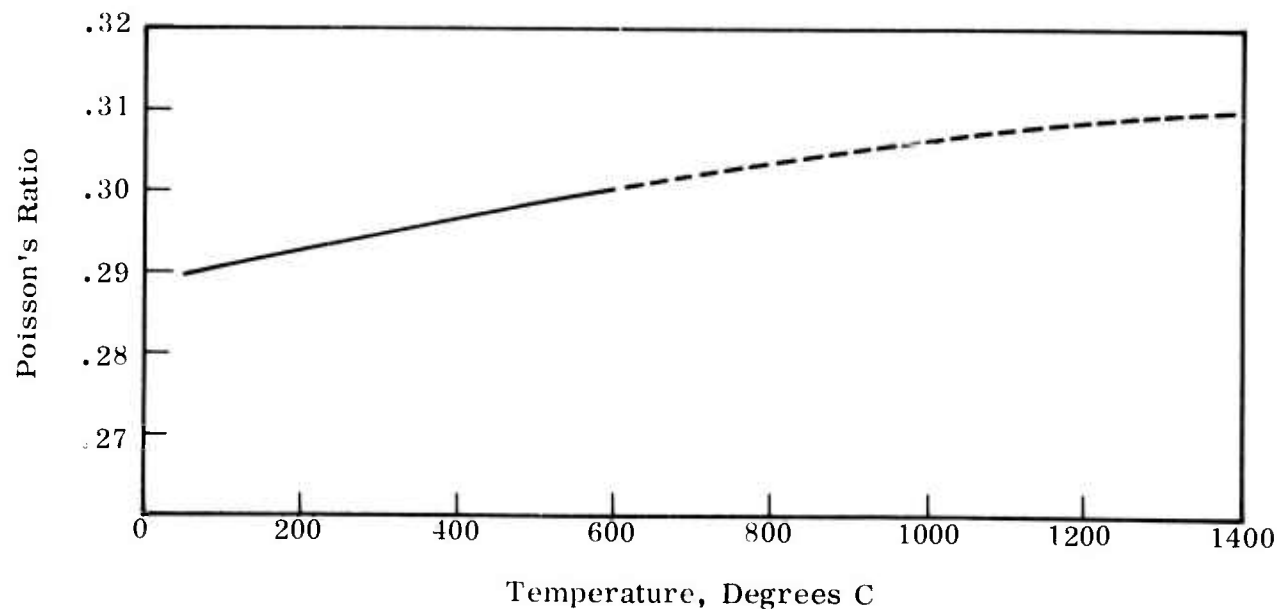


Figure 5.56 — Poisson's Ratio vs Temperature for Hot Pressed  
Silicon Nitride Assumed from Low Temperature Data  
and Shape of SiC Curve

### 5.2.3 MICROSTRUCTURE CHARACTERISTICS OF HOT PRESSED SILICON NITRIDE

#### Introduction

The microstructural details that control the physical properties of silicon nitride and silicon carbide must themselves be controlled in order to make these materials behave properly and reliably in service. Since fabrication procedures originally determine the microstructure and ultimately affect the engineering performance of the ceramic, correct interpretation of microstructure effects is the first order requirement to be able to correlate properties, microstructure, and fabrication.

Improved processing controls, both in powder preparation and hot pressing, need to be exercised in order to improve the properties and reliability of available hot-pressed silicon nitride.

#### Microstructural Aspects of Hot Pressed Si<sub>3</sub>N<sub>4</sub>

Two grades of Si<sub>3</sub>N<sub>4</sub>, designated HS-110 and HS-130, respectively, were received from the Norton Company in the form of hot pressed billets 6.3 x 6.3 x 1.3 inches thick. Characterization of the material consisted of the following investigations: chemical analysis; powder and diffractometer x-ray diffraction; grain morphology using scanning, replica, and transmission electron microscopy; inclusion and impurity distribution using light and transmission microscopy; microprobe analysis; and dislocation structure and distribution. Where dislocation structures were discussed in the First Semi-Annual Report<sup>(1)</sup>, this report discusses the current results on grain morphology, inclusions, defects, and impurities.

Typical spectrographic analyses of the two grades of material are shown in Table 5.8. The analysis of the NBS standard for commercially pure silicon is also shown. It is apparent that the major impurities, apart from magnesium in the hot pressed material, can be traced to the starting silicon powder. One should also note the lower levels of calcium and aluminum in the HS-130 grade. So far, no other major differences between the two grades of material have been found. It is shown in Section 5.1.3 of this report that the difference in the mechanical behavior of these two grades of material is in the improved high temperature tensile, flexural, and fatigue strengths of the HS-130 grade, while no difference in the room temperature strengths was found. This suggested that the improved strength is due mainly to the low calcium level. An investigation is now underway to obtain a quantitative correlation between the amount of calcium and high temperature strength.

TABLE 5.8  
SPECTROGRAPHIC ANALYSIS OF Si<sub>3</sub>N<sub>4</sub> (ABOVE 0.001 W/O)

Material	Si	Mg	Fe	Ca	Cr	Co	Mo	Mn	Cu	Ti	Al	Ni	C	B	Na
NbS #57 Refined Si	96.8	0.01	0.65	0.73	0.025	—	—	0.034	0.02	0.10	0.67	0.002	0.09		
HS-110	Major	0.8	0.8	0.5	0.01	—	0.02	0.03	0.005	0.01	1.0	0.02	0.19	0.1	0.002
HS-130	Major	0.8	0.9	0.04	0.05	0.04	—	0.05	0.004	0.02	0.1	0.01	0.49	0.1	0.002

Anisotropy in flexural strength, at all temperatures, was related to the position of the test specimens with respect to the original billet. Specimens machined with the tensile axis parallel to the hot pressing direction exhibit lower strength, by about 25%, when compared to specimens cut with the tensile axis perpendicular to the hot pressing direction. It was initially postulated that this phenomenon is due to a preferred orientation of elongated grains. The data presented here do not confirm this hypothesis, but do indicate the apparent reasons for the observed anisotropy in strength.

Figure 5.57a shows a composite micrograph of replicas taken off the three perpendicular faces of the hot pressed billet. One cannot detect any apparent difference in grain orientations. In all cases a bimodal distribution of grain sizes was measured — about 80% of the grains are equiaxed and vary in size between 0.5 and 2  $\mu\text{m}$ . The other 20% of the grains have an elongated appearance with the short axis between 1-2  $\mu\text{m}$  and the long axis 4-10  $\mu\text{m}$ . Both types of grains have been identified by electron diffraction as the  $\beta$  phase of  $\text{Si}_3\text{N}_4$ . About 1% of the elongated grains are larger, up to 30  $\mu\text{m}$  long. These grains were identified as the  $\alpha$  phase of  $\text{Si}_3\text{N}_4$ . Pole-figure analysis on both the (0002) and (10 $\bar{1}\bar{1}$ ) reflections indicated a complete random orientation of grains.

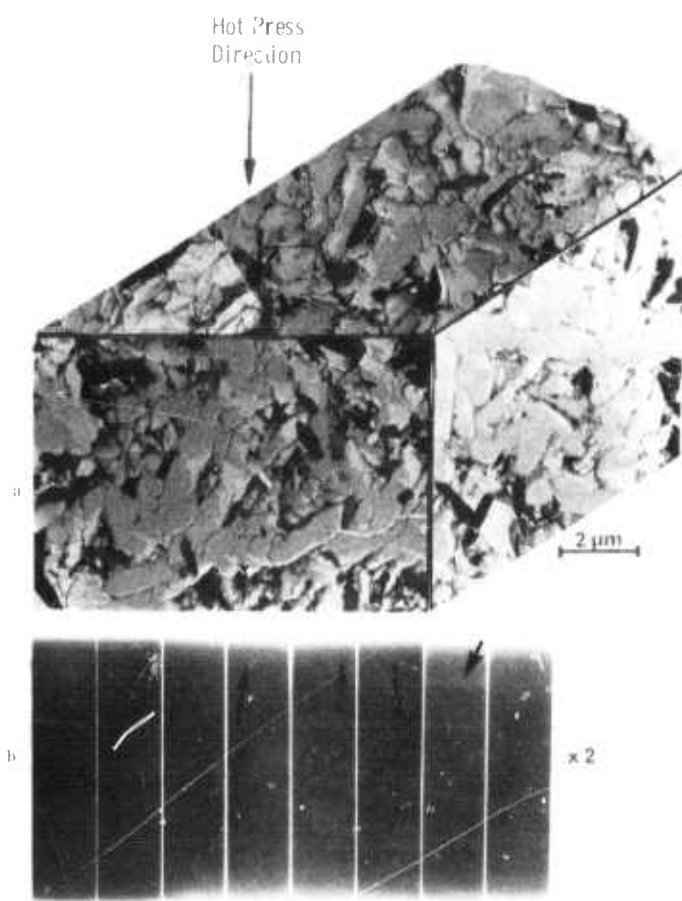


Figure 5.57 — Typical Features of an As-Received  $\text{Si}_3\text{N}_4$  Billet

- Composite replica micrograph showing grain morphology on three perpendicular faces
- Radiograph of specimens cut along the billet thickness showing flaws and variable density layers

Figure 5.57b is a print (2X) of an x-ray radiograph taken from specimens cut along the thickness of the billet so that when tested in a four-point flexural mode the tensile axis is parallel to the hot pressing direction. A close examination of the radiograph shows two possible reasons for the lower strength displayed by these specimens. The variations in intensity indicate layers of varying density which may be a result of gradients in pressure along the pressure axis. The boundaries between the zones of varying density could cause a decrease in strength when the applied stress acts perpendicular to these boundaries. One should also note the numerous flaws marked by arrows. The dark flaws indicate inclusions of higher density than the parent material, while the white flaws indicate areas of lower density, possibly small cracks.

Almost all the marked flaws are elongated in the same orientation, and could be envisioned as spherical flaws (particles or voids) which were squashed to a lenticular shape during hot-pressing. If we assume that the fracture strength of the material is generally governed by the Griffith relation

$$\sigma = A \sqrt{\frac{\gamma E}{c}} \quad (1)$$

where  $\gamma$  is the fracture energy,  $E$  the elastic modulus and  $c$  the critical crack size, it is easy to show that a lenticular flaw will contribute a different crack length  $c$  depending on the orientation of the flaw with respect to the applied stress  $\sigma$ . Figure 5.57b indicates that  $c$  is larger when the applied stress is parallel to the hot pressing direction, hence, the lower strength measured in this orientation. Although one obtain an estimate for  $c$  from Fig. 5.57b, comparison of the fracture stress,  $\sigma$ , calculated from Eq. (1) with the flexural test data is not yet possible, because the exact location of the flaws with respect to the tensile surface is not known. Further work is planned to establish these relations in a quantitative manner.

In a few cases, however, the large inclusions were directly related to premature failures of flexural specimens as shown in Fig. 5.58, and fatigue specimens, Fig. 5.59. The three specimens shown in Fig. 5.58 were selected from a group of 20 specimens tested at 2350°F, in air, at a cross head velocity of 0.02 in/min. The average strength of this group was 69,000 psi, and the decrease in strength due to the presence of inclusions would amount to as much as 35%.

The most commonly found inclusion is a particle of free silicon, as shown in Fig. 5.58a. This particle is located below the most highly stressed portion of the tensile surface. The micrograph indicates clearly that failure originated at the particle-matrix interface.

Another frequently observed inclusion is an iron rich particle, as shown in Fig. 5.58b. Probe analysis indicates that these inclusions are some form of an iron-silicon compound. A rarely found inclusion is shown in Fig. 5.58c which depicts a magnesium rich particle, probably a magnesium silicate, at the bottom of the round hole.

If the assumption is made that the inclusions define the size of a critical flaw, Eq. (1) can be applied. Since  $\gamma$  and  $A$  are not known for these particular test conditions, Eq. (1) is rewritten in the form

$$\sigma \sqrt{e} = \text{constant} \quad (2)$$

where  $\sigma$  is the stress at the flaw and  $e$  is the flaw size. The estimated flaw sizes are marked by the arrows in Fig. 5.58 and are, respectively,  $270 \mu\text{m}$ ,  $220 \mu\text{m}$  and  $140 \mu\text{m}$ .

The corresponding stresses at the flaw are:  $\sigma = 40,000$  psi for the silicon particle, which is below the surface and hence the real stress is lower than that calculated from the overall specimen's dimension;  $\sigma = 45,500$  psi for the iron

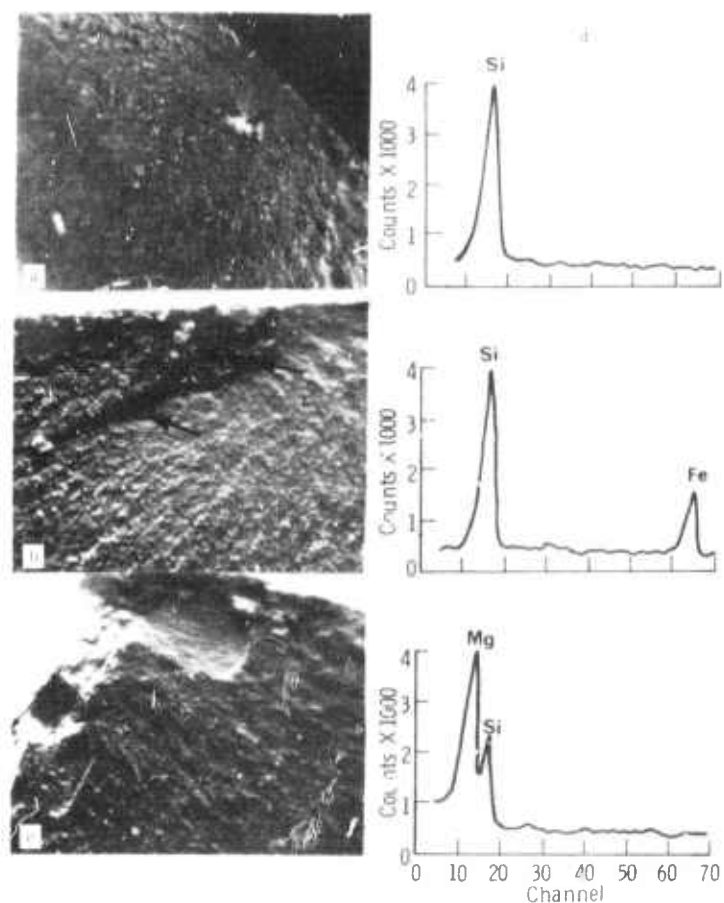


Figure 5.58 — Common Inclusions on Fractured Surfaces Causing Strength Degradation. Four Point Bend Specimens, Tested at  $2350^{\circ}\text{F}$ . Average Strength (20 Specimens) 69,000 psi

- Free silicon inclusion failed at 58,000 psi light micrograph 35X
- Iron-rich inclusion. Failed at 45,500 psi, SEM micrograph, 130X
- Mg-rich inclusion. Failed at 57,800 psi, SEM micrograph, 140X
- Energy dispersive x-ray analysis of Inclusions

rich particle; and  $\sigma = 57,800$  psi for the magnesium rich inclusion. Thus, we obtain.

	<u>Particle A</u>	<u>Particle B</u>	<u>Particle C</u>
$c \mu m$	290	220	140
$\sigma$ psi	40,000	45,500	57,800
$\sigma \sqrt{c} \times 10^6$	680	675	685

The above table demonstrates that inclusions, such as shown in Fig. 5.58, may be regarded as critical flaws that cause a serious degradation in the strength of the material.

The foreign inclusions shown in Fig. 5.59 were found to affect fatigue tests as well. Figure 5.59 shows two examples where the free silicon inclusions acted as stress raisers. Slow crack growth was induced at the particle matrix interface, which is clearly evident in Fig. 5.59b. Figure 5.59a shows shear marks similar to fatigue marking found on metal specimens. Failure of the specimen could have been initiated by the fatigue failure of the soft silicon inclusion.



Figure 5.59 — Large Inclusions That Caused Premature Failures in Fatigue Specimens

- Room temperature fatigue tests, HS-110 material, specimen failed at 60,000 psi. Fatigue limit 70,000 psi
- Fatigue Specimen tested at 2350°F, 40,000 psi. HS-130 material. Specimen failed after 8 min. Average life for these conditions — 1 hr. See section 5.1.3 of this report

The distribution of the major impurity elements was examined by microprobe analysis. Typical results for the HS-110 material are shown in Fig. 5.60. Similar results, with lower levels of calcium and aluminum, were obtained for the higher grade HS-130 material. The scanning of the five elements was done over the same area but no correlation between the signatures of the various elements is obvious, nor is it possible to state whether the elements are concentrated in the boundaries or the grain interior. This is due to the fact that the probe beam diameter is about  $2 \mu m$ , which is of the order of the grain size. Figure 5.61 indicates numerous clusters of iron which, in a few cases, extend

over  $50 \mu\text{m}$  length. Most of these clusters are about  $10 \mu\text{m}$  in diameter, as shown in Fig. 5.60b. There is no apparent change in intensity of the silicon count (Fig. 5.60a) over the iron rich areas which is interpreted to indicate that iron is present as an iron-silicon compound. More detailed analytical work is planned to define the composition and distribution of the iron rich clusters.

Impurity distributions on a microscopic level are shown in Fig. 5.62. Figure 5.62a is a replica transmission micrograph taken off the fractured surface of a fatigue specimen near the fracture origin. This particular specimen failed prematurely in a fatigue test. It is possible that the concentration of fine impurity particles was the source of failure. Figure 5.62b shows an area occasionally found in thin foil transmission micrographs, depicting a cluster of particles within a large grain. These particles were too small for a positive electron diffraction identification. One should note the strain fields (dark semi-rings) that are associated with the particles. This could be due to strains that occurred during cooling after hot pressing, as a result of differential thermal expansion between the particles and the  $\text{Si}_3\text{N}_4$  matrix.

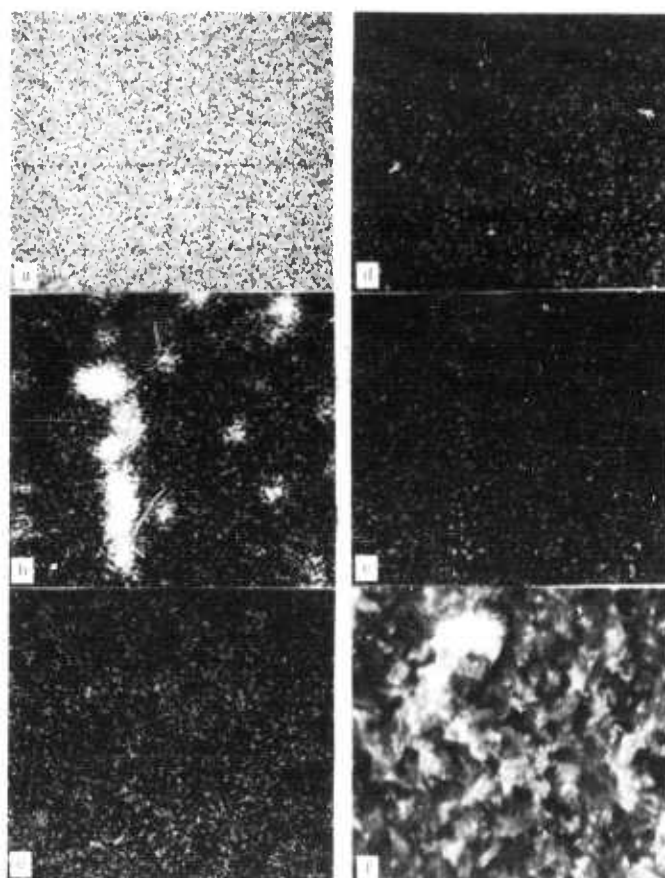


Figure 5.60 — Distribution of Impurity Elements. Microprobe Analysis, HS-110 Material. 1600X

- a)  $\text{Si K}_\alpha$ , 400 c/s. b)  $\text{Fe K}_\alpha$ , 62 c/s. c)  $\text{Mg K}_\alpha$ , 76 c/s.
- d)  $\text{Ca K}_\alpha$ , 40 c/s. e)  $\text{Al K}_\alpha$ , 76 c/s. f) Reference scanning electron micrograph. Note segregation of iron, without depletion of Si

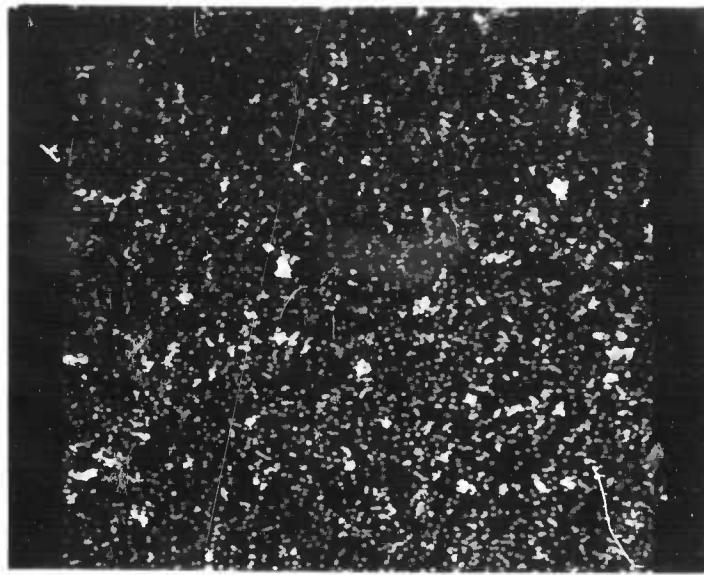


Figure 5.61 — Low Magnification (335X) Microprobe Scanning Micrograph Showing Fe Distribution in HS-130 Grade Material. Clusters are About  $10 \mu\text{m}$  in Diameter

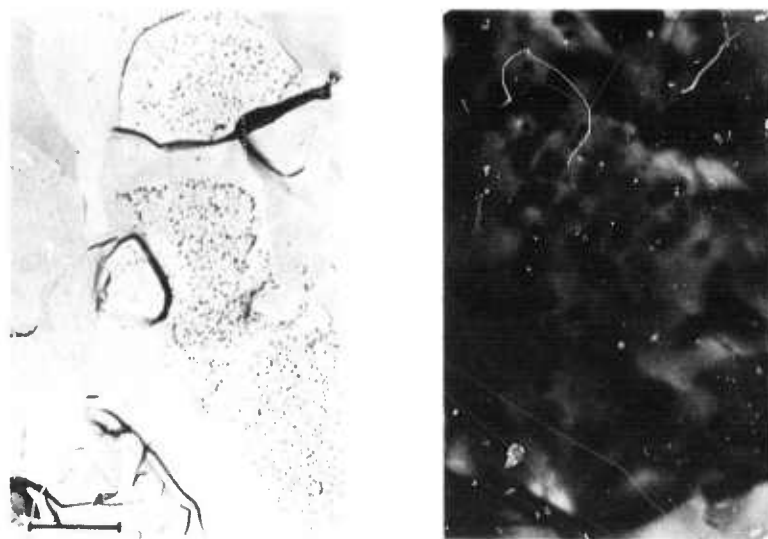


Figure 5.62 — Microscopic Distribution of Impurity Particles.  $0.5 \mu\text{m}$  Scale Bars

- a) Two stage carbon replica, fracture surface, premature failure of fatigue specimen. HS-110
- b) Transmission micrograph, HS-130

The First Semi-Annual Report (1) stated that no evidence was found for the existence of a grain boundary phase. The existence of a glassy phase, probably magnesium-silicate, is inferred from the theories advanced to explain the process of densification of  $\text{Si}_3\text{N}_4$ . It was postulated that during hot pressing and the transformation from the  $\alpha$  to the  $\beta$  structure, a low melting ( $\sim 1450^\circ\text{C}$ ) magnesium silicate is forming, which promotes densification by a liquid-sintering mechanism. Indirect evidence in support of a glassy boundary phase is implied in the creep data which indicate a grain boundary sliding mechanism. It was assumed that failure to observe a boundary phase in the Norton hot pressed material may be due to its small volume. Thin foils were examined which were prepared from material hot pressed with 5% MgO, as compared to about 1% MgO in the Norton material. Figure 5.63 shows two areas in a thin foil prepared from the 5% MgO material, which indicate a boundary phase (marked by arrows). The location of this dark phase at grain junctions is particularly significant. It should also be mentioned that many of these areas did not change contrast upon tilting, an effect usually displayed by an amorphous phase.

Six powder patterns from different billets were run for each of the two grades of  $\text{Si}_3\text{N}_4$ . It is of interest to note that the impurities and inclusions discussed earlier are not detected by powder x-ray diffraction. For both materials the  $\beta$  structure is the only recorded phase of  $\text{Si}_3\text{N}_4$ . There is, however, one difference between the two grades —  $\text{SiO}_2$  lines are observed in the HS-110 material, while  $\text{Si}_2\text{ON}_2$  lines are observed in the HS-130.

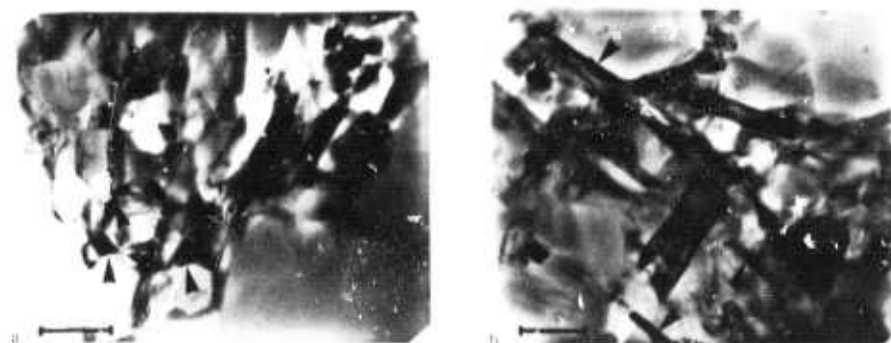


Figure 5.63 — Transmission Electron Micrographs of  $\text{Si}_3\text{N}_4$  Hot Pressed With 5% MgO. 1  $\mu\text{m}$  Scale Bars. Arrows Indicate a Grain Boundary Phase, Possibly Amorphous

#### 5.2.4 GAS-SOLID REACTIONS

##### Introduction

Compared to the thousands of hours expected from gas turbine components, the few hundred hours of testing possible in the pressurized test passage leaves unanswered questions about the effect of impurities on the long-term corrosion-erosion resistance of silicon nitride and silicon carbide. Since this long term reliability depends on the nature and stability of an oxide surface layer, the oxidation and sulfidation kinetic processes are important. This section discusses progress on the static oxidation of hot-pressed silicon nitride and the results obtained from characterizing the oxide film that develops.

##### Thermochemical Considerations

When silicon nitride is exposed to oxidizing atmospheres at elevated temperatures, a passive layer of  $\text{SiO}_2(\text{s})$  is formed on the surface. At low oxygen pressures, several gaseous species, e.g.,  $\text{Si}(\text{g})$ ,  $\text{Si}_2(\text{g})$ ,  $\text{Si}_3(\text{g})$ ,  $\text{SiO}(\text{g})$ ,  $\text{SiO}_2(\text{g})$  can form by the volatilization of this surface oxide. Table 5.9 gives Gibb's free energy of formation of these gaseous species at 1200 to 1600°K, taken from the JANAF Tables. (19) Using these data, the partial pressures of various volatile species over  $\text{SiO}_2(\text{s})$  were calculated at 1600°F. These values are shown in Fig. 5.64 as a function of oxygen partial pressure in the surrounding atmosphere.

TABLE 5.9  
Thermochemical Data For The Si-N-O System

Species and Compounds	$G_f^\circ$ , cal mole $^{-1}$		
	1200°K	1400°K	1600°K
$\text{Si}_3\text{N}_4(\text{s})$	- 83,008	- 67,354	- 51,850
$\text{SiO}_2(\text{s})$	- 166,296	- 158,134	- 150,027
$\text{Si}(\text{g})$	65,257	58,335	51,459
$\text{Si}_2(\text{g})$	87,392	78,806	70,306
$\text{Si}_3(\text{g})$	93,331	84,131	75,084
$\text{SiO}(\text{g})$	- 48,672	- 52,491	- 56,244
$\text{SiO}_2(\text{g})$	- 73,755	- 73,753	- 73,722

Gas turbines operate with highly oxidizing gas mixtures, typically with air to fuel ratio of 50:1. Therefore, the oxygen partial pressure in a gas turbine is close to 0.2 atm, the oxygen partial pressure in air. It is evident from Fig. 5.64 that the predominant volatile species over  $\text{SiO}_2(\text{s})$  at this oxygen pressure is  $\text{SiO}_2(\text{g})$  with a partial pressure of about  $10^{-10}$  atm, which is negligible. The

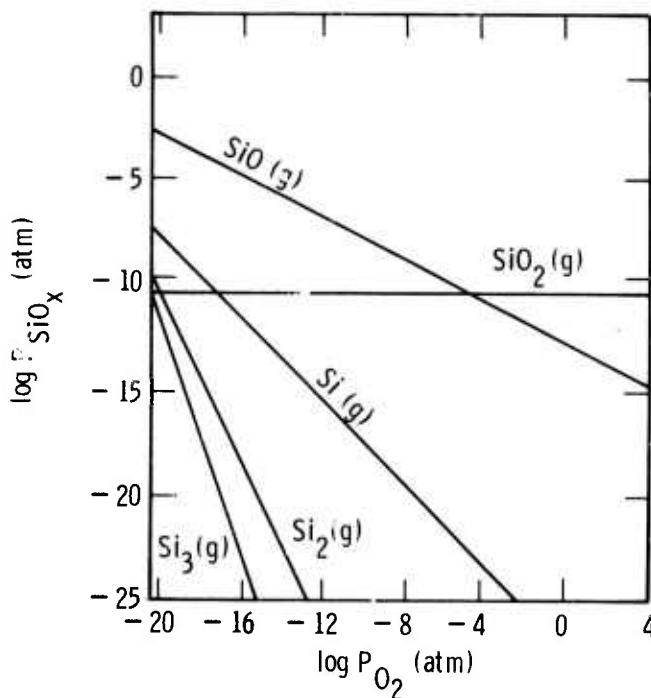
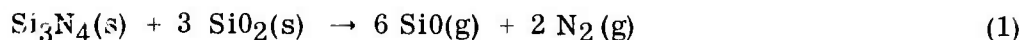


Figure 5.64 — Pressures of Various Volatile Species Over  $\text{SiO}_2$  (s) at  $1600^\circ\text{K}$

partial pressures of  $\text{SiO(g)}$  and other volatile species which can form over  $\text{SiO}_2(\text{s})$  are even lower than that of  $\text{SiO}_2(\text{g})$ , and therefore, the volatilization of the surface oxide ( $\text{SiO}_2$ ) to form various volatile species will not play any important role in the oxidation of  $\text{Si}_3\text{N}_4$  in gas turbines.

However,  $\text{SiO}_2(\text{s})$  formed at the surface of  $\text{Si}_3\text{N}_4$  can react at the  $\text{Si}_3\text{N}_4$  -  $\text{SiO}_2$  interface to produce  $\text{SiO(g)}$  according to the reaction:



At low enough oxygen pressures, if all the surface oxide is reacted according to the above reaction, then a bare  $\text{Si}_3\text{N}_4$  surface will be exposed causing active oxidation of  $\text{Si}_3\text{N}_4$  by the formation of volatile  $\text{SiO(g)}$ . Wagner<sup>(20)</sup> has developed a theory to interpret the transition between active (weight loss by the formation of  $\text{SiO(g)}$ ) oxidation of silicon found at low oxygen partial pressures and passive (weight gain by the formation of  $\text{SiO}_2(\text{s})$ ) oxidation at higher oxygen partial pressures. He derived the following equation for calculating the maximum partial pressure of oxygen,  $P_{\text{O}_2}$  (max), for maintaining an oxide-free surface of silicon:

$$P_{\text{O}_2} \text{ (max)} \approx 1/2 (D_{\text{SiO}}/D_{\text{O}_2})^{1/2} P_{\text{SiO}} \text{ (eq)} \quad (2)$$

where  $P_{\text{SiO}} \text{ (eq)}$  is the equilibrium pressure of silicon monoxide at the  $\text{Si}(\text{s})$  -  $\text{SiO}_2(\text{s})$  interface.  $(D_{\text{SiO}}/D_{\text{O}_2})$  is the ratio of diffusion constants for  $\text{SiO(g)}$  and  $\text{O}_2(\text{g})$  in the boundary layer gas mixture which Wagner estimated to have a value of 0.64 from the molecular weights and diameters of  $\text{SiO(g)}$  and  $\text{O}_2$  molecules. Equation (2) can therefore be written as

$$P_{\text{O}_2} \text{ (max)} \approx 0.4 P_{\text{SiO}} \text{ (eq)} \quad (3)$$

The same analysis has been made for the oxidation of  $\text{Si}_3\text{N}_4$  to calculate  $P_{\text{O}_2}$  (max.), the oxygen pressure below which surface oxide reacts with silicon nitride to form volatile  $\text{SiO(g)}$  according to reaction (3), and above which a stable  $\text{SiO}_2(\text{s})$  layer is maintained. The values of  $P_{\text{SiO}}(\text{eq})$  were calculated by using the thermodynamic data in Table 5.9 assuming stoichiometric formation of  $\text{SiO(g)}$  and  $\text{N}_2(\text{g})$  in reaction(1). Table 5.10 lists  $P_{\text{SiO}}(\text{eq})$  and  $P_{\text{O}_2}$  (max) values at different temperatures in the range 1200 to 1600°K. Since oxygen pressures encountered in gas turbines are much higher than the values of  $P_{\text{O}_2}$  (max) in Table 5.10, a stable  $\text{SiO}_2(\text{s})$  layer will be maintained on the surface of  $\text{Si}_3\text{N}_4$ . Any  $\text{SiO(g)}$  formed at the  $\text{Si}_3\text{N}_4(\text{s})$  -  $\text{SiO}_2(\text{s})$  interface by reaction diffuses outwards through the pores and/or fissures in the surface oxide layer and is oxidized to  $\text{SiO}_2(\text{s})$  by reaction with oxygen. This helps in healing of the pores and fissures in the surface oxide layer.

### Static Oxidation

The dynamic corrosion erosion testing in the turbine test passage is being supplemented by static oxidation studies on  $\text{Si}_3\text{N}_4$ . Static oxidation testing is necessary to understand the long term corrosion-kinetics of  $\text{Si}_3\text{N}_4$  in a gas turbine. Static oxidation testing also provides a quick method for comparing oxidation resistance of different grades of  $\text{Si}_3\text{N}_4$  and thus helps in the development of material with improved oxidation resistance and other related properties.

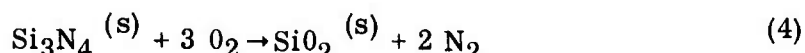
TABLE 5.10

Theoretical Values of Maximum Oxygen Pressures to Remove All the Oxide on Silicon Nitride Surface

Temperature °K	$P_{\text{SiO}}$ (eq) atm	$P_{\text{O}_2}$ (max) atm
1200	$3.3 \times 10^{-7}$	$1.32 \times 10^{-7}$
1400	$4.9 \times 10^{-5}$	$1.96 \times 10^{-5}$
1600	$2.0 \times 10^{-3}$	$8.0 \times 10^{-4}$

The oxidation kinetics of  $\text{Si}_3\text{N}_4$  was studied by continuous thermogravimetry using an automatic Cahn electrobalance with a sensitivity of  $2 \times 10^{-6}$  gram. The details of the experimental apparatus and procedure are given in the first semi-annual report<sup>(1)</sup>. In short, the specimen to be studied was cut in the form of a 0.5" x 0.5" x 0.050" plate and maintained at the desired temperature in pure dried oxygen flowing at the rate of 50 ml/min. The changes in the weight of the specimen were continuously recorded as a function of time on a strip chart recorder.

Silicon nitride oxidizes to silicon oxide ( $\text{SiO}_2$ ) according to the reaction:



The weight gained on oxidation represents the weight difference between  $\text{Si}_3\text{N}_4$  and 3  $\text{SiO}_2$ .

### Oxidation of Different Grades of $\text{Si}_3\text{N}_4$

Figure 5.65 summarizes weight gain data as a function of time for oxidation of different grades of  $\text{Si}_3\text{N}_4$  at  $2300^{\circ}\text{F}$  in 1 atm oxygen. Curve A gives oxidation rate for Norton HS-110 silicon nitride while curves B, C and D show oxidation rates for specimens from three different billets of Norton HS-130 silicon nitride. The weight gain for HS-110 silicon nitride after 29 hours of oxidation is more than twice as large as that for HS-130 silicon nitride. This increased oxidation rate of HS-110 silicon nitride is due to a much higher level of impurities (Ca, Fe, Al, Mn) as shown in Table 5.8. The weight gains for three different billets of HS-130  $\text{Si}_3\text{N}_4$  are nearly the same and fall within the range of experimental error. All further oxidation work reported in this section was carried out on Norton HS-130 silicon nitride.

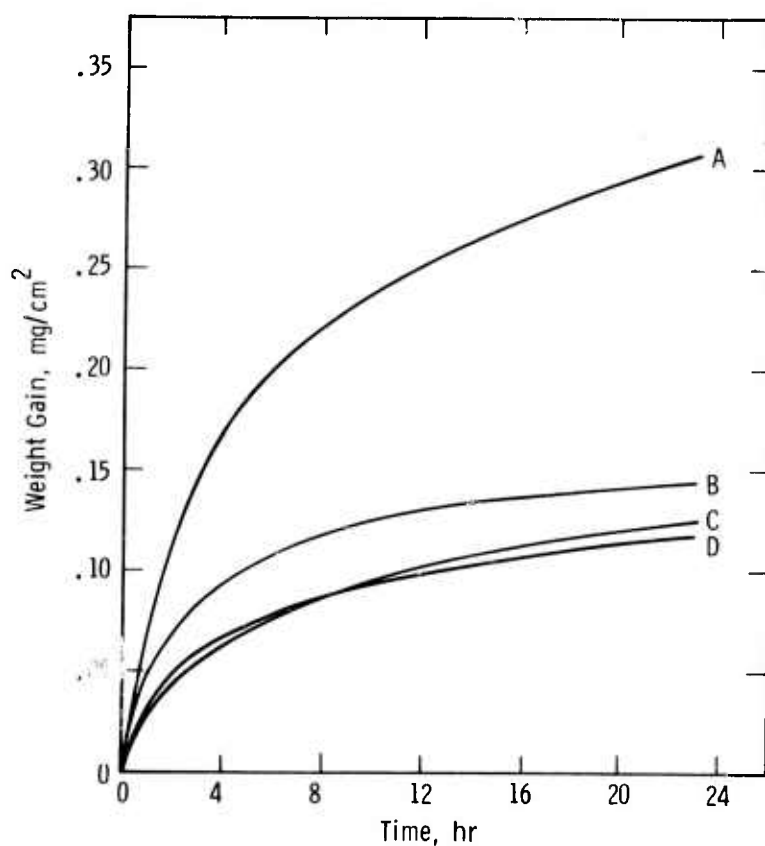


Figure 5.65 — Comparison of Oxidation Rates of Different Grades of Norton  $\text{Si}_3\text{N}_4$  at  $2300^{\circ}\text{F}$  in Oxygen at 1 Atmosphere Pressure  
Curve A: Grade HS-110  
Curve B: Grade HS-130 Billet #309902-1  
Curve C: Grade HS-130 Billet #309902-2  
Curve D: Grade HS-130 Billet #309902-3

### Effect of Temperature on Oxidation of $\text{Si}_3\text{N}_4$

Figure 5.66 shows weight gain data for oxidation of silicon nitride in 1 atm oxygen at temperatures in the range  $2000$  to  $2500^{\circ}\text{F}$ . No detectable weight gain was observed for oxidation at  $1800^{\circ}\text{F}$ . For initial oxidation up to about 8-10

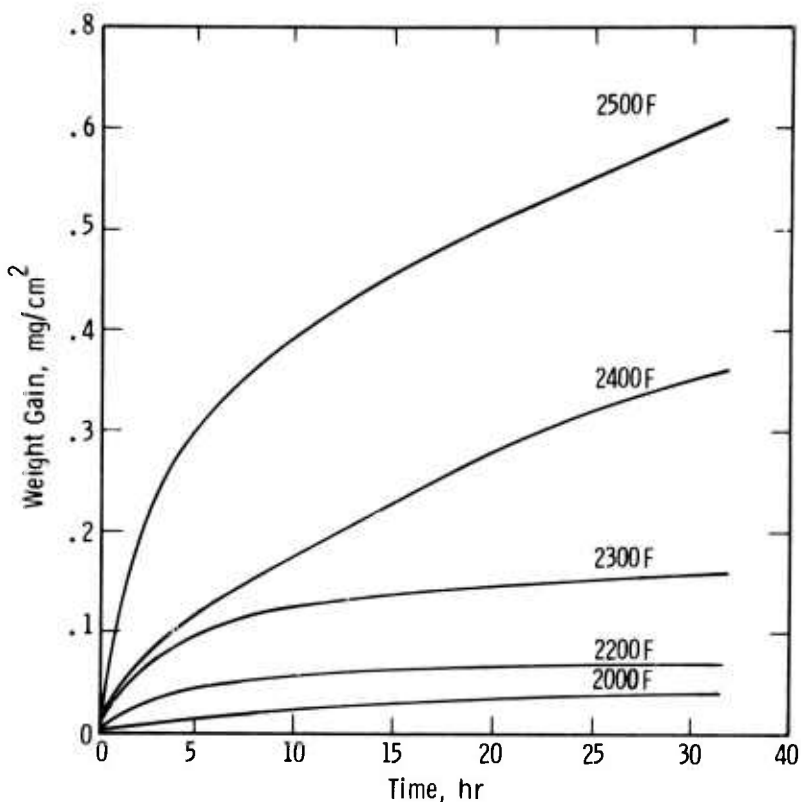


Figure 5.66 — Effect of Temperature on Oxidation of Norton HS-130  $\text{Si}_3\text{N}_4$  in Oxygen at 1 Atmosphere Pressure

hours, the weight gain vs time curve at each temperature approximates a parabola. This parabolic oxidation behavior can be represented by the equation:

$$W^2 = K_p t$$

where  $W$  is the weight gain at time  $t$ , and  $K_p$  is the parabolic rate constant. Figure 5.67 shows a plot of square of the weight gain ( $W^2$ ) as a function of time ( $t$ ) for several different temperatures. The straight lines represent a region of initial parabolic oxidation. After this initial oxidation for about 8-10 hours, the curves start to deviate from the parabolic behavior and the weight gain data do not follow any generalized mathematical behavior.

During initial oxidation, a compact oxide layer is formed on the surface of silicon nitride which grows by the inward diffusion of oxygen ions, giving the parabolic oxidation behavior as derived by Wagner.<sup>(20)</sup> However, during this stage, nitrogen gas is formed at the  $\text{Si}_3\text{N}_4(\text{s}) - \text{SiO}_2(\text{s})$  interface according to reaction (1). As oxidation progresses and more  $\text{N}_2(\text{g})$  is formed, it eventually builds up pressure at the interface and then bursts out, causing fissures and pores to form in the surface oxide film. This oxide film may continue to grow by diffusion of oxygen ions through the oxide lattice and also by gaseous diffusion of oxygen along cracks and pores. Such gas phase transport may cause healing of cracks and pores in the surface oxide film. Also, as explained under thermochemical considerations, any  $\text{SiO}(\text{g})$  formed at the  $\text{Si}_3\text{N}_4(\text{s}) - \text{SiO}_2(\text{s})$  interface is oxidized to  $\text{SiO}_2(\text{s})$  in pores and fissures by

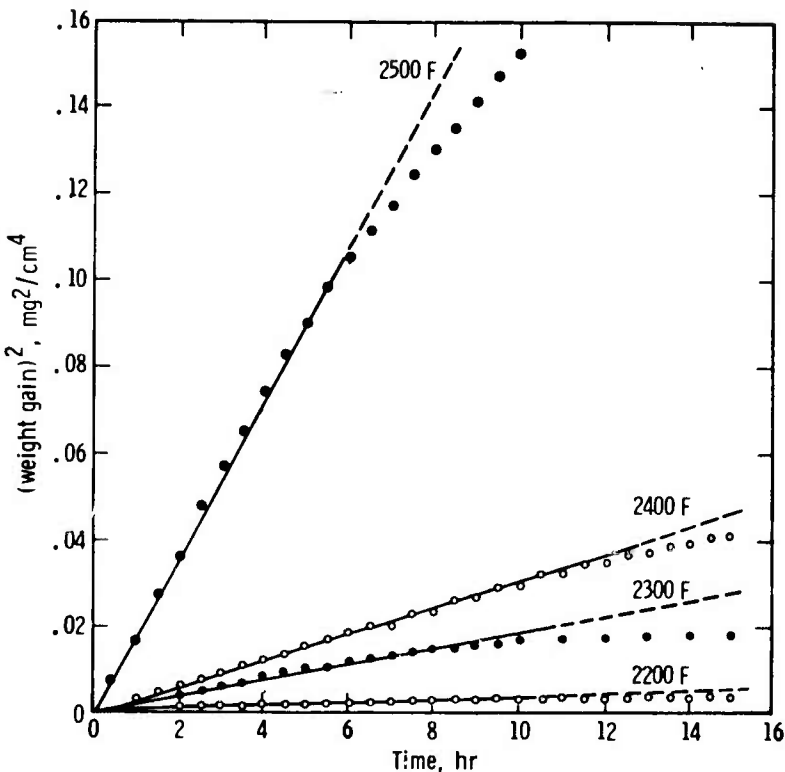


Figure 5.67 — Parabolic Plot of Oxidation of  $\text{Si}_3\text{N}_4$  in Oxygen at 1 Atmosphere Pressure

gas phase transport of oxygen. In addition to such gas phase transport, Impurities like Mg, Ca, Fe, Al, Mn, etc., present in silicon nitride diffuse out during oxidation, and either react with or dissolve in surface silica to form  $\text{MgSiO}_3$  and possibly other mixed silicates or glasses. All these processes give a variable oxidation behavior along the length of a reacting specimen, causing the weight gain vs time curves to deviate from the initial parabolic oxidation behavior.

The parabolic rate constants,  $K_p$ , for oxidation of silicon nitride in 1 atm oxygen at different temperatures are listed in Table 5.11. Each value of  $K_p$  was determined from the slope of the straight lines in Fig. 5.68. A plot of  $\log K_p$  against reciprocal temperature is shown in Fig. 5.68, where a straight line was drawn through all the experimental points by a least mean square analysis. Using Arrhenius equation:(21)

$$K_p = A \exp(-E/RT)$$

where  $E$  is the activation energy,  $R$  is the gas constant, and  $T$  is the absolute temperature, an activation energy of 89.5 kcal/mole is calculated from the slope of straight line in Fig. 5.68 for the oxidation of  $\text{Si}_3\text{N}_4$  at 1 atm oxygen pressure in the temperature range  $2000^{\circ}\text{F}$  to  $2500^{\circ}\text{F}$ .

Table 5.12 compares this activation energy with literature values for the parabolic oxidation of silicon and silicon carbide, which might be expected to show oxidation kinetics similar to that for silicon nitride since  $\text{SiO}_2(\text{s})$  is formed in all three cases. However, except for silicon, the variation in the activation energies in Table 5.12 is rather large, and suggests the possibility of different

TABLE 5.11  
 PARABOLIC RATE CONSTANTS FOR OXIDATION OF  
 $\text{Si}_3\text{N}_4$  IN 1 ATMOSPHERE OXYGEN

Temperature $^{\circ}\text{F}$	Parabolic Rate Constant, $K_p$ $\text{g}^2 \text{cm}^{-4} \text{sec}^{-1}$
2000	$1.52 \times 10^{-14}$
2200	$1.07 \times 10^{-13}$
2300	$5.16 \times 10^{-13}$
2400	$8.33 \times 10^{-13}$
2500	$5.00 \times 10^{-12}$

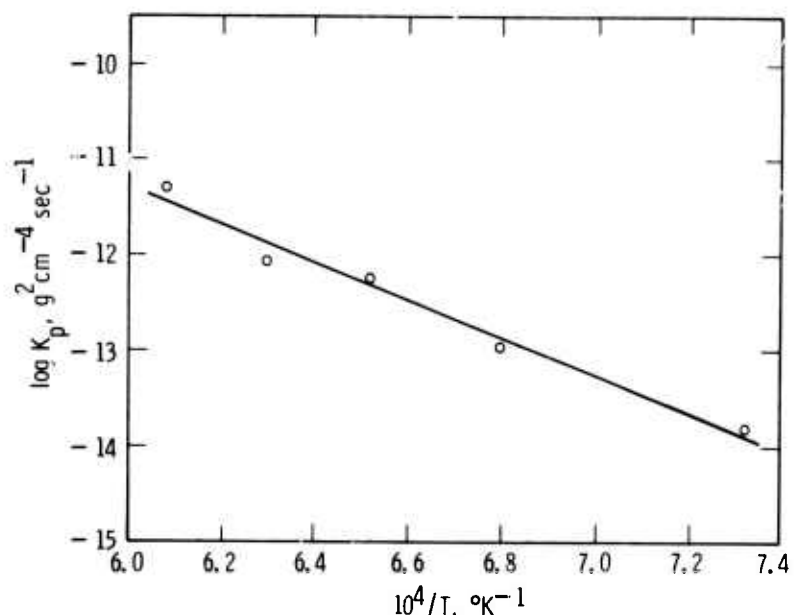


Figure 5.68 — Arrhenius Type Plot Showing Parabolic Rate Constant for Oxidation of  $\text{Si}_3\text{N}_4$  in 1 Atmosphere Oxygen as a Function of Temperature

mass transport mechanisms. Several factors might cause different activation energies for parabolic oxidation in a given system. Kofstad (22) discusses this in considerable detail; for example, a change from extrinsic to intrinsic controlled diffusion is possible with an increase in temperature, causing the activation energy to depend on both the purity of the material and the temperature.

The activation energies for the diffusion of oxygen in fused  $\text{SiO}_2$  range from 71 kcal/mole reported by Sucov (23) to 29 kcal/mole

TABLE 5.12  
COMPARISON OF ACTIVATION ENERGIES FOR PARABOLIC OXIDATION

<u>System</u>	<u>Temp. Range °F</u>	<u>Activation Energy kcal/mole</u>	<u>Reference</u>
$\text{Si}_3\text{N}_4$ in $\text{O}_2$	2000-2500	89.5	This Work
$\text{Si}_3\text{N}_4$ in air	1950-2445	68	(24)
$\text{Si}_3\text{N}_4$ in $\text{O}_2$	1950-2445	61	(24)
$\text{SiC}$ in $\text{O}_2$	1650-2910	20.2	(25)
$\text{SiC}$ in $\text{O}_2$	2200-2730	66	(21)
$\text{SiC}$ in $\text{O}_2$ or air	1830-2200	60	(26)
$\text{Si}$ in $\text{O}_2$	1830-2200	29.8, 30, 30.6	(27, 28, 29)

reported by Williams.<sup>(31)</sup> Sucov suggests the diffusion of oxygen ions as the dominant diffusion mechanism in fused  $\text{SiO}_2$ . The Norton HS-130 silicon nitride contained about 1%  $\text{MgO}$  in addition to smaller quantities of  $\text{Ca}$ ,  $\text{Fe}$ ,  $\text{Al}$ ,  $\text{Mn}$ , etc., and the surface oxide film consisted of  $\text{MgSiO}_3$  and possibly other mixed silicates. Comparing with Sucov's work, an activation energy of 89.5 kcal/mole suggests that the oxidation of  $\text{Si}_3\text{N}_4$  is controlled by the diffusion of oxygen ions through a surface film containing  $\text{SiO}_2$ ,  $\text{MgSiO}_3$  and possibly other mixed silicates of  $\text{Ca}$ ,  $\text{Fe}$ ,  $\text{Al}$ , etc.

#### Effect of Oxygen Partial Pressure on Oxidation of $\text{Si}_3\text{N}_4$ -

Figure 5.69 summarizes weight gain data for oxidation of  $\text{Si}_3\text{N}_4$  in various oxygen-nitrogen gas mixtures at  $2300^{\circ}\text{F}$  temperature and 1 atm total pressure. The oxidation rate of  $\text{Si}_3\text{N}_4$  decreases with decreasing oxygen partial pressure in the gas mixture. However, the range of oxygen pressure studied, 0.25 to 1 atm, is very small and no attempt has been made to study the oxidation kinetics of  $\text{Si}_3\text{N}_4$  at very low oxygen partial pressures since these are not encountered in gas turbines.

#### Characterization of Surface Oxide Film -

The surface films on  $\text{Si}_3\text{N}_4$  specimens oxidized for 30 hours in 1 atm oxygen at temperatures of 1800 to  $2500^{\circ}\text{F}$  were characterized using x-ray diffraction, scanning electron microscopy, and electron microprobe analyses.

The oxide film from the surface of oxidized silicon nitride specimens was scraped and analyzed by taking x-ray Debye-Scherrer patterns using  $\text{Cu-K}\alpha$  radiation with an exposure time of 24 hours. The following phases were identified for specimens oxidized at different temperatures:

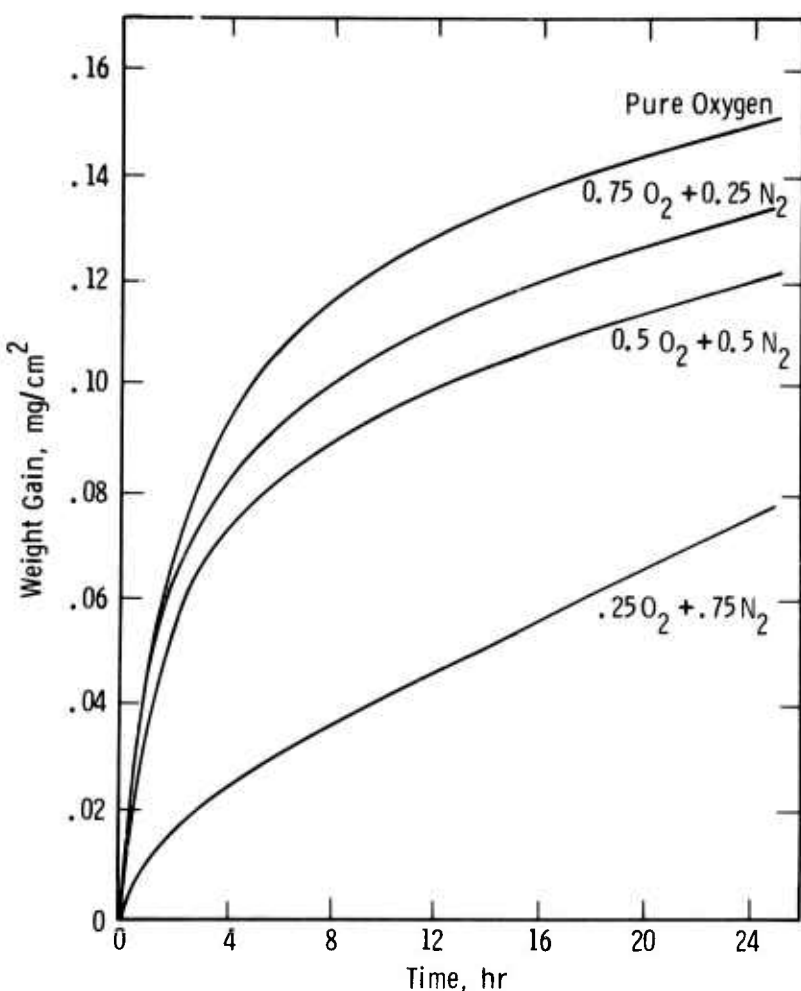


Figure 5.69 — Oxidation Rates for Norton HS-130  $\text{Si}_3\text{N}_4$  in Various Oxygen-Nitrogen Gas Mixtures at  $2300^{\circ}\text{F}$  and 1 Atmosphere Total Pressure

Unoxidized  $\text{Si}_3\text{N}_4$  -  $\beta$   $\text{Si}_3\text{N}_4$  (major),  $\text{Si}_2\text{ON}_2$  (trace)

Oxidized at  $1800^{\circ}\text{F}$  -  $\beta$   $\text{Si}_3\text{N}_4$  (major),  $\text{Si}_2\text{ON}_2$  (trace),  $\text{SiO}_2$  (trace)

Oxidized at  $2000^{\circ}\text{F}$  -  $\beta$   $\text{Si}_3\text{N}_4$ ,  $\text{Si}_2\text{ON}_2$  (trace),  $\text{SiO}_2$  (major),  $\text{MgSiO}_3$  (trace)

Oxidized at  $2200$ ,  $2300$ ,  $2400$  and  $2500^{\circ}\text{F}$  -  $\beta$   $\text{Si}_3\text{N}_4$ ,  $\text{Si}_2\text{ON}_2$  (trace),  $\text{SiO}_2$  (minor),  $\text{MgSiO}_3$  (enstatite) and  $\text{MgSiO}_3$  (clinoenstatite)

The amount of  $\beta$   $\text{Si}_3\text{N}_4$  in the surface scrapings decreased as other phases increased, while the amount of  $\text{Si}_2\text{ON}_2$  appeared to remain constant with increasing temperature of oxidation. The cristobalite ( $\text{SiO}_2$ ) phase appeared in specimens oxidized at  $1800^{\circ}\text{F}$ , its amount increased in specimens oxidized at  $2000$  and  $2200^{\circ}\text{F}$ , and then leveled off in specimens oxidized at  $2300$ ,  $2400$  and  $2500^{\circ}\text{F}$ . Enstatite and clinoenstatite ( $\text{MgSiO}_3$ ) phases appeared in specimens oxidized at  $2200^{\circ}\text{F}$  and their amounts increased with increasing temperature of oxidation. In addition to these crystalline phases, the surface oxide film likely contained an amorphous (glass) phase.

Even though x-ray diffraction analysis did not detect any phases containing Ca, F, Al and Mn, these elements were present in the surface oxide film as identified by scanning electron microscopy and electron microprobe analysis reported below. These impurity elements either form crystalline silicates with surface silica in amounts too small to be detectable by x-ray diffraction analysis, or they dissolve in surface silica to form an amorphous glass which cannot be detected by x-ray diffraction analysis.

The surfaces of an unoxidized  $\text{Si}_3\text{N}_4$  specimen and those oxidized at different temperatures were examined by scanning electron microscopy to determine the morphology of the oxide layer and other characteristic features. The micrograph in Fig. 5.70 shows the polished surface of an as-received  $\text{Si}_3\text{N}_4$  specimen. The surface is fairly uniform with some very fine inclusions indicated by white spots in the micrograph. Non-dispersive x-ray analysis, also shown in Fig. 5.70, indicates that these white spots contain mainly tungsten. These inclusions are believed to be very fine tungsten carbide particles coming from the milling of silicon nitride powder with tungsten carbide balls. The Au and Pd peaks in the x-ray scan are from the surface film of Au-Pd alloy deposited on  $\text{Si}_3\text{N}_4$  specimen to obtain a conducting surface for SEM examination.

Figures 5.71 and 5.72 show scanning electron micrographs of the surface oxide film on silicon nitride specimens oxidized at temperatures in the range 1800 to 2500°F. For the specimen oxidized at 1800°F, Fig. 5.71a, the surface appears to be covered with a layer of glass which is severely cracked. At an oxidation temperature of 2000°F, a long needle-like crystalline phase starts to

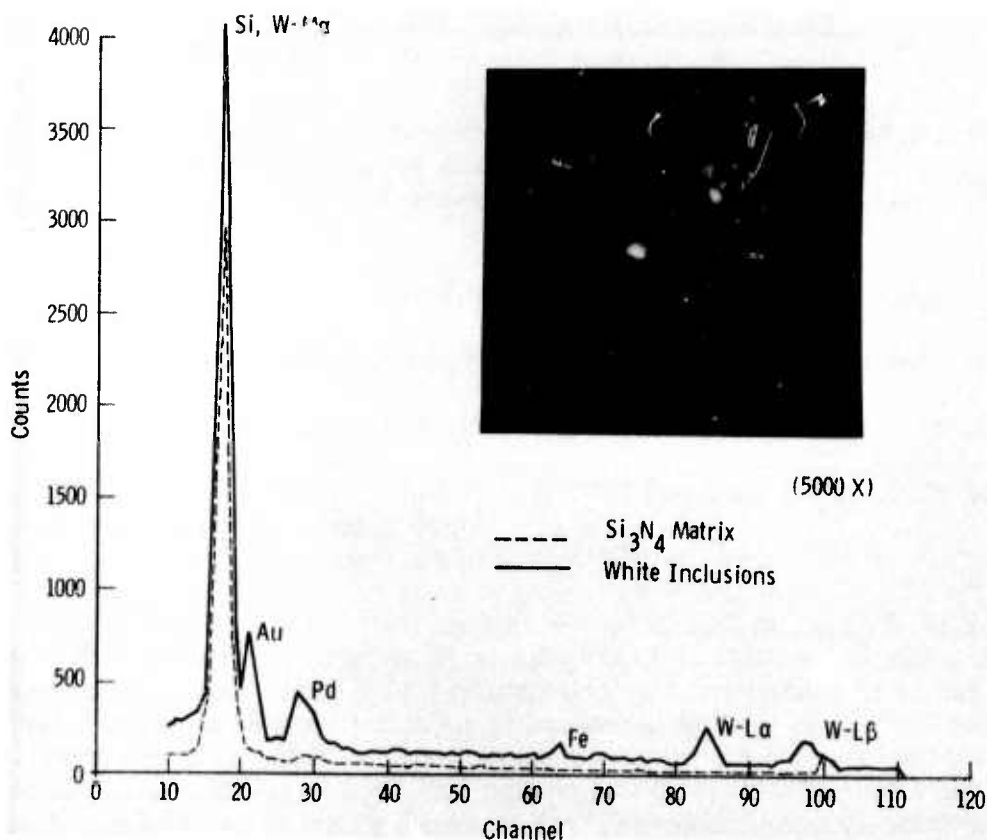


Figure 5.70 — Non-Dispersive X-Ray Analysis of Unoxidized Silicon Nitride Specimen Showing Tungsten Carbide Inclusions



Figure 5.71 — Scanning Electron Micrographs of Surfaces of Silicon Nitride Specimens Oxidized for 30 Hours in 1 Atmosphere Oxygen at Different Temperatures (1000X)

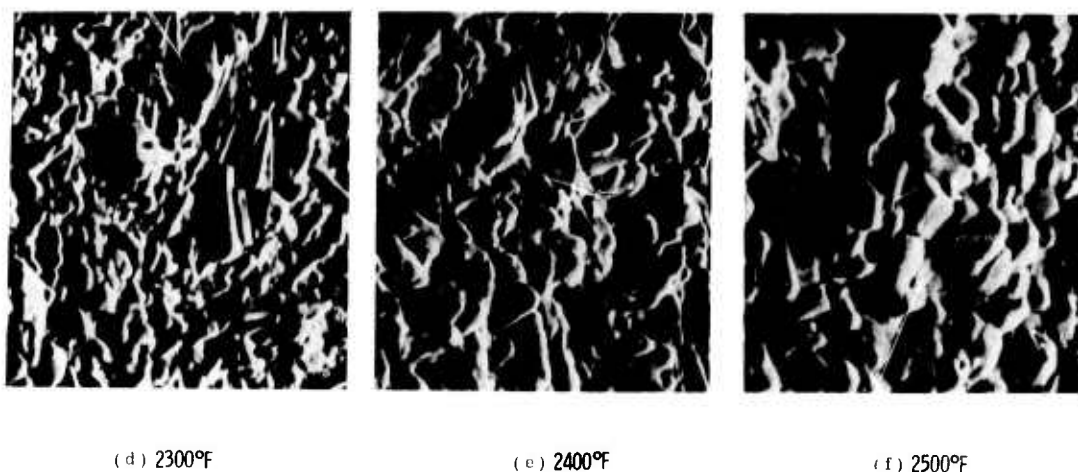


Figure 5.72 — Scanning Electron Micrographs of Surfaces of Silicon Nitride Specimens Oxidized for 30 Hours in 1 Atmosphere Oxygen at Different Temperatures (1000X)

appear which consists mainly of  $\text{MgSiO}_3$ , as identified by x-ray diffraction analysis. The amount of this crystalline phase increases with increasing temperature until at  $2400^{\circ}\text{F}$  and  $2500^{\circ}\text{F}$ , the surface is completely covered with the needle-like  $\text{MgSiO}_3$  phase and probably some cristobalite.

The surface oxide films, shown in Figs. 5.71b and 5.71c, are severely cracked. There is a large volume increase when silicon nitride is oxidized to silica which may generate compressive stresses in the oxide causing the surface silica layer to crack. Alternatively, cracks might have also formed during cooling of the oxidized specimen. Cristobalite undergoes a phase transformation at about  $500^{\circ}\text{F}$  with an accompanying decrease in volume of about 5%. During this transformation, therefore, large tensile stresses are generated in the oxide which could directly lead to cracking.

Another prominent feature evident in the scanning micrographs is the presence of pores and fissures in the oxide layer, particularly at higher oxidation temperatures. During the oxidation of  $\text{Si}_3\text{N}_4$ , nitrogen and  $\text{SiO(g)}$  are formed at the  $\text{Si}_3\text{N}_4(s)$  -  $\text{SiO}_2(s)$  interface according to reactions (1) and (4), which burst out through the oxide layer causing the formation of these pores and fissures.

Figure 5.73 shows a SEM micrograph of the transverse section of a  $\text{Si}_3\text{N}_4$  specimen oxidized for 30 hours at  $2300^{\circ}\text{F}$ , along with the non-dispersive x-ray scans in the  $\text{Si}_3\text{N}_4$  substrate as well as in the oxide layer. Only the silicon peak could be detected in the unoxidized silicon nitride substrate, while Mg, Ca, Fe, and Mn peaks were also present in the oxide layer. These impurity elements, therefore, diffuse out of the  $\text{Si}_3\text{N}_4$  substrate during the oxidation process and get concentrated in the oxide layer. The concentration of these impurity elements Mg, Ca, Fe, and Al in the oxide layer is also confirmed by the scanning x-ray pictures shown in Figs. 5.74 and 5.75. These were taken on both unoxidized and oxidized surfaces using the electron beam microprobe analyzer. A similar behavior was observed at other oxidation temperatures in the range of 2000 to  $2500^{\circ}\text{F}$ . Thus, these impurities play an important role in the oxidation behavior of hot-pressed silicon nitride, and decreasing their concentration level results in a reduced oxidation rate as already shown in Fig. 5.65.

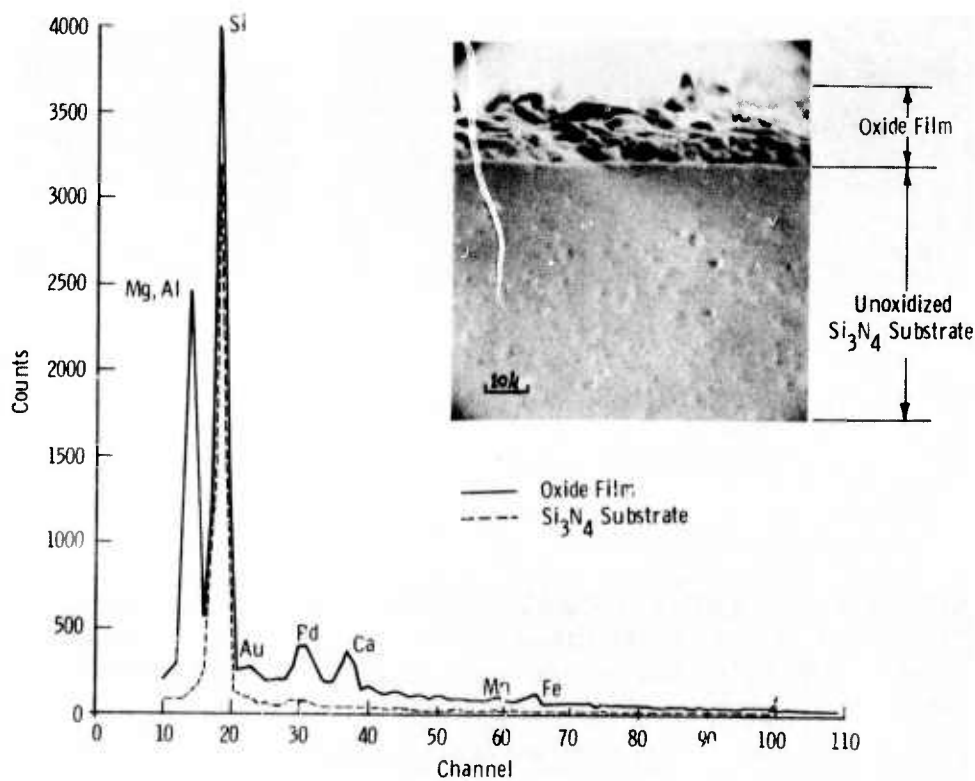
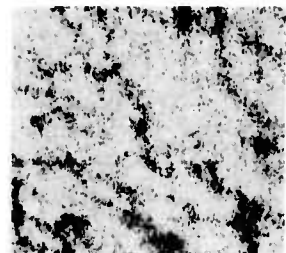


Figure 5.73 — Scanning Electron Micrograph of a Transverse Section of a  $\text{Si}_3\text{N}_4$  Specimen Oxidized at  $2300^{\circ}\text{F}$  for 30 Hours in 1 Atmosphere Oxygen, With Non-Dispersive X-Ray Analysis in the Oxide Layer and in the  $\text{Si}_3\text{N}_4$  Substrate



Mg K $\alpha$ , background



Mg K $\alpha$ , oxide layer



Ca K $\alpha$ , background



Ca K $\alpha$ , oxide layer

**Figure 5.74 — Scanning X-Ray Pictures Showing Concentrations of Mg and Ca in the Surface Oxide on Silicon Nitride, Oxidized for 30 Hours in 1 Atmosphere Oxygen at 2300°F (435 X)**



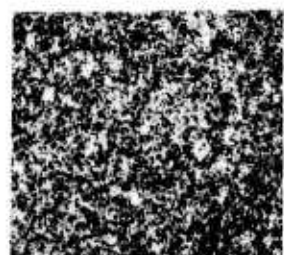
Al-K $\alpha$ , background



Al-K $\alpha$ , oxide layer



Fe K $\alpha$ , background



Fe K $\alpha$ , oxide layer

**Figure 5.75 — Scanning X-Ray Pictures Showing Concentrations of Al and Fe in the Surface Oxide on Silicon Nitride, Oxidized for 30 Hours in 1 Atmosphere Oxygen at 2300°F (435 X)**

### 5.3 NON-DESTRUCTIVE EVALUATION OF MATERIALS

#### SUMMARY

A very important aspect of the development of ceramic gas turbine engines is the need to meaningfully inspect and test ceramic components before installation in the engine. The objectives of the NDE work are to identify and classify defects and to gain as much information as possible on the properties of the material from which the component is manufactured. Both property and defect information are being related to the performance of the component, leading eventually to routine inspection and acceptance/rejection based upon established actual performance.

All available non-destructive means must be used to accomplish this goal and new methods must constantly be evaluated to determine their usefulness. Procedures utilizing ultrasonics, x-ray radiography, and acoustic emission (AE) are currently being applied to ceramic systems for evaluation purposes.

During this reporting period, ultrasonic and radiographic NDE procedures were used to evaluate reaction-sintered SiC and hot pressed  $\text{Si}_3\text{N}_4$ . A program to identify subsurface flaw types using an RF display of the received signals was also initiated on lithium aluminum silicate material.

Radiographic analysis resulted in the detection of small inclusions not detected ultrasonically, while ultrasonic evaluation revealed density gradients and very small voids not observed by x-ray. Identification of flaw types using an RF display of the signals showed much promise in the identification of major voids and segregated porosity.

Flexure testing incorporating acoustic emission has shown a relationship between the type of AE vs stress curve and the location of the flaw controlling final fracture. Examples of regions of fast and slow crack propagation were observed. The potential to determine the size and morphology of critical flaws was noted.

"PRECEDING PAGE BLANK-NOT FILMED."

### 5.3.1 ULTRASONIC NDE

#### Introduction

The non-destructive evaluation of various ceramic systems has been significantly improved by utilizing ultrasonic sub-surface flaw detection procedures and by measuring homogeneity with sonic velocity measurements. Subsurface flaws located initially by radiographic means were detected during ultrasonic evaluation. The sensitivity of the ultrasonic method is greater than the radiographic method, so that other flaws not previously detected were readily observed.

Material inhomogeneity was identified by observing the sonic velocity gradients within the ceramics evaluated. It was found that these data were more reproducible when the immersion technique was employed instead of the contact technique, since the errors associated with varying surface roughness conditions are negated. It appears that longitudinal velocity data, rather than dynamic modulus of elasticity data, would be of most value in determining the level of material inhomogeneity.

#### Ultrasonic Evaluation of Hot-Pressed Silicon Nitride Disks

Machined disks of hot pressed silicon nitride (Norton HS-110) were obtained and checked for defects using ultrasonics and x-ray radiography. Since no standards such as those fabricated during the previous reporting period (1) were available, the C-scanning instrumentation was set up to record those flaws visible in the radiographic reversal prints shown in Figure 5.76.

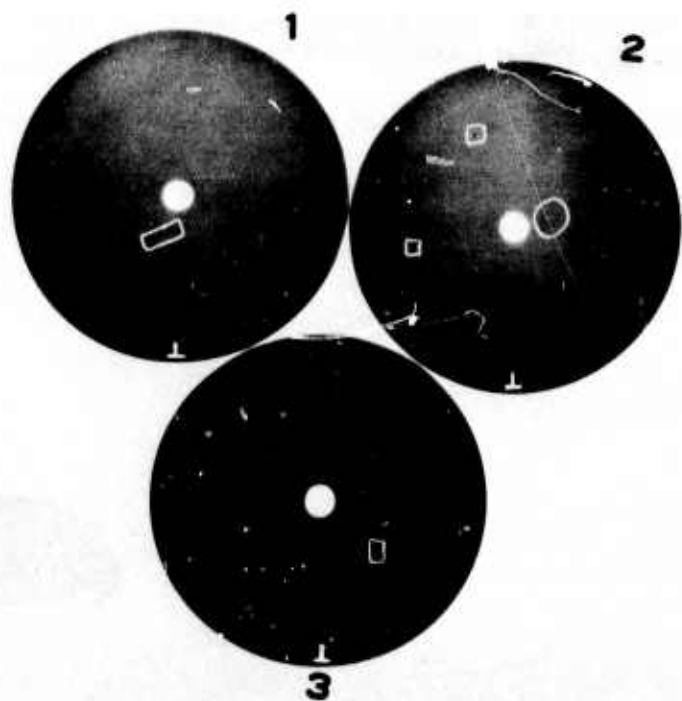
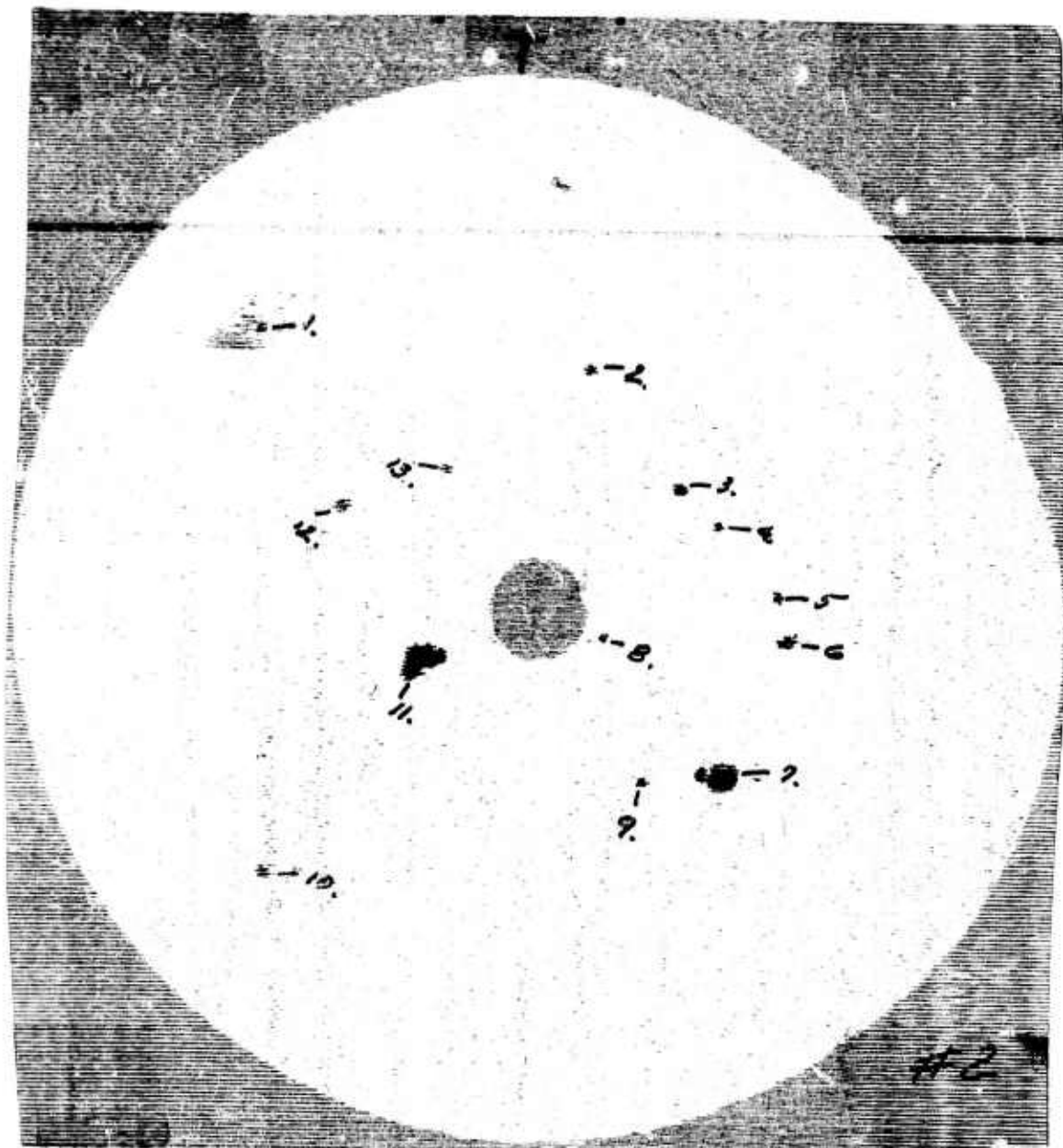


Figure 5.76 — X-Ray Radiographic Reversal Print of Hot Pressed Silicon Nitride Disks

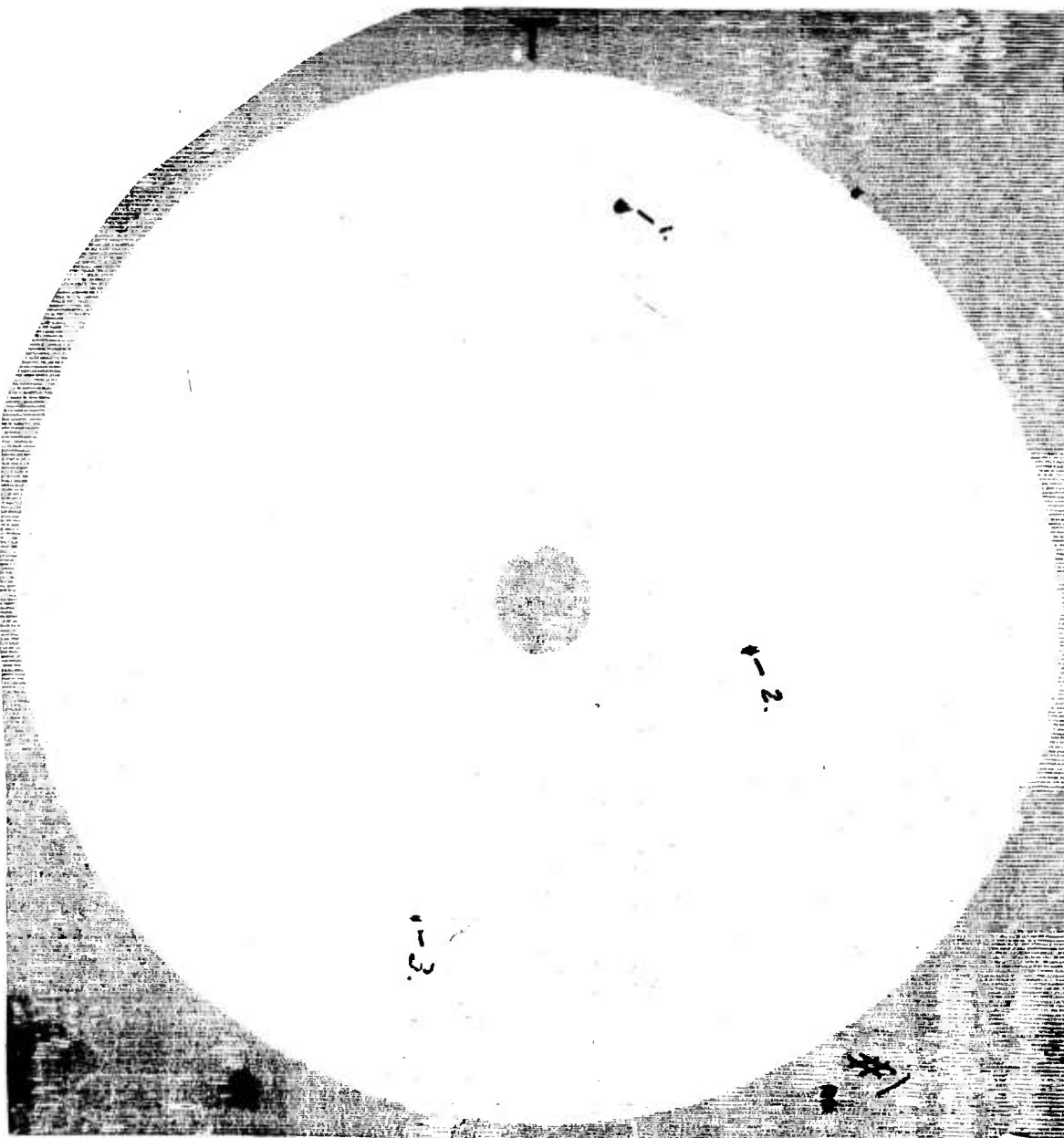
The dark spots, outlined by rectangles, are suspected high density particles. The circled area in disk No. 2 is flaw 11 in the ultrasonic C-scan (Fig. 5.77) and was used to establish the flaw monitoring threshold. It is interesting to note that flaw 7, (Figure 5.77) while large in the recorded C-scan, is not seen in the radiograph.



<u>Flaw No.</u>	<u>Depth (In.)</u>	<u>Flaw No.</u>	<u>Depth (In.)</u>
1.	.33	8.	.44
2.	.25	9.	.33
3.	.25	10.	.33
4.	.39	11.	.33
5.	.33	12.	.33
6.	.39	13.	.33
7.	.39		

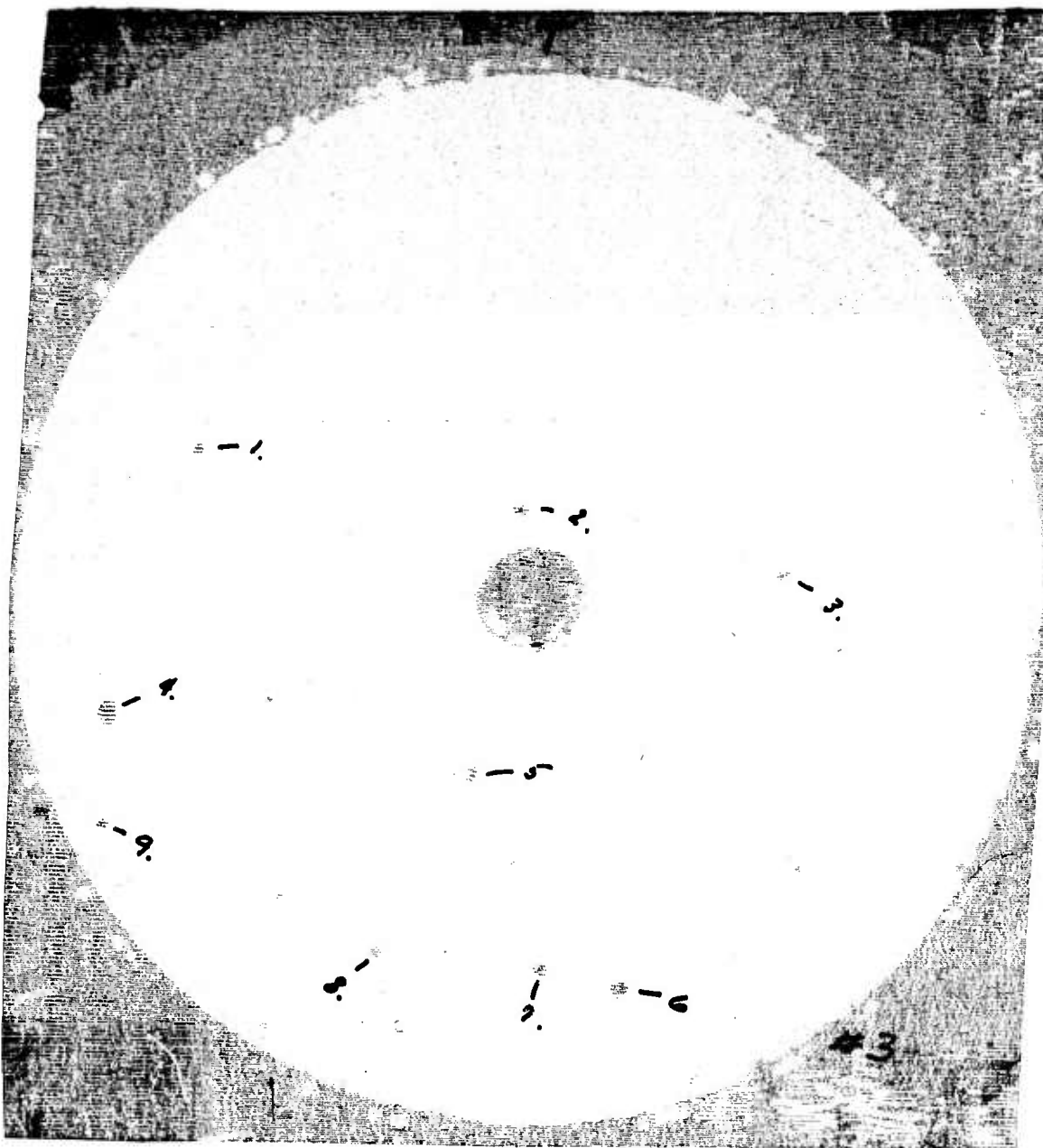
Figure 5.77 — C-Scan of Silicon Nitride Disk No. 2

As shown in the C-scans of the disks, Figures 5.77, 5.78 and 5.79, many other flaws were found. These flaws were numbered and located within the disk by depth as indicated on the ultrasonic display unit presentation. However, it is also significant that the suspected high density particles were not detected ultrasonically at the sensitivity levels used. A possible explanation is that a coherent interface exists between the high density particles and the matrix with a low acoustic impedance resulting in a signal of insufficient amplitude to be detected.



<u>Flaw No.</u>	<u>Depth (In.)</u>
1.	.33
2.	.44
3.	.33

Figure 5.78 — C-Scan of Silicon Nitride Disk No. 1



<u>Flaw No.</u>	<u>Depth (In.)</u>
1.	.25
2.	.25
3.	.20
4.	.30
5.	.30
6.	.35
7.	.30
8.	.25

Figure 5.79 — C-Scan of Silicon Nitride Disk No. 3

A sonic velocity gradient was also observed in the three disks. Values were obtained at 1/2 inch intervals from the center to the outer diameter using procedures established previously (1). As shown in Table 5.13 the dynamic modulus of elasticity varies only with the bulk density since the velocity values are the same at the outside diameters. Neglecting the correction for Poisson's ratio in calculating the elastic modulus, and using the equation

$$E = (V_L)^2 d$$

where  $V_L$  is the longitudinal sonic velocity and  $d$  is the density, the elastic modulus at the center of the disks is reduced approximately 10% for disk Nos. 1 and 3 and 20% for disk No. 2.

TABLE 5.13

Dynamic Modulus of Elasticity of Silicon Nitride Disks

Disk No.	Density(d) (g/cc)	Sonic Velocity ( $10^5$ cm/sec)		Location	Poisson's Ratio	Dynamic MOE ( $10^6$ psi)
		Long( $V_L$ )	Trans( $V_T$ )			
1	3.12	10.6	5.81	O.D. CTR	.28	39.8
		10.0	----			
2	3.07	10.6	5.81	O.D. CTR	.28	39.2
		9.5	----			
3	3.09	10.6	5.81	O.D. CTR	.28	39.4
		10.0	----			

Disk No. 2 also had the lowest bulk density and the C-scan indicates a higher number of flaws with respect to the other disks. Characterization of all the recorded flaws was accomplished by obtaining the major dimension on the C-scans, location (determined by depth in the disks), and amplitude of the received signals, plotted against the specific radial location from the center of each disk. The results are shown in Figures 5.80, 5.81, and 5.82. Each disk has a propensity towards a common range of flaw size and location in the disk. The signal amplitudes of the flaws in disk No. 3 suggest that a common flaw morphology may be present but destructive analysis, which could not be accomplished since these disks were scheduled for spin testing, would be necessary for confirmation.

Ultrasonic Evaluation of Lithium Aluminum Silicate (LAS) Disks

Several disks of this material, previously C-scanned for subsurface flaws, were also analyzed in terms of dynamic modulus of elasticity prior to spin testing. Seven disks had an average elastic modulus of  $9.11 \times 10^6$  psi with a coefficient of variation of 3%. The corresponding ranges of longitudinal and transverse sonic velocity were  $5.89 - 6.13 \times 10^5$  cm/sec and  $3.25 - 3.41 \times 10^5$  cm/sec respectively. One disk had a low elastic modulus of  $7.8 \times 10^6$  psi with a  $5.43 \times 10^5$  cm/sec longitudinal and  $3.10 \times 10^5$  cm/sec transverse sonic velocity, and was not averaged with the other disks.

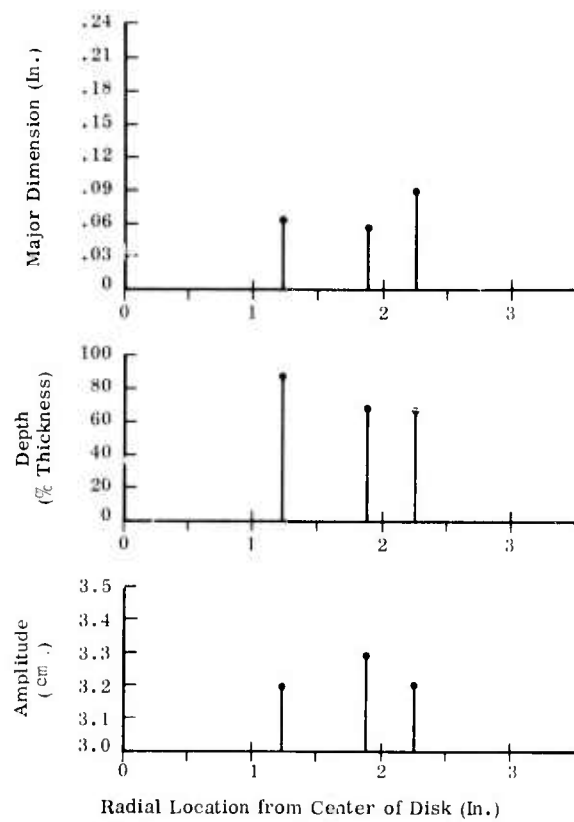


Figure 5.80 -- Flaw Characterization — Disk No. 1

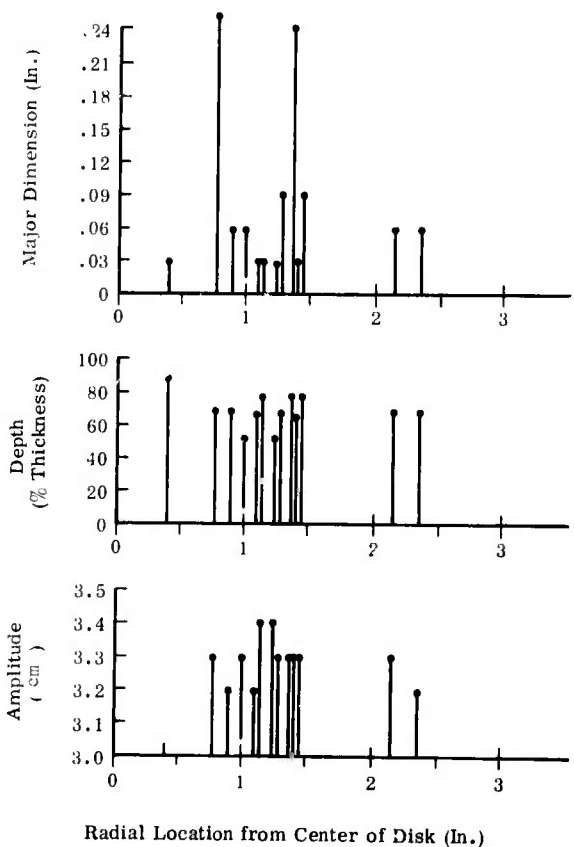


Figure 5.81 — Flaw Characterization — Disk No. 2

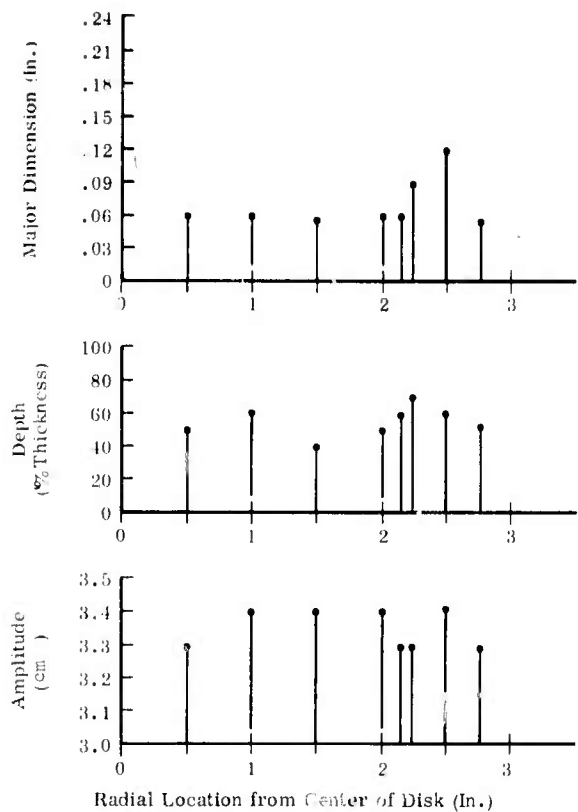


Figure 5.82 — Flaw Characterization — Disk No. 3

#### Ultrasonic Evaluation of Silicon Carbide Disks

Machined disks of reaction-sintered silicon carbide (REFEL) were C-scanned for subsurface flaws and the dynamic modulus of elasticity was determined by measuring the sonic velocity. The procedures for optimizing the ultrasonic instrumentation for flaw detection were the same as those reported in the previous discussion on hot-pressed silicon nitride. The circled area in the x-ray radiograph, Figure 5.83, of disk No. 5 was used to establish the flaw sensitivity levels. More areas are suspect from an ultrasonic analysis basis as shown on the C-scans of the disks (Figures 5.84 through 5.86).

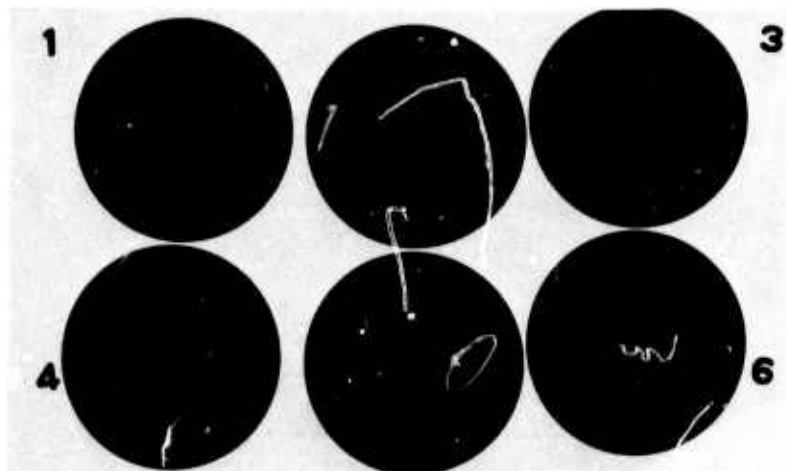


Figure 5.83 — X-Ray Radiographic Reversal Print of Reaction-Sintered Silicon Carbide Disks

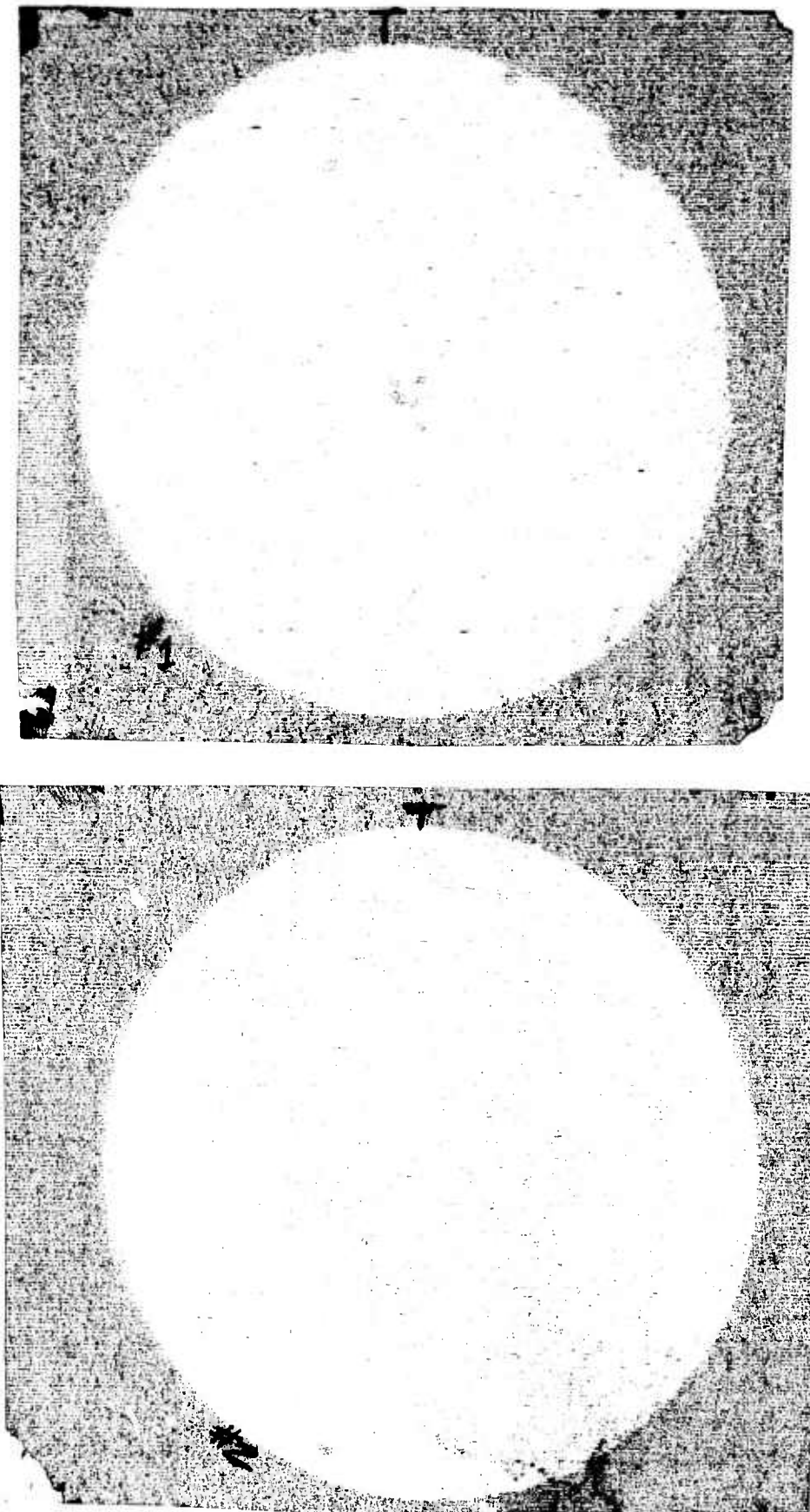


Figure 5.84 — C-Scans of Silicon Carbide Disks Nos. 1 and 2

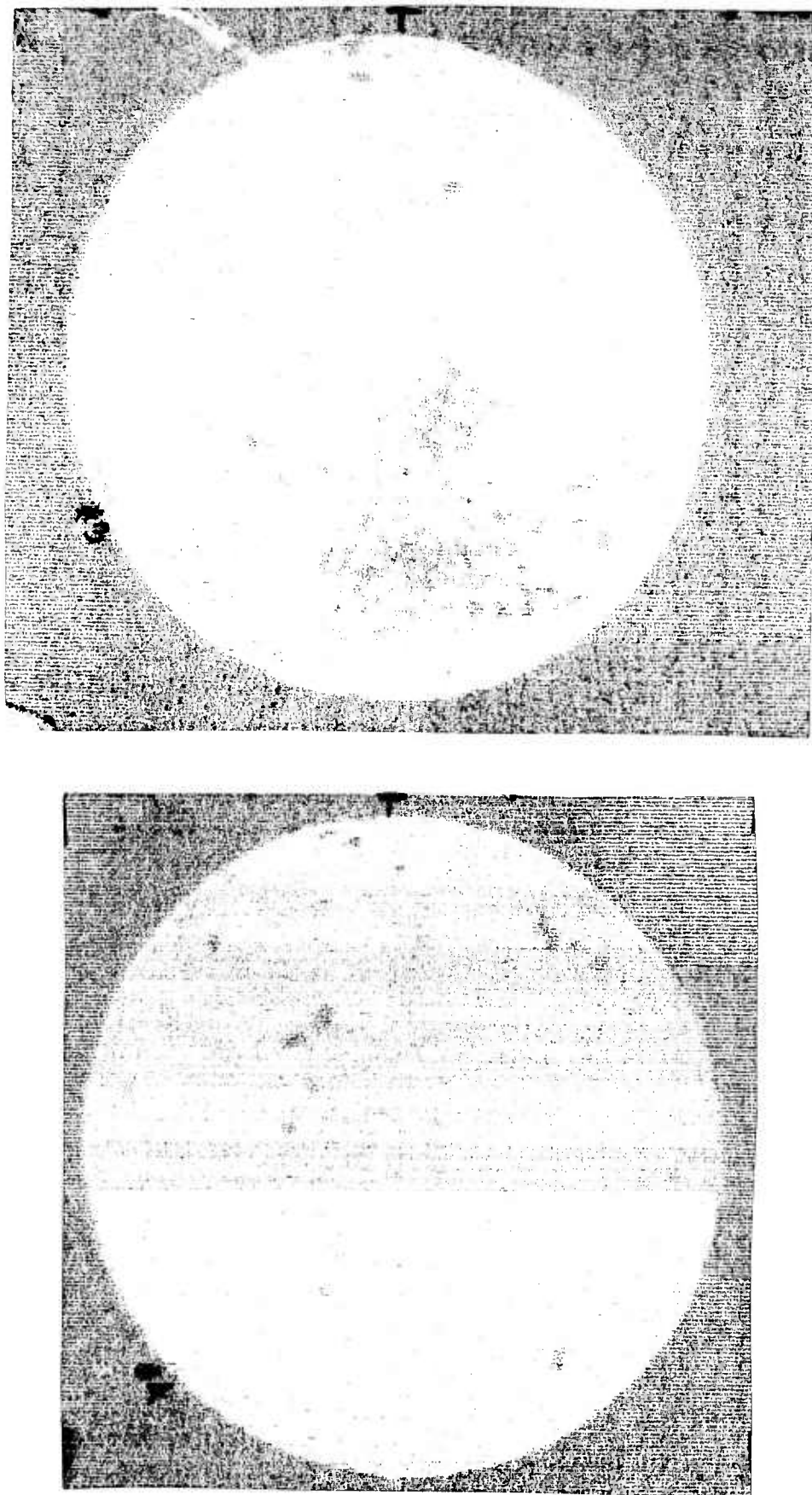


Figure 5.85 — C-Scans of Silicon Carbide Disks Nos. 3 and 4

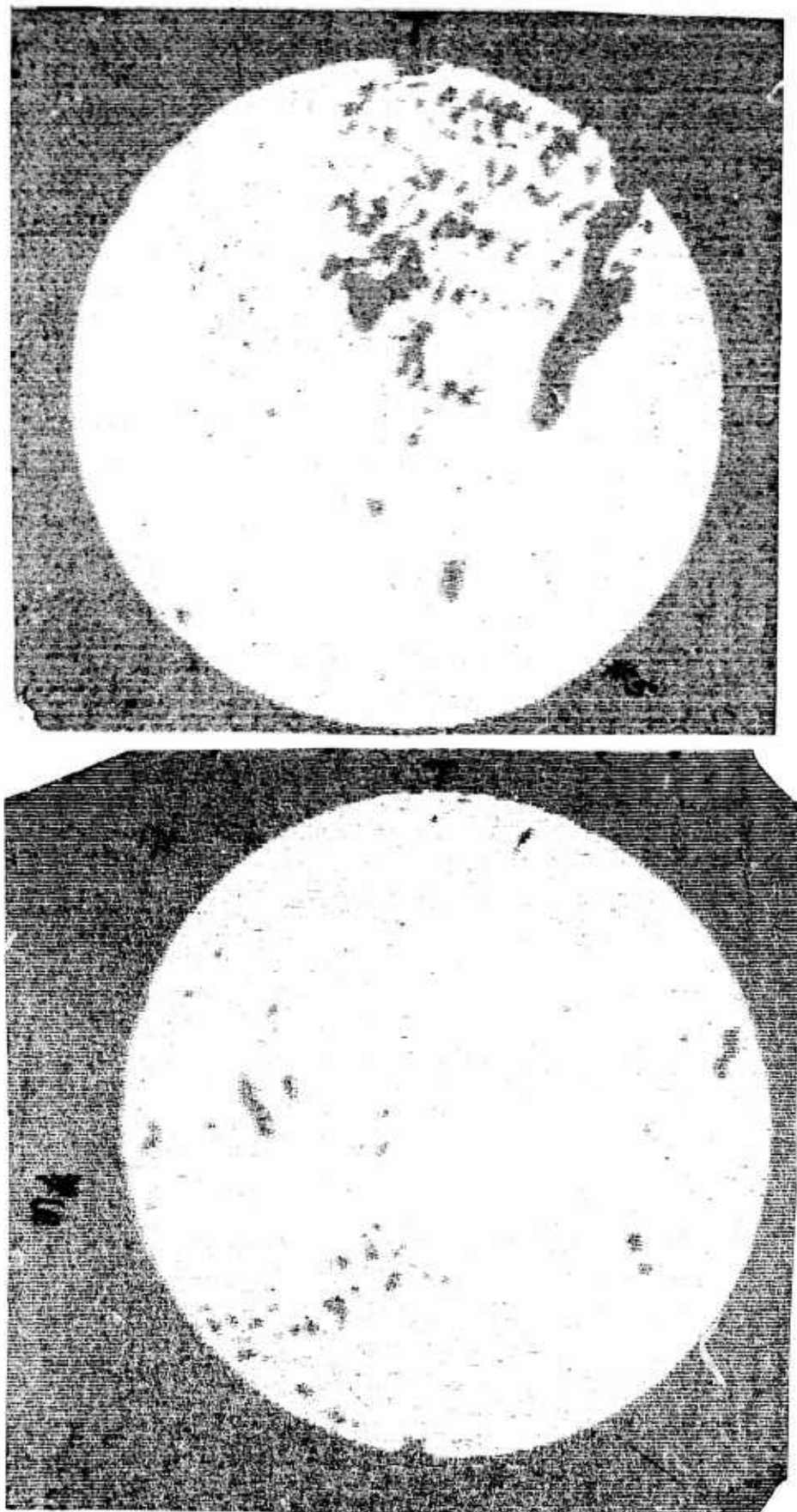


Figure 5.86 — C-Scans of Silicon Carbide Disks Nos. 5 and 6

The mechanical properties of the disks, determined ultrasonically, are shown in Table 5.14.

Some of the ceramic disks evaluated were later destructively tested in the spin pit. The procedures and results appear in Section 5.1.1.

TABLE 5.14  
Properties of Silicon Carbide Disks

Disk No.	Density(d) (g/cc)	Sonic Velocity ( $10^5$ cm/sec)		Poisson's Ratio	Dynamic MOE ( $10^6$ PSI)
		Long(V <sub>L</sub> )	Trans(V <sub>T</sub> )		
1	3.09	10.5	6.28	.20	44.6
2	3.09	10.5	6.26	.20	44.6
3	3.13	11.3	6.92	.19	53.0
4	3.08	10.6	6.32	.20	45.0
5	3.15	11.3	6.90	.19	53.0
6	3.09	10.5	6.30	.20	44.6

On the stationary turbine project, an ultrasonic non-destructive test, which is very sensitive to the presence of any material discontinuity, has been used to detect the location of internal flaws in hot-pressed silicon nitride. This test uses carrier frequencies between 100 and 200 MHz so that flaws extending only tens of microns are capable of being detected. In preliminary experiments, several tensile test specimens were examined and internal flaws were detected in each case. Typical results are illustrated in Fig. 5.87.

Once the instrument outputs are better correlated with actual failure origins or confirmed by microscopic examination, this ultrasonic method will be developed for routine inspection of hot-pressed billets. This will provide an effective way of rejecting faulty materials prior to any machining operation.

#### Defect Signature

This investigation was initiated in an attempt to determine, non-destructively, the nature of the flaws recorded ultrasonically. The goal was to discriminate between various types of flaws by observing the characteristics of the flaw signals received. These signals were displayed in two modes, modulated and unmodulated. Specific aspects of each presentation were then documented. The LAS system was used for this initial signature analysis.

The sequence followed was; (1) find the flaw by C-scanning procedures and record the sensitivities used by C-scanning the appropriate calibration block, (2) obtain photographs of the modulated (vidco) and unmodulated (RF) signals from the area in question, (3) find the flaw by sectioning and obtain photographs and micrographs.

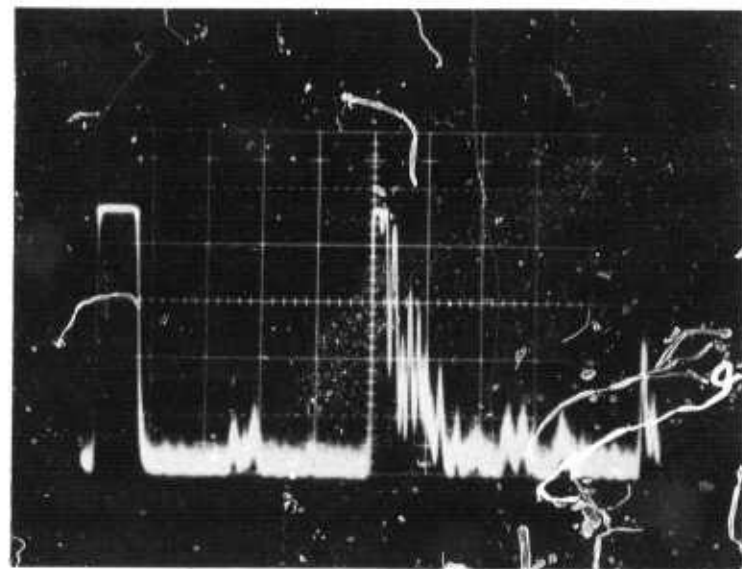
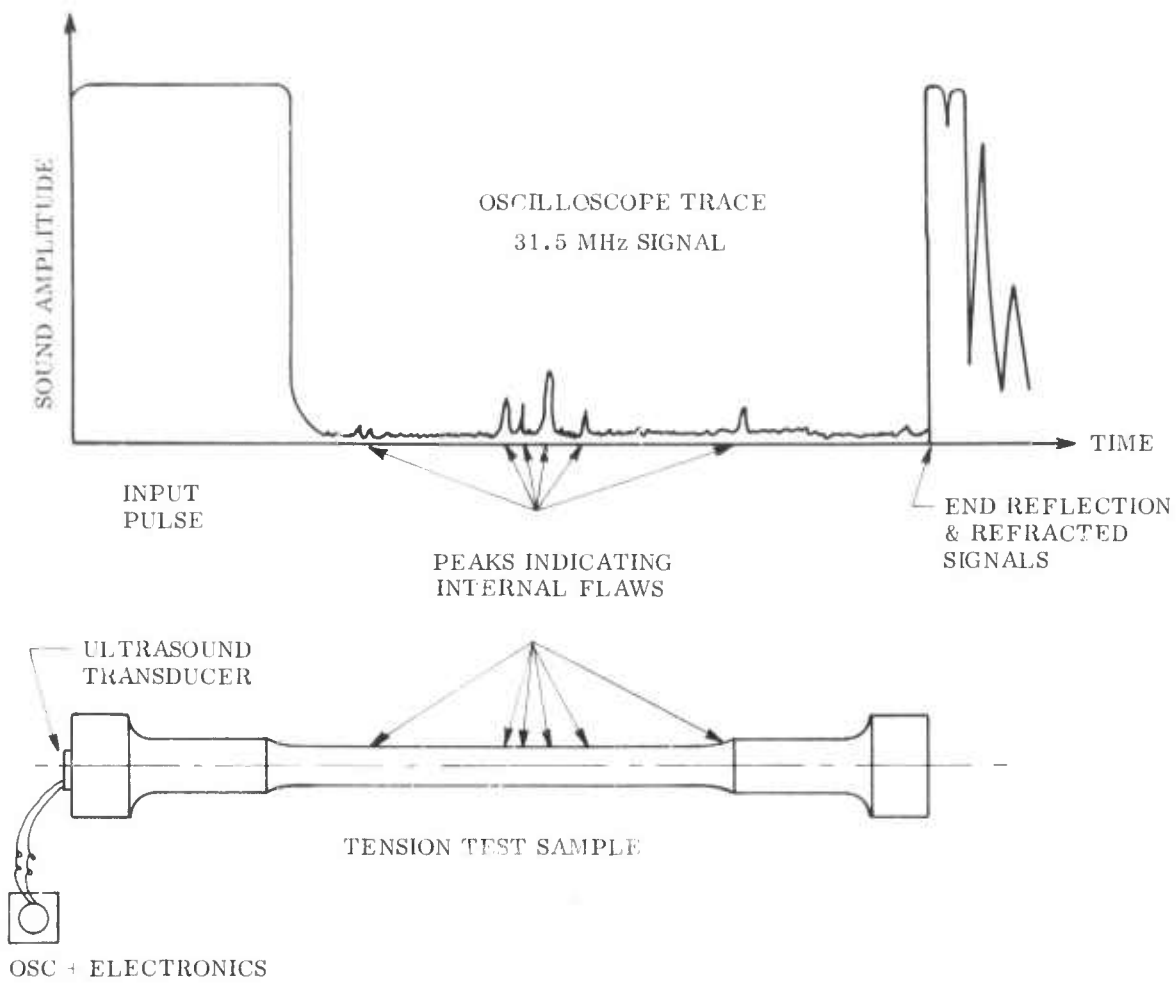


Figure 5.87 — Ultrasonic Nondestructive Test of Hot Pressed Silicon Nitride

Sectioning of suspect areas in LAS material resulted in cataloging three types of flaws. They were identified as major voids, segregated porosity, and inclusions. The first two tend to locate in preferential areas due to their dependency on the procedures used to cast the disks. The inclusion defect locates randomly within this material and does not exhibit a dependency on the fabrication procedures.

The results thus far point out discrete differences in the received signals from the three types of flaws. Variations in these signals such as the signal amplitude, waveform, and width of the signal package, coupled with a loss in the back reflection, present information concerning the flaw morphology.

The C-scans of one LAS disk and the calibration block used to establish the flaw sensitivity level are shown in Figure 5.88. Although two flaws are indicated, the enlargements in Figure 5.89 indicate a varying degree of porosity segregation with a large associated dimension parallel to the direction of the ultrasonic flaw detecting wave. This effect is pointed out by the oscilloscope display of the flaw signals in Figure 5.90c and d. The top surface signal is on the extreme left and the back surface signal is the third isolated waveform from the left. The flaws are shown to extend over a significant portion of the spin disk thickness while retaining much of the amplitude of the back surface signal. This occurs since the flaw is made up of many smaller flaws, each reflecting a limited amount of energy such that sufficient energy is still available to propagate to the back of the disk. A loss in back surface amplitude is shown in the display of flaw 2 (Figure 5.90d) since a greater density of these small flaws are observed and therefore less energy is available at the back surface. It must be pointed out, however, that the back surface morphology would also contribute to the shape and amplitude of the received signal; therefore these subtle differences in back surface amplitude may not be a function of the flaws only.

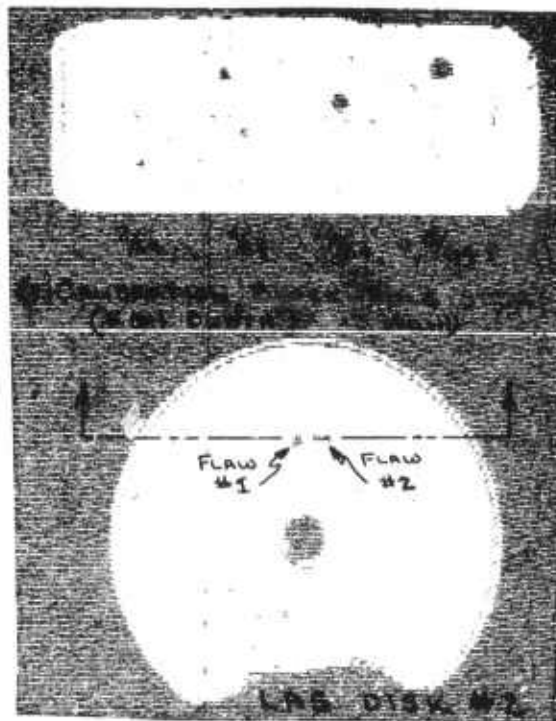
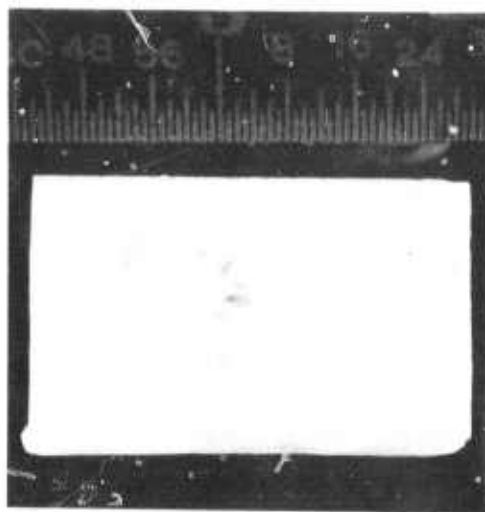
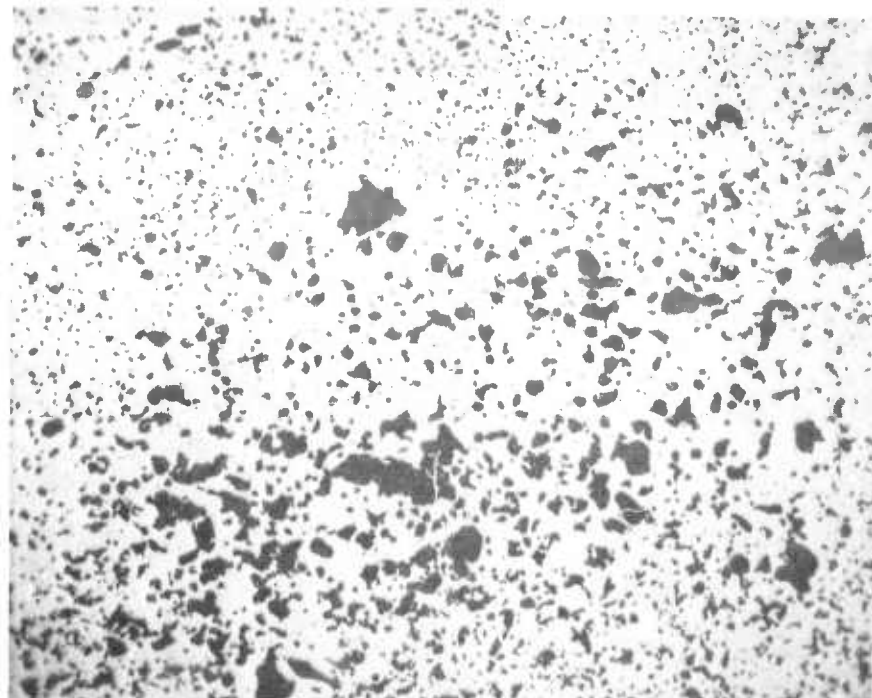


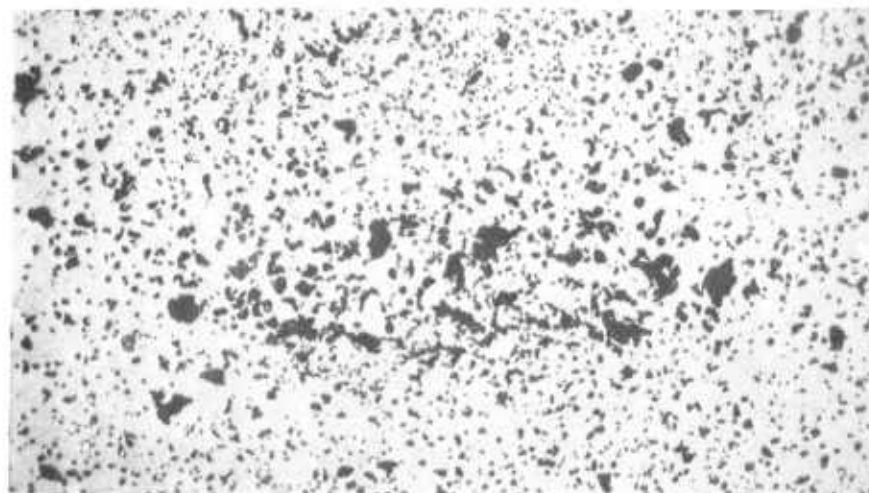
Figure 5.88 — C-Scan of LAS Calibration Block and LAS Spin Test Specimen with the Flaw Analysis View Direction Shown



a.) Porosity Segregation at 2.4X

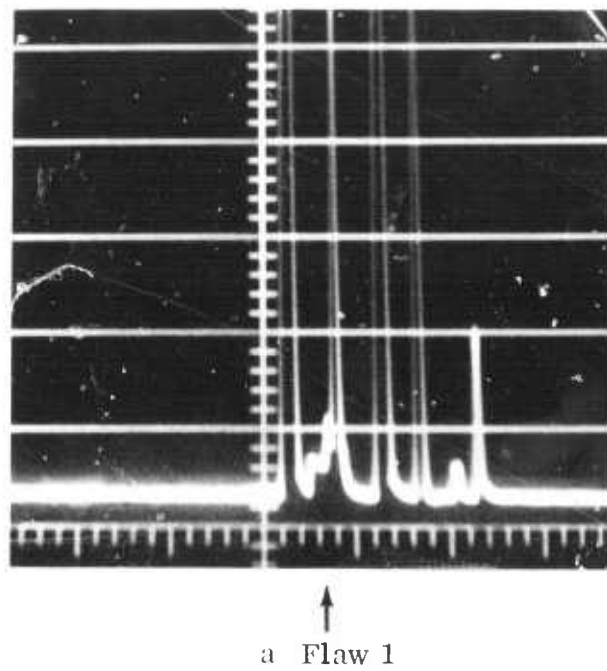


b.) Area A at 50X

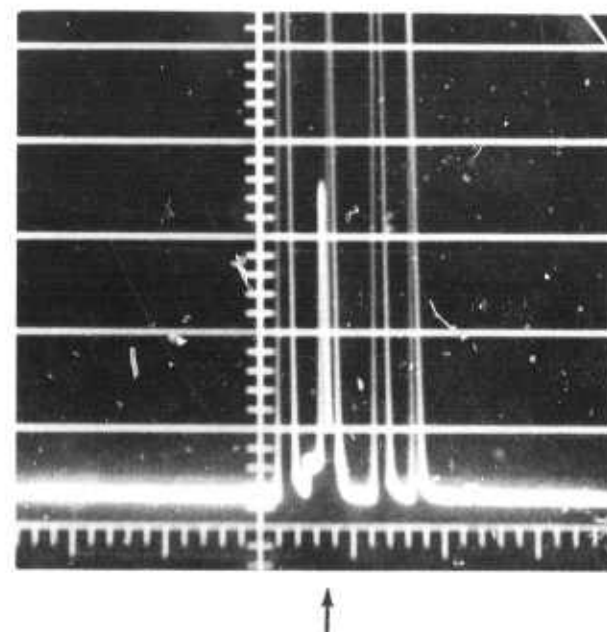


c.) Area B at 50X

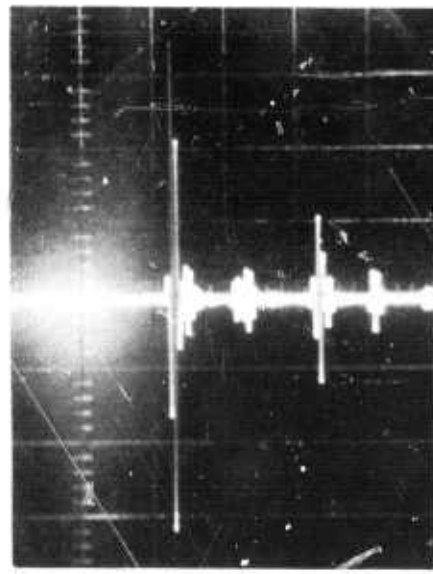
Figure 5.89 — Enlargements of Flaws 1 and 2 in LAS Disk No. 2



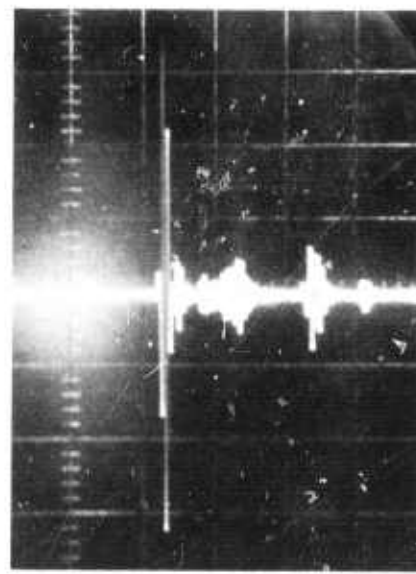
a Flaw 1



b Flaw 2



c Flaw 1



d Flaw 2

Figure 5.90 — Flaw Signals (Arrow) from LAS Disk No. 2, a) and b) — Display Unit, c) and d) — Oscilloscope

The segment of LAS spin disk No. 13 shown in the C-scan in Figure 5.91 has a flaw which is quite different. As can be seen in Figure 5.92 there is a definite shape to the defect and it resembles an impurity surrounded by small voids. The flaw signals, shown in Figure 5.93 indicate a cleaner waveform package as compared to the porosity segregation in the previous disk. In this case the orientation of the defect would certainly affect the displayed signal and, as is shown in the enlargements, the top of the flaw is somewhat parallel to the top surface; therefore the c-scan results in a flaw indication of approximately 3/32 inch diameter. If there were no interface formed by the surrounding porosity, the acoustic impedance of this defect may have been low enough to make detection very difficult. In this case it was very obvious.

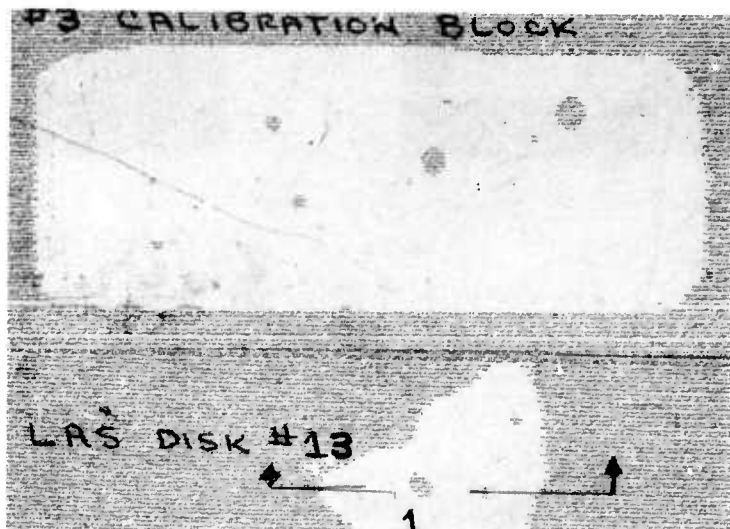


Figure 5.91 — C-Scan of LAS Calibration Block and Segment of LAS Spin Test Specimen 13 with the Flaw Analysis View Direction Shown.

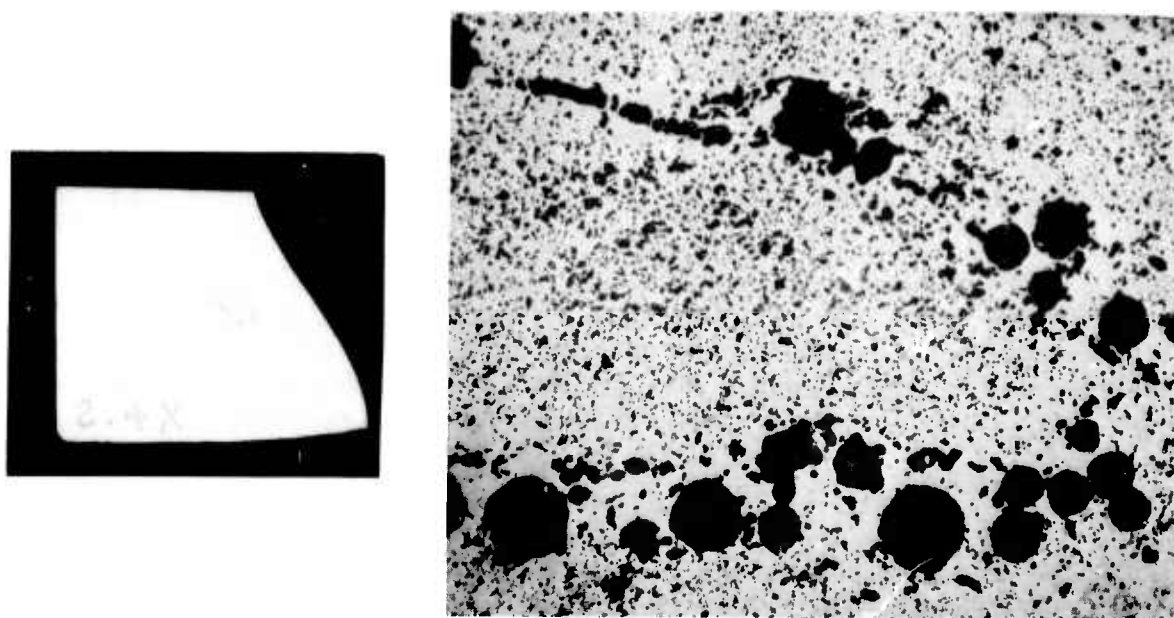


Figure 5.92 — Enlargements of Flaw 1 in Segment of LAS Spin Test Specimen No. 13

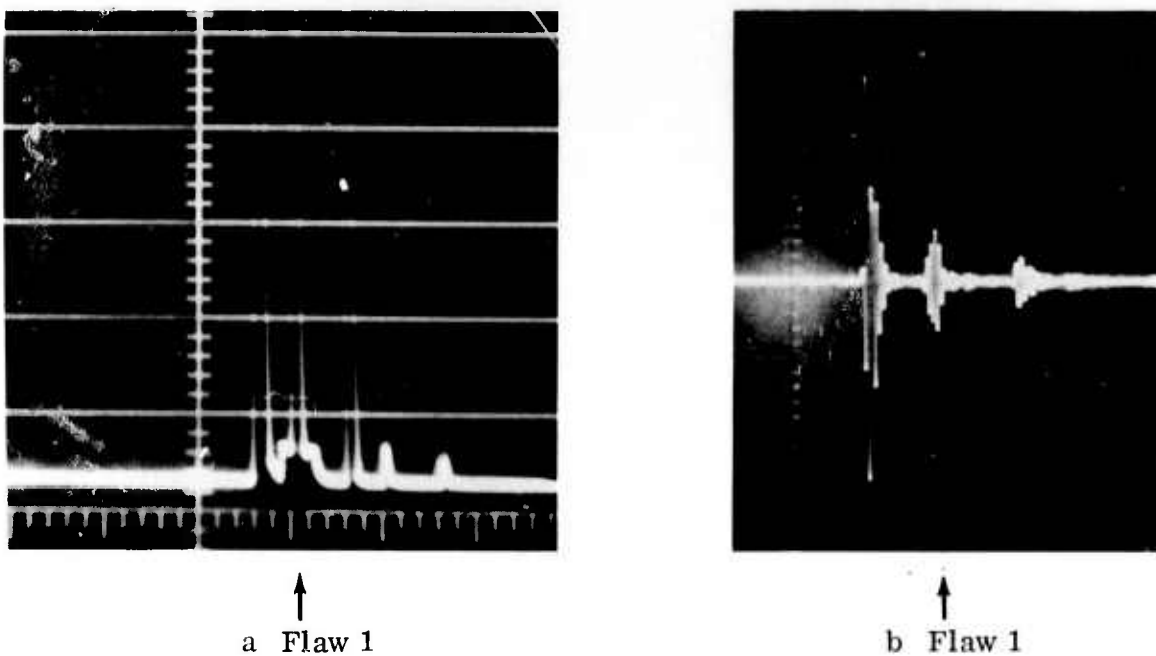


Figure 5.93 — Flaw Signals (Arrow) from Segment of LAS Spin Test Specimen No. 13, a) — Display Unit, b) — Oscilloscope

The third type of defect, a major void, was found in a 1.25 inch thick section of LAS test block. The calibration block and flaw specimen c-scans are shown in Figure 5.94. The void identified as 1 is quite large and the received signals, shown in Figure 5.95, reveal a waveform with a rather large amplitude. This void is shown to have a signal quite different than the two previous types of flaws discussed. An enlargement of the void appears in Figure 5.96.

Figure 5.95a, shows the gated area being monitored within the specimen. It is actually below the center of the specimen and consequently the top surface of the void did not trigger the C-scan instrumentation. This signal is shown immediately to the left of the gate. The signal which produced the C-scan result can be seen within the gated area and is actually the bottom of the void.

The void thickness, represented as two distinct signals, is displayed in a magnified condition. This occurs because the void was filled with water and there is a reduction in sonic velocity between the LAS material and the water. The time delay in propagating the signal results in displaying a much thicker void. In this case, about four times the actual width is represented.

While much more testing and analysis is needed to verify these results, it is encouraging to see the possibility of non-destructively obtaining information about the defects recorded ultrasonically. The differences between the three types of flaws discussed are more than subtle and should prove useful in determining the quality of ceramic materials.

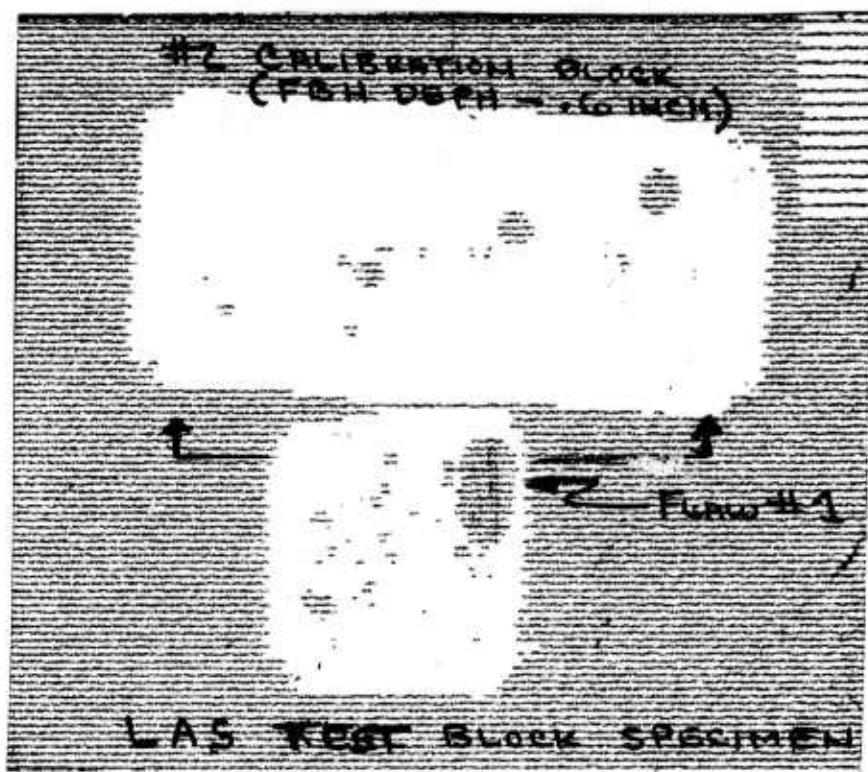


Figure 5.94 — C-Scan of LAS Calibration Block and LAS Test Block Specimen with the Flaw Analysis View Direction Shown

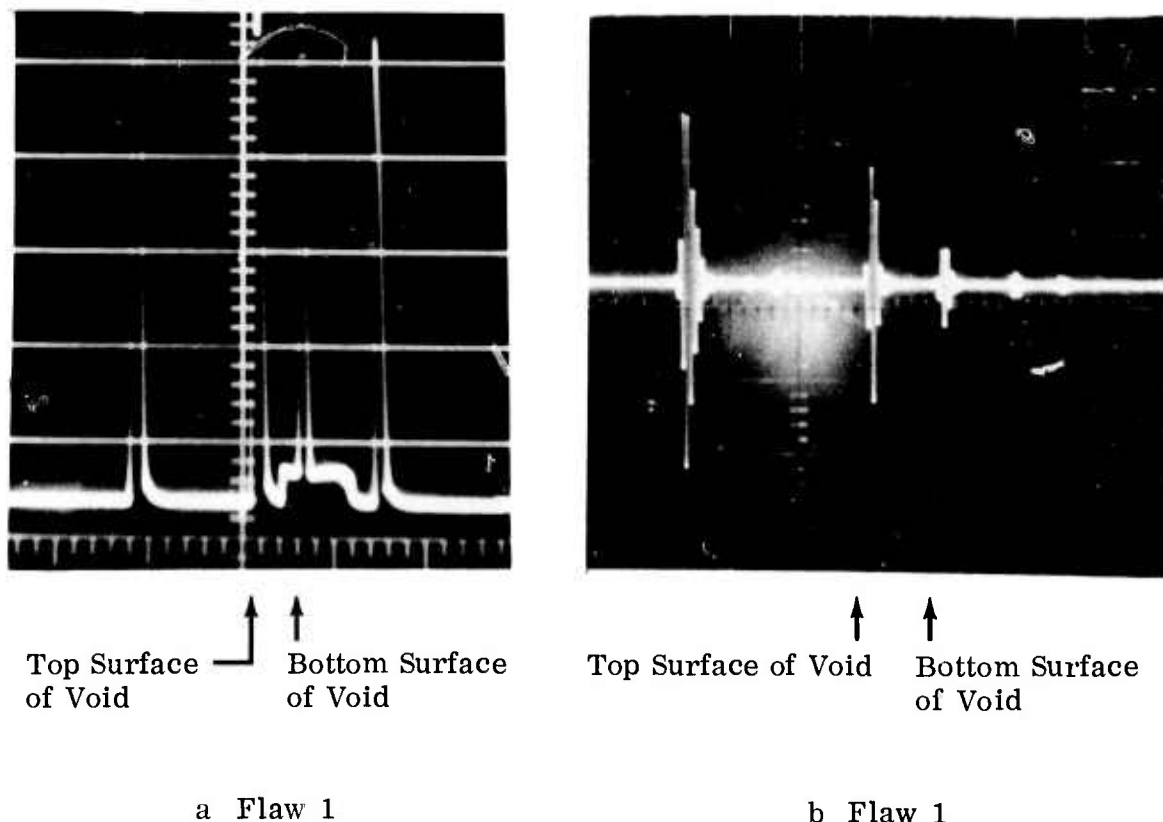


Figure 5.95 — Flaw Signals (Arrows) from LAS Test Block Specimen, a — Display Unit, b — Oscilloscope

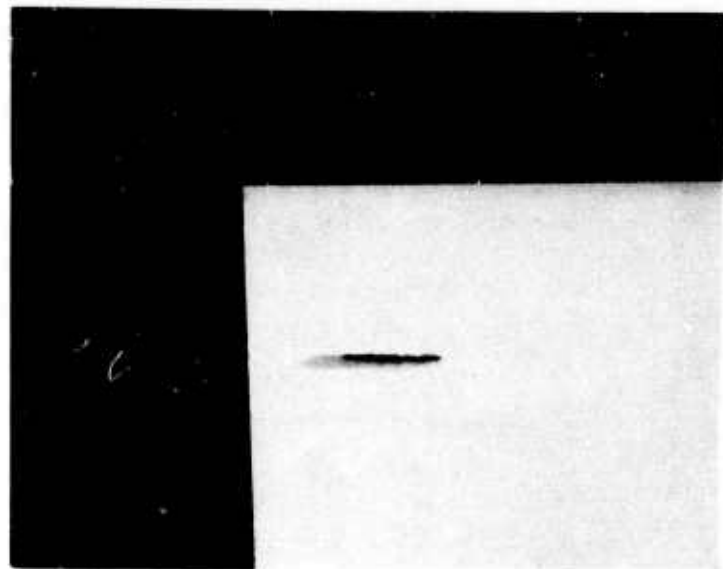


Figure 5.96 — Enlargement of Flaw 1 in LAS Test Block Specimen

### 5.3.2 ACOUSTIC EMISSION

#### Introduction

From work reported earlier (1) it was concluded that since various test specimens exhibited a different acoustic emission (AE) response to stress, the fracture surfaces should reveal the particular failure morphology associated with the detected acoustic emission. Examination of the fractured surfaces was initiated to establish this correlation, since this relationship could result in obtaining more meaningful information relating to the manner in which a ceramic material fractures.

#### Discussion

In analyzing the fracture surface of LAS test bars with the express purpose of identifying the characteristics which will help to separate the many active variables affecting the ceramic's response to stress, two obvious points of interest were observed. (1) The acoustic emission summation curves with the best indication of impending failure exhibit a classical fracture morphology, and (2) extremely high summations of acoustic emission events at low stress levels are associated with a fracture origin outside of the central area on the tensile surface of the flexure bars.

Some of the fracture characteristics associated with the AE curves with the best indication of impending failure were:

1. A small zone of fast crack propagation surrounded the flaw and expanded towards the neutral axis of the test bar.
2. Areas of slow crack propagation (hackle) were observed at the tensile corners which resulted in a reduction of the fast crack wave front propagation through the bar.
3. Surface macrocracks were oriented approximately parallel to the fracture surface but did not intersect the final failure initiation site.
4. The extent of macrocracking seems to be associated with the slow propagation region since a greater amount of hackle tends to also exhibit a greater amount of macrocracking on the near tensile surface.

The fracture characteristics associated with those specimens with little precursor to final failure were:

1. Failure was located outside the central area of the surface of maximum tension, usually at a tensile corner of the flexure bar.
2. A small zone of fast crack propagation surrounded the initiator which in turn was surrounded by an area with much crack branching resulting in gross undulation of the surface.
3. Surface macrocracking was not observed on the tensile surface.

Flaws located within 1/32 of an inch of surfaces of maximum tension were found on fracture surfaces of samples which exhibited both types of AE response.

This latter type of behavior is shown in Figure 5.97, by the acoustic emission vs relative load curve for test bar No. 7-15. The fracture morphology is shown in Figure 5.98. The magnitude of acoustic emission events shown in Fig. 5.97, is much higher than the curves depicting classical fracture, shown in Fig. 5.99 for bar No. 3-4.

The acoustic emission curve depicting the failure of bar No. 3-4 (classical fracture morphology as shown in Fig. 5.100) was accomplished on a more sensitive acoustic emission scale than bar No. 7-15. The precursor to failure was evident at this sensitivity but not at the level used in Figure 5.97 for the bar No. 7-15.

During the previous phase of test program, it was noted that the curves obtained by a continuous loading process had a specific geometry (1). This can be visualized as a three-stage process suggesting the following:

1. An initial high rate of acoustic emission at low stress levels.
2. A mid-range stress level where little acoustic emission was noted.
3. A final range where resumption of acoustic emission is followed by catastrophic failure.

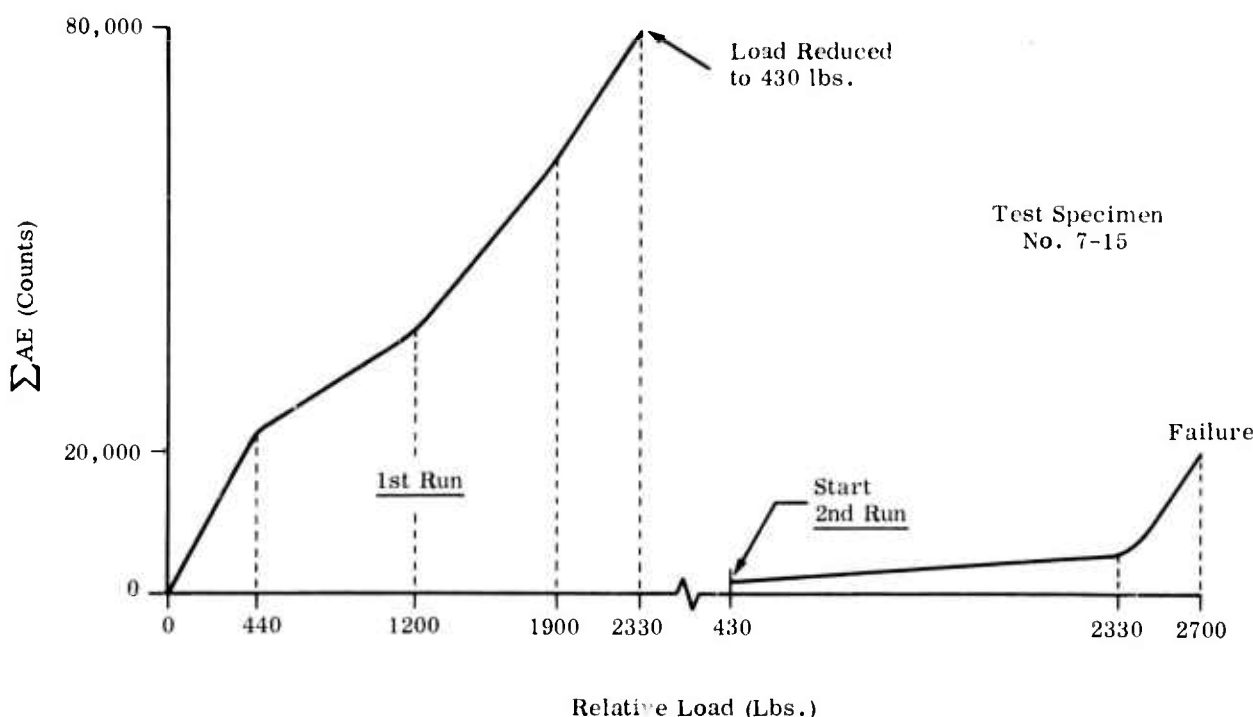


Figure 5.97 — Reproduction of AE vs Relative Load Curve Showing the Magnitude of Events Occurring at Low Loads

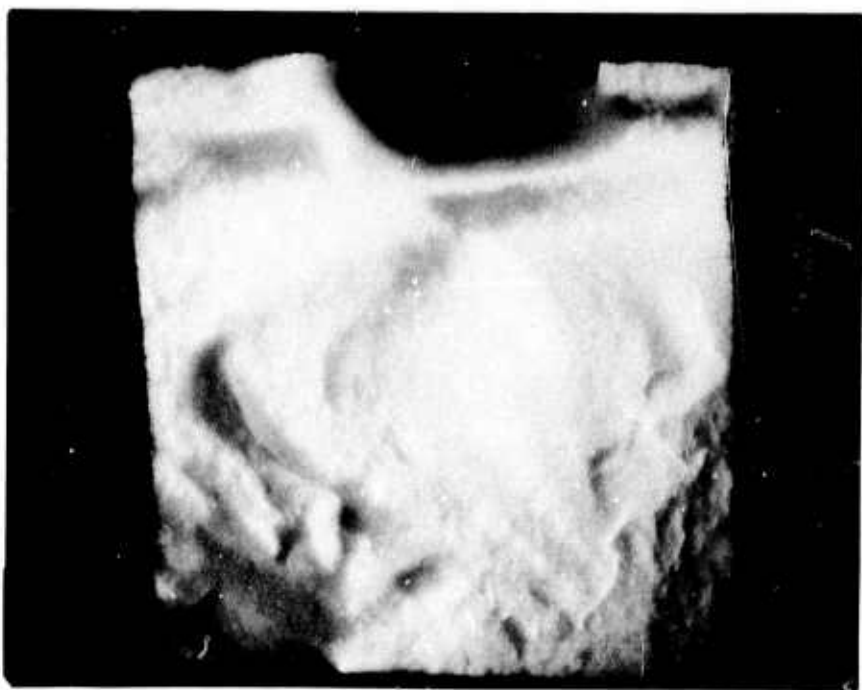


Figure 5.98 — Fracture Surface of Test Specimen No. 7-15 Showing the Crack Initiation Site in the Lower Right Hand Corner

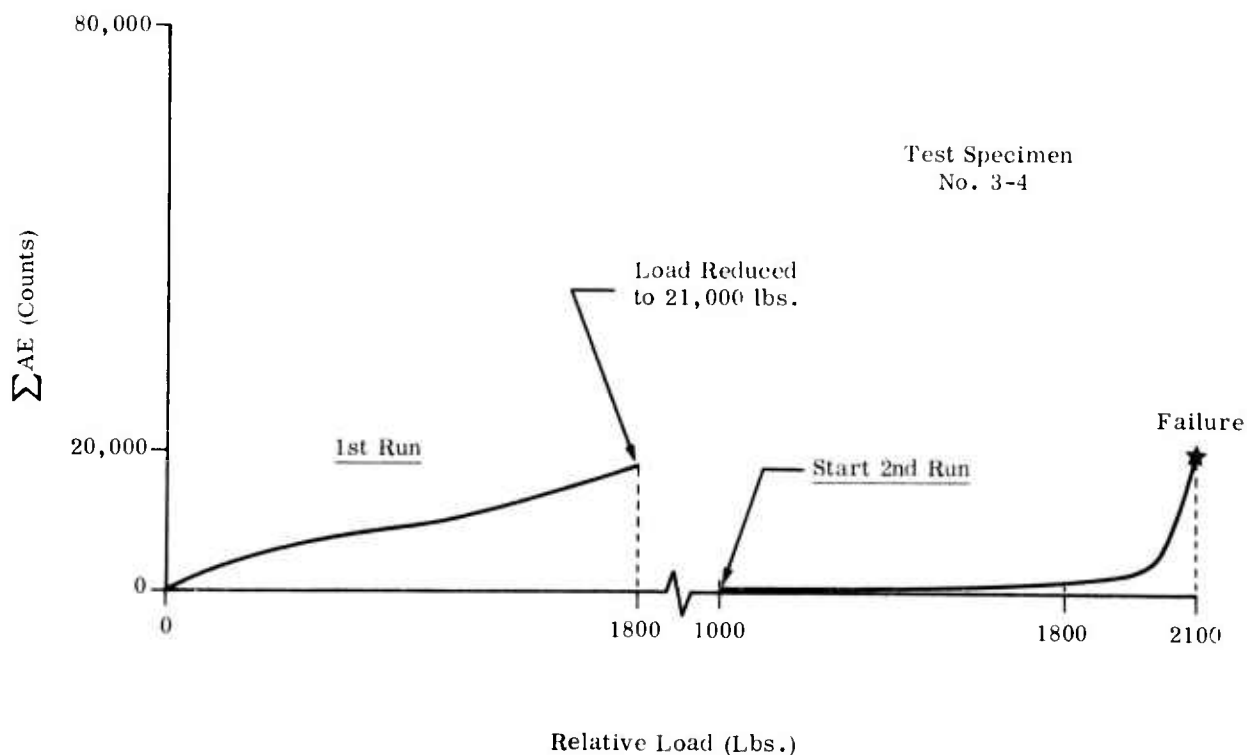


Figure 5.99 — Reproduction of AE vs Relative Load Curve Showing the Magnitude of Events Occurring at Low Loads



Figure 5.100 — Fracture Surface of Test Specimen No. 3-4 Showing the Crack Initiation Site in the Middle of the Lower Surface

The resulting curve is comparable to that of a metal system having primary, secondary, and tertiary stages of associated creep. Although this is a very interesting aspect to pursue and would imply that a means of identifying various modes of fracture was possible, further substantiation is needed. It is intended to evaluate this effect in the future with improved instrumentation capability.

This preliminary investigation has led to identifying other characteristics which are meaningful in terms of establishing parameters for failure analysis. One of these effects, to be studied in future tests, is the relationship of the fast crack propagation area surrounding the initiating flaw to the strength and acoustic emission response of the ceramic system. Since a critical fracture velocity is necessary to form a mirror boundary, (31) the presence of mirror boundaries of varying size fracture velocity may yield subsequent information relating to the structure of the ceramic material (32).

Other characteristics pointed out during this investigation were the size, type, and morphology of the flaws initiating the final fracture surface. During the next phase of testing, the size effect will be examined by introducing flaws in the flexure bar by machining. This should allow for more meaningful acoustic emission data because the location of the flaw necessary for failure will not be located at random and the material's response to stress will be more dependent on the inherent material structure since surface effects will be eliminated.

### 5.3.3 X-RAY RADIOGRAPHY

#### Introduction

In order to optimize a given inspection or evaluation system, several available means must be employed to establish the relationships being developed. The method being developed can then be evaluated on a comparison basis and the advantages and disadvantages determined. This initial study to determine the effects of low voltage x-rays on ceramics, was formulated with the purpose of ultimately detecting unwanted phases. Previous work at the Army Materials and Mechanics Research Center, Watertown, Massachusetts, showed that low x-ray voltages provided a high degree of sensitivity relative to impurity and undesirable phases (33). These phases may not be detectable ultrasonically because their interface with the matrix material may not have sufficient acoustic impedance.

Lithium-aluminum-silicate (LAS) ceramic material was chosen as the initial material for this study, since the knowledge gained from previous ultrasonic testing would be helpful in interpreting defect indications. The ultrasonic signals associated with the porous nature of this LAS material are such that a certain level of background indication is normally received. Flaws with a low acoustic impedance can be hidden in this background level. Alternate means then be taken to detect these indications, one of which is radiographic analysis.

Research work on the stationary turbine project for the radiographic examination of hot pressed billets and airfoils produced by the Norton Company, was initiated in cooperation with the Army Materials and Mechanics Research Center. Preliminary results indicate that flaws and inclusions can be identified in hot pressed  $\text{Si}_3\text{N}_4$ .

#### Discussion

To begin the study, a LAS ultrasonic calibration block with flat-bottomed holes at a depth of 50% of the block thickness was used. The various kilovolts and exposure times are presented in Table 5.15. The film type of all cases was Kodak type MM with a 36 inch source-to-film distance. The x-ray machine was rated at 140 KV maximum and an 8 milliamp level was maintained for all tests.

Several radiographic reversal prints are shown in Figure 5.101. The optimum level is 75 kv for a period of 90 seconds, based on the variations made during this study. Also seen in these prints is a line running the complete length of the block, and a moon shaped indication about mid-way in the lower half of the block. The long line is the plane of low density associated with the fabricating techniques for this material. The moon shaped indication is probably a small shrinkage crack. In both cases the defects observed are of the void type which ultrasonically are easily detected. No indication of unwanted phases were observed, either because they were not present or because they do not absorb x-rays to the extent of providing sufficient film contrast. This study indicates that standards, containing known quantities of the impurities or phases sought, would be necessary in order to optimize the variables associated with x-ray methods.

**TABLE 5.15**  
**Kilovolt Levels and Exposure Times**  
**Used for Low Voltage X-Ray Study**

<u>Kilovolt Level</u>	<u>Exposure Time (Sec.)</u>
50	15
50	30
50	45
50	60
65	60
70	60
75	60
75	75
75	90
75	105
75	120



a.) 50 Kv for 45 sec.



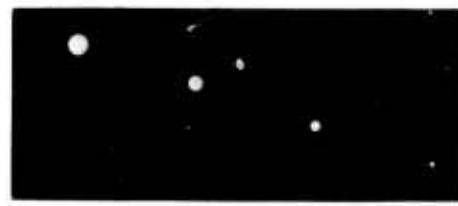
b.) 50 Kv for 60 sec.



c.) 75 Kv for 60 sec.



d.) 75 Kv for 90 sec.



e.) 75 Kv for 105 sec.

**Figure 5.101 — X-Ray Radiographic Reversal Prints of Ultrasonic Calibration Block No. 2**

Stator airfoils machined from hot-pressed silicon nitride were radiographed at AMMRC.

An example of a radiographed airfoil (designated #5) is shown in Fig. 5.102. X-ray parameters were: voltage 100 kv, current 5 milliamps, 40 inch focal film distance, and 2 minutes exposure using Eastman fine grain single emulsion (R) film. The negative was processed for 5 minutes in standard solutions at 68°F. Figure 5.102 is a positive print on a standard paper. No special arrangement was made to compensate for variation in the thickness of the airfoil from the leading to the trailing edges; hence, in order to bring out the most of the details for the purpose of illustration, the print was made in two parts. Therefore, the overall intensity variations as seen in Fig. 5.102 are not real.

Since the intensity differences in Fig. 5.102 do show flaws that may not be readily discernible, attention should be focused on the flaws marked by white circles. In all cases except the one marked with the black arrow, the flaws appear dark, indicating inclusions of higher density than the matrix material. The white flaw marked by the arrow has lower density, and thus could be a crack.

This program is continuing, and attempts will be made towards a positive identification of the various flaws. The radiography of test specimens is executed to assist in obtaining direct correlation between flaws and their effect upon mechanical properties.

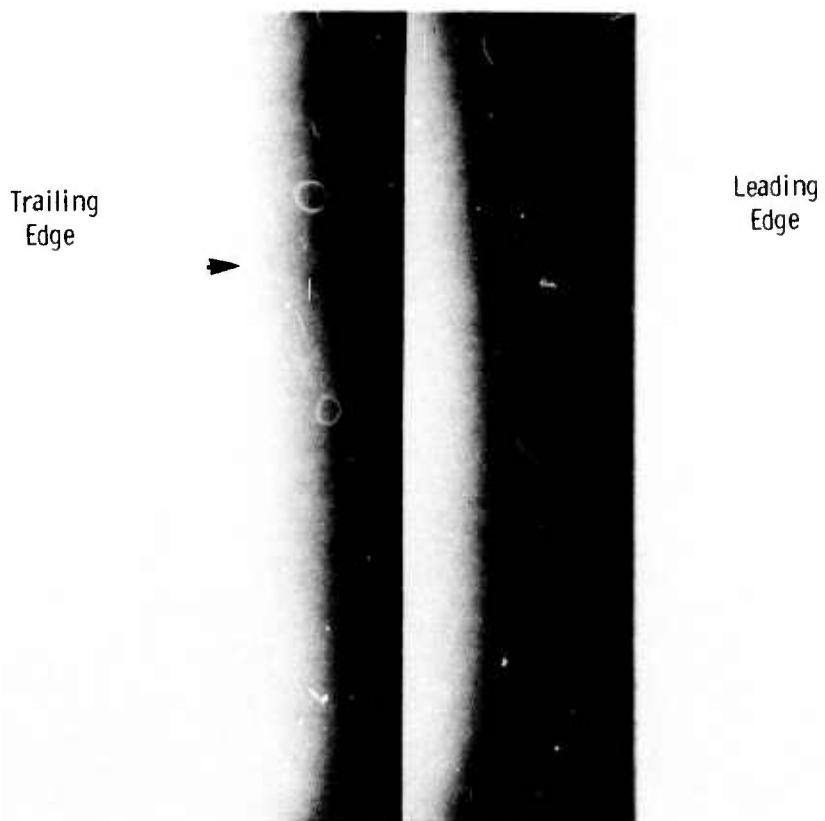


Figure 5.102 — Adjusted Positive Print of Radiographed Air Foil. Norton Company Vane #5 (Overall Intensity Variations not Real)

## 6. REFERENCES

1. McLean, A. F., Fisher, E. A., and Harrison, D. E., "Brittle Materials Design, High Temperature Gas Turbine," AMMRC CTR 72-3, Interim Report, July 1, 1971 to December 31, 1971.
2. Lumby, R. J. and Coe, R. F., "The Influence of Some Process Variables on The Mechanical Properties of Hot Pressed Silicon Nitride," Proceedings of the British Ceramic Society, No. 15, January, 1970.
3. Wilson, J. and Jack, K. H., "New Ceramic Materials Based on the Al-Si-N-O and Related Systems," Presented at the 74th Meeting of the American Ceramic Society, Washington, D.C., May, 1972.
4. Poritsky, H., "Stress and Deflections of Cylindrical Bodies in Contact," Journal of Applied Mechanics, (1950).
5. Weibull, W., "A Statistical Distribution Function of Wide Applicability," J. Appl. Mech., 18, (1951) p. 293-297.
6. Evans, A. G. and Sharp, J. V., "Transmission Electron Microscopy of Silicon Nitride," Proceedings, 5th Berkeley International Materials Symposium, Berkeley, California, September, 1971, p. 1141.
7. Heuer, A. H., Firestone, R. F., and Snow, J. D., "Non-Basal Slip in Aluminum Oxide," Proceedings 2nd International Conference on Strength of Metals and Alloys, (1971), Asilomar, ASTM, p. 1765.
8. Evans, A. G. and Sharp, J. V., "Microstructural Studies on Silicon Nitride," J. Mat. Sci. 6 (1971) p. 1292.
9. Farnsworth, P. L. and Coble, R. L., "Deformation Behavior of Dense Polycrystalline Silicon Carbide," J. Am. Cer. Soc., 49 (1966), p. 264.
10. Hirth, J. P., and Lothe, J., "Theory of Dislocation," McGraw-Hill, (1968), p. 498.
11. Hillig, W. B. and Charles, R. J., "Delayed Failure of Polycrystalline and Single Crystal Alumina," John Wiley & Sons Inc. New York (1965).
12. Charles, R. J. and Shaw, R. R., General Electric Corp. Report 62-41-3081M, (1962).
13. "Phase Diagrams for Ceramists," American Ceramic Society, (1964), p. 210.
14. Mencik, Z., and Short, M. A., "Quantitive Phase Analysis of Synthetic  $Si_3N_4$  by X-Ray Diffraction," Ford Motor Company Report No. SRM 72-06, March 1972.
15. Wild, S., Grieveson, P., and Jack, K. H., "Role of Silicon Monoxide in The Production and Stability of Silicon Nitrides and Oxynitrides", Presented at 74th Annual Meeting of the American Ceramic Society, Washington, D. C., May 1972.

16. Stokes, R. F., Lumby, R. J., and Coe, R. F., "Hot Pressing of Alpha Silicon Nitride Powder," Presented at the 74th Meeting of the American Ceramic Society, Washington, D.C., May 1972.
17. Frangos, T. F., "Silicon Nitride Refractories Offers . . .," Design Engineering, Vol. 47, No. 1, p. 116, January 1958.
18. Evans, A. E. and Davidge, R. "The Strength and Oxidation of Reaction Sintered  $\text{Si}_3\text{N}_4$ ," Journal of Materials Science 5 (1970) p. 314-325.
19. Stull, D. R., Prophet, H., et al., JANAF Thermochemical Tables, NSRDS-NBS 37, (1971).
20. Wagner, C., "Passivity During the Oxidation of Silicon at Elevated Temperatures," J. Appl. Phy., 29, (1958), p. 1295.
21. Adamsky, R. F., "Oxidation of Silicon Carbide in the Range 1200 to 1500°C," J. Phys. Chem., 63, (1959), p. 305.
22. Kofstad, P., "High Temperature Oxidation of Metals," John Wiley & Sons, Inc., New York (1966).
23. Sucov, E. W., "Diffusion of Oxygen in Vitreous Silica," J. Am. Ceram. Soc., 46, (1963), p. 14.
24. Horton, R. M., "Oxidation Kinetics of Various Silicon Nitrides," J. Am. Cer. Soc., 52, (1969), p. 121.
25. Jorgensen, P. J., Nadsworth, M. E. and Cutler, I. B., "Oxidation of Silicon Carbide," J. Am. Cer. Soc., 42, (1959), p. 613.
26. Nakatogawa, T., "Silicon Carbide and Non-Ohmic Resistors - Part II -," Chem. Soc. of Japan, 2nd Chem. Sect. 57, (1954), p. 348.
27. Ainger, F. F., "Formation and Devitrification of Oxides in Silicon," J. Mat. Sci. 1, (1966).
28. Deal, B. E., "Oxidation of Silicon in Dry Oxygen, Wet Oxygen, and Steam," J. Electrochem. Soc. 110, (1963), p. 527.
29. Evith, H. C., Cooper, H. F. and Flaschem, S. C., "Rate of Formation of Thermal Oxides of Silicon," J. Electrochem. Soc. 111, (1964), p. 699.
30. Williams, E. L., "Diffusion of Oxygen in Fused Silica," J. Am. Cer. Soc., 48, (1965), p. 190.
31. "Chemical Strengthening of Ceramic Materials," Ceramic Finishing Company Summary Report, Contract N0019-71-C-0208, December 1971.
32. Katz, R. N., and Brantley, W. A., "Fractography of High Boron Ceramics Subjected to Ballistic Loading," Material Science Research, Vol. 5, Edited by W. Worth Kriegel and Hayne Palmour II, Plenum Publishing Corp., New York, p. 271.
33. Harris, G. M. and DerBoghosian, S., "Detection and Classification of Imperfections in Ceramic Armour Materials," Presented at the 74th Meeting of the American Ceramic Society, Washington, D.C. May 1972.

ARMY MATERIALS AND MECHANICS RESEARCH CENTER  
WATERTOWN, MASSACHUSETTS 02172

TECHNICAL REPORT DISTRIBUTION

No. of Copies	To
1	Office of the Director, Defense Research and Engineering, The Pentagon, Washington, D. C. 20301
12	Commander, Defense Documentation Center, Cameron Station, Building 5, 5010 Duke Street, Alexandria, Virginia 22314
1	Metals & Ceramics Information Center, Battelle Memorial Institute, 505 King Avenue, Columbus, Ohio 43201
2	Chief of Research and Development, Department of the Army, Washington, D.C. 20310 ATTN: Physical and Engineering Sciences Division (CRD PES - Dr. Sullivan)
1	Commanding Officer, Army Research Office (Durham), Box CM, Duke Station Durham, North Carolina 27706 ATTN: Dr. H. M. Davis
1	Commanding General, U. S. Army Material Command, Washington, D. C. 20315 ATTN: AMCRD-TC (Dr. El-Bisi)
1	ATTN: ANCDL (Dr. Dillaway)
1	Commanding General, U. S. Army Missile Command, Redstone Arsenal, Alabama 35809 ATTN: Technical Library
1	Commanding General, U. S. Army Munitions Command, Dover, New Jersey 07801 ATTN: Technical Library
1	Commanding General, U. S. Army Tank-Automotive Command, Warren, Michigan 48090 ATTN: AMSTA-BSL, Research Library Br
1	Commanding General, U. S. Army Weapons Command, Research and Development Directorate, Rock Island, Illinois 61201 ATTN: AMSWE-RDR
1	Commanding Officer, Aberdeen Proving Ground, Maryland 21005 ATTN: Technical Library, Building 313
1	Commanding Officer, U. S. Army Aviation Material Laboratories, Fort Eustis, Virginia 23604

No. of Copies	To
1	Librarian, U.S. Army Aviation School Library, Fort Rucker, Alabama 36360 ATTN: Bldg. 5907
1	Commanding Officer, USACDC Ordnance Agency, Aberdeen Proving Ground, Maryland 21005 ATTN: Library, Building 350
1	Commanding Officer, U.S. Army Engineer Waterways Experiment Station, Vicksburg, Mississippi 39180 ATTN: Research Center Library
1	Commanding Officer, U.S. Army MERDC, Fort Belvoir, Virginia 22060
1	ATTN: SMEFB-EP (Mr. James Horton)
1	ATTN: SMEFB-EP (Mr. W. McGovern)
	Director, Army Materials and Mechanics Research Center, Watertown, Massachusetts 02172
2	ATTN: AMXMR-PL
1	AMXMR-PR
1	AMXMR-CT
1	AMXMR-AP
1	AMXMR-X (Dr. Gorum)
1	AMXMR-EO (Dr. Katz)
1	AMXMR-TM (Dr. Lenoie)
1	AMXMR-D (Dr. Priest)
1	AMXMR-EO (Dr. Messier)
2	AMXMR-P (Dr. Burke)
	Advanced Research Projects Agency, 1400 Wilson Blvd., Arlington, Virginia 22209
2	ATTN: Director
1	ATTN: Dep. Director (Dr. Sinnott)
1	ATTN: Director for Materials Sciences
1	ATTN: Dep. Director Materials Sciences (Dr. Stickley)
1	Mr. R. M. Standahar, Office of the Director of Defense, Research and Engineering, Room 3D1085, Pentagon, Washington, D.C. 20301
1	Mr. Charles F. Bersch, Department of the Navy, Naval Air Systems Command, Washington, D.C. 20360
1	Dr. A. M. Diness, Metallurgy Branch, Code 471, Office of Naval Research, 800 N. Quincy Street, Arlington, Virginia 22217

---

No. of Copies	To
1	Mr. Irving Machlin, High Temperature Materials Div., Materials and Processes Branch, (NAIR-52031D), Naval Air Systems Command, Department of the Navy, Washington, D. C. 20360
1	Mr. Keith Ellingsworth, Office of Naval Research, Power Program, Arlington, Virginia 22217
1	Mr. John Fairbanks, Naval Ships Engineering, Prince Georges Center, Hyattsville, Maryland 20782
1	Lt. A. Hober, Air Force Aeropropulsion Lab, Wright-Patterson Air Force Base, Ohio 45433
1	Capt. Smyth, Air Force Materials Laboratory, Wright-Patterson Air Force Base, Ohio 45433
1	Mr. S. Lyons, Wright-Patterson Air Force Base, Ohio 45433
1	Dr. Henry Graham, Aerospace Research Laboratory, ATTN: ARL-LL, Wright-Patterson Air Force Base, Ohio 45433
1	Mr. W. Sanders, NASA Lewis Research Center, 21000 Brookpark Road, Cleveland, Ohio 44135
1	Dr. Hubert Probst, NASA Lewis Research Center, 21000 Brookpark Road, Cleveland, Ohio 44135
1	Dr. G. C. Deutsch, Ass't Director of Research (Materials), Code RR-1 NASA, Washington, D. C. 20546
1	Mr. George Staber, Office of Coal Research, U. S. Department of the Interior, Washington, D. C. 20240
1	Mr. S. Wiederhorn, Physical Properties Section, Institute for Materials Research, National Bureau of Standards, Washington, D. C. 20234
1	Mr. R. Reynik, Director, Div. of Materials Research, National Science Foundation, 1800 G. Street, N.W., Washington, D. C. 20550
1	Dr. Robb Thomson, Senior Research Scientist, Room B109, Building 225, National Bureau of Standards, Washington, D. C. 20234
1	Mr. H. Morrow, Eustis Directorate, AMRDL, Fort Eustis, Virginia 23604

---

No. of Copies	To
1	Dr. R. Warren, Contact Officer, Defense Research & Development Staff, British Embassy, 3100 Massachusetts Avenue N.W., Washington, D. C. 20008
1	Mr. Robert Schulz, Thermal & Mechanical Systems Branch, Div. of Advanced Automotive Power Systems Development, 2565 Plymouth Road, Ann Arbor, Michigan 48105
1	Mr. Thomas Sebestyen, Environmental Protection Agency, Div. of Advanced Automotive Systems, 2565 Plymouth Road, Ann Arbor, Michigan 48105
1	Dean Daniel C. Drucker, Engineering College, University of Illinois, Urbana, Illinois 61801
1	Professor Merton Flemings, Massachusetts Institute of Technology, Cambridge, Massachusetts 02139
1	Professor Edward E. Hucke, Materials and Metallurgical Engineering, The University of Michigan, Ann Arbor, Michigan 48104
1	Professor Frank A. McClintock, Department of Mechanical Engineering, Massachusetts Institute of Technology, Cambridge, Massachusetts 02139
1	Dr. R. M. Spriggs, Assistant to the President, Lehigh University, Bethlehem, Pennsylvania 18015
1	Mr. J. D. Walton, Jr., EES, Georgia Tech., Atlanta, Georgia 30332
1	Mr. Y. Baskin, Manager Inorganic Chemical Research, Technical Center, Ferro Corporation, 7500 East Pleasant Valley Road, Independence, Ohio 44131
1	Mr. Robert Beck, Dept. Head, Development Materials, Teledyne CAE, 1330 Laskey Road, Toledo, Ohio 43601
1	Dr. J. E. Burke, General Electric Company, Corporate Research & Development, P. O. Box 8, Schenectady, New York, 12301
1	Mr. Ken Zeman, Turbine and Combustor Design, General Electric Company, Aircraft Engine Group, Cincinnati, Ohio 45215
1	Dr. C. A. Bruch, Manager, Advanced Studies, General Electric Company, Aircraft Engine Group, Cincinnati, Ohio 45215
1	Mr. A. R. Canady, Caterpillar Tractor Company, Technical Center, Bldg. F, Peoria, Illinois 61602

No. of Copies	To
1	Mr. William B. Crandall, IIT Research Institute, 10 West 35 Street, Chicago, Illinois 43601
1	Mr. L. M. Donley, Owens Illinois Glass, 1900 North Westwood Avenue, Toledo, Ohio 43601
1	Mr. E. J. Dulis, President, Colt Industries, Materials Research Center, Box 88, Pittsburgh, Pennsylvania 15230
1	Mr. O. Prachar, Passenger Car Turbine Department, Engineering Staff, General Motors Technical Center, Warren, Michigan 48090
1	Mr. Winston Duckworth and Mr. Lewis E. Hulbert, Battelle Columbus Laboratories, 505 King Avenue, Columbus, Ohio 43201
1	Mr. R. Engdahl, Energy Research Corporation, Bethel, Connecticut 06801
1	Mr. Peter L. Fleischner, National Beryllia Corp., Haskell, New Jersey 07420
1	Mr. O. I. Ford, Technical Manager, Combustor Systems, Aerojet Liquid Rocket Company, P. O. Box 18222, Sacramento, California 95813
1	Mr. A. D. Foster, Manager, High Temperature Materials Engineering, General Electric Company, Corporate Research & Development, P. O. Box 8, Schenectady, New York 12301
1	Mr. John V. E. Hansen, Norton Company, 1 New Bond Street, Worcester, Massachusetts 01606
1	Mr. M. Herman, Detroit Diesel Allison Division, General Motors Corporation, Indianapolis Operations, P. O. Box 894, Indianapolis, Indiana 46206
1	Mr. C. Vigor, Engineering Sciences, Detroit Diesel Allison Division, General Motors Corporation, Indianapolis Operations, P. O. Box 894, Indianapolis, Indiana 46206
1	Mr. J. B. Mann, Director of Research, Chrysler Corporation, P. O. Box 1118 Detroit, Michigan 48231
1	Mr. James F. Holloway, Materials Project Engineer, Pratt & Whitney Corporation, 400 Main Street, E. Hartford, Connecticut 06108
1	Dr. Paul Jorgensen, Associate Director, Materials Laboratory, Stanford Research Institute, Menlo Park, California 94025

No. of Copies	To
1	Dr. A. V. Illyn, Technical Director, Refractories Division, Babcock & Wilcox, Old Savannah Road, Augusta, Georgia 30903
1	Mr. Paul F. Jahn, Vice President, Fiber Materials, Inc., Broadway and Main Streets, Graniterville, Massachusetts 01829
1	Dr. Robert F. Kirby, Materials Engineering Dept. 93-393M, AiResearch Manufacturing Company, Div. of the Garrett Corporation, Sky Harbor Airport, 402 South 36th Street, Phoenix, Arizona 85034
1	Mr. John G. Lanning, Corning Glass Works, Corning, New York 14830
1	Mr. William D. Long, Manager, Product Development, K-Ramics, Kaman Sciences Corporation, Garden of the Gods Road, Colorado Springs, Colorado 80907
1	Mr. James Lynch, Metals & Ceramics Information Center, Battelle Columbus Laboratories, 505 King Avenue, Columbus, Ohio 43201
1	Mr. L. Lucarelli, Manager of Materials, Corporate R&D Center, Kelsey-Hayes Company, 2500 Green Road, Ann Arbor, Michigan 48105
1	Mr. C. H. McMurtry, Project Manager, Research and Development Div., The Carborundum Company, Niagara Falls, New York 14302
1	Dr. Deo Mattoon, Sing Sing Road, Horseheads, New York 14845
1	Mr. G. Kookootsedes, Market Development, Resins and Chemicals, Dow Corning, Midland, Michigan 48640
1	Professor Burton Paul, Dept. of Mechanical Engineering, University of Pennsylvania, Philadelphia, Pennsylvania 19104
1	Mr. Y. K. Pei, Owens Illinois Glass, 1020 North Westwood Avenue, Toledo, Ohio 43607
1	Dr. Jerry D. Plunkett, President, Material Consultants, Inc., 2150 South Josephine Street, Denver, Colorado 80210
1	Mr. J. A. Rubin, President, Ceradyne Incorporated, 8948 Fullbright Avenue, Chatsworth, California 91311
1	Mr. P. Hansen, Director or Corporate Dev., Kawecki-Beryleco Industries, Inc., P.O. Box 1462, Reading, Pennsylvania 19603

---

No. of Copies	To
1	Mr. Jack W. Sawyer, Gas Turbine International, 4519 Eighteen Street North, Arlington, Virginia 22207
1	Mr. D. W. McLaughlin, Research & Development Div., Mechanical Technology, Inc., 968 Albany-Shaker Road, Latham, New York 12110
1	Mr. A. R. Stetson, Chief, Process Research Laboratories, Mail Zone R-1, Solar Div. of Int. Harvester Company, 2200 Pacific Highway, San Diego, California 92112
1	Mr. R. Graham, Managing Director, Advanced Materials Engineering, Ltd., AIDAN House, Tynegate Precinct, Gateshead, County Durham, NE83HX, England
1	Dr. M. L. Torti, Norton Company, 1 New Bond Street, Worcester, Massachusetts 01606
1	Dr. Rhodes, Applied Technology Division, Avco Corporation, Lowell Industrial Park, Lowell, Massachusetts 01851
1	Mr. Francis L. VerSnyder, Manager, Materials Engineering and Research Lab, Pratt & Whitney Corporation, 400 Main Street, E. Hartford, Connecticut 06108
1	Mr. McCoy, Materials Engineering, Garrett-AirResearch Dept. 93-393M, 412 South 36th Street, Phoenix, Arizona 85034
1	Mr. Donald E. Weyer, Dow Corning Corporation, Midland, Michigan 48640
1	Dr. Michael Guinan, B Div./L-24, P. O. Box 808, Lawrence Livermore Laboratory, Livermore, California 94550
1	Dr. Mark Wilkins, B Div./L-24, P. O. Box 808, Lawrence Livermore Laboratory, Livermore, California 94550
1	Mr. Charles J. McMahon, Jr., Assoc. Prof. Materials Science, School of Metallurgy & Materials Science, University of Pennsylvania, 3231 Walnut Street, Philadelphia, Pennsylvania
1	Mr. Gaylord D. Smith, The International Nickel Co., Inc., 1 New York Plaza, New York, New York 10004

---

No. of Copies	To
1	Mr. H. R. Schelp, Garrett Corporation, 9851 Sepulveda Blvd., Los Angeles, California 90009
1	Mr. Robert Widner, President, Industrial Materials Technology 19 Wheeling Avenue, Woburn, Massachusetts
1	Dr. William Wells, Lawrence Livermore Lab, Livermore, California 94550
1	Prof. R. P. Kroon, University of Pennsylvania, Philadelphia, Pennsylvania
1	Mr. Paul G. Shewmon, D212, Argonne National Laboratory, 9700 South Cass Ave., Argonne, Illinois 60439
1	Dr. Thomas D. McGee, Professor of Ceramic Engineering, Iowa State University, Ames, Iowa 50010
1	Mr. Joe Glotz, Department of the Navy, Naval Air Propulsion Test Center, Trenton, New Jersey 08628
1	Mr. John Miguel, Naval Underwater Systems Center, Newport, Rhode Island
1	Mr. Robert Benham, AEP-22, U.S. Naval Air Propulsion Test Center (AE), Philadelphia, Pa. 19112
1	Mr. R. Barry Strachan, Williams Research Corp., Walled Lake, Michigan 48088
1	Mr. S. Walosin, Curtis-Wright Corp. One Passaic Street, Woodridge, N.J. 07075
1	Prof. Marc Richman, Engineering Division, Brown University, Providence, Rhode Island 02912
1	Mr. R. Rice, Naval Research Laboratory, Washington, D.C. 20390
1	Mr. George A. Wacker, Head Metal Physics Br., Naval Ships Research & Development Center, Annapolis, Md. 21402, ATTN: Code 2812
1	Dr. R. Charles, Manager Ceramics Branch, General Electric Co., Corporate R. & D Center, P.O. Box 8, Schenectady, New York 12301
1	Mr. C. F. Cline, Manager, Strength Physics Department, Allied Chemical Corporation, P.O. Box 1021R, Morristown, New Jersey 07960
1	Dr. J. T. Bailey, American Lava Corp., Chattanooga, Tennessee 37405
1	Mr. S. T. Wlodek, Cabot Corp. Stellite Div., 1020 West Park Avenue, Kokomo, Indiana 46901
1	Mr. K. J. Mather, Cummins Engine Company, Inc., Columbus, Indiana 47201
1	Mr. J. D. Mote, EF Industries, Inc., 1301 Courtesy Rd. Louisville, Colo. 80027
1	Mr. William E. Gurwell, Eaton Corporation, Research Center 26201 Northwestern Highway, Southfield, Michigan 48076

No. of Copies	To
1	Mr. Robert W. Gibson, Jr., Head, Library Dept. General Motors Corporation GM Technical Center, Warren, Michigan 48090
1	Mr. R. L. Lormand, Lawrence Radiation Lab, P.O. Box 808, Livermore, California 94550
1	Ms. Kathie Bolick, National Aeronautics and Space Administration, Goddard Space Flight Center, Greenbelt, Maryland 20771
1	Mr. Neil T. Saunders, Ch. Mat'l's Appl'n Branch, National Aeronautics and Space Administration, Lewis Research Center, Cleveland, Ohio 44135
1	Ms. Rayna Lee Caplan, Librarian, Northern Research and Engineering Corp., 219 Vassar Street, Cambridge, Massachusetts 02139
1	Mrs. Jame Bookmyer, Info. Services Div., PPG Industries, Inc., P.O. Box 11472 Pittsburgh, Pennsylvania 15238
1	Mr. F. W. Parsons, Manager, Commercial Research Dept., Stackpole Carbon Company, St. Marys, Pennsylvania 15857
1	Ms. Lucille Steelman, Order Librarian, Stanford Research Institute ATTN: G-037 Library, Menlo Park, California 94025
1	Technical Library, TRW Equipment, TRW Inc., 23555 Euclid Avenue Cleveland, Ohio 44117
1	Ms. Marlene S. Dowdell, Librarian, Teledyne CAE, 1330 Laskey Road, Toledo, Ohio 43601
1	Dr. E. P. Flint, U.S. Department of Interior Bureau of Mines, Room 4513, Interior Bldg., Washington, D.C. 20240
1	Mr. W. Wheatfall, Naval Ship R & D Lab, Code 2812, Annapolis, Maryland 21402
1	Dr. Joseph E. Motherway, University of Bridgeport, Bridgeport, Connecticut 06602
3	Authors
160	Total Copies Distributed



Unclassified

Security Classification

DOCUMENT CONTROL DATA - R & D

(Security classification of title, body of abstract and indexing annotation must be entered when the overall report is classified)

1. ORIGINATING ACTIVITY (Corporate author)		2a. REPORT SECURITY CLASSIFICATION Unclassified
Ford Motor Company Dearborn, Michigan 48121		2b. GROUP
3. REPORT TITLE  Brittle Materials Design, High Temperature Gas Turbine		
4. DESCRIPTIVE NOTES (Type of report and inclusive dates) Interim Report, January 1, 1972 to June 30, 1972		
5. AUTHOR(S) (First name, middle initial, last name)  Arthur F. McLean Eugene A. Fisher Raymond J. Bratton		
6. REPORT DATE  September, 1972	7a. TOTAL NO. OF PAGES 210	7b. NO. OF REFS 33
8a. CONTRACT OR GRANT NO.  DAAG 46-71-C-0162	9a. ORIGINATOR'S REPORT NUMBER(S)  AMMRC-CTR 72-19	
b. PROJECT NO.  ARPA Order No. 1849	9b. OTHER REPORT NO(S) (Any other numbers that may be assigned this report)	
c. Project Code No. 1D10		
d. Agency Accession No. DA OD 4733		
10. DISTRIBUTION STATEMENT  Distribution limited to U.S. Government agencies only; Test and Evaluation data; September 1972. Other requests for this document must be referred to the Director, Army Materials & Mechanics Res. Center, ATTN: AMXMR-PL, Watertown, Massachusetts 02172		
11. SUPPLEMENTARY NOTES	12. SPONSORING MILITARY ACTIVITY  Army Materials and Mechanics Research Center Watertown, Massachusetts 02172	
13. ABSTRACT  The "Brittle Materials Design, High Temperature Gas Turbine" program is to demonstrate successful use of brittle materials in demanding high temperature structural applications. A small vehicular gas turbine and a large stationary gas turbine, each utilizing uncooled ceramic components, will be used in this iterative design and materials development program. Both the contractor, Ford Motor Company, and the subcontractor, Westinghouse Electric Corporation, have had in-house research programs in this area prior to this contract.  In the vehicular turbine project, the improved second generation (Design B) stationary ceramic components made of reaction bonded silicon nitride have undergone initial engine tests successfully. A computer program has been developed to determine heat transfer in the rotor, attachment, and shaft assembly. A design study was completed for the attachment of the rotor to the shaft. A complete integral rotor has been fabricated by chemical vapor deposition of silicon carbide, although material quality needs improvement. An etching technique has been developed permitting microstructure study of any form of silicon nitride, and significant determinations were made of ceramic material properties.  In the stationary turbine project, a first generation 3-piece vane assembly was designed and analyzed. A complete set of silicon nitride airfoil vanes were fabricated. Engineering properties of silicon nitride and silicon carbide have been characterized. A better understanding of the effects of microstructure on properties of hot pressed silicon nitride was obtained. Data was obtained on static oxidation kinetics and corrosion-erosion behavior.		

Unclassified

Security Classification

KEY WORDS	LINK A		LINK B		LINK C	
	ROLE	WT	ROLE	WT	ROLE	WT
Gas turbine engine						
Brittle design						
Ceramics						
High-temperature materials						
Silicon nitride						
Silicon carbide						
Non-destructive tests						

Unclassified

Security Classification